

Morphology and Large-Scale Structure within the Horologium-Reticulum Supercluster of Galaxies

Matthew Clay Fleenor

A dissertation submitted to the faculty of the University of North Carolina at Chapel Hill in partial fulfillment of the requirements for the degree of Doctor of Philosophy in the Department of Physics & Astronomy.

Chapel Hill

2006

Approved by
Advisor: James A. Rose
Reader: Gerald Cecil
Reader: Wayne A. Christiansen
Reader: Dan Reichart
Reader: Paul Tiesinga

©2006
Matthew Clay Fleenor

ABSTRACT

MATTHEW CLAY FLEENOR: Morphology and Large-Scale Structure within the
Horologium-Reticulum Supercluster of Galaxies
(Under the Direction of James A. Rose)

We have undertaken a comprehensive spectroscopic survey of the Horologium-Reticulum supercluster (HRS) of galaxies. With a concentration on the intercluster regions, our goal is to resolve the “cosmic web” of filaments, voids, and sheets within the HRS and to examine the interrelationship between them. What are the constituents of the HRS? What can be understood about the formation of such a behemoth from these current constituents? More locally, are there small-scale imprints of the larger, surrounding environment, and can we relate the two with any confidence? What is the relationship between the HRS and the other superclusters in the nearby universe? These are the questions driving our inquiry.

To answer them, we have obtained over 2500 galaxy redshifts in the direction of the intercluster regions in the HRS. Specifically, we have developed a sample of galaxies with a limiting brightness of $b_J < 17.5$, which samples the galaxy luminosity function down to one magnitude below M^* at the mean redshift of the HRS, $\bar{z} \approx 0.06$. Exclusively, these intercluster redshifts were obtained with the six-degree field (6dF), multi-fiber spectrograph at the Anglo-Australian Observatory. In conjunction with the wide-field, 1.2m UK Schmidt, 6dF is the ideal supercluster observatory. Because it deploys the 150 fiber buttons over a 6-degree field, we are able to obtain coherent information over large areas of the sky, as is the case with a supercluster.

In addition, we have obtained a complete sample of mean cluster redshifts and velocity dispersions for Abell clusters in the HRS using the Australian National University/2.3m, primarily. For most of the clusters, more than 10 galaxies were observed, and a reliable mean cluster redshift is determined. Furthermore, we have a near complete sample of $b_J < 18.6$ galaxies over a $4^\circ \times 4^\circ$ region that encompasses several HRS

clusters. With these datasets, we are able to “piece” together various structures over a large range of scales. We have also obtained high-resolution radio imaging over much of this smaller area.

We find six void structures in the region with $10 \leq R_{\text{VOID}} \leq 15 h^{-1} \text{ Mpc}$ that are completely absent of 6dF galaxies (except for one void that contains a single galaxy down to our observational limits). To discover the voids, we implement the GyVe software tool that provides a 3-D, interactive visualization environment. Furthermore, four of these voids are embedded within the supercluster environment, while the other two are located at the observed boundaries of the HRS. This is reflected in the intrinsically different galaxy number counts profiles as a function of radius. The voids maintain their distinct profiles despite the fact that the 6dF sample is augmented with thousands of previously published redshifts. We also observe that matter (galaxies and clusters) is not distributed evenly around these voids, but seems to follow a highly ordered arrangement.

Lastly, the intercluster regions ($5\text{--}10 h^{-1} \text{ Mpc}$) within one of the most dense HRS volumes are examined. We define three different intercluster extensions varying in overdensity from 20–60, which is 7–10 times the adjacent control volumes. Furthermore, we calculate a velocity dispersion of $\sim 350 \text{ km s}^{-1}$ within one intercluster filament $\sim 11 h^{-1} \text{ Mpc}$ in projected length. While varying in projected spatial width, the extended collection of intercluster galaxies joins the two richest complexes in the region. These galaxies also exhibit a preferred orientation of $60\text{--}90^\circ$ along its length. We further note that while some preferred orientations are found within smaller substructures, e.g., galaxy groups, these characterizations do not match the larger-scale galaxy distributions.

ACKNOWLEDGMENTS

“Every moment & every event of every person’s life on earth plants something in his soul.” –Thomas Merton

I know it sounds cliché, but this chapter of my life is really about other people. Know that your presence has planted good things in my soul. In these past five years, it is you who have been patient with me, listened to me, reminded me, taught me, and even disagreed with me. I am the most regretful person I know; and yet, when I survey the past five years, I have very few regrets, which is saying a lot of my experiences and the people who’ve shared it with me. So, thank you. I am always a debtor to your care.

“A pupil from whom nothing is ever demanded which s/he cannot do, never does all that s/he can.” –JS Mill

To **Jim**– I don’t think there is a better person on this earth, who could have been my adviser. You are so patient with my questions, with my misunderstandings, and with my mistakes. Thank you for taking a chance on me and letting me work with such a great project. It was such a travesty when you moved downstairs, and I am thankful for your open door. You’ve always helped me to take things in stride and maintain some balance, which I need. Thank you for trusting me and allowing me to see Down Under. I am thankful for your commitment to your family, to the observational world, to vacations without email, and of course, to the greatest Game ever played by boys. I am thankful that the HRS project is not complete, because I have good reason to come back and say hello.

To **Chuck**– I was saddened when I couldn’t come sit in your GR and E&M classes, but I know now that I wouldn’t be finishing right now if I had. As a student and the two classes I did have with you, it was a pleasure to sit in every class. Most days it was like taking a drink from a fire hydrant, and my understanding of the physical world would not be the same without your instruction. If you ever do teach a class on astrophysical radiation, I may ask for a sabbatical to come and listen and learn. As an educator, I have learned much about the use of time– every word packed with meaning, every problem bringing me to the brink of despair, and yet providing a wealth of understanding for those who persevered. Your notes will serve me well in the coming years; what a gift they are. Thank you for loving your vocation.

To **Dr. Becker**– for instilling in me an interest in the interconnection of structural phenomena and effects on microscopic scales. Thank you for your tough skin and your

kind heart, and also for the lessons of justice and truthfulness in the classroom. You are missed.

To **Wayne**– Thank you for trusting me with the valuable experience of teaching the Planetarium Lab. It was such an encouragement for three years, when I had no other teaching outlet. Thanks also for your creative mind regarding the formation of astrophysical structure; your collaboration and friendship are appreciated.

In fact, I thank all the astronomy professors– **Bruce, Chris, Dan,** and **Gerald**– who’ve always given their time, when I’ve asked it of them.

To **Paul**– for providing helpful input for the project and reading the thesis.

To **Russ**– for your creative exuberance toward the integration of visualization and the physical sciences, it is appreciated. Thanks for organizing the class and sticking with the project.

To **Dick**– for the many hours you’ve invested in the HRS project, and especially in my development as an observer and a writer. Even though your editing resulted in many hours, the explanation was always better as a result of your labor. I’m grateful for the time we shared at ATNF, Siding Spring, and of course, the Hunter Valley.

To **Rien**– Thank you for making ‘much ado about nothing.’ For the time I was able to spend at Kapteyn, it has increased my understanding of cosmology immensely.

To **Hugon**– for allowing an old geezer like me to experience such a wonderful department. For the encouragement and gentle (or not so gentle) prodding I received from you. Above all, I’m appreciative of your commitment to the people under your care, the grad students, and their intended purpose, getting out.

To **Duane**– Thanks for being yourself, writing those letters, and giving me the book on Teaching Portfolios. I know it made a difference.

To **Tom Lored**– for your honesty and openness and approachability. Our conversation will not soon be forgotten.

To **Michiel van Haarlem**– whose work of typing out the Mathams data has greatly aided this study and my understanding of the region.

To **Marc Lachiéze-Rey**– for writing a book with ‘beginners’ in mind, and for opening up the Universe to me.

To **Will, Saleem, Martin, Manolis**– for talking about, listening to, and answering my questions about the science.

To all the observers at the UKST- **Paul, Malcolm, Ken, Kristen,** Thank You.

To **Jane, Rich,** and all the faculty at **Roanoke College**– for allowing me to begin a new chapter, I’m honored.

“Real education should educate us out of self into something far finer– into selflessness which links us with all humanity...” –Nancy Astor

You’ve heard me say it before, but “What a wonderful place to work!” For **Barbara, Celeste, Sallie, Jean, Maryanne, Maggie, Donna, Carol, Marie, and Carolyn**– you folks are the foundation, and I’m thankful for your service and your kindness.

Laurie and Bruce– Thanks for running a tight ship, for listening to the peasants, and for smiling while you do it.

PANIC– where would I be without you. Thanks for answering promptly and fixing the problem.

Stephen, all the best to you, thanks for helping me understand ‘the black box.’

Brian P., “bp”, thanks for helping me understand **IRAF**, organizing my **login.cl**, providing helpful discussions, and lots of laughs on tough days. Hang in there, Bro.

Shane and Christy– thanks for keeping up with my computer requests, and also being my friend.

To the curator and volunteers at the **Coker Arboretum**– thanks for your time and attention to beauty, as well as providing a refuge and a haven. It will be sorely missed, but the memories of sunlight beaming through the thick canopy will be not forgotten.

“Really great things, when discussed by little folks, can usually make such folks grow big.” –Augustine

Melanie– Can you believe it? What a pleasure it’s been to learn about radio astronomy from you, and then to discover and ponder what is actually going on out there in A3128/25. Thanks for all the encouragement regarding grad school, writing, and applying for jobs. For all the work it took to arrange my stay in Tassie, it was like a dream. For Christmas dinner with your family, you made us feel at home. I hope our chapter is not over, and we can continue to work together.

Emilio– My friend, when I came to Kapteyn two years ago, you were so kind to talk and answer and explain, even though you were trying to finish your thesis. Now I know how you felt. Thanks for explaining to me the world of cosmological simulations and constrained realizations; over and over again. When you came last summer, I am thankful for that one question that has turned over in mind, “What is a supercluster?” For the two weeks in Groningen– movies, Euro cup, and the Grotomart, thanks for making me feel at home. May we endeavor to “constrain the HRS,” selection function and all. All the best to you and Sjouke.

Chris– For the density map codes that I’ve put to good use. And of course, for your hospitality in Tassie; thanks for your friendship and treating us like family.

Cory, Jameson– For GxV, I mean GyVe, and your partnership in collaboration, I’m thankful.

Jesse– Fellow member of the Nation. What can I say, my Friend. I’m thankful you’ll continue to put the pressure on Jim and his waywardness regarding the best

team in the AL East. Maybe they'll ACTUALLY win the East, before you graduate. Who knows? They won it all before I did. Peace to you, and I'm thankful there's much promise of continuing to examine the HRS together.

Clair– Thanks for your help in observing at the 2.3m. It wouldn't have been the same without you tapping the slit and keeping those galaxies centered. And for being nice to me when I was in a new place. It meant alot.

Pablo– Thanks for your friendship while I was in Groningen. I hope our paths cross soon.

“For one human being to love another; that is perhaps the most difficult of all our tasks, the ultimate, the last test & proof, the work for which all other work is but preparation.” –Rilke

Marianne– for being there in my sadness, my brokenness, my anger, and my jubilation. For sending my heart on pilgrimage, and sharing in that pilgrimage- in longing pursuit of that perfect love, where the joy of *both* the lover and the loved are consummated, I am a debtor to your love. ... “Catch for us the little foxes ...;” for sharing the joy of parenting with me, for which you deserve most of the credit.

Mom & Dad– For an infinite amount of encouragement and care, you've never stopped. You've been such wonderful role models as I'm now a parent. You've been such a support for us in this difficult place in our lives as a family of 3, 4, and now 5. You've given all, regardless of my response. What a model of True Love, and what a reminder it's been to me.

Charissa– Thank you for treating me like a big brother and loving me in that way. For looking up to me, when you probably shouldn't, and for allowing me to share in your life. What a wonderful little sister; it's my honor.

Lucinda, Chris, Logan & Melissa, Lori, Allen– Ahh, my adopted family that loves me like their own. Who's worthy of such great in-laws?! I'm thankful we're tied by law, because it's sad to think we'd never know each other otherwise.

“invent your world...surround yourself with people, color, sounds, and work that will nourish you.” –Sark

To my “older” friends– **Kristi**, thanks for taking the Big Sister bit seriously. I’ve needed it when we’ve talked. I don’t know if I’d made it through that first summer without you in 271. And now look at us, (the real) Dr. Concannon. **Jane**, all the best to you, and I’m so thankful for the pleasure of knowing you. May you find what makes your heart at rest. **Big Jim**, you are missed, but if I’d stayed in 271, I wouldn’t be defending on MON. It’s been my pleasure. **Calin**, thanks for being yourself, and helping us out with Stat mech, especially. If I got a problem correct, it was because of you. **Lindsay, Mercedes, Scott, Celeste, and Melissa**, thanks for your encouragement and your friendship.

The Crew of ’01, **Miles, Rachel, and Lorenza**– Thanks for your partnership in my career. Thanks for studying with me and encouraging me and disagreeing with me and pushing me to really understand what in the heck is actually going on inside a star. Thanks for thinking of me. You’ll never be forgotten. And now **Haw**, I’m glad you persevered.

The expanded crew of ’01– To **Mark and Val**, thanks for making me laugh and listening to me, even when you thought I was wrong. For always being available, I hope our paths cross often.

To **Leslie**– Thanks for caring and listening. It’s been a pleasure to call you friend.

Brian V., thanks for being my Partner-in-crime in the Planetarium; I learned a ton, and we had some good laughs. Peace to you in the Journey.

Mark and Juliellen– To the best neighbors in the whole world, we are saddened to move away. Yet, I’m thankful we love each other enough that our friendship will continue. Thanks for always saying ‘Yes.’ We are debtors.

Fred and Nancy Brooks– Thanks for letting me stay at your place during this time.

“Nothing, I suspect, is more astonishing in any man’s life than the discovery that there do exist people very, very like himself.” —CSL

mb, where would my heart be without your friendship in these days? You are a true brother, and I will never fail to keep you in my prayer.

thadd, andy, ulus, robert, peter, frankie, hank, frank, tim, brantley, bob, and geoff– my companions in the Way; you’re held fast in my heart.

To **Bill and Donna Barton**– thanks for your continued support and encouragement; it is always timely and needed.

“Christ is more of an artist than the artists; He works in the living spirit & the living flesh; he makes men instead of statues.” –Vincent

Jesus– If this story is really about other people, then it is really about you. Thank you for making life possible- for putting sound in my motion picture, for plugging me in, for adding color to my black-and-white world. For the beauty of the outdoors,

the study of the physical world, and the comfort of relationships, I would have never known otherwise. Thank you for this chapter and these people. You know where I'd be otherwise; where I was, in fact- at the very least miserable, but more often hating and being hated. You know that for which I long- **"You are the Dreamer, and we are your dream."**

And now I end, as I've ended so many times before- the Leap, UMass, GRE³, Paper I, NSF, RC, and MON, 3 JUL; in life's pivotal moments that seem to balance on a knife's edge within my heart, between sorrow and joy, defeat and triumph, depravity and glory.

My Lord God, I have no idea where I am going. I do not see the road ahead of me. I cannot know for certain where it will end. Nor do I really know myself, & the fact that I think I am following your will does not mean that I am actually doing so.

But I believe the desire to please you does in fact please you. And I hope that I will never do anything apart from that desire. And I know that if I do this you will lead me by the right road, though I may know nothing about it. Therefore I will always trust you though I may seem to be lost & in the shadow of death. I will not fear, for you are ever with me, & you will never leave me to face my perils alone.

Matthew Clay Fleenor
July 2006

“All Nature seems to speak ... As for me, I cannot understand why everybody does not see it or feel it; Nature or God does it for everyone who has eyes & ears & a heart to understand.” –Vincent

for Anna Clare, Boone, and Eliza– may you each have ears to hear &
eyes to see, & a heart to understand,

and for Greg–
a man who truly understood and appreciated the value of education.

CONTENTS

	Page
LIST OF TABLES	xvi
LIST OF FIGURES	xvii
LIST OF ABBREVIATIONS	xx
Chapter	
I. Introduction	1
1.1 Where Does This Fit?	1
1.2 History of Second-Order Clusters	3
1.3 Basic Observational Toolbox	7
1.4 Current Observational State	9
1.4.1 Intercluster Filaments of Galaxies	9
1.4.2 Galaxy Voids	11
1.5 Why Horologium-Reticulum?	12
II. Observational Data	16
2.1 6dF Spectroscopic Observations: 2002	17
2.1.1 Sample Selection	17
2.1.2 Observations	18
2.1.3 Reductions	19
2.1.4 Redshift Determination	23
2.1.5 Coverage	24
2.2 6dF Spectroscopic Observations: 2004	24
2.2.1 Sample Characteristics	26
2.2.2 Selection Effects	30
2.3 Supplemental Intercluster Observations	39

2.4	ANU/2.3m Cluster Observations	40
2.4.1	2004 Cluster Sample	40
2.4.2	Observations and Reductions	42
2.4.3	2005 Cluster Sample	43
2.5	Previously Observed Cluster Galaxies	44
2.6	Cluster Sample Summary	45
2.7	AAT & 2.3m Compact Group Spectroscopy	49
III.	Large-Scale Velocity Structures in the Horologium-Reticulum Supercluster	52
3.1	Kinematic Extent of the HRS	52
3.2	Inter-cluster Galaxy Overdensity	53
3.3	Large-Scale Redshift Trend	54
3.4	Bi-Modal Kinematics of the HRS	56
3.5	Comparisons with the Shapley Concentration	58
3.5.1	Extent and Overdensity	58
3.5.2	Morphological Considerations	59
3.6	Conclusions	61
IV.	Redshifts and Velocity Dispersions of Galaxy Clusters in the Horologium-Reticulum Supercluster	68
4.1	Determination of Mean Cluster Redshifts and Dispersions	68
4.2	Results for Individual Clusters	70
4.2.1	Abell 3047/ APMCC 290 ($02^{\text{h}} 45^{\text{m}} 25 - 46^{\circ} 26' 0$)	71
4.2.2	Abell 3109 ($03^{\text{h}} 16^{\text{m}} 5 - 43^{\circ} 51' 0$)	72
4.2.3	Abell 3120 ($03^{\text{h}} 22^{\text{m}} 0 - 51^{\circ} 19' 0$)	72
4.3	Redshift Distribution of the HRS Clusters	73
4.3.1	Consistency with the intercluster Galaxies	73
4.3.2	Re-determination of the Kinematic Core	75
4.4	Comparisons with the Shapley Supercluster	76
4.5	Conclusions	77
V.	The Panorama of the HRS	82
5.1	Galaxy Viewer Visualization Software, GyVe	82

5.2	Largest-scale Visual Impressions	83
5.3	The Complete Cluster Picture	85
5.4	Determination of Mean Cluster Masses	88
VI.	Voids in the HRS	91
6.1	Void Definition and Examination	91
6.2	Void Sizes and Galaxy Underdensity	95
6.3	Are Voids Spherical?	97
6.4	Void Volume within the HRS	99
6.5	Internal Structure of HRS Voids	100
6.5.1	Comparisons with CDM simulations	100
6.5.2	Unique structure of Void 4	102
6.6	Reality of the HRS Voids	103
6.6.1	Overview	103
6.6.2	Augmented sample for the northern HRS	104
6.6.3	Augmented sample for the south HRS	106
6.7	Summary: Voids	107
VII.	Intercluster Overdensities of the HRS	120
7.1	Overview	120
7.2	A3158/A3125 “Bridge:” Hints of Superclustering	121
7.2.1	Spatial and Redshift Distribution	122
7.2.2	Galaxy Overdensity	124
7.2.3	Galaxy Alignments in Intercluster Overdensities	127
7.2.4	Summary	130
7.3	A3128/3125: A Preferred Axis for Merging Clusters	131
7.3.1	Overview	131
7.3.2	APMCC399 + A3128/25: An Axis?	132
7.3.3	A3125: A Crossroad?	133
7.3.4	A3128: Mixed Signals?	136
7.4	Summary: Overdensities	139
VIII.	CONCLUSION	155

8.1	Our Initial Look at the HRS	155
8.2	A Fifth Wheel?	156
8.3	Continuing Work!	157
REFERENCES		159

LIST OF TABLES

2.1	2002 6dF Observational Fields	22
2.2	Velocity Data for 6dF Galaxy Spectra	26
2.3	2004 6dF Observational Fields	27
2.4	Supplemental Spectroscopic Observations	41
2.5	Redshift Data for Galaxy Clusters in Horologium-Reticulum	48
2.6	A3128 Hickson Compact Group	51
3.1	Clusters of Known Redshift in the Observed Region	67
4.1	Revised Mean Redshifts and Velocity Dispersions for HRS Clusters	78
4.2	Reliable Cluster Redshifts in the HRS Kinematic Core	81
5.1	Galaxy Clusters Throughout the HRS Region	90
6.1	Voids Throughout the Surveyed Region	93

LIST OF FIGURES

1.1	Venn diagram relating the HRS survey project to the relevant fields of astronomy, astrophysics, and cosmology.	14
1.2	Cone diagram as a function of redshift showing the Northern and Southern portions of the 2dFGRS.	15
2.1	Observed fields in the 2002 study as conducted by the 6dFGS team.	20
2.2	Histogram showing the magnitude distribution for the 6dF observations compared to the SuperCOSMOS inter-cluster galaxy list with limiting magnitude $b_J = 17.5$	21
2.3	The HRS region under study displaying both 6dF observations from 2002 and other previous inter-cluster redshifts.	25
2.4	Sky map showing the increase of area with the 2004 observations when compared to those of 2002.	28
2.5	Spatial map outlining the 6dF field centers for all stages of the current HRS survey.	31
2.6	Histogram displaying the number of intercluster galaxies in the HRS survey as a function of nearest-neighbor projected separation, $d_{\text{gx-gx}}$	34
2.7	Line-of-sight velocity differences, $\Delta_{cz_{\text{los}}}$, for observed nearest-neighbor galaxies as a function of projected spatial separations for $d_{\text{gx-gx}} \leq 5'7$	35
2.8	Equal area survey mask displaying observational completeness as a function of greyscale with excised clusters shown as open circles.	36
2.9	Normalized contribution for each degree of completeness presented as a function of offset α from $3^{\text{h}}24^{\text{m}}$	37
2.10	Number of 6dF intercluster galaxies observed as a function of cz is shown as an open histogram up to $60,000 \text{ km s}^{-1}$	46
2.11	Hammer-Aitoff, equal-area projection map of the HRS region, with galaxy clusters represented as circles.	47
2.12	DSS image of the A3128 southwest compact group.	50
3.1	Redshift histograms of the 6dF inter-cluster galaxies (open) and the clusters with known redshifts (filled).	62
3.2	Coordinate-redshift plots for the 6dF galaxies. Left panel: $\alpha - cz$. Right panel: $\delta - cz$	63

3.3	Redshift slices are plotted for the 6dF data in the range of the HRS. Each panel covers a 1500 km s^{-1} redshift slice.	64
3.4	Projected angular S -coordinate (see text) is plotted versus redshift for 6dF galaxies between 17,000 and 22,500 km s^{-1}	65
3.5	Separation of the 16000-18000 km s^{-1} redshift slice into low- and high-redshift bins.	66
3.6	Residual redshift histograms for galaxies and clusters within 17,000 – 22,500 km s^{-1}	66
4.1	Projected angular S -coordinate is plotted versus redshift for 6dF in- tercluster galaxies from Paper I (small filled circles) between 17,000 and 22,500 km s^{-1} at a PA = -80°	79
4.2	Histograms of residual redshifts along the best-fit line at a PA = -80° , shown as the solid line in Figure 4.1.	80
5.1	Preferred viewing angle snapshot of the 6dF sample from 12,000– 27,000 km s^{-1} , as taken from the GyVe software	86
5.2	Hammer-Aitoff, equal-area projection map of the complete cluster sample for the HRS region.	87
6.1	Radial profile distribution of galaxy number counts as a function of incremental changes in the α -coordinate of the void center.	94
6.2	Equal area survey mask displaying observational completeness as a function of grayscale with void extents shown as open circles.	110
6.3	Volume-normalized, galaxy number counts as a function of scaled radius for the 6 large voids in our survey.	111
6.4	Hammer-Aitoff, equal-area projection maps for Void 1.	112
6.5	Hammer-Aitoff, equal-area projection maps for Void 2.	113
6.6	Hammer-Aitoff, equal-area projection maps for Void 3.	114
6.7	Hammer-Aitoff, equal-area projection maps for Void 4.	115
6.8	Hammer-Aitoff, equal-area projection maps for Void 5.	116
6.9	Hammer-Aitoff, equal-area projection maps for Void 6.	117
6.10	Incremental radial profile of intercluster galaxy counts for Voids 1 and 2.	118
6.11	Volume-normalized, galaxy number counts with the augmented sam- ples included as a function of scaled radius for the 6 HRS voids.	119
7.1	Equal-area, sky map of the A3128/3158 region showing all galaxies with an observed redshift in our catalog as small open circles.	125

7.2	A3128/3158 spatial map showing all SuperCOSMOS galaxies with $b_J \leq 17.75$	142
7.3	A3128/3158 spatial map showing all SuperCOSMOS galaxies with $b_J \leq 18.60$	143
7.4	Fractional number of galaxies with $b_J < 18.60$ as a function of PA for the $3^\circ 0' \times 3^\circ 0'$ area in Fig. 7.3 and larger $10^\circ 0' \times 10^\circ 0'$ area.	144
7.5	A3128/3158 spatial map displaying the different areas for which the galaxy PA orientation test was completed.	145
7.6	Orientation parameter, ϵ , as a function of PA for the individual sub-volumes in Fig.7.5.	146
7.7	Orientation parameter, ϵ , as a function of PA for stacked volumes in the A3128/58 region.	147
7.8	Spatial map of the $2^\circ \times 3^\circ$ A3128/25 region with $b_J < 18.50$ galaxies shown as small filled circles.	148
7.9	Smoothed distribution of $b_J < 18.50$ galaxies in the A3128/25 region.	149
7.10	Map of $b_J < 19.0$ galaxies within the inner $0^\circ 5'$ of A3125.	150
7.11	20cm image, obtained with the ATCA, of tailed radio sources in A3125.	151
7.12	Orientation parameter, ϵ , as a function of PA for the two individual populations in A3125.	152
7.13	Equal-area sky map of A3128 galaxies within the pre-defined A3128-G1 (open circles) and A3128-F1 (open squares) designations by RGC02.	153
7.14	Digitized sky survey image of the southwest compact group in A3128.	154

LIST OF ABBREVIATIONS

2dFGRS	Two-degree Field Galaxy Redshift Survey
2MASS	Two Micron All-Sky Survey
6dFGS	Six-degree Field Galaxy Survey
AAO	Anglo-Australian Observatory
AAT	Anglo-Australian Telescope
ACO	Abell et al. (1989) Cluster Catalog
AGN	Active Galactic Nuclei
ANU	Australian National University
APMCC	Automated Plate Measuring machine Cluster Catalog
ATCA	Australia Telescope Compact Array
CDM	Cold Dark Matter
BCG	Brightest Cluster Galaxy
BFG90	Beers et al. (1990)
DBS	Dual Beam Spectrograph
DEMS94	Dalton et al. (1994)
ENACS	ESO Nearby Abell Cluster Survey
HCG	Hickson Compact Group
HRS	Horologium-Reticulum Supercluster
HV04	Hoyle & Vogeley (2004)
ICM	Intra-cluster Medium
L83	Lucey et al. (1983)
LCRS	Las Campanas Redshift Survey

LF	Luminosity Function
los	Line-of-sight
MAD	Median Absolute Deviation
MF	Minkowski Functional
PA	Position Angle
RGC02	Rose et al. (2002)
SCDM	Standard Cold Dark Matter
SDSS	Sloan Digital Sky Survey
SSC	Shapley Supercluster
SvdW04	Sheth & van de Weygaert (2004)
UKST	United Kingdom Schmidt Telescope

Chapter 1

Introduction

In theory, there is no difference between practice and theory. In practice, there's a big difference. –Jan L. A. van de Snepscheut

With the advent of multi-object spectroscopy that has birthed hundred-thousand redshift surveys and the parallel-processing supercomputer that fathered large-scale N-body simulations of cold, dark-matter (CDM), the two prongs of cosmological study (i.e., the observational and the theoretical) have been altered unequivocally. With titans such as these pushing back the frontiers of astrophysical inquiry, one may offer the following perfectly valid challenge: “What does a relatively small and shallow redshift survey focusing on the composition and substructure within one individual supercluster of galaxies have to offer the ‘land of giants’?” Well, I’m glad you asked...

1.1 Where Does This Fit?

In trying to describe where the Horologium-Reticulum supercluster (HRS) galaxy survey project fits into the myriad of observational programs and theoretical studies regarding large-scale (i.e., megaparsec-scale) structure, it seems quite natural for me to begin with the idea of relationships. A Venn diagram is often helpful to illustrate the relationship between distinct groups and/or sets. In this case, I use a Venn diagram to show where this project fits within the inter-related fields of astronomy, astrophysics, and cosmology. Figure 1.1 shows such a diagram with the gray shaded circle situated to show the relative contribution of each of these fields of study. That is, the

overlapping area of the three different fields relates to the degree in which each field contributes to the HRS project (the shaded circle). From the diagram, one can deduce that the project is primarily focused on observational astronomy, and most specifically cosmography- mapping various astrophysical features with an eye toward understanding their relationship to the environment in which they are situated.

The idea of relationships also serves to describe the primary scientific impetus of the project, as to how structures that share environment interact and influence one another. Specifically, what are the specific structures that comprise the HRS, and how do these structures of varying scales inter-relate to one another? It is for this reason primarily, that a project focusing on the large-scale structure and morphology of only one particular supercluster is interesting to me. Furthermore, as in dealing with all relationships, the case for connectivity is not based on irrefutable evidence. Rather, we are building a case for relationship, and for the reality of the structures themselves, from the presentation of repeated confirmation of similar effects. That is, either by applying multiple tests to the same proposed structure, or by observing a similar effect in multiple areas within the supercluster, we are able to infer an astrophysical relationship between these structures.

Lastly, relationship serves to describe the partnership between the HRS project and the six-degree field galaxy survey (6dFGS, Jones et al. 2004), which has provided the instrument, allocation, and support to carry out such an observational effort. The 6dFGS is one of the largest, active redshift surveys with goals of mapping the Southern sky and obtaining peculiar velocities of 10% of the galaxies down to $b_J < 16.75$. Two separate observing runs were allocated for the HRS project, where priority was given to the slightly fainter HRS targets. The 6dF multi-fiber spectrograph (Parker et al. 1998) is the ideal instrument for collecting a relatively moderate number of galaxy spectra (~ 130) over an extremely large area of the sky ($5^\circ 8$). Therefore, it is uniquely suited for observing the supercluster environment, which for the HRS extends over $15^\circ \times 15^\circ$ on the sky.

The remainder of the Introduction is dedicated to providing the reader with a proper context for understanding the observations and conclusions of the HRS project. As one

is surely aware, there is a mountain of observation and study that has taken place in the arena of large-scale structure. So if nothing more in the remaining portion, I hope to provide an adequate array of the literature leading the reader in the proper direction for a more detailed analysis of a particular effect/structure. Therefore, we begin with the historical context of the observations of “second-order” clusters (i.e., superclusters of galaxies). This naturally leads into a brief overview of the rather simple, yet fundamental, measurement tools employed for the project. Next, we show how more recent observations of individual structures and specific features have helped to shape our theories of supercluster composition. Lastly, we motivate the current observations of the HRS by highlighting their uniqueness in helping us better understand the inter-related nature of astrophysical structures.

1.2 History of Second-Order Clusters

The notion of second-order clusters, or superclustering, dates back to at least the mid '50s in photometric galaxy counts (Neyman et al. 1954; Shane & Wirtanen 1954; de Vaucouleurs 1956), though de Vaucouleurs (1961) mentions even Shapley (1938) as evidence “pointing to the reality of large-scale irregularities ... of the order of 50 Mpc³.” Furthermore, the approximately perpendicular arrangement on the sky of nearby superclusters, like Coma-A1367 (Gregory & Thompson 1978) and Perseus-Pisces (Gregory et al. 1981; Giovanelli & Haynes 1985), aided astronomers in understanding the extent of large-scale structures (Joeveer & Einasto 1978; Chincarini et al. 1983). Quantitative confirmation of such structures was given a foundation in the “strong and consistent” (Bahcall & Soneira 1983) spatial correlations of galaxy clusters, which revealed that the universe was *not* isotropic on these large scales of up to $\sim 100 h^{-1}$ Mpc (Hauser & Peebles 1973; Klypin & Kopylov 1983). These statistical findings (and the theoretical inferences that followed) were largely dependent on the observational efforts to catalog the Northern galaxy clusters (Abell 1958), where the all-sky Abell catalog (ACO) came later in Abell et al. (1989), and the initial determination of most of the cluster’s (photometric) redshifts (Hoessel et al. 1980). Specifically, the cluster-cluster correlation

function was found by Bahcall & Soneira (1983) to have a similar power-law slope as the galaxy-galaxy correlation function, but with an amplitude 18 times larger, and a scale length 5 times greater as well. In the midst of these distinct pile-ups of matter, there were also regions where seemingly *no* galaxies (so-called voids, with radii of up to $60 h^{-1}$ Mpc, Kirshner et al. 1981) or no rich clusters (on the order of $300 h^{-1}$ Mpc, Bahcall & Soneira 1982; Frith et al. 2003) resided. In fact, Bahcall & Soneira (1982) observed that the largest, densest superclusters were located near and around the Boötes void observed by Kirshner et al. (1981). Therefore throughout the '80s, a major thrust in cosmological physics was to explain how both voids and clusters arose from a nearly homogeneous state at the epoch of recombination, as evidenced by the near-isotropy of the cosmic microwave background radiation (CMB). In short, a successful model for structure formation needs to account for the scales and morphologies of both overdense and underdense regions.

Even before the '80s, theoretical cosmologists were showing how the formation of cosmological structures could arise from small (e.g., $\delta = \Delta\rho/\rho \sim 10^{-4}$) density perturbations within the CMB (e.g., Doroshkevich, Zel'Dovich, & Novikov 1967). Throughout the '70s and early '80s, two distinct models of structure formation were developing into the dominant archrivals. The adiabatic, or 'top-down,' model states that substructure is formed by the fragmentation of larger-scaled structures, called 'pancakes,' via shock wave heating of the gas (Zel'Dovich 1970; Sunyaev & Zeldovich 1972; Doroshkevich et al. 1974). Alternatively, an isothermal, or 'bottom-up,' scenario predicts the hierarchical buildup of structures from surviving pre-recombination perturbations (Peebles & Dicke 1968; Peebles 1974). Both models predict similar perturbation amplitudes at recombination and invoke gravitational instability as the mechanism of structure growth, yet the ordering of the appearance of specific structures remains quite opposite. Around this time, Press & Schechter (1974) formulated a mass-scale spectrum as a result of the condensations of cold (i.e., non-interacting) gas via self-gravitation for expanding cosmologies, which was later revised by Schechter (1976) to incorporate the predicted universal spectrum of galaxy luminosities. Aarseth et al. (1979) presented N-body computer simulations as means of testing the self-gravitation and clustering

theories of galaxies and their initial cosmological conditions (see a similar method in Soneira & Peebles 1978). Though the problem of “missing mass” in galaxy clusters had been raised decades earlier in Zwicky (1933) and Smith (1936), the ubiquitous presence of dark matter, as the early-epoch, self-gravitating non-interacting “gas,” was only recognized and accepted by most astronomers in the 1970s (see reviews by Faber & Gallagher 1979; Trimble 1987, and references therein).

The mid 80’s to 90’s saw the rise of two dominant tools in cosmological studies: the observational redshift survey and the numerical N-body simulation. Thousand redshift surveys began to reveal a sponge-like interconnected pattern of galaxies and their absence (e.g., Gott, Dickinson, & Melott 1986, who used the CfA catalog in Huchra et al. 1988). Also through redshift surveys, systems of galaxies (e.g., multiple adjacent clusters) were targeted and observed to be connected by coherent organizations of individual galaxies (e.g., hereafter L83, Lucey et al. 1983; Postman et al. 1988; Geller & Huchra 1989), which often included calculations of the velocity dispersion and mass of the system. On the theoretical side, the modeling of the inter-connective supercluster-void network via phenomenological models (Icke 1984; Bahcall 1988) and more developed N-body simulations (Regos & Geller 1991; van Haarlem & van de Weygaert 1993) continued to keep pace with the increase in observational understanding. Bond, Kofman, & Pogosyan (1996) introduced the picture of a “cosmic web” as a theoretical construct where filaments are the preferred, collapsed structures that connect clusters, which has since become the manner of qualitatively characterizing the observed large-scale structure. Figure 1.2 shows such an observational picture taken from the two-degree field galaxy redshift survey (2dFGRS, Colless et al. 2001), which is the common arrangement in other surveys also (e.g., Las Campanas redshift survey, LCRS, Shectman et al. 1996). We are now in the age of million redshift surveys (e.g., the Sloan Digital Sky Survey (SDSS) in York et al. 2000) and cosmological CDM simulations that encompass a significant fraction of the observable universe (e.g., the Virgo Consortium, Colberg et al. 2000b).

Superclusters of galaxies represent the largest known conglomerations of both visible and dark matter in the universe (Kalinkov et al. 1998). Though ranging in galaxy

overdensity just out of the linear regime of structure growth (i.e., $\delta = \Delta\rho_{\text{OBS}}/\rho_c < 10$), superclusters are formed by the connection of clusters over distances of $\sim 70 h^{-1}$ Mpc. In fact, the range of structures identified as superclusters varies widely in terms of morphology and size. On the one hand, there are superclusters containing just a few major galaxy clusters connected by long spiral-rich galaxy filaments (e.g., Coma and Pisces-Perseus, Gregory & Thompson 1978; de Lapparent et al. 1986; Giovanelli et al. 1986; Chamaraux et al. 1990). In contrast, other structures are perhaps more readily characterized by the presence of rich clusters- up to twenty or greater- as in the case of the Shapley supercluster (e.g., Quintana et al. 1995, 2000; Bardelli et al. 1998, 2000; Drinkwater et al. 1999, 2004). Therefore given their complex morphologies, as well as their huge scale (e.g., Zucca et al. 1993; Einasto et al. 1994, 2001) and potential alignment within the local universe (Tully et al. 1992), superclusters pose unique challenges for scenarios of the growth of and inter-relationship between structures on all scales. This includes both competing models for structure formation, namely the hierarchical structure formation picture (Baugh et al. 2004) and the “pancake” models (Zel’Dovich 1970). Detailed studies of the supercluster environment require extensive redshift information over large areas of the sky, sampling both the intra- and inter-cluster regions (Bardelli et al. 2000). Wide-field, multi-fiber spectrographs are ideally suited to this task, as they permit three-dimensional probing of structures on megaparsec scales.

In typical superclusters comprised of numerous galaxy clusters, there is evidently a rich variety of substructure present in these large-scale entities. For example, orientations of individual member galaxies (Binggeli 1982; Fuller et al. 1999), subclustering within the constituent clusters (West et al. 1995), and even the shapes of the galaxy clusters themselves (Plionis & Basilakos 2002) are all presumed to be influenced (and/or instigated) by their parent supercluster. N-body simulations of CDM halos also predict a rich array of substructures linked to the surrounding megaparsec-scale landscape (Colberg et al. 1999). Therefore, we may deduce that much could be understood regarding structure formation were we able to tie the local effects (mentioned above) to actual structural phenomena within the surrounding supercluster environment. Before exam-

ining in more detail the primary players at the supercluster regime, we must discuss the observational tools used to detect cosmological structural features on these scales.

1.3 Basic Observational Toolbox

Without doubt, the fundamental measurement of galaxies when inferring the large-scale structure is the cosmological redshift. Due to the universal cosmological expansion (Hubble 1929), emitted light from receding galaxies is reddened according to the relativistic Doppler relation. The ratio between an object’s observed and emitted light at a particular wavelength defines the spectroscopic redshift, z . While the redshift is a direct measure of the scale factor of the Universe when the radiation was emitted by the object, it may stand as a surrogate for the inferred radial distance (Longair 1998). These artificially inferred distances are susceptible to distortion by the galaxy’s peculiar velocity, which can arise from either bound orbital motions within galaxy clusters (Kaiser 1987), or bulk motions of galaxies, like infall streaming motions (Praton et al. 1997). Outside of rich galaxy clusters, line-of-sight (los) radial distances inferred from spectroscopic redshifts are thought to have distortions of $1 - 3\%$ at the average HRS redshift (Bothun et al. 1992; Padilla et al. 2005). We discuss in more detail the confidence with which we are able to interpret relative distances between various HRS structures in following sections (e.g., §6.1).

From this approximate volumetric rendering of galaxies, the number density contrast for specific large-scale structures is calculated. To do so, an accurate estimate of the mean density of galaxies for a uniform background must be taken into account. These predicted background counts vary with redshift and are derived from the radial selection function, which is fully discussed in §2.2.2. The over/underdensity with respect to the mean serves as a fundamental parameter to estimate the dynamical state of the particular object or region. For example, structures with overdensities less than 1.0 are expected to be in the linear regime, which means that the governing motion is that of the Hubble flow. However, as the overdensity increases, structures move into the non-linear regime, and their dynamical histories are intractable from redshift measurements.

A corollary for underdensities in voids was shown by van de Weygaert (1991). As with the inferred radial distance, we would ideally like to measure the actual *mass* density in a given area. However, our inability to accurately account for the presence of dark matter, either directly or indirectly (e.g., through biasing), requires us to proceed with an observed galaxy number density for a given volume. While CDM simulations have little difficulty calculating a mass density, there is a “trade-off” due to the difficulty in predicting the exact spectrum of galaxy types and masses in a given region. In other words, observations of large-scale structure are completely biased to the visible baryonic minority component of the mass density. In contrast, CDM simulations easily produce information about the status of dark matter halos, but can only follow the development of the visible matter through highly parametrized, semi-analytic methods (Benson et al. 2001). However, with an accurately counted background, the observed over/underdensity of galaxies in a given region provides a valuable measure of the underlying large-scale structure.

The orientation of a galaxy’s semi-major axis with respect to some larger-scale, preferred axis, e.g., that of a galaxy cluster, provides a potential measure of the effect of large-scale structure on its constituents. Several studies examine the alignment of individual (and collections of) galaxies with respect to cluster (Binggeli 1982; Struble & Peebles 1985) and even supercluster (West 1994) axes. When the filamentary network connecting clusters is thought of as a funnel preferentially directing material onto galaxy clusters (Plionis & Basilakos 2002; Colberg et al. 2000a), a laminar flow model describes that galaxy elongation will take place in the direction of these funnels (Kitzbichler & Saurer 2003; Aubert et al. 2004). Such observations are also reinforced in the simulated world with CDM halos (e.g., Dekel et al. 1984; Knebe et al. 2004). Though all observational studies show some positive signals of preferred orientations in certain cases, the universal effect is sometimes overstated or wrongly extrapolated (again, e.g. in Struble & Peebles 1985). Therefore, while we have in the alignment test a potentially useful measure of phenomenological connection between structures, it must be interpreted judiciously.

All of these tools lead us in the direction of observing the connected nature of a

galaxy supercluster. Galaxy redshifts provide us with some measure of the volumetric arrangement of structures. Overdensity measurements inform of the comparative arrangement between various structures/regions. Orientations indicate the relative association of an individual object (or a collection of objects) to a group (to the surrounding environment). While galaxy-galaxy correlation functions are a useful measure of the general statistical clustering in a given volume, they do not provide ample information about the preferred direction of such clustering. Higher-order correlation functions do better but in a laborious and inefficient manner. Minkowski Functionals (MFs), which are applied to isodensity surfaces derived from the point galaxy data, give a basic description of the topological characteristics of a given volume (Mecke et al. 1994; Sheth & Sahni 2005). Shapefinder statistics further use these MFs to extract information regarding the shapes (planarity, filamentarity, etc.) of the large-scale structure in CDM simulations (Sathyaprakash et al. 1998). However, these statistical tools are less useful for describing the particular connections between specific structural constituents of a supercluster. Therefore, we have chosen a somewhat more hands-on approach in examining the unique interconnection within the HRS between structures on various scales. In summary, we hope to provide a picture of how a seemingly vast region of interesting structural phenomena, both underdense and overdense, can be viewed comprehensively (and coherently) as one supercluster, the HRS.

1.4 Current Observational State

1.4.1 Intercluster Filaments of Galaxies

Since the preferred constituents of the “cosmic web” are filaments and voids (Bond et al. 1996), these two structures become the focus of the following study. Hereafter, we reserve the word ‘filament’ to describe the spatially (and kinematically) confined, interconnective density enhancements between galaxy clusters. Besides their association with the “web,” filaments of galaxies have become an important observational part of large-scale structure programs for two reasons. First, intercluster filaments are

purported to aid in filling the “missing” baryons (Fukugita et al. 1998; Cen & Ostriker 1999), because they are thought to contain a significant amount of hot ($> 10^5$ K), dilute gas. For example, both observations (Davé & Tripp 2001) show and hydrodynamic simulations (Cen et al. 2001; Evrard et al. 2002) suggest that O VI absorption in gas filaments is observable at lower redshifts (Tripp et al. 2001). Secondly, filament intersections are thought to be the progenitors of rich galaxy clusters, in that filaments preferentially funnel (dark, light, and gaseous) matter along their axes (e.g., Bond et al. 1996; Colberg et al. 1999). Such propositions, if shown to be true, would significantly impact our insights about structure formation and evolution.

Since a significant amount of the matter in filaments remains dilute, their low-density environment makes them difficult to detect. Because they are thought to contain significant amounts of gas, observational programs have aimed (with mild success) at detecting the X-ray emission resulting from the gaseous filament bath (Kull & Böhringer 1999; Scharf et al. 2000). Other observational mechanisms have also been employed to detect intercluster filaments, either by ultraviolet absorption of the gas within background AGN spectra (Bregman et al. 2004) or by gravitational weak lensing (Gray et al. 2002; Dietrich et al. 2005).

More directly, intercluster filaments are confirmed through the optical detection of the galaxies that populate them. Almost all of these studies incorporate the spectroscopic redshift of the galaxy (e.g., Ebeling et al. 2004), though the utilization of galaxy color (Kodama et al. 2001; Pimbblet et al. 2004a) and position angle (Pimbblet 2005) are also explored. Several theoretical predictions regarding the (qualitative) filament type, radius, number and mass density, and length have been set forth in Colberg et al. (2005a) via CDM simulations from Kauffmann et al. (1999). Pimbblet et al. (2004b) have classified filaments in the 2dFGRS in a similar manner to estimate the number density of filaments as they are related to the environment in which they reside. Again, the low density environment of intercluster filaments translates to a sparse number of galaxies connecting galaxy clusters. It is for these reasons that we have focused intently on the intercluster regions of one particular supercluster to detect galaxy filaments. We will explore the use of other observational techniques to help confirm the redshift

detection of intercluster filaments in the HRS (e.g., σ_{los}).

1.4.2 Galaxy Voids

While consisting primarily of empty space, it is ironic that void regions have been more easily characterizable from an observational standpoint. Specifically, for both the SDSS (York et al. 2000) and the 2dFGRS (Colless et al. 2001), multiple detailed studies of the observable voids were conducted (e.g., Croton et al. 2004; Hoyle & Vogeley 2004; Goldberg et al. 2005). This is usually reported as a void probability function (VPF Lachièze-Rey & Maurogordato 1987; Einasto et al. 1991), though other significant properties like the underdensity are also calculated. The relative ease of void discovery is due primarily to their large volume (up to 40% of total in the 2dFGRS, Hoyle & Vogeley 2004) and their relaxed (i.e., nearly spherical), vacuous ($\bar{\delta} \sim -0.9$) nature. Though voids with radius up to $60 h^{-1}$ Mpc are well-studied (most notably Boötes in Kirshner et al. 1987), the majority of voids have defined radii between $10 - 20 h^{-1}$ Mpc. In fact, Colberg et al. (2005b) show that in simulations of CDM halos, $\sim 90\%$ of the total void volume is filled by those with $R_{\text{VOID}} < 10 h^{-1}$ Mpc. Such small vacant regions are difficult to detect in the observable realms, since galaxies are not continuous space-filling objects and their volumetric number density is low.

The potential population of voids by individual galaxies, gas, and simulated amounts of CDM has also received much attention. For example, the photometric (Rojas et al. 2004), spectroscopic (Rojas et al. 2005), luminosity function (Hoyle et al. 2005), and the mass function (Goldberg et al. 2005) of void galaxies in the SDSS have all been studied in detail. In summary, these studies show that voids are dominated by fainter, bluer, more disk-like galaxies with younger stellar populations. More recently, Patiri et al. (2006) find that faint galaxies in 2dFGRS voids are not distributed randomly but align in filamentary structures *within* the voids themselves. This observational result is not unlike the low-mass CDM halo simulations of Gottlöber et al. (2003) that reveal a “miniature” universe of filamentarity that populates each void. Apparently, the hierarchy of structures extends down to the current observable limits of both brightness

and density, further pressing our cosmological theories into uncharted waters.

1.5 Why Horologium-Reticulum?

Originally noted by Shapley (1935) as exhibiting “a considerable departure from uniform distribution,” the HRS is now recognized as one of the largest superclusters in the local universe (L83; Zucca et al. 1993; Einasto et al. 2003; Fleenor et al. 2005), containing more than twenty ACO clusters. The HRS covers an area of the sky in excess of 200 square degrees, centered at approximately $\alpha = 03^{\text{h}}20^{\text{m}}$, $\delta = -50^{\circ}00'$. In fact, in terms of mass concentrations within the nearest 200 Mpc, the HRS stands as second only to the Shapley supercluster (Hudson et al. 1999; Einasto et al. 2001). It is of interest to note that while the Shapley supercluster lies within the preferred plane discussed by Tully et al. (1992), the HRS lies more than 150 Mpc outside of that plane.

Recent studies in the HRS have focused exclusively on the rich clusters in the region. Katgert et al. (1998) summarize the redshift information from the ESO Nearby Abell Clusters Survey (ENACS), which investigated ACO cluster cores throughout the HRS (specifically A3093, A3108, A3111, A3112, A3128, A3144, and A3158). Rose et al. (2002) examined the merging double-cluster system A3125/A3128, which is located in the Southeast portion of the HRS. This multi-wavelength study revealed a number of rapidly infalling groups and filaments, which are accelerated by the HRS potential. The results from their observations imply that the HRS contains evolving substructures on a wide range of mass scales.

To date, few studies have been carried out that concentrate upon the dynamical state of the HRS environment outside of the rich clusters. The foundational paper by L83 only concentrated on a $6^{\circ} \times 6^{\circ}$ in the southern HRS region. To remedy this situation for the HRS, we have initiated a wide-field, spectroscopic study of the inter-cluster regions. Because of its enormous size and state of dynamical evolution, the HRS is readily present with ample opportunities to explore and examine the filamentary nature of the supercluster environment. Moreover, with ample spectroscopic information on various scales (cluster, intracluster, and intercluster), we are in a position to present a coherent

picture of the entire supercluster.

The thesis contains our findings from various stages of the project. After a detailed summary of the spectroscopic observations, including sample selection and its effects in §2, we describe the initial results relating to large-scale kinematic features in the HRS in §3, which is presented in the thesis as Fleenor et al. (2005, or Paper I). §4 contains our observations and calculations of the mean redshift and velocity dispersion of several HRS clusters with previously sparse information. This work is presented in the thesis as Fleenor et al. (2006, or Paper II). §5 provides some brief highlights of the structures observable within the HRS, as it relates in particular to the visualization tool, GyVe (Miller et al. 2006, Appendix A). §6 is an analysis of six voids in the immediate HRS region with $R_{\text{VOID}} \geq 10 h^{-1} \text{ Mpc}$. We find that these voids not only help to define the boundaries of the HRS but are also embedded within the supercluster region. §7 examines specific overdense regions of the HRS, with a particular eye toward defining intercluster filaments and establishing the HRS as a coherent entity. We summarize our findings in §8. Throughout, the following cosmological parameters are adopted: $\Omega_m = 0.3$, $\Omega_\Lambda = 0.7$, and $H_o = 100h = 70 \text{ km s}^{-1} \text{ Mpc}^{-1}$, which implies a scale of $4.6 \text{ Mpc degree}^{-1}$ ($77 \text{ kpc arcmin}^{-1}$) at the $\sim 20,000 \text{ km s}^{-1}$ mean redshift of the HRS.

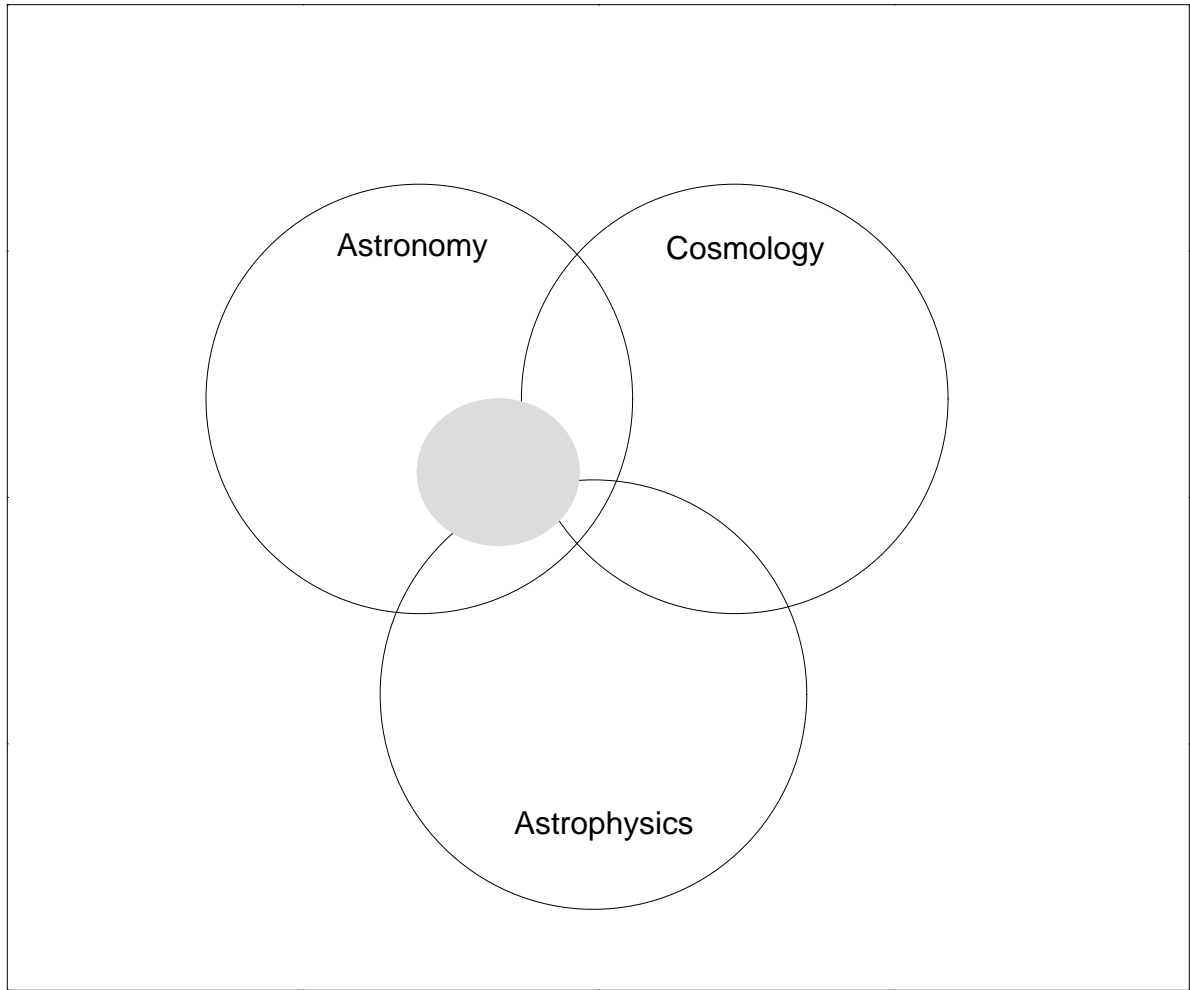


Figure 1.1 Venn diagram relating the HRS survey project to the relevant fields of astronomy, astrophysics, and cosmology. The scope of the project is shown by the filled gray circle, where the majority of the circle's area is covered by observational astronomy.

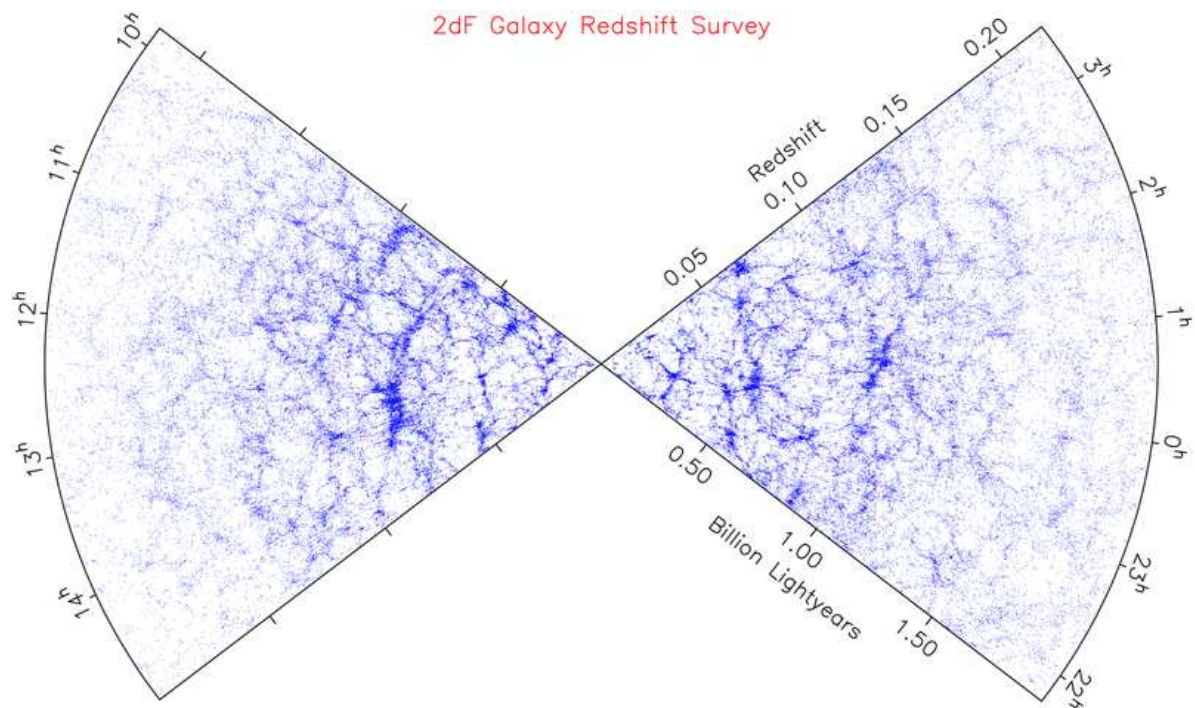


Figure 1.2 Cone diagram as a function of redshift showing the Northern and Southern portions of the 2dFGRS. The total survey contains over 200,000 galaxy redshifts out to $z \approx 0.2$. The qualitative evidence for a cosmic web pattern is readily seen.

Chapter 2

Observational Data

“The hardest thing about really seeing ... is that then you really have to do something about what you have seen ...” –Fredrick Buechner

The HRS galaxy survey contains a unique combination of spectroscopic observations from both intercluster and cluster galaxies. This affords the opportunity to locate galaxy clusters as members of the HRS and to examine the intercluster arrangement around these most dense regions. Specifically, there are 2 6dF samples used primarily for observing intercluster galaxies in the HRS. The initial 2002 sample of 547 galaxies was used for the analysis in Paper I, while the larger 2004 sample consists of 1235 galaxies. In addition, spectroscopic observations of cluster galaxies were obtained with the ANU 2.3m in 2004, which comprises the sample for Paper II, and a follow-up study with the same instrument in 2005. There are several published and unpublished datasets also incorporated into the survey, and each is discussed as it relates to the project, intercluster or cluster, respectively. Lastly, a complete sample of quality spectra were obtained for a compact galaxy group in A3128 with a combination of AAT and ANU/2.3m data. A description of the intercluster samples are discussed first, since they comprise the majority of the survey dataset, which is followed by a discussion of the cluster data.

2.1 6dF Spectroscopic Observations: 2002

2.1.1 Sample Selection

The UK Schmidt Telescope (UKST) six-degree field (6dF), multi-fiber system is uniquely suited to survey large supercluster regions in the nearby universe. 6dF deploys 150 fibers over a circular field of diameter $5'.7$ with a minimum required spacing between fibers of $5'.7$, set by the magnetic prism buttons (see §2.2.2). Light is fed from the fibers into a fast $f/0.9$ CCD spectrograph (Parker et al. 1998). Two interchangeable field plate units allow for the simultaneous observation of the current field and configuration of the next. A practical limiting magnitude for the system is $b_J = 17.5$. All of these attributes taken together imply that the 6dF is most effectively used to probe the large-scale inter-cluster environments of local superclusters, while avoiding the more densely crowded cluster members. Consequently, in studying the HRS our goal was to produce a catalog of galaxies for the inter-cluster region.

Galaxy selection took place in the following manner. A $12^\circ \times 12^\circ$ area of the sky centered upon $\alpha = 3^h19^m$, $\delta = -50^\circ00'$ was chosen for the region of observation based upon previously published literature (Zucca et al. 1993). A complete catalog of all galaxies down to a b_J magnitude of 17.5 was extracted in four $6^\circ \times 6^\circ$ regions from the UKST survey plates previously scanned by the SuperCOSMOS machine (Hambly et al. 2001b). There was also the addition of a fifth rectangular region ($3^\circ \times 6^\circ$) in the far Southern portion to incorporate the field surrounding ACO clusters 3106 and 3164. The galaxy classification flag assigned by SuperCOSMOS was used for the initial sample selection. The $b_J = 17.5$ magnitude limit was adopted as a practical limiting magnitude for the 1.2-m aperture UKST. To avoid expending fibers on galaxies within clusters, our original intention was to excise from the catalog all galaxies within a 1° radius circle of sixteen ACO clusters listed by Zucca et al. (1993) as members of the HRS and intersecting our observing region. The 1° radius exclusion corresponds to ~ 2 Abell radii (where $1 R_A = 2$ Mpc) at the mean redshift of the HRS. This would ensure that new spectroscopic information relates only to the inter-cluster regions of the HRS.

However, a coding error was discovered in the program that excises galaxies from the cluster regions only after the observations were made. The $\cos(\delta)$ conversion factor in the Right Ascension (RA) coordinate, when expressed in degrees, was not included in the calculation of angular distances of galaxies from cluster centers. As a result, the actual excision regions are elongated in the RA coordinate and correspondingly more so at higher Declination. The typical elongation is a factor of 1.6. Nevertheless, the result remains that we have generated a sample that is almost entirely comprised of inter-cluster galaxies.

After the above constraints were applied, there remained 2848 galaxies (Figure 2.1). The maximum number of optical galaxy redshifts that could be obtained under optimal observing conditions was estimated at 1500. Consequently, we produced a subcatalog of 1500 targets from the original list of 2848. This was accomplished as follows. Galaxies in each $6^\circ \times 6^\circ$ region were assigned a random number and then arranged in ascending order. This ordering provides a basis for selecting an unbiased subsample from the larger complete sample. The numbering schemes from the individual $6^\circ \times 6^\circ$ regions were merged into a final catalog of 1500 objects with each region weighted according to the fraction of galaxies found in that region. That is, if 25% of the galaxies in the original catalog came from a particular region, the subcatalog of 1500 galaxies also contained 25% from that region. Hence the method preserves natural galaxy overdensities while randomly sampling the entire extracted region. Finally, a Digitized Sky Survey (DSS) ¹ image of each target was examined to further reduce the number of misclassified galaxies in the sample.

2.1.2 Observations

Observations covering the $12^\circ \times 14^\circ$ area in the HRS were carried out on the 1.2m UKST of the Anglo-Australian Observatory (AAO) in 2002 October/November. All observations were carried out in conjunction with the 6dF Galaxy Survey (6dFGS) pro-

¹The Digitized Sky Surveys were produced at the Space Telescope Science Institute under U.S. Government grant NAG W-2166.

gram being undertaken by the AAO (Wakamatsu et al. 2003). Specifically, the 6dFGS and our HRS program observations were folded together to allow for joint execution of both programs, since many of our survey targets were not included in the original 6dFGS database. When allocating fibers, the 1500 galaxies in the study were given highest priority within the 6dFGS for the selected fields of observation. However, whenever a 6dF fiber became unassigned due to a conflict with the fiber selection from another target galaxy, the fiber was then reassigned to a target from the 6dFGS. The blue magnitude limit for the 6dFGS is 16.75 (i.e., $b_J < 16.75$), hence there is considerable overlap between our target lists and the 6dFGS. Over all the observed fields, approximately 70% of all targets were taken from our original list of 1500 galaxies. As can be seen in Figure 2.2, our observed galaxy magnitude distribution closely follows the magnitude distribution of the post-extraction HRS area of 2848 galaxies. Due to the brighter limiting magnitude of 6dFGS, we have slightly less proportional coverage at our faint limit. In addition, a few very faint objects were included as part of the 6dFGS, which again can be seen in Figure 2.2. Finally, a small number of 6dFGS objects lie within our 1° excision radii around clusters, which is evident in Figure 2.1.

Observations were carried out along standard 6dFGS procedures, which are summarized here and detailed in Jones et al. (2004). A combination of the 580V and 425R volume-phase holographic transmission gratings were used to optimize spectral coverage. This procedure yielded an instrumental resolution of 4.9 Å (580V) and 6.6 Å (425R), while covering the wavelength range 3900 – 7600 Å, i.e., from [OII]λ3727 through Hα over the HRS redshift range. Exposure times for each grating are listed in Table 2.5. HgCdNe arc and quartz flat exposures were carried out before and after primary fields. Eight nights were allocated to this project by the 6dFGS team, but three were adversely affected by weather (Tab. 2.1).

2.1.3 Reductions

In total, 547 usable galaxy spectra were obtained from the eight nights allocated. In Figure 2.1, individual field centers are labeled and shown in reference to the survey

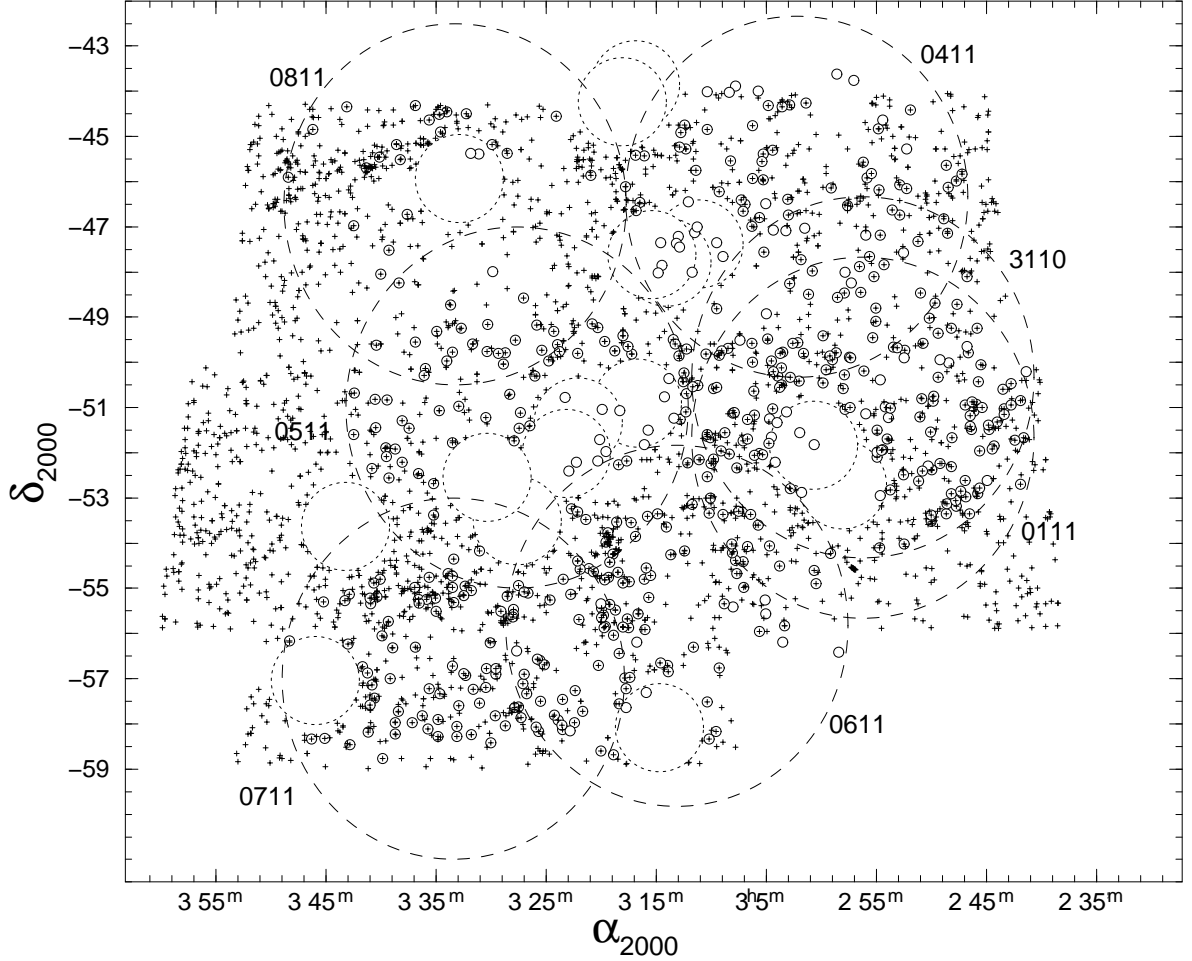


Figure 2.1 Observed fields in the 2002 study as conducted by the 6dFGS team. Crosses represent all 2848 galaxies from the SuperCOSMOS catalog, which constitutes our original target list. Note that, as described in the text, one degree radius regions ($\sim 2 R_A$) around 16 ACO clusters listed as members of the HRS by Zucca et al. (1993) are excluded from the catalog. The excised regions are shown as dotted circles. Small, open circles represent galaxies for which optical redshifts were obtained. Open circles *without* crosses denote galaxies that were added from the 6dFGS to prevent unused fibers. The 6dF $r-\theta$ positioner selects a 6-degree diameter region from the UKST field plates, which are denoted by large dashed circles. Labels refer to the spectroscopic observations detailed in Table 2.1 (column 4).

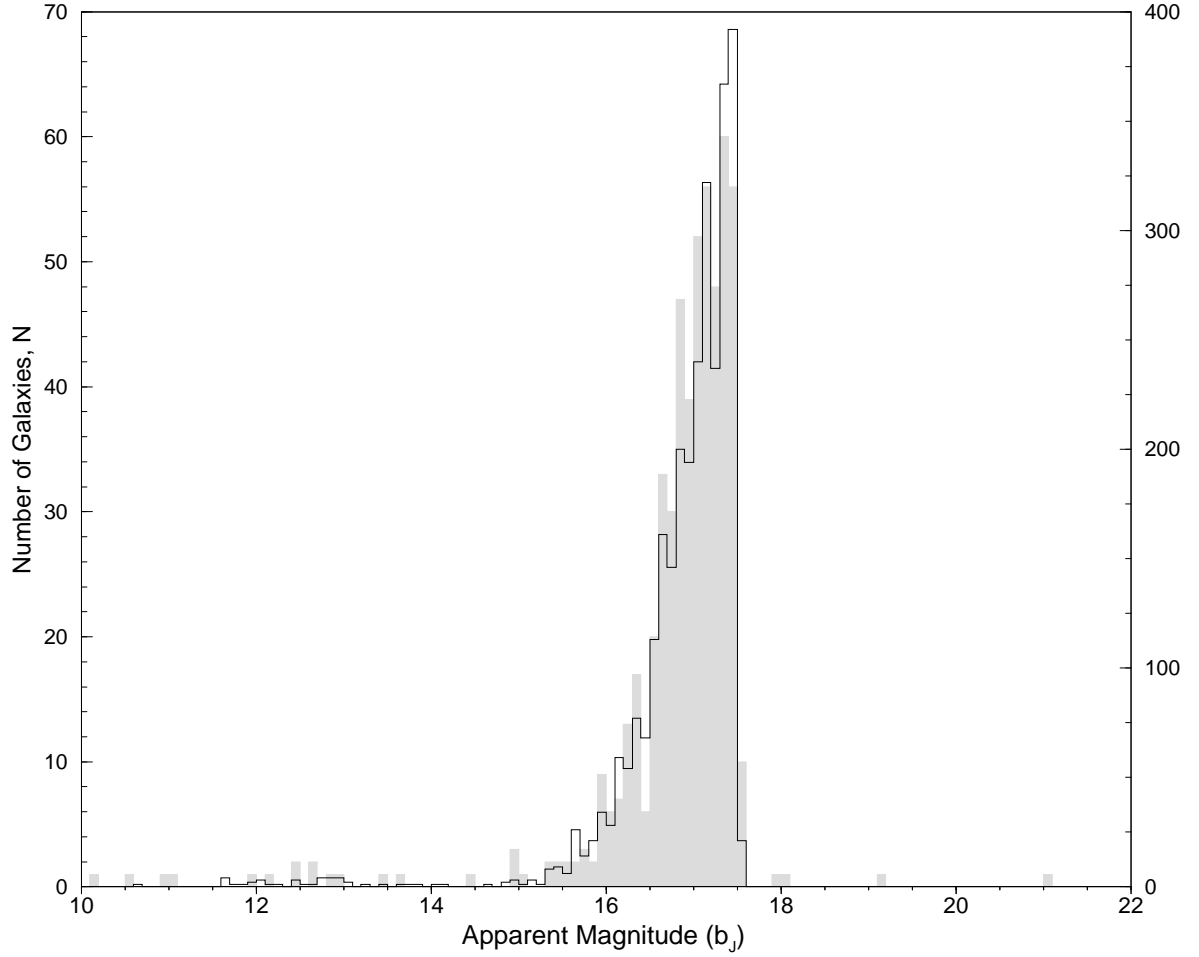


Figure 2.2 Histogram showing the magnitude distribution for the 6dF observations compared to the SuperCOSMOS inter-cluster galaxy list with limiting magnitude $b_J = 17.5$. Filled histogram shows the magnitude distribution of the observed objects (547) and correlates with the y-axis labeled on the left-hand side. Outlined histogram shows the original list of galaxies (2848) after the cluster galaxies were removed and correlates with the labels on the right-hand side. Extremely bright galaxies with $b_J < 10.0$ were excluded from the survey.

Table 2.1. 2002 6dF Observational Fields

Date	α_{2000}	δ_{2000}	ID	Field No.	Grating	$t_{exp}(s)$	Seeing	S/N
2002 Oct 31	02 55 57.9	−50 18 20	3110	198,199	580V	4×1200	2–3''	7.5
...	154	425R	4×600	3–5''	9.0
2002 Nov 01	02 55 57.9	−51 38 12	0111	198,199	580V	4×1200	1–2''	9.0
...	154	425R	4×600	1–2''	11.7
2002 Nov 03	03 02 00.4	−46 18 17	0411	247, 248	580V	4×600	3–5''	4.6
2002 Nov 04	03 02 00.5	−46 18 15	0411	247, 248	425R	4×600	2–3''	10.8
...	580V	4×1200	3–4''	8.7
2002 Nov 05	03 24 57.6	−50 58 17	0511	200	425R	4×600	2–3''	12.6
...	580V	4×1200	2.2''	9.8
2002 Nov 06	03 17 55.5	−55 48 06	0611	155	425R	4×600	2–3''	10.8
...	580V	4×1200	3–4''	7.8
2002 Nov 07	03 28 54.8	−56 58 04	0711	155, 156	425R	4×600	1–2''	10.5
...	580V	6×1200	3–4''	8.6
2002 Nov 08	03 33 02.2	−46 28 04	0811	200, 248	425R	4×600	1–2''	5.4
...	249	580V	4×1200	1–2''	—

Note. — Numbers in parentheses refer to the column numbers. (1) Date of observation, (2) Right Ascension of the field center in hours, minutes, and seconds (J2000), (3) Declination of the field center in degrees, arcminutes, and arcseconds (J2000), (4) Identification number as found in Figure 2.1, (5) Schmidt field number, (6) Grating, (7) Exposure time, (8) Approximate seeing, (9) Average signal-to-noise.

area. Altogether, 100 fibers were operational during our sequence of observations. With 9 fibers donated to sky, this leaves a total of 91 possible galaxy redshifts per imaged field. Night 7 with the 580V grating was not reduced due to a telescope focus error, so redshifts were obtained for only 25% of the 0811 field (Tab. 2.1). Although the signal-to-noise ratio was relatively low in many of our spectra (< 10), over 95% yielded reliable redshifts (excluding 0811). Due to 6dFGS priorities and galaxy overcrowding, redshifts were obtained for some galaxies not originally included in our source lists. There remained 3 Galactic stars and 27 objects with unusable spectra in the sample.

The automatic 6dF data reduction (6DFDR) package completes the following steps directly after observation: debiasing, fiber extraction, cosmic-ray removal, flat fielding, sky subtraction, and wavelength calibration (Jones et al. 2004). As a final step, the

post-6DFDR files from each exposure were co-added into single spectra.

2.1.4 Redshift Determination

Methods for the determination of galaxy redshifts fit into three basic categories depending on their spectral characteristics: absorption, emission, and those spectra containing both absorption and emission features. For spectra exhibiting absorption features, the IRAF ² based cross-correlation package, *rvsao*, was utilized to determine radial velocities against four template spectra: two stellar spectra obtained from the Coudé Feed spectral library (Jones 1998) and two spectra obtained from the sample (a Galactic star and a nearby galaxy whose redshift was also determined by *rvsao*).

The method of determining redshifts for emission-dominated galaxy spectra was completed in two steps. First, JAR and MCF independently measured wavelength centers for each detectable spectral line via Gaussian fitting then determined its redshift. Second, each emission line was assigned a weight by MCF based upon the sharpness of the line and the surrounding noise level. The assigned weight was based upon a 5 point scale, where a “5” denoted a peak height greater than three times the FWHM with minimal background. For expected emission lines that were faintly detectable from the background, a weighting of “1” was assigned. This appropriately distinguished between emission lines with robust redshift determinations from those compromised by noise. Redshifts were averaged for galaxy spectra exhibiting both strong emission and absorption features. Whenever there was a discrepancy of $\Delta cz > 100 \text{ km s}^{-1}$ between the two methods, preference was given to the emission line value. As a last step, heliocentric corrections were applied to all redshifts. Coordinate and redshift information for the 547 observed objects is compiled in Table 2.2.

²Image Reduction and Analysis Facility (IRAF) is written and supported by the National Optical Astronomy Observatories (NOAO) and the Association of Universities for Research in Astronomy (AURA), Inc. under cooperative agreement with the National Science Foundation.

2.1.5 Coverage

Outside the previously determined cluster areas that were excised, there were 2848 potential targets selected by SuperCOSMOS (galaxies with $b_J < 17.5$). It was found from a comparable sub-sample selection that $\sim 15\%$ of the targets labeled as ‘galaxies’ by SuperCOSMOS were actually stars. Therefore, the completeness of the survey is $547/2420$, or 23% . The optical redshifts obtained in this survey more than double the previously published information for the HRS (Fig. 2.3). Previous inter-cluster observations were limited spatially, primarily focused in the southeast portion of the supercluster. Overlap with previously observed galaxies was not intended, but for the 10 cases, 6dF redshifts are $\leq \pm 250 \text{ km s}^{-1}$ the previous measurements from L83 and Chincarini et al. (1984).

It is noticeable from Figure 2.1 that the coverage is not uniform over the original $12^\circ \times 14^\circ$ area. In fact, the total area covered by the observations is more accurately $9^\circ \times 14^\circ$. Furthermore, the galaxies in the Western portion are more heavily sampled than those in the East. This non-uniformity is primarily a result of the weather problems coupled with the competing demands of both HRS and 6dFGS surveys when selecting field centers for the observations. Although the mean completeness is 23% , the field centers in the Western portion are sampled closer to 28% completeness, while the Eastern field centers are at $\sim 22\%$.

2.2 6dF Spectroscopic Observations: 2004

All observations of intercluster galaxies were carried out on the 1.2m UKST in conjunction with the six-degree field galaxy survey (6dFGS, Jones et al. 2004). The semi-automated 6dF data reduction system (6DFDR) extracts, flat-fields, sky subtracts, and coadds spectra from multiple exposures (3 per field per filter). As a final step, 6DFDR splices the two filtered spectra for continuous wavelength coverage from $3900\text{--}7600 \text{ \AA}$ (i.e., $[\text{OII}]\lambda 3727$ through $\text{H}\alpha$ at the mean HRS redshift). Next the automated *runz* software was utilized, where each target spectrum is compared to 8 rest-frame spectral

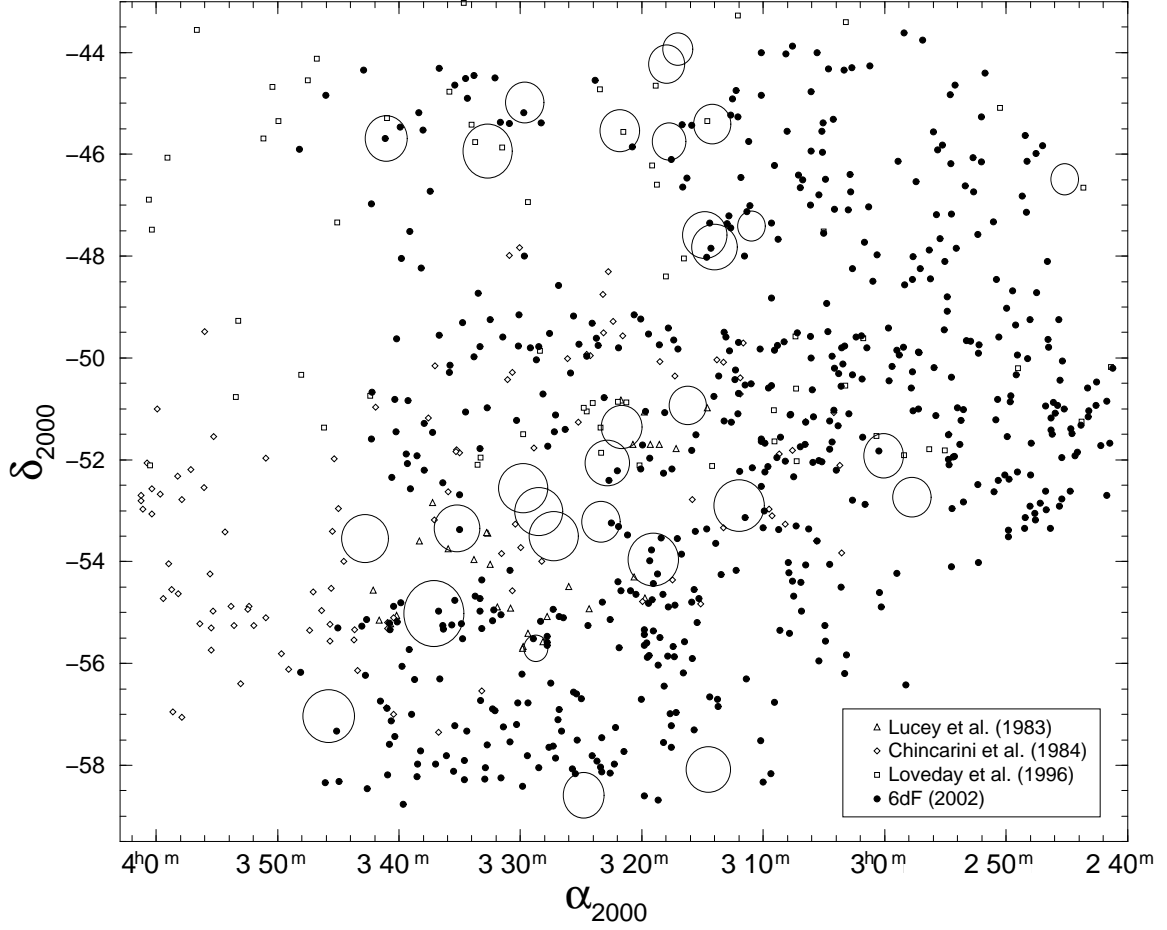


Figure 2.3 The HRS region under study displaying both 6dF observations from 2002 and other previous inter-cluster redshifts. Previously observed galaxies are plotted with different symbols to show the increased amount of information with our 6dF study. Redshifts from our 2002 study are shown as filled circles. Clusters in the observing region with known redshift (Tab. 3.1) are shown as large open circles with radii of 2 Mpc ($1 R_A$).

Table 2.2. Velocity Data for 6dF Galaxy Spectra

ID	α_{2000}	δ_{2000}	b_J	Reference	cz (km s $^{-1}$)	σ_{cz}
HRS J024113–501154	02 41 13.42	–50 11 54.1	13.41	e	27662	40
HRS J024126–514012	02 41 26.02	–51 40 12.0	17.36	e	30523	86
HRS J024141–524151	02 41 41.38	–52 41 51.7	17.17	e	14078	52
HRS J024141–505106	02 41 41.86	–50 51 06.1	16.93	e	18818	47
HRS J024213–514333	02 42 13.22	–51 43 33.2	17.45	e	22710	50
...

Note. — Numbers in parentheses refer to the column numbers. (1) IAU name, (2) Right ascension in hours, minutes, and seconds (J2000), (3) Declination in degrees, arcminutes, and arcseconds (J2000), (4) b_J magnitude as listed in SuperCOSMOS, (5) “a”= absorption lines used to calculate redshift, “e”= emission lines used to calculate redshift, “ae”= both absorption and emission lines used, (6) Velocity, cz , (7) Velocity error. The complete version of this table is in the electronic edition of the Journal. The printed edition contains only a sample.

templates, 5 (morphology-specific) galaxy spectra from Kennicutt (1992) and 3 stellar spectra from Jacoby et al. (1984). Automated cross-correlation is used for “absorption” spectra (Tonry & Davis 1979), and “emission” redshifts are obtained by Gaussian-fitting typical spectral features (e.g., OII, OIII, Balmer) and multi-line matching. A quality flag, Q , from 1–5 is then assigned by the observer, where over 95% of all object spectra led to redshift determinations with $Q \geq 3$ (Jones et al. 2004). These software packages are modified extensions of the data reduction techniques developed for the now-complete, two-degree field galaxy redshift survey (2dFGRS, Colless et al. 2001). Since both interchangeable 6dF field plate units were available with ≥ 120 usable fibers each, the observations were optimized by simultaneously observing the current field while configuring the subsequent one. A journal of the observations is found in Table 2.3.

2.2.1 Sample Characteristics

An original target list of $b_J \leq 17.5$ galaxies was constructed for the $20^\circ \times 20^\circ$ area proposed to cover the HRS. This magnitude limited sample was drawn from the

Table 2.3. 2004 6dF Observational Fields

Date	α_{2000}	δ_{2000}	ID	Field No.	Grating	$t_{exp}(s)$	Seeing	S/N
2004 Nov 06	02 48 00.0	−57 00 00	0611a	154, 155	580V	3×1200	2''	7.4
...	115, 116	425R	3×600	2''	8.8
...	03 51 00.0	−52 00 00	0611b	200, 201	580V	3×1200	3–4''	7.5
...	156	425R	3×600	3–4''	8.9
2004 Nov 07	02 54 00.0	−45 00 00	0711a	247, 248	580V	3×1200	2–3''	9.2
...	300, 301	425R	3×600	2–3''	10.5
...	03 48 00.0	−46 00 00	0711b	249, 250	580V	4×1200	3–4''	5.2
...	302, 303	425R	3×600	3–4''	8.3
2004 Nov 08	02 48 00.0	−57 00 00	0811a	154, 155	580V	2×1200	3–4''	5.7
...	115, 116	425R	3×600	3–4''	6.6
2004 Nov 09	03 15 00.0	−56 10 00	0911a	200, 201	580V	3×1200	3–4''	9.6
...	155	425R	3×600	3–4''	9.7
...	03 51 00	−52 00 00	0911b	200, 201	425R	3×600	4''	6.7
2004 Nov 10	03 51 00.0	−52 00 00	1011a	156	580V	4×1200	4.5''	9.4
2004 Nov 10	03 35 00.0	−44 30 00	1011b	248, 249	580V	1×1200	4.5''	9.4
2004 Nov 11	03 35 00.0	−44 30 00	1111a	248, 249	580V	3×1200	3–4''	8.4
...	301, 302	425R	3×600	3–4''	7.7
...	03 45 00.0	−57 30 00	1111b	156, 157	580V	2×1200	5–6''	3.0
...	117, 118	425R	5×600	4–5''	7.2
2004 Nov 12	03 45 00.0	−57 30 00	1211a	156, 157	580V	4×1200	1–2''	10.0
...	04 11 00.0	−60 45 00	1211b	117, 118	580V	3×1200	1–2''	11.9
...	425R	3×600	1–2''	13.3
2004 Nov 13	03 28 00.0	−49 30 00	1311a	200	580V	4×1200	2–3''	9.1
...	425R	3×600	2–3''	9.0
...	03 21 00.0	−44 30 00	1311b	248	580V	3×1200	2''	11.5
...	425R	3×600	3–4''	13.0

Note. — Numbers in parentheses refer to the column numbers. (1) Date of observation, (2) Right Ascension of the field center in hours, minutes, and seconds (J2000), (3) Declination of the field center in degrees, arcminutes, and arcseconds (J2000), (4) Identification number as found in Figure 2.4, (5) Schmidt field number, (6) Grating, (7) Exposure time, (8) Approximate seeing, (9) Average signal-to-noise.

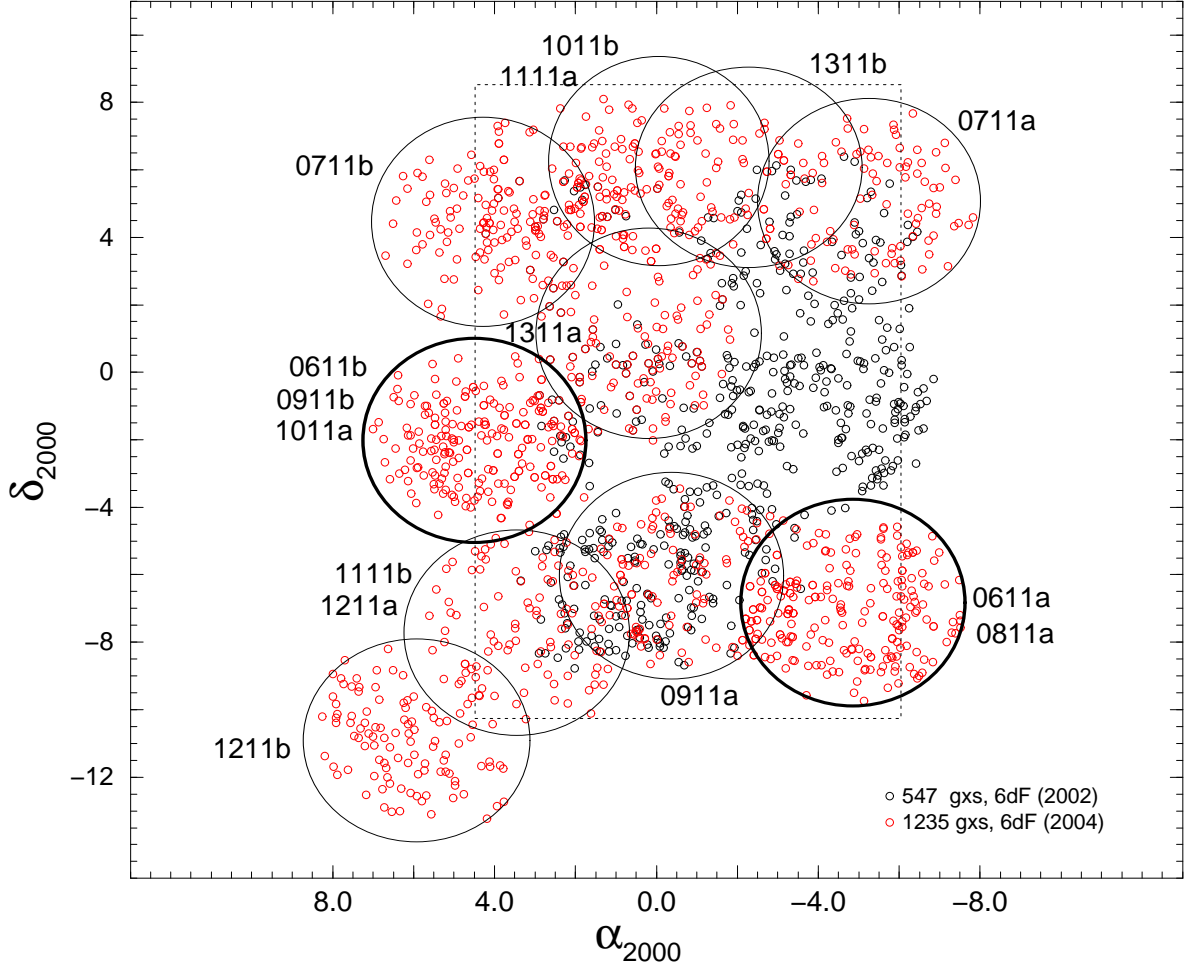


Figure 2.4 Sky map showing the increase of area with the 2004 observations when compared to those of 2002. The figure coordinates are offset from the chosen HRS center $3^{\text{h}}20^{\text{m}} -51^{\circ} 00'$. The small open circles represent galaxies for which quality spectra were observed, and the 100% increase in the 2004 dataset is clear. The 2004 6dF fields are shown as large open circles, where the bold lines represent a double configuration for this survey (i.e., with the same 6dF field center). The alphanumeric tags associated with each field correspond to the journal of observations in Table 2.3. The rectangular area given by the dotted lines shows the inner $14^{\circ} \times 20^{\circ}$, over which there is the most uniform coverage.

SuperCOSMOS catalog database for the UKST IIIaJ (Blue) Survey (Cannon 1984) covering the specified area. The b_{J} magnitude is defined by the response of the Kodak

IIIaJ emulsion in combination with the GG395 filter. SuperCOSMOS is an advanced photographic plate digitizing machine that provides high-resolution ($0''.7$), multi-color (b_J and r_F) information over the entire Southern sky (Hambly et al. 2001b). Most pertinent to the HRS survey are the positional and brightness information for galaxies selected by an automated, two-stage classification scheme (star-galaxy separation) based on brightness profiles and similarity to related objects (Irwin & McMahon 1992; Hambly et al. 2001a). However, rather than relying exclusively on the star-galaxy classifier, a visual inspection was conducted of the target list using 1 arcmin^2 postage stamp images from the DSS. Therefore, noticeable stars, crowded galaxies, and other misidentified objects were eliminated by visual inspection to give a final target list of 4626 assumed intercluster galaxies.

As with the previous survey in Paper I, rich galaxy clusters with reliable mean redshifts in/near the HRS were excised, since the design of 6dF is uniquely suited to probe the intercluster regions. In equal area projection centered on each cluster, all galaxy targets were excised with a radius of 0.5 ($1R_{\text{Abell}} \sim 2 \text{ Mpc}$), and the cluster was denoted with a “Y” in Table 4.2, column 9. Our survey limiting magnitude of $b_J = 17.5$ (where $b_J = B - 0.28(B - V)$ in Blair & Gilmore 1982) was imposed by the science goals and the instrumentation. The HRS survey observations were folded in with the 6dFGS, which has a limiting blue magnitude of $b_J = 16.75$. When configuring each 6dF field, the HRS survey targets took precedent. Otherwise unused fibers which were not assigned to our intercluster targets were then configured to 6dFGS targets. In this way, some coverage occurred within the cluster regions originally excised from our survey. Since previous spectroscopic observations of the intercluster HRS region were conducted with 6dF (Jones et al. 2005; Fleenor et al. 2005), any galaxy with an acceptable ($Q \geq 3$) measured 6dF redshift was automatically excluded from the target list. Figure 2.4 shows the increase of the survey area beyond the 2002 observations in Paper I as approximately 75% from 170 to 300+ deg^2 . The small red open circles represent galaxies that were observed in 2004 when compared to the black open circles from the 2002 observations. The large open circles show the 6dF field centers listed in Table 2.3.

Two specific technical issues influenced the construction of the survey and the selection of 6dF field centers. First, since the observations from Paper I were sparse within the inner $12^\circ \times 12^\circ$ of the HRS ($\sim 23\%$), one objective was to increase and maintain a uniform completeness across the previously observed region. The second objective was push out toward rich galaxy clusters listed as HRS members in Einasto et al. (1997), but not included in the original 2002 survey (e.g., A3266 and A3122). With these goals in mind, Figure 2.5 shows the 2004 field centers for the survey as solid lines in relationship to the original 2002 fields shown as dotted circles. The addition of 9 6dFGS fields (long-dashed circles) in the north aided the augmentation to have more uniformity within the $14^\circ \times 20^\circ$ area. The equal-area projection is offset from the approximate HRS center at $3^{\text{h}}50^{\text{m}}, -51^\circ00'$. The two bold, solid circles show where a double configuration was observed with the same field center. The rectangular region denotes the observing region from which the areal mask was calculated, an area of $\sim 280 \text{ deg}^2$ (see §2.2.2).

2.2.2 Selection Effects

As with any survey or observing program, the specific combination of the target characteristics and the instrumentation imposes certain biases on the resulting sample. There are at least 3 major selection effects caused by the 6dF instrument and the observing allocation: *i*) spatial crowding of intercluster galaxies, *ii*) areal incompleteness, and *iii*) radial selection due to brightness limit. Each selection effect is discussed and measured, and its impact on the science results is explored. Ideally, one would completely account for each selection effect and restore the observations to reflect the characteristics of the original population. Unfortunately, this is not possible, due to the unpredictable combination of 6dF fiber/button collisions with the overlap of observed fields. The last two effects, however, are quantified and accounted for in our calculations and results. By quantifying the constraints of the observed sample, we are able to better understand the results of the data.

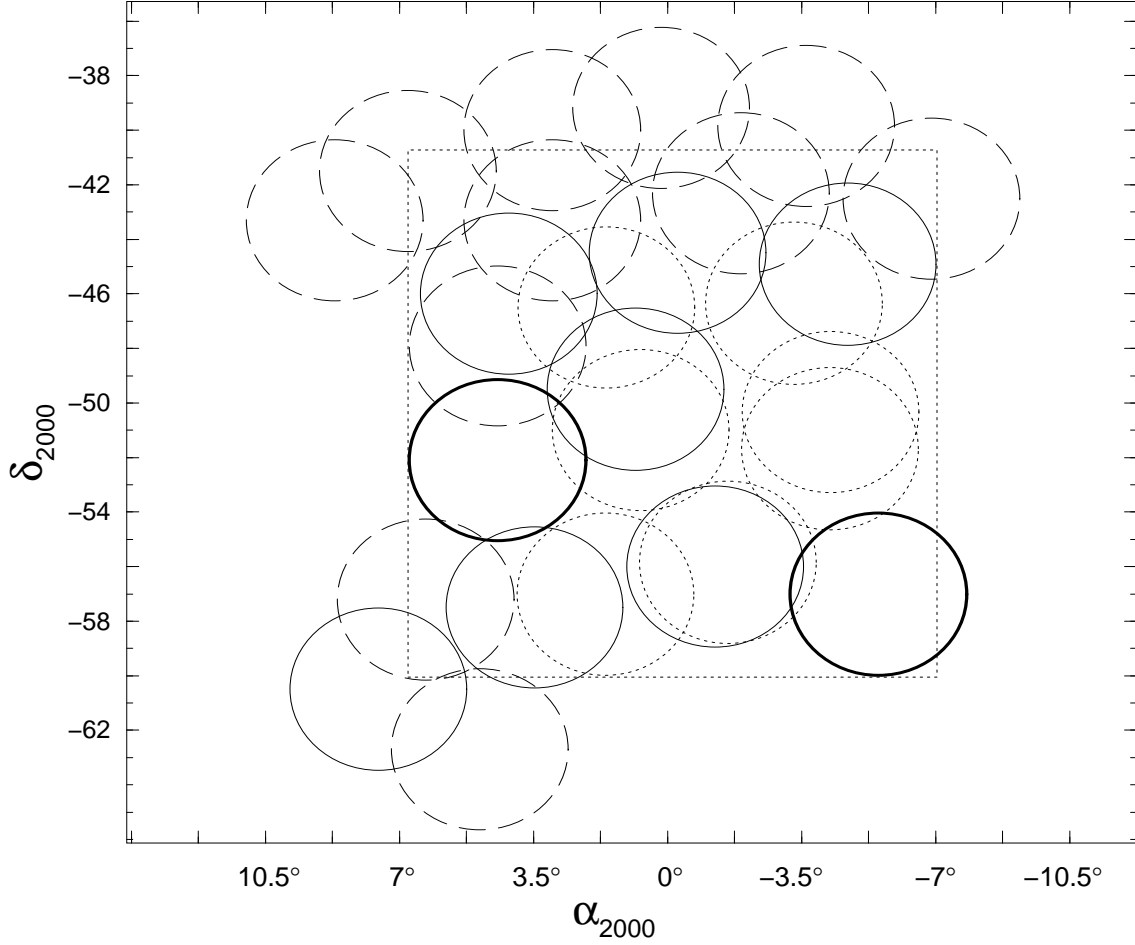


Figure 2.5 Spatial map outlining the 6dF field centers from the various stages of the current HRS survey. Each circle represents the $5^{\circ}.7$ field-of-view, whose coordinates are offset from the chosen HRS center $3^{\text{h}}20^{\text{m}} -51^{\circ} 00'$. The dotted circles represent field centers from Paper I, the long-dashed circles from the 6dFGS, and the solid lines show the fields for the 2004 6dF observations. The bold lines represent a double configuration for the 2004 survey (i.e., with the same 6dF field center). The intended overlap of the fields allows for the observing of otherwise over-crowded galaxies. The rectangular area given by the dotted lines shows the inner $14^{\circ} \times 20^{\circ}$, where the average completion is $\sim 50\%$.

Fiber Button Collisions

Although the actual light-collecting area of the 6dF magnetic buttons is sufficiently small to resolve galaxies at $6''.7$, the prism housing is much larger and creates a mini-

mum spacing between simultaneously observed galaxies of $5'.7$ (~ 0.5 Mpc at $z = 0.06$). Therefore, 6dF is not well-suited to observations in rich clusters (and presumably much of the surrounding infall region) for which galaxy nearest neighbor separations tend to be $< 5'$. As mentioned previously, we excised the regions around galaxy clusters. There is also a field arrangement constraint set by the configuration software, CONFIGURE, which prevents optic fibers crossing or stretching beyond a set limit (Jones et al. 2004). Accounting for this constraint is quite intractable, because each button has a different fiber length and the field orientation is unpredictable. In an attempt to estimate the number of galaxies affected by the button-size constraint, the projected center-to-center distance for the intercluster, nearest-neighbor galaxies, $d_{\text{gx-gx}}$, in our survey was measured. Figure 2.6 shows a histogram of the number of intercluster galaxies as a function of $d_{\text{gx-gx}}$. By noting the vertical dashed line at $5'.7$, it is apparent that approximately half the *intercluster* sample (52%, 2172 galaxies) cannot be observed with only a single configuration for any one 6dF field. Furthermore, the inset histogram shows a vertical line at a nearest-neighbor separation of $10''$, which gives the cut-off for using 6dF to obtain a galaxy spectrum. Approximately 200 galaxies have smaller separations than $10''.0$ and were eliminated from the survey.

To remedy the instrumental problems associated with the automated configuration of the fiber optic magnetic prism buttons, all 6dF survey fields partially overlap with the adjacent neighboring fields. This effect, clearly noticeable in Figure 2.5, provides multiple opportunities for crowded galaxies (i.e., those with neighbors at $\leq 5'.7$ and/or fiber collisions) to be observed. Because crowded galaxies are not localized but rather found throughout the survey region, significant field overlap aids in alleviating the potential bias that could enter if a double configuration was not available. Approximately 20% (420) of the 6dF galaxies determined to be in crowded fields were observed with the field overlap in our survey. Since one of the goals of this study is to examine potential substructure in these intercluster regions, the inability to properly sample crowded fields could introduce a bias against this determination. This is particularly the case, if we presume that structure assembles in a hierarchical fashion, i.e., via merging. We attempt to show the potential kinematic association of crowded intercluster galaxies in

Figure 2.7, where the line-of-sight velocity difference of 225 galaxy pairs is plotted as a function of $d_{\text{gx-gx}}$. The long-dashed line marks a $|\Delta cz| = 700 \text{ km s}^{-1}$, which is the approximate upper limit for loose group associations in the Las Campanas Redshift Survey (LCRS, see Fig. 5 in Tucker et al. 2000, and Shectman et al. 1996 for survey details). Note that there is a greater fraction of galaxy pairs (80%) with $|\Delta cz| < 700 \text{ km s}^{-1}$ for separations of $d_{\text{gx-gx}} < 2'$ ($\sim 0.1 \text{ Mpc}$) than the 50% found for $d_{\text{gx-gx}} > 2'$. When considering the entire $d_{\text{gx-gx}} \leq 5'.7$ sample, there is equal probability that a pair has either $\Delta cz < 700 \text{ km s}^{-1}$ or $> 5000 \text{ km s}^{-1}$. Den Hartog (1997) finds that within rich clusters 6% of the galaxies are binaries that meet the criteria $d_{\text{gx-gx}} \leq 0.1 \text{ Mpc}$ and $\Delta v_{\text{los}} \leq 300 \text{ km s}^{-1}$. Only 10% (29) of our nearest-neighbor pairs fit the $\Delta v_{\text{los}} \leq 300 \text{ km s}^{-1}$ constraint, which amounts to $\sim 3\%$ of the observed 6dF sample (58/2106). We will return to this observation in later sections, when considering the organized arrangement of galaxies in the HRS.

Observational Incompleteness and Areal Mask

Of the 4142 intercluster galaxies in the “inner” $14^\circ \times 20^\circ$ survey region, 6dF redshifts were collected for 2106 objects (including those from Paper I and the 6dFGS). Though the mean completeness for intercluster galaxies with $b_J \leq 17.5$ is approximately 51%, we quantify the completeness as a function of spatial location by creating an areal mask. Because the UKST/6dF field-of-view is much larger than the structures we seek to resolve, increasing the spatial resolution of the observational completeness will aid in describing and understanding substructure in the HRS. We grid the survey region into squares with area of 1 deg^2 ($\sim 18 \text{ Mpc}^2$) and count the number of unobserved and observed galaxies per cell. By dividing these totals for each cell, we calculate a fractional observational completeness as a function of area. Figure 2.8 shows the greyscale completeness for each cell within the effective, inner $14^\circ \times 20^\circ$, where darker cells are more complete. The increments of completeness are binned as increases of 20%, and the excised clusters are represented by the white open circles. Since clusters were excised with circular area and the grids are rectangular, not every excised cluster presents a fully empty cell (as well because some 6dFGS targets fell within the cluster

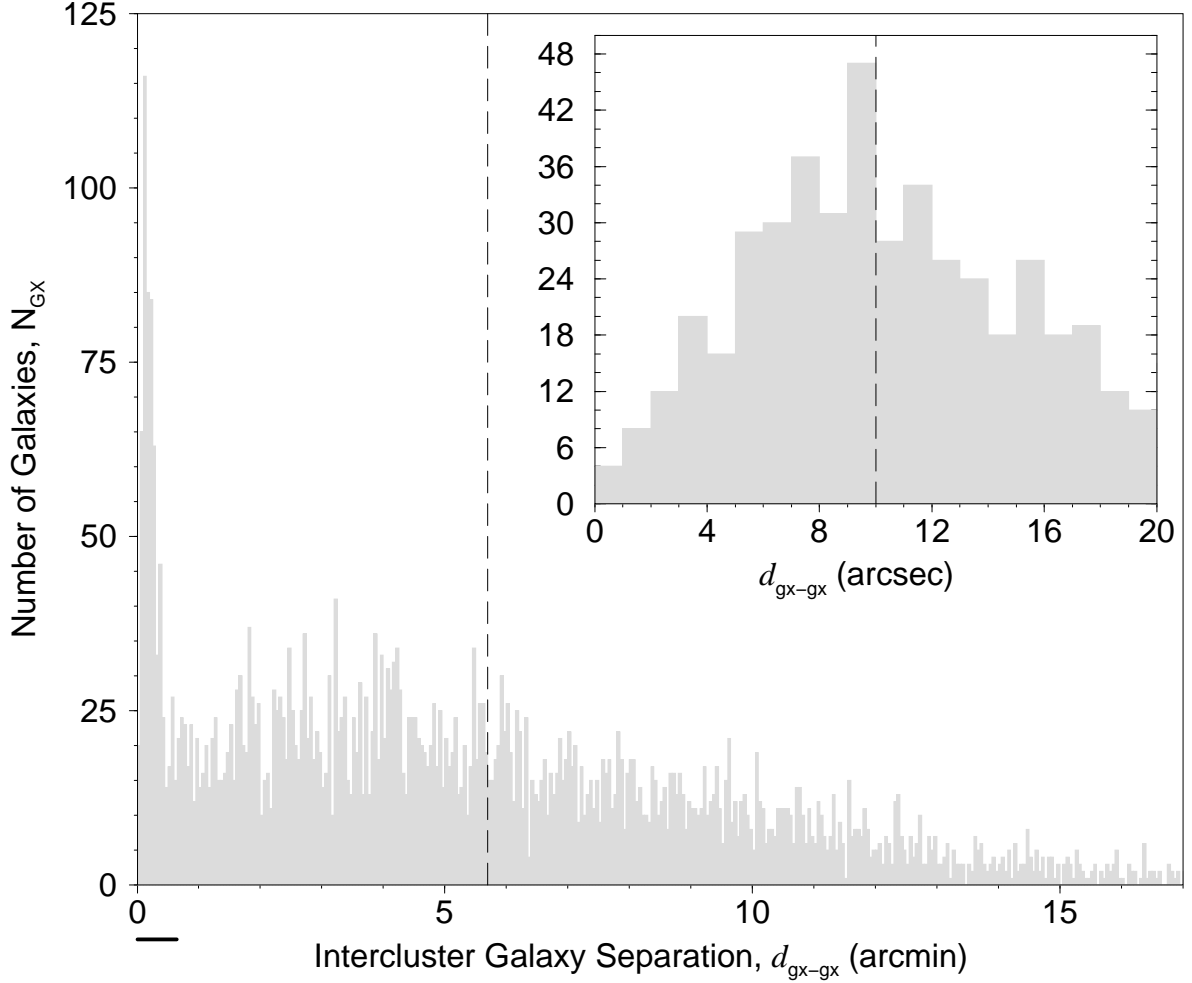


Figure 2.6 Histogram displaying the number of intercluster galaxies in the HRS survey as a function of nearest-neighbor projected separation, $d_{\text{gx-gx}}$. Over half of the 4626 targets have separations of less than $5'.7$ given by the dashed, vertical line. This distance marks the minimum single-pass separation for simultaneously observing two galaxies with 6dF (see §2.2.2). The small, bold line shows the effective distance of the inset histogram (in *arcsecs*), whose dashed vertical line at $10''$ represents separations that are unresolvable with 6dF. Approximately 200 galaxies were eliminated from the survey because $d_{\text{gx-gx}} < 10''$.

boundaries). This is an effective rectangular area because the smaller 16 deg^2 block to the southeast effectively covers the blank space on the outer edges of the larger $14^\circ \times 20^\circ$ rectangle. Since there is little overlap of 6dF fields outside of the inner area,

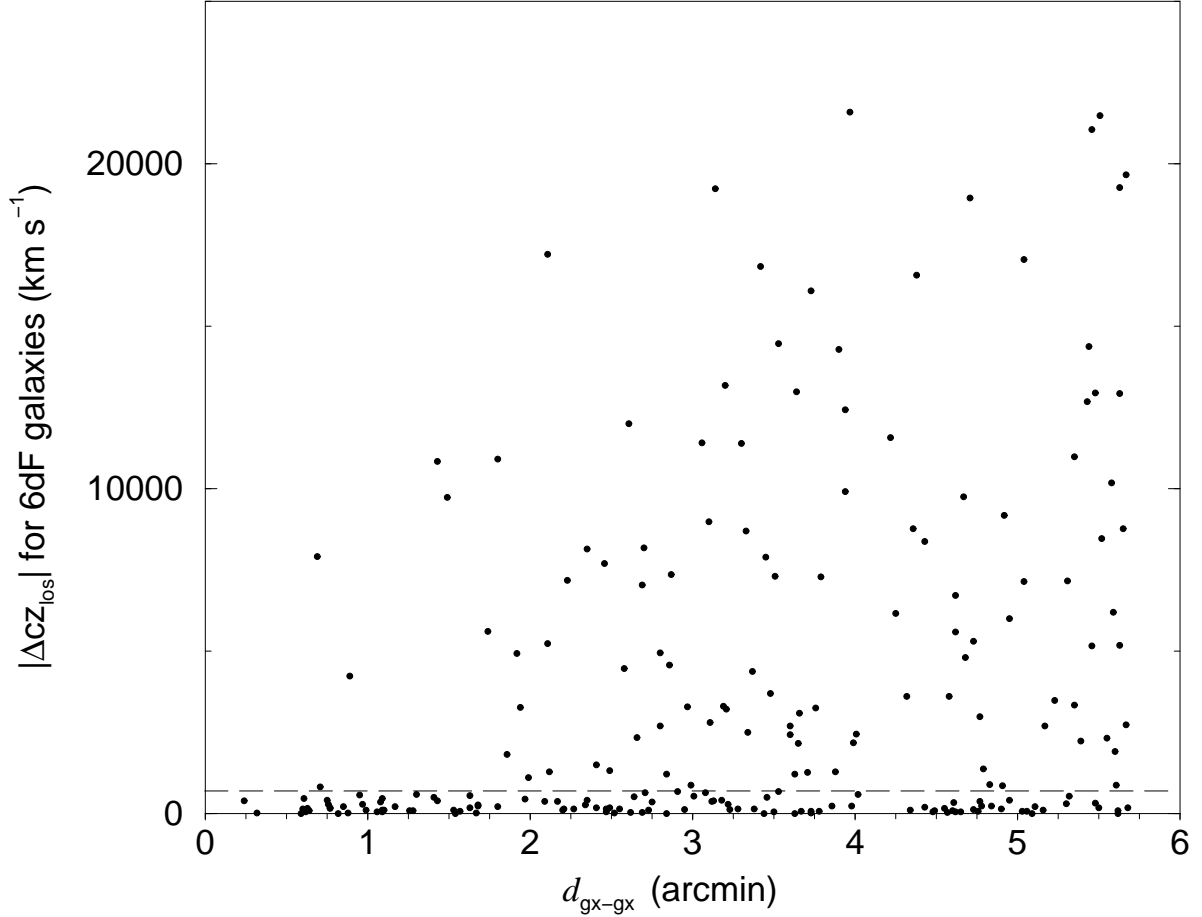


Figure 2.7 Line-of-sight velocity differences, $\Delta_{cz_{los}}$, for observed nearest-neighbor galaxies as a function of projected spatial separations for $d_{gx-gx} \leq 5'.7$. Horizontal dashed line at 700 km s^{-1} marks the probable upper limit for kinematic association between galaxy pairs (see §2.2.2). For $d_{gx-gx} \leq 2'.0$, the probability that $|\Delta_{cz_{los}}| \leq 700 \text{ km s}^{-1}$ increases from 50% to 80%.

the completeness decreases dramatically and is not shown for those areas. Figure 2.9 shows the contribution of each degree of fractional completeness as a function of α . It is clear that the completeness is highest within the central portion of the survey area, even though the average throughout the inner region is $> 50\%$. Since the existence of substructure is observed and verified through the arrangement of galaxy populations, we rely heavily on the completeness mask to calculate accurate overdensities throughout the paper.

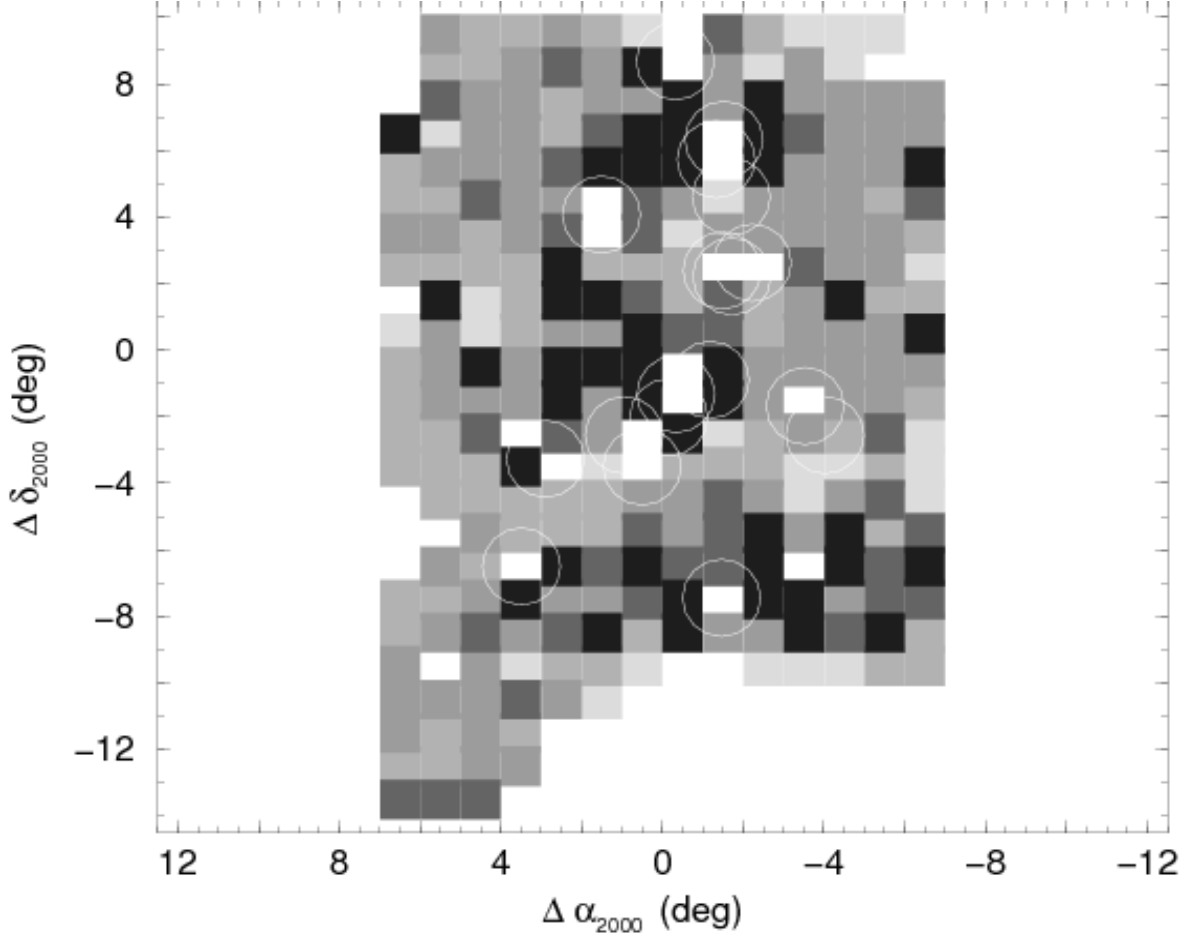


Figure 2.8 Equal area survey mask displaying observational completeness as a function of greyscale. The entire 300+ deg² are delineated into 1 deg² blocks with five levels of greyscale measuring the completeness of SuperCOSMOS galaxies with $b_J \leq 17.5$: 0.0 (white), 0.00–0.20, 0.20–0.40, 0.40–0.60, 0.60–0.80, 0.80–1.00 (black). Open white circles show ACO clusters with reliable redshifts in the HRS, which were excised from the observations with a radius of 0.5 ($1R_{\text{ABELL}} \sim 2.0$ Mpc). The completeness in each non-overlapping cell was computed by taking the ratio of observed to available intercluster galaxies. Though white boxes denote empty areas of survey galaxies (both observed and available), all clusters are not necessarily associated with whitespace since the cell grid was constructed independent from galaxy cluster centers. All coordinates are offset from the chosen HRS center at 3^h20^m, –51° 00′.

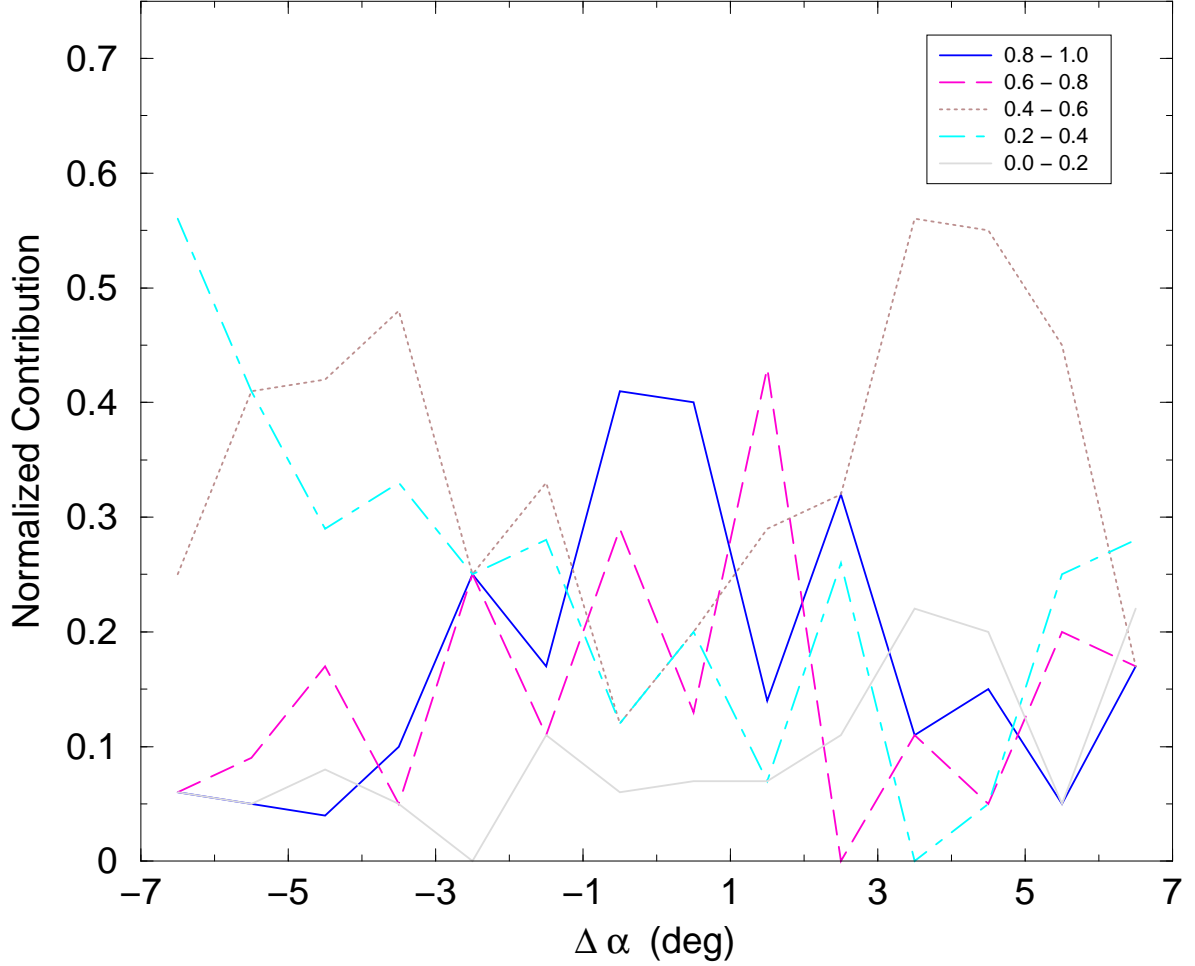


Figure 2.9 Normalized contribution for each degree of completeness presented as a function of offset α from $3^{\text{h}}24^{\text{m}}$. We easily observe that the completeness is higher toward the middle of the survey area than on the edges, i.e., there is a larger contribution of higher completeness (dark) than away from the center. This is due partly to the fact that a higher number of HRS clusters reside closer to the middle of the spread in $\Delta\alpha$.

Radial Selection Function

Since we are interested in measuring and comparing the number density of different substructures within the HRS, there must be a baseline to which to compare our observations. A correct modeling of a uniform distribution of background galaxies assumes an accurate accounting for the luminosity function (LF). Specifically, the selection function gives a prediction of the number of galaxies that *should be* observable for a uniform

distribution of background galaxies given the limiting magnitude, the area, and the completeness of the survey. Regardless of the particulars, all selection functions have a general bell-shaped profile, where the increase of the observing volume as redshift increases is modulated by the drop-off of observable galaxies due to the limiting magnitude constraint on the fraction of the LF that is observed..

Given a universal differential LF, $\Phi(L)$, the radial selection function, $\phi(r)$, provides a way to choose the decreasing fraction of the LF at increasing distances because the survey is magnitude-limited ($b_J \leq 17.5$):

$$\phi(r) = \frac{\int_{L(r)}^{\infty} \Phi(L) dL}{\int_{L_{\min}}^{\infty} \Phi(L) dL}, \quad (2.1)$$

where $L(r)$ is the minimum luminosity detectable at the distance r , and $L_{\min} = \text{Min}[L(r), L_{\text{com}}]$ with L_{com} as the minimum luminosity for which the catalog is complete (Yahil et al. 1991; Erdoğdu et al. 2004). Because deviations from the Hubble flow by local gravitational perturbations are assumed slight, we take $\phi(r) = \phi(cz)$. Although modeling the LF via the number counts method from Metcalfe et al. (1991) was used in Paper I (and is still upheld as valid to fainter magnitudes in the Herschel and Hubble Deep Fields, see Metcalfe et al. 2001), methods that assume a universal LF and utilize spatially unbiased, maximum likelihood estimators have gained in popularity in larger surveys (e.g., SDSS and 2dFGRS, Sandage et al. 1979; Efstathiou et al. 1988). Since a magnitude-limited sample is restricted to observing only the intrinsically more luminous galaxies with increasing redshift, an accurate representation of the galaxy LF is critical to a reliable prediction of the radial selection function. We choose the volume-limited calculations of the Schechter-form LF (Schechter 1976) and its associated parameters from the 2dFGRS (Norberg et al. 2002):

$$\Phi(M) dM = (0.4 \ln 10) \Phi^* 10^{0.4(\alpha+1)(M^*-M)} \exp\left(-10^{0.4(M^*-M)}\right) dM, \quad (2.2)$$

where we use the type-specific values from Croton et al. (2005, Tab. 1) for the parameters Φ^* , α , and M^* . The values of these observationally-established constants are crucial as they govern the Schechter-form LF curve characteristics such as the knee in

the LF separating bright and faint galaxies (M^*), the faint-end galaxy slope (α), and the overall normalization (Φ^*).

Furthermore, we have also used the type-dependent, 2dFGRS-established k -corrections (Norberg et al. 2002) and e -corrections (Croton et al. 2005) to model the distribution of background galaxies at higher redshifts. While the “ k ” effect is an instrumental constraint due to the difference in the values of ν_{emitted} and ν_{observed} (Humason et al. 1956; Oke & Sandage 1968), the e factor depends heavily on our assumptions and predictions regarding galaxy evolution modeling (Tinsley 1970; Bruzual A. 1983; Poggianti 1997). Though there is little doubt that higher redshift galaxies were bluer at earlier epochs, the precise manner in which to model such behavior is not completely worked out. To examine the various effects of LF modeling on the expected galaxy counts, we present in Figure 2.10 the number of observed intercluster galaxies in our survey as a function of redshift. Overlayed smooth curves that contain LF differences model the predicted number of galaxies for the specified survey area (280 deg²) and overall completeness (51%). The curves differ slightly based on their method and/or parameters used when calculating the LF and how it varies as a function of redshift. While the differences between number counts and maximum likelihood methods may be significant when considering the LFs, we note that there is little change in the k -corrected model distributions when predicting galaxy populations over such large survey areas (solid and dashed lines in Figure 2.10). Though most of the differences between the curves are slight, we do report an increase of $\sim 10\%$ for the predicted number of galaxies when evolutionary ($k + e$) corrections are included.

2.3 Supplemental Intercluster Observations

Because there is an ever-increasing amount of redshift information publicly available, we will draw from the published redshifts of various surveys in the vicinity of the HRS. In general, these observations are directed toward specific galaxy clusters, and some care must be taken to alleviate contamination of the intercluster regions from individual galaxies belonging to the clusters (see §6.6). Our goal is to detect *intercluster*

members of the HRS near the previously excised clusters. In particular, the following two regions contain several overlapping HRS clusters (and therefore overlapping excised regions): A3125–A3128–A3158 around Void 2, and A3104–A3109–A3111–A3112 around Voids 1 and 3. In both regions, the extra contributing surveys provide redshifts for significantly fainter objects ($b_J < 20.5$) than the original 6dF targets. Table 2.4 summarizes the pertinent information regarding each survey, including the HRS area of focus (col. 2), the publication reference (col. 3), the number of redshifts employed (col. 4), and the stated limiting magnitude (col. 5). Before utilizing the redshifts from these surveys, we checked for velocity offsets between shared targets with the 6dF survey. As discussed in §2.5, we only found a significant effect in the case of the Mathams data. Offsets between the overlapping galaxies of the 6dF dataset and other surveys were found negligible (i.e., within the cross-correlation error, $\leq 65 \text{ km s}^{-1}$). We acknowledge that these errors, though relatively small, produce potentially significant distortions in the perceived distances of the galaxies ($\sim 1.5 \text{ Mpc}$). Though incomplete at fainter magnitudes, these observations provide an opportunity to examine how diverse (in brightness) populations of galaxies respond to the large-scale structures defined by the 6dF intercluster galaxies (e.g., voids in §6.6).

2.4 ANU/2.3m Cluster Observations

2.4.1 2004 Cluster Sample

Lists of galaxy clusters in the region of the HRS have been taken from two major studies. The first is the Abell catalog extension (hereafter ACO in Abell et al. 1989), while the second is the Automated Plate Measuring Machine cluster catalog (hereafter APMCC in Dalton et al. 1994, 1997). Since galaxy clusters represent the largest (at least partly) virialized structures, they serve as massive signposts for identifying and studying superclusters of galaxies. Based on the ACO, Zucca et al. (1993) identified 18 HRS clusters using a combination of partial redshift information and percolation algorithms. While working with the same list of ACO clusters, Einasto et al. (1994)

Table 2.4. Supplemental Spectroscopic Observations

Region (1)	Reference (2)	N_{GX} (3)	Flux limit, b_{rmJ} (4)	Completeness, f (5)
intercluster	Loveday et al. (1996)	150	16.75	~ 0.10
inter/ cluster	Shectman et al. (LCRS, 1996)	2990	“18.5”	~ 0.60
inter/ cluster	Mathams, unpublished (1989)	900	19.5	~ 0.60
inter/ cluster	Klamer, unpublished (2002)	300	19.5	~ 0.30
inter/ cluster	Lucey et al. (L83, 1983)	40	“17.5”	~ 0.20
cluster	Katgert et al. (ENACS, 1998)	400	“19.0”	??
cluster	Rose et al. (RGC02, 2002)	350	18.5	~ 0.65
cluster	Fleenor et al. (Paper II 2006)	75	18.25	< 0.25
cluster	Alonso et al. (1999)	47	18.5	??
cluster	Caldwell & Rose (1997)	35	18.5	??
cluster	HRS 6dF survey	20	17.5	0.51

Note. — (1) Type of observations; (2) Literature reference; (3) Number of galaxy redshifts; (4) b_{rmJ} magnitude limit, parentheses refer to approximate flux limit; (5) fractional completeness to flux limit.

identified 26 members of the HRS. In Paper I, we used the 17 ACO clusters common to both studies to define the mean redshift of the HRS ($\bar{cz} = 19,900 \text{ km s}^{-1}$), and we adopted the FWHM of the cluster redshift distribution as defining the HRS kinematic core to lie between 17,000 and 22,500 km s^{-1} (see Fig. 4, Paper I). However, the mean redshifts are uncertain for 10 of the 17 ACO clusters because they are based on fewer than four galaxy redshifts each (“ $N_{\text{gx}} < 4$ ” in Struble & Rood 1999, hereafter SR99). Here we report new spectroscopic observations, together with previously unpublished redshifts, for 9 of these 10 clusters with the aim of determining a more accurate mean redshift and dispersion for each cluster. Published data for the tenth cluster, A3109, have been reassessed, and additional spectra have been obtained for a further three clusters with sparse data in the literature.

Figure 2.11 shows the spatial locations of the thirteen clusters in this study as dotted circles. A further 15 clusters with secure redshifts, based on 10 or more galaxies, are also displayed; those that fall within the kinematic core of the HRS are shown as solid-

line open circles. Clusters that fall outside the statistically-defined kinematic core may still, in fact, be members of the larger supercluster complex. Of the thirteen clusters in the current study, eleven are ACO, Richness 0 clusters, and the remaining two are from the APMCC. Since the values of cluster richness for the APMCC are not assigned in the same way as the ACO, comparative determinations were taken from Einasto et al. (2001) for the two APMCC clusters, and they were found to be similar to ACO Richness 0.

2.4.2 Observations and Reductions

Spectroscopic observations were conducted on 2004 November 14–17 with the 2.3m telescope of the Australian National University (ANU) at Siding Spring Observatory. The Dual Beam Spectrograph (DBS) was utilized in conjunction with a coated SiTE 1752×532 CCD. The 300B grating was used with all light directed into the blue arm via the insertion of a reflective mirror instead of the customary dichroic. With a central wavelength of 5200 Å, the above arrangement yielded a dispersion of 2.18 Å pix⁻¹ from [OII]λ3727 through Mg Ibλ5175 for the mean redshift of the HRS. Wavelength calibration was based on CuAr lamp exposures carried out after each object exposure. For each observation, the spectrograph was rotated to place two or more galaxies on the slit. Galaxies were selected based on their spatial proximity and their apparent brightness. Specifically, all galaxies within a spatial radius of $\leq 15'$ ($= 0.5R_{\text{Abell}} \sim 1$ Mpc) to the published cluster center were examined and arranged in order of decreasing brightness. We targeted only those galaxies with a blue, b_J , magnitude brighter than 18.25, as given in the SuperCOSMOS catalog (Hambly et al. 2001b). With a typical exposure time of 30 minutes, all spectra had signal-to-noise ratios of 15:1 or greater and yielded accurate redshift determinations.

Object exposures were reduced in the standard manner via the IRAF software package. Specifically, the following steps were completed: debiasing, flat fielding, sky subtraction, cosmic-ray removal, and wavelength calibration. Cosmic rays were removed using the variance weighting option in the `apall` routine for aperture extraction. For

those objects with multiple exposures, the reduced spectra were co-added. Because the spectrograph position angle was adjusted to allow two galaxies to be centered on the slit, observations did not occur at the parallactic angle, and the uncertainty from atmospheric dispersion could in principle be as much as 40 km s^{-1} . Radial velocities were determined for the galaxy spectra by the standard technique of cross-correlating the galaxy spectra against those of template stars. Stellar spectra of the G8III star HD 80499 and of the G4V star HD 106116 from the Indo-US Coudé Feed Spectral Library (Valdes et al. 2004) and two de-redshifted DBS stellar spectra (the G0 star HD 33771 and a serendipitous Galactic G dwarf at $\alpha_{\text{J2000}} = 03:29:38.44$ and $\delta_{\text{J2000}} = -52:36:08.5$) were utilized as templates for the redshift determination using the `xvsao` routine. Only cross-correlation fits with $R > 4$ (Tonry & Davis 1979) were considered reliable and then averaged. For the ten galaxies with emission-dominated features, procedures were followed in a manner similar to that detailed previously in Paper I. As a final step, all redshifts were corrected to the heliocentric reference frame. In all, 76 usable galaxy spectra were obtained over the four nights of observations, and they are listed in Table 2.5 with their determined redshift and associated uncertainty.

2.4.3 2005 Cluster Sample

Due to the success of the first round of DBS observations in clarifying the large-scale picture in the HRS, we sought to obtain a complete sample of rich ($R \geq 1$) ACO clusters with the aim of probing the finer scales of the filamentary network. A second round of 2.3m spectroscopy was allocated to establish adequate mean cluster redshifts and velocity dispersions for 6 HRS clusters in which no published observations previously existed, with follow-up observations in 2 other clusters. These observations were conducted on 2004 November 26–30 with the 2.3m/DBS in the same manner as detailed in §2.4.2. Though severely hampered by weather, a total of 36 spectra were obtained in these 8 clusters. Because less than 10 individual galaxies were observed in each cluster, only a somewhat reliable mean cluster redshift was established. Most of these clusters are located in the background with respect to the HRS. Each mean velocity is listed

with the respective cluster in Table 5.1.

2.5 Previously Observed Cluster Galaxies

In addition to the new data from the ANU/DBS, 42 galaxy redshifts for various clusters in our sample were obtained from other sources (see Tab. 2.4). Eighteen cluster galaxies were observed during our survey with the multi-fiber, 6° field instrument (6dF, Parker et al. 1998) on the UKST in 2004 November. Although that survey focused on the inter-cluster galaxies in the HRS, otherwise unused fibers were placed on galaxies within the clusters themselves. UKST/6dF spectra covered the wavelength range from 3900–7600 Å and yielded average instrumental resolutions of 4.9 Å and 6.6 Å, for the 580V and 425R gratings respectively. The automatic 6dF data reduction package completed the following: debiasing, fiber extraction, cosmic-ray removal, flat-fielding, sky subtraction, wavelength calibration, splicing, and co-addition (Jones et al. 2004). The optical redshift for each galaxy was determined via the semi-automated `runz` software (see §2.2), which employed both cross-correlation for absorption features and emission-line matching for typical features (e.g., [OII]λ3727, [OIII]λ4959/5007, and Balmer lines).

Furthermore, two previously unpublished datasets obtained with the Anglo-Australian Telescope (AAT) were relied on for establishing properties of certain clusters. Specifically, T. Mathams used the fibre-optic-coupled aperture plate system (FOCAP, see Gray 1983) during 1986–1988 to observe galaxies within A3123 and APMCC 421 with a dispersion of $\sim 2 \text{ Å pix}^{-1}$ from 3600–5600 Å. I. Klammer used the 2° field instrument (2dF, Lewis et al. 2002) in 2002 January to observe galaxies within A3104 with $\sim 4 \text{ Å pix}^{-1}$ dispersion (or 8 Å resolution FWHM) from 3600–8000 Å. The overlap between the Mathams dataset and the observations from Rose et al. (2002, hereafter RGC02) of 270 galaxies within the velocity range 15,000–25,000 km s^{−1} revealed a mean velocity offset, $\overline{\Delta cz} = cz_{\text{RGC02}} - cz_{\text{Mathams}}$, of -82 km s^{-1} . Consequently, this average offset value of 82 km s^{-1} was subtracted from all Mathams observations in the following analysis. Average velocity offsets in the other two surveys in the A3128/25 region, ENACS and

Caldwell & Rose (1997, CR97), were examined previously in RGC02 and found to be within the errors ($< 40 \text{ km s}^{-1}$).

2.6 Cluster Sample Summary

The results of our observations, together with the other previously unpublished data, are summarized in Table 2.5. The first column contains the galaxy ID, while columns (2) and (3) list the J2000 coordinates, and column (4) gives the SuperCOSMOS b_J magnitude. In column (5) we give the velocity (cz) and its associated uncertainty obtained from our ANU/DBS spectra. The iterative method of calculating the mean cluster redshift and velocity dispersion (described in §4) shows that some galaxies are either foreground or background to the cluster. We label those galaxies with an asterisk (*) in column (5). Galaxy redshifts from the literature (via the NASA Extragalactic Database, NED) are also utilized in our calculations. All previously existing redshifts, either published or unpublished, are listed in column (6) with their respective source in column (7).

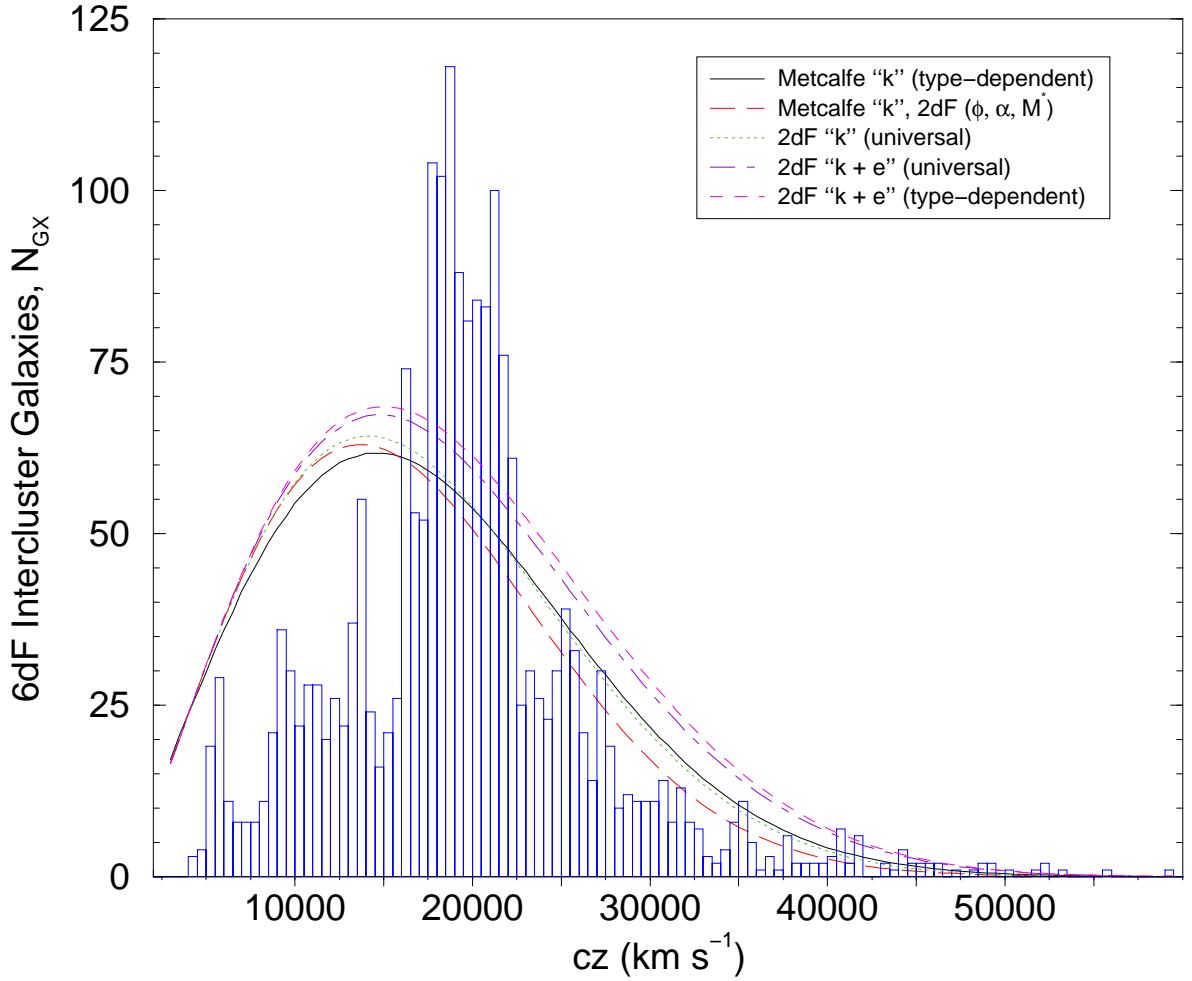


Figure 2.10 Number of 6dF intercluster galaxies observed as a function of cz is shown as an open histogram up to $60,000 \text{ km s}^{-1}$. The primary HRS region from $17,000\text{--}23,000 \text{ km s}^{-1}$ is quite noticeable. Various curves represent the predicted counts for a uniform galaxy distribution using a variety of methods and assumptions, where the survey area and limiting-magnitude are considered. All “Metcalfe” curves use faint galaxy number counts to construct the LF (Metcalfe et al. 1991), where “2dF” uses maximum likelihood techniques (see Norberg et al. 2002; Croton et al. 2005). Though all curves are “k” corrected, note that there is an increase of $\sim 10\%$ in galaxy numbers for those curves that include evolutionary, “e” corrections. The underdensity in galaxies for $cz < 10,000 \text{ km s}^{-1}$ is due to our deletion of extremely bright galaxies, $b_J < 10.0$, from the target list.

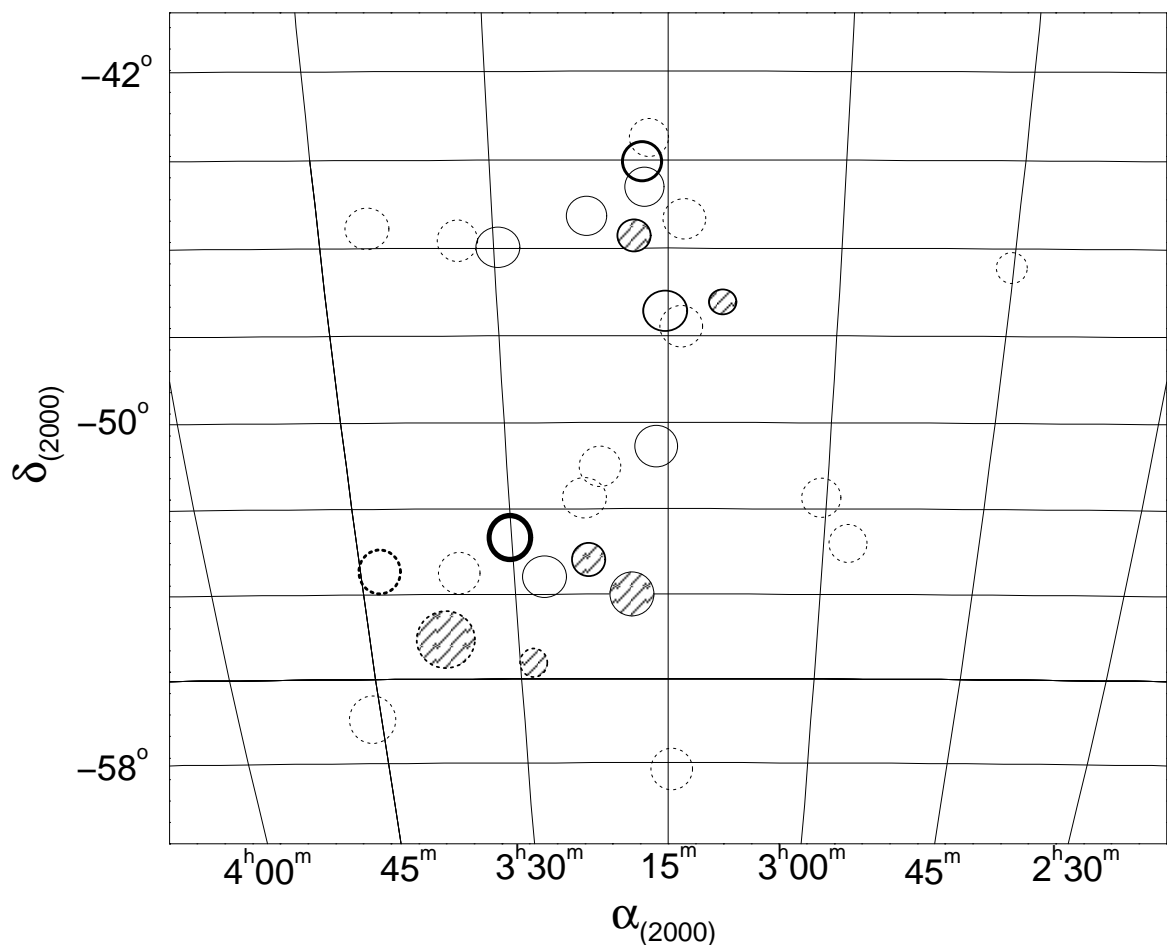


Figure 2.11 Hammer-Aitoff, equal-area projection map of the HRS region, with galaxy clusters represented as circles. The radius of each cluster is scaled with the mean redshift to 0.5 Abell radii (~ 1 Mpc). The thickness of each outline represents the Abell Richness, where thicker lines are clusters of greater Richness Class. Dotted lines are for clusters with previously unreliable redshifts that have been improved in the 2004 DBS observations. Solid circles represent clusters whose mean redshifts from previous studies are reliable; these clusters are hatched if their redshifts fall outside the kinematic core of the HRS.

Table 2.5. Redshift Data for Galaxy Clusters in Horologium-Reticulum

IAU Name	α_{2000}	δ_{2000}	b_J	$cz \pm u_{cz}$ (km s ⁻¹)	cz_{pub} (km s ⁻¹)	Source
(1)	(2)	(3)	(4)	(5)	(6)	(7)
Abell 3047						
2MASX J02445221-4630015	02 44 52.22	-46 30 01.3	17.15	26252 ± 63	26355	1
2MASX J02450315-4628464	02 45 03.10	-46 28 46.2	18.24	28108 ± 72		
2MASX J02450401-4626435	02 45 03.98	-46 26 43.6	17.56	26921 ± 72		
2MASX J02450895-4626245	02 45 08.96	-46 26 24.9	18.24	27396 ± 53		
2MASX J02451207-4628013	02 45 12.14	-46 28 00.9	17.97	28181 ± 82		
.....

Note. — Numbers in parentheses apply to column numbers. (1) IAU Name; (2) Right Ascension (J2000); (3) Declination (J2000); (4) SuperCOSMOS b_J apparent magnitude; (5) radial velocity, cz , with associated uncertainty; (6) Previously published redshift; (7) Source of published redshift: 1— 6dF observations, unpublished (2004),... Table 2.5 is published in its entirety in the electronic edition of the *Astronomical Journal*. A portion is shown here for guidance regarding its form and content.

2.7 AAT & 2.3m Compact Group Spectroscopy

Two different observing runs were utilized to obtain redshift information on specific individual targets using the longslit spectroscopic capabilities of telescopes located at the Anglo Australian Observatory (AAO). Specifically, AAT service mode observing was used to observe the brightest members of the apparent compact group in A3128 (see discussion in §7.3.4) on 2003 December 12. Due to inclement weather at the AAT, fainter members in the apparent group were re-observed with the Australia National University (ANU) 2.3m on 2004 November 14–18. Other possible faint counterparts and/or crowded targets were also observed during this run. Both sets of observations utilized the 300B grating to give adequate resolution for obtaining confident redshifts (0.8 \AA pix^{-1} on the AAT and 2.2 \AA pix^{-1} on the ANU). With a central wavelength of 5000 \AA , coverage from [OII] $\lambda 3727$ through $\text{Mg}^{3+} \lambda 5175$ was obtained at the mean HRS redshift. CuAr arc exposures were taken at each of the various position angles as often multiple galaxies were placed on the slit.

All reductions were carried out along standard procedures in the IRAF package, which includes debiasing, cosmic-ray removal, flat fielding, sky subtraction, and wavelength calibration. If multiple exposures were obtained, the spectra were then co-added for increased signal-to-noise. Resulting spectra were subjected to the cross-correlation routine, `xcsao` (also a part of IRAF), against two absorption templates. In this way, reliable heliocentric redshifts were obtained. Details are listed in Table 2.6 for each galaxy in the apparent compact group as they are labeled in Figure 2.12.

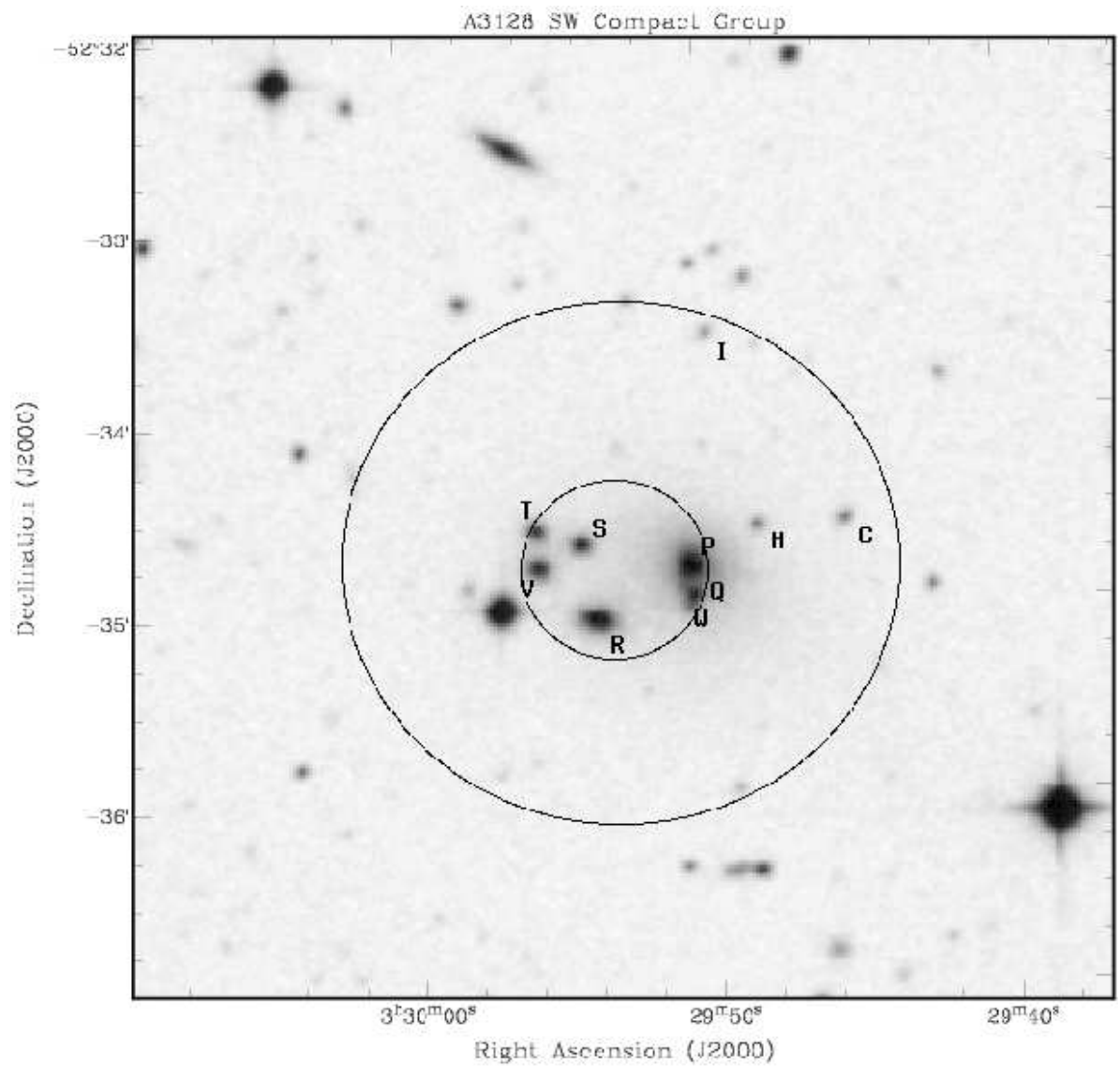


Figure 2.12 DSS image of the SWCG with letters referring to Table 2.6 and other galaxies referenced in text. The inner circle refers to the smallest area that contains the geometrical centers of all HCG members, while the outer circle is three times the inner diameter.

Table 2.6. A3128 Hickson Compact Group

ID	#	α_{2000}	δ_{2000}	$cz + cz_{err}$ (km s $^{-1}$)	b_J	b_J	type
P J03295060-523447	1	03 29 50.61	-52 34 47.0	19228 24	15.50	(15.93)	S0p
Q J03295046-523455	2	03 29 50.47	-52 34 55.9	19180 26		(17.60?)	
R J03295379-523503	3	03 29 53.56	-52 35 03.0	18341 24	16.57	(17.33)	
S J03295433-523439	4	03 29 54.32	-52 34 39.4	18954 30	17.68	(18.34)	
V J03295576-523446	5	03 29 55.71	-52 34 46.1	18533 29	17.40	(17.40)	E
T J03295587-523435	6	03 29 55.84	-52 34 35.1	19823 24	17.83	(17.83)	E
W J03295058-523459	7	03 29 50.58	-52 34 59.9	19149 27		(18.75?)	

Note. — Numbers in parentheses refer to the column numbers. (1) Letter Identification + IAU name, see Fig. 2.12; (2) Number; (3) Right ascension in hours, minutes, and seconds (J2000); (4) Declination in degrees, arcminutes, and arcseconds (J2000); (5) Radial velocity with error estimate; (6) Optical magnitude; (7) Morphological type (if known).

Chapter 3

Large-Scale Velocity Structures in the Horologium-Reticulum Supercluster

3.1 Kinematic Extent of the HRS

We begin by briefly considering the kinematic extent of the HRS. While a supercluster clearly will not be in a state of dynamical equilibrium with well-defined boundaries, we establish provisional kinematic limits from previous studies of the Horologium-Reticulum (HR) cluster population. Specifically, two separate studies applied a friends-of-friends analysis to the ACO clusters within the HR region and identified between 18 and 24 clusters as related to the HRS (Zucca et al. 1993; Einasto et al. 2001). Within our region of observation, seventeen ACO clusters were combined from these two catalogs (column 4, Table 3.1). The mean redshift of these clusters is $19,900 \text{ km s}^{-1}$, with a dispersion σ of 2300 km s^{-1} . We define the “kinematic core” of the HRS to be roughly bounded by the FWHM of the observed redshift distribution of ACO clusters, namely 5400 km s^{-1} . When rounded to the nearest 500 km s^{-1} , we determine the core of the HRS to be between cz of $17,000$ and $22,500 \text{ km s}^{-1}$.

The above kinematic extent of $\sim 5500 \text{ km s}^{-1}$ is basically consistent with the fact that the Zucca et al. (1993) and Einasto et al. (2001) analyses find the HRS to contain ~ 20

major galaxy clusters. Assuming a mean cluster mass of $10^{15} M_{\odot}$ and the cosmological parameters stated in §1, we calculate the spherical Hubble Flow volume required to contain a mass of 20 such clusters. The calculated diameter of that volume (95 Mpc) does indeed correspond to a velocity spread of $\sim 6500 \text{ km s}^{-1}$, i.e., similar to our defined kinematic limits.

The adopted boundaries for the HRS are examined with respect to both the distribution of cluster redshifts and the distribution of 6dF inter-cluster galaxy redshifts in Figure 3.1. For inset (a), all galaxy clusters with known redshifts in the region (Table 3.1) are plotted, including the seventeen ACO clusters considered above. Although the redshift histogram for the inter-cluster galaxies is clearly clumped into several redshift concentrations, the main concentration of galaxies ($\sim 48\%$ of the sample) lies within the selected HRS kinematic boundaries. As shown in Figure 3.1(b), the HRS kinematic core is bordered by a depletion in galaxy numbers both at lower ($14,000 - 16,000 \text{ km s}^{-1}$) and higher ($22,500 - 24,000 \text{ km s}^{-1}$) redshift ranges. While the higher redshift limit to the HRS near $cz = 22,500 \text{ km s}^{-1}$ is quite well defined, the lower redshift limit is less clearly defined. Specifically, there is a clump of galaxies present between $16,000$ and $17,000 \text{ km s}^{-1}$, which is not included in our definition of the HRS “core”. The nature of the inter-cluster galaxies in this redshift regime is further clarified in Figure 3.2, where we plot coordinate versus redshift in both α and δ . Note that the galaxies between $16,000$ and $17,000 \text{ km s}^{-1}$ in redshift are highly concentrated in δ at $\sim -54^{\circ}$. These same galaxies are more substantially spread in α , although confined to the Western side of the HRS. We return to this component of the HRS in subsequent sections.

3.2 Inter-cluster Galaxy Overdensity

Our extensive new redshift database allows us to calculate the mean galaxy overdensity in the *inter-cluster* regions of the HRS. The expected galaxy counts for a uniform distribution are based on estimates of the local galaxy luminosity function (LF). To facilitate the comparison between the HRS and the SSC, we follow as closely as possible the methods described by Drinkwater et al. (2004). Specifically, the expected number

of galaxy counts as a function of redshift and limiting magnitude are calculated from the same Metcalfe et al. (1991) galaxy LF as used by Drinkwater et al. (2004) in their calculation of the overdensity in the SSC. The resulting function is plotted as a solid curve in Figure 3.1, with an assumed limiting magnitude of $b_J = 17.5$. To calculate the expected number of galaxies within the HRS redshift and angular limits, we adopted the previously established redshift limits of $17000 - 22500 \text{ km s}^{-1}$, and assumed the $9^\circ \times 14^\circ = 126 \text{ deg}^2$ areal coverage of our survey. However, the latter figure required reduction to 107 deg^2 , due to the areas excised around clusters. Finally, we observed only 23% of the total number of galaxies brighter than b_J of 17.5 within the 107 deg^2 . Of the observed galaxies, $\sim 48\%$ fall within the redshift limits of the HRS. Taking these factors into account, we arrive at a mean density of 2.4:1 for the inter-cluster regions of the HRS (assuming that light traces mass). In following a common definition of the galaxy overdensity, we find that $\bar{\delta} = 1.4$, where $\bar{\delta} = (\rho_{HRS} - \bar{\rho})/\bar{\rho}$. Given the rather uncertain redshift and angular boundaries of the HRS, as well as uncertainty in the shape and normalization of the local LF, we estimate an uncertainty of $\sim 25\%$ in the overdensity.

3.3 Large-Scale Redshift Trend

Having examined the overall redshift histograms for both clusters and inter-cluster galaxies, we now utilize two-dimensional redshift slices of our 6dF data as a further means of assessing the dynamical state of the HRS. In Figure 3.3, we present a sequence of redshift cuts through the kinematic extent of the HRS, each cut containing a redshift bin size of 1500 km s^{-1} . An examination of Figure 3.3 gives the impression of a systematic trend between spatial position in the HRS and redshift. Specifically, we note that galaxies in panel (a) ($17,000 - 18,500 \text{ km s}^{-1}$) appear preferentially located in the South and East, while the galaxies in panel (d) ($21,500 - 23,000 \text{ km s}^{-1}$) preferentially populate the West and North. In other words, there appears to be a trend of systematically increasing redshift along a principal axis in the HRS that extends from the Southeast to the Northwest end of the supercluster.

To quantify the significance of a large-scale redshift trend with spatial position in the HRS, we conducted a correlation analysis as a function of position angle (PA) on the sky. To begin, we selected the center of the HRS to be at $(\alpha = 3^h 16^m, \delta = -52^\circ)$ and assumed the principal axis of the HRS to be aligned along the West-East direction. Each galaxy was projected onto this principal axis, and we defined the S -coordinate to be the projected angular position of the galaxy along the assumed principal axis. Furthermore, the S -coordinate was defined to run negative to positive from West to East. A linear regression analysis was carried out between the redshift and the S -coordinate, which yields both the correlation coefficient, R , and the likelihood that the null hypothesis (*no* correlation between redshift and projected S position) is correct (Bevington 1969). We repeated the correlation analysis at 5° increments in position angle (PA) of the assumed principal axis over the full 180° range. When the assumed principal axis is running from SE to NW, positive S values are in the NW. In the same way, when the assumed principal axis is running from SW to NE, positive S values are in the NE. The correlation analysis was completed both for the 263 6dF inter-cluster galaxies with redshifts between 17,000 and 22,500 km s^{-1} and for the 21 clusters with mean redshifts over the same interval.

For both clusters and inter-cluster galaxies, we find that the null hypothesis is rejected at probability (P) levels of $P < 1\%$. At certain PAs, the plots of R versus PA show a broad peak over an interval of $20 - 40^\circ$. 6dF galaxies show the highest correlation coefficient ($R = 0.3$) and lowest probability for the null hypothesis ($P < 10^{-6}$) at a PA $\approx -80^\circ$ (as measured East from North). The clusters also show a significant correlation, with a peak at a PA of -50° . In Figure 3.4, we show the projected S position plotted versus redshift for all inter-cluster galaxies and clusters with redshift between 17,000 and 22,500 km s^{-1} at a PA of -80° . The expected cluster peculiar velocities are suppressed for clarity of the inter-cluster galaxy distribution. The linear regression fit for the inter-cluster galaxies is plotted as a solid line. Note that the best fit line actually passes through a zone of low galaxy density; this is examined further in §3.4.

We are now in a position to revisit the substantial population of galaxies from 16,000 to 17,000 km s^{-1} . To determine whether or not these galaxies are associated with the

large-scale redshift trend, we repeat the correlation analysis as a function of PA now expanding the redshift range to $16,000 - 22,500 \text{ km s}^{-1}$. When the galaxies between $16,000$ and $17,000 \text{ km s}^{-1}$ are included, the correlation coefficient is weakened ($R = 0.2$), and the probability of no correlation increases to $P \sim 10^{-3}$. The deviation of the $16,000 - 17,000 \text{ km s}^{-1}$ galaxies from the redshift trend is evident in their spatial segregation (especially in δ). We display the spatial location of these galaxies on the sky in Figure 3.5, where the galaxies from $16,000 - 18,000 \text{ km s}^{-1}$ are separated into 1000 km s^{-1} slices. Although the galaxies from $16,000 - 17,000 \text{ km s}^{-1}$ only represent $\sim 5\%$ of the total population, the spatial segregation of this clump does not follow the overall trend of the higher redshift galaxies in the HRS and provides a significant lever arm by which the best fit correlation axis is altered. In short, while the spatially-localized galaxies from $16,000 - 17,000 \text{ km s}^{-1}$ may reside within the HRS, they do not appear to follow the large-scale redshift trend established by the clusters and inter-cluster galaxies over the range $17,000 - 22,500 \text{ km s}^{-1}$.

3.4 Bi-Modal Kinematics of the HRS

As noted above, the best linear fit between projected S coordinate and redshift actually runs through a zone of low galaxy density (Figure 3.4). The implication is that the HRS has a bi-modal redshift distribution, i.e., the HRS kinematic extent consists of two major components in redshift. The redshift bi-modality of the HRS is most clearly observed by fitting and removing the systematic spatial-redshift trend at $PA = -80^\circ$, then plotting the histogram of residual redshifts, as shown in Figure 3.6. Fitting each component of the histogram with a Gaussian reveals that the overall number of galaxies is roughly equal in the two components, which are separated by $\sim 2500 \text{ km s}^{-1}$ (35 Mpc). However, the FWHM of the higher-redshift component (i.e., corresponding to the galaxies with original redshift centered at $\sim 21,000 \text{ km s}^{-1}$) is approximately twice as large as for the lower redshift component, 2200 and 1100 km s^{-1} , respectively. Furthermore, the two components show no spatial distinction from each other and are spread throughout the entire observed region of the HRS.

To quantify the likelihood of bi-modality in the redshift distribution, we first assess the likelihood that a single Gaussian provides an adequate fit to the data. At each PA, we determine the residual redshift of all galaxies from the systematic position-redshift trend, and then we employ KMM statistics to assess the likelihood of a two-Gaussian versus a single-Gaussian fit (Ashman et al. 1994). For *all* position angles, a common covariance, two-Gaussian fit is preferred to a single Gaussian with a high degree of confidence ($> 99\%$). The average peak-to-peak separation of the two components over the entire PA range is $3014 \pm 712 \text{ km s}^{-1}$, with the separation along the best-fit line (PA = -80°) being $3003 \pm 174 \text{ km s}^{-1}$. Next, we utilize χ^2 statistics to test the goodness-of-fit for two Gaussian distributions with differing FWHM as a function of PA. The reduced χ^2 values range from 0.95 to 4.91 with the best fit value at PA = -60° . In summary, the statistical tests confirm the bi-modal nature of the HRS redshift distribution, with the clearest distinction between the two redshift components occurring along the principal spatial-redshift axis of the supercluster.

Finally, we have utilized the same KMM statistical methods to assess the redshift distribution of clusters in the HRS with known redshift. For the clusters, the best fit correlation axis was found at PA = -50° . However when considering the broad nature of the correlation-PA relationship for clusters, we used the best fit line from the inter-cluster galaxies at a PA of -80° (cf., Figure 3.4). We fitted the systematic position-redshift trend of the galaxies and found the residual mean redshift for each cluster from that trend. The resulting histogram of cluster residual redshift was plotted in Figure 3.6 (right). We then applied KMM statistics to the cluster histogram. Unlike the test on the galaxies, the cluster histogram showed no clear signature of a bi-modal redshift distribution. Specifically, the cluster redshifts fitted a bi-modal distribution with $\sim 75\%$ confidence as compared to a single Gaussian distribution. However, as can be seen in Figure 3.6 (right), the cluster redshift data were sparse and little could be concluded from their redshift distribution.

3.5 Comparisons with the Shapley Concentration

The HRS is generally referred to as the second largest supercluster within 200 Mpc, second only in mass to the Shapley Supercluster (SSC) (Hudson et al. 1999). Since the SSC is both well-studied and the most comparable supercluster in the local universe, we use it as a benchmark for assessing the properties of the HRS. The comparison between these two largest structures is somewhat hindered by the fact that most of the SSC studies combine inter-cluster and cluster galaxies, while our 6dF data for the HRS samples only the inter-cluster galaxies.

3.5.1 Extent and Overdensity

We begin by comparing the kinematic extent of the HRS (from 17,000 to 22,500 km s^{-1}) with that of the SSC. The velocity boundaries of the entire SSC are generally cited as extending from 8,000 to 18,000 km s^{-1} (Quintana et al. 2000; Drinkwater et al. 2004). To put the SSC on the same quantitative footing as the HRS, we compare the cluster populations of the two superclusters. Specifically, when compared with the 18 ACO clusters found in the HRS by Zucca et al. (1993), the same authors find 24 ACO clusters in the SSC, while Einasto et al. (2001) find 25. Hence the numbers of clusters in the SSC are comparable to, perhaps slightly larger than, those in the HRS. For the 24 ACO clusters combined from these studies, we used published mean redshift data from Quintana et al. (2000) to calculate a comparative kinematic extent for the SSC. We determine the FWHM of the redshift distribution of the SSC clusters to be $\sim 6000 \text{ km s}^{-1}$, very similar to the $\sim 5500 \text{ km s}^{-1}$ found for the HRS. As is discussed below, the redshift distribution of the SSC clusters is distinctly bi-modal, thus the FWHM metric is rather an oversimplification of a complex environment. However, the basic result is that the HRS and SSC are similar in regard to their total number of ACO clusters and overall kinematic extent.

Next, we seek to make a valid comparison between the inter-cluster overdensities of the SSC and the HRS. Three studies have examined in detail the inter-cluster overdensity of the SSC (Drinkwater et al. 1999; Bardelli et al. 2000; Drinkwater et al. 2004).

Of these, only Drinkwater et al. (2004) considers a similar area on the sky, so we draw a comparison with this study. The SSC inter-cluster overdensity is 3.3 ± 0.1 over 151 deg^2 , as compared with an overdensity of 2.4 that we find for the HRS. A radius of 0.5° ($\sim 2 \text{ Mpc}$ at SSC mean redshift) was excised around ACO clusters within the survey area. This radius in the SSC corresponds to 0.35° at the HRS redshift. Consequently, the HRS sample is slightly more restrictive in selecting only inter-cluster galaxies, but this is likely a small difference. Overall, we find a somewhat smaller, but similar, overdensity in the HRS compared to that in the SSC.

In addition, we compare the total mass in the HRS inter-cluster galaxies to that in the SSC. Given the differences between the HRS and SSC studies in overdensity ($2.4/3.3$), angular survey region ($107/151 \text{ deg}^2$), and relative distance ($\sim 20,000/15,000 \text{ km s}^{-1}$), we conclude that the total masses of the inter-cluster regions of the HRS and SSC are virtually identical. Thus our data indeed support the conclusion of previous studies of the distribution of galaxy clusters (Zucca et al. 1993; Hudson et al. 1999; Einasto et al. 2001) that the SSC and HRS constitute the two largest mass concentrations in the local universe.

3.5.2 Morphological Considerations

In §3.2, we found an overall spatial-redshift trend in the HRS, in that a systematic increase in redshift is present with increasing position along a SE–NW axis. Bardelli et al. (2000) have fitted a plane in (α, δ, cz) space to their inter-cluster observations in the SSC. They note a $\sim 3000 \text{ km s}^{-1}$ increase in average galaxy velocity along the best fit plane over the 8° (40 Mpc) region, a result reminiscent of the position-redshift tilt in the HRS. However, when the area on the sky is expanded (cf., Figure 4 of Bardelli et al. 2000) to include the inter-cluster galaxies in Drinkwater et al. (1999), the main peak of the galaxy distribution shifts by 7 Mpc, and the entire distribution is broadened. In short, while there appears to be a kinematic gradient in the SSC, it is not clear whether that feature extends over the entire region of the supercluster.

As is discussed in §3.3, when the spatial-redshift trend along the $\text{PA} = -80^\circ$ axis

in the HRS is fitted and removed, the redshift distribution is bi-modal (Figure 3.6). In fact, the bi-modal signature is observed even in the original redshift histogram in Figure 3.1. Redshift bi-modality is also strikingly evident in the SSC (cf., Figure 6 of Drinkwater et al. 2004; Quintana et al. 2000, Figure 5). There is a lower redshift component to the SSC (at $\sim 8,000 - 12,000 \text{ km s}^{-1}$) that is quite distinct from the higher component at $\sim 14,000 - 18,000 \text{ km s}^{-1}$. While it was originally thought that the SSC redshift components are substantially different in size, an extensive follow-up study by Drinkwater et al. (2004) reveals the *inter-cluster* populations of the two components to be roughly equal (cf., Figure 5 of Drinkwater et al. 2004). On the other hand, the distribution of the *clusters* within the SSC is also bi-modal and more heavily weighted to the higher redshift component at $13,000 - 18,000 \text{ km s}^{-1}$. Specifically, 16 clusters have redshifts above $13,500 \text{ km s}^{-1}$, while only 6 have redshifts below $12,500 \text{ km s}^{-1}$. The higher redshift component coincides with what is designated by Reisenegger et al. (2000) as the collapsing “Central Region,” centered on the cluster A3558. As a result, the higher redshift component dominates when both the cluster and inter-cluster galaxies are considered. More reliable redshift data for the clusters in the HRS is probably required before a definitive statement can be made about their redshift distribution, but the available data (cf., Figure 3.6, Right panel) indicate that such a 3:1 imbalance in cluster numbers between lower and higher redshift components is not present.

Although our observations reveal a distinct arrangement of field galaxies marking the HRS, the extent and/or boundaries of the supercluster are not easily determined. In fact, percolation and friends-of-friends algorithms include other clusters in the HRS besides those listed in Table 3.1 (Kalinkov et al. 1998; Einasto et al. 2002). Recent studies of the SSC cover a similar area on the sky and also leave some ambiguity as to the spatial and kinematic extent of the supercluster (Quintana et al. 2000; Drinkwater et al. 2004). It is quite possible that the boundaries of the HRS extend beyond the region surveyed by us with 6dF.

3.6 Conclusions

We have obtained optical redshift data for 547 inter-cluster galaxies in the region of the Horologium-Reticulum Supercluster (HRS). This extensive coverage of the inter-cluster galaxies provides an opportunity to define large-scale kinematic structures within the HRS. Our initial result is the detection of a main concentration of inter-cluster galaxies from $17,000 - 22,500 \text{ km s}^{-1}$, which we refer to as the HRS kinematic extent. This was followed by the comparison of our observations with a smooth, homogeneous galaxy distribution. An overdensity of 2.4 was calculated, or $\delta\rho/\bar{\rho} \sim 1.4$, which reveals that the HRS complex has entered the non-linear regime. Through visual inspection of redshift slices, reinforced with correlation analysis, the galaxies within the kinematic extent are found to exhibit a significant trend in redshift with position along a SE–NW axis in the sense that redshift increases by $\sim 1500 \text{ km s}^{-1}$ along this axis. Furthermore, the resulting position angle of the trend is closely aligned with that found in the clusters within the HRS. In addition, when the kinematic trend found above is accounted for and removed, we find a distinct bi-modality to the redshift distribution of the inter-cluster galaxies within the HRS. Thus, the HRS can be viewed as consisting of two major components in redshift space, separated by 2500 km s^{-1} (35 Mpc), each with a similar position-redshift tilt at the same position angle.

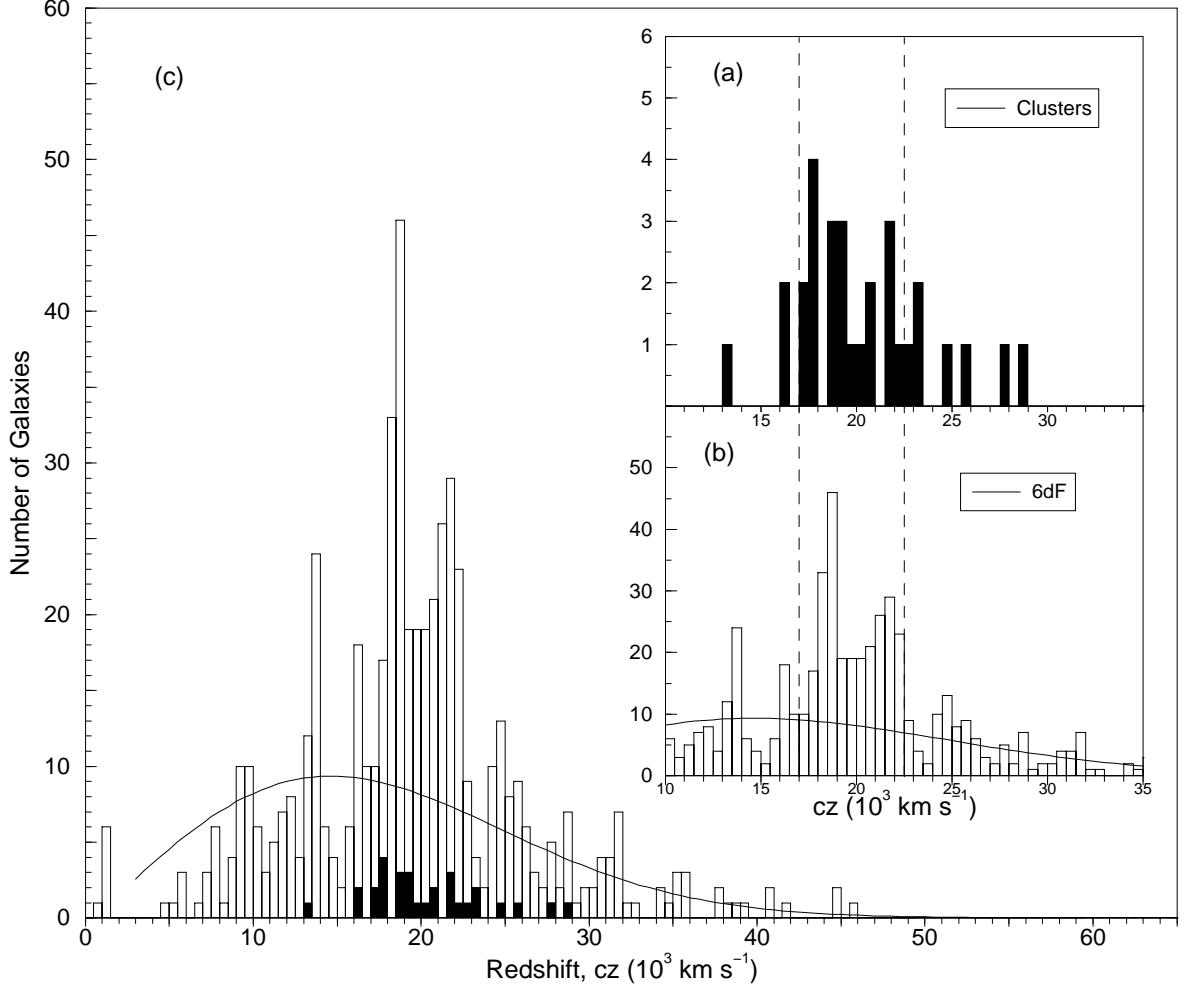


Figure 3.1 Redshift histograms of the 6dF inter-cluster galaxies (open) and the clusters with known redshifts (filled). Panel (a): Cluster redshifts from Table 3.1. Panel (b): Redshifts for inter-cluster galaxies covering the same range as clusters in panel (a). Dashed lines in both inset histograms represent the kinematic “core” discussed in the text. In panel (c), we show the entire redshift histogram for the inter-cluster galaxies with the clusters overlaid. Solid line shown in both inter-cluster galaxy histograms is the expected number of counts for a smooth, homogeneous distribution. The redshift bin size is 500 km s^{-1} .

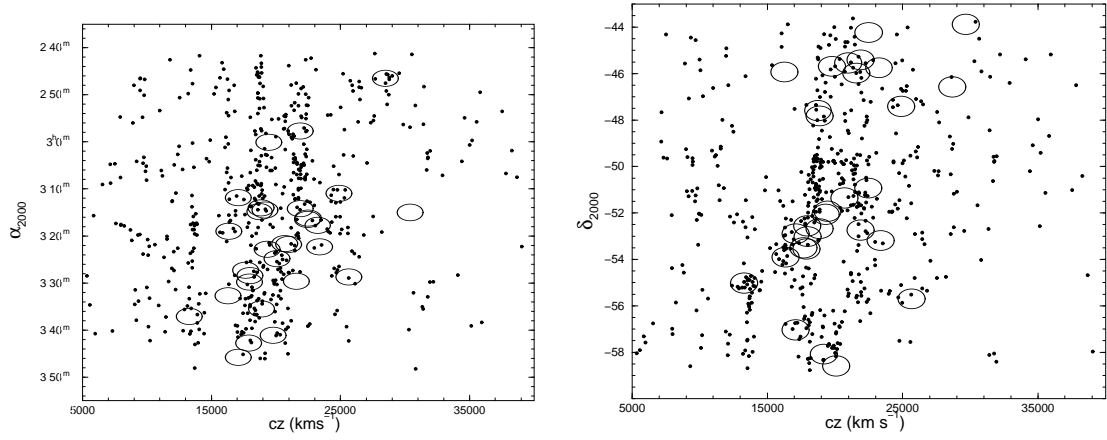


Figure 3.2 Coordinate-redshift plots for the 6dF galaxies. Left panel: $\alpha - cz$. Right panel: $\delta - cz$. Clusters in Figure 2 are shown as ellipses with an estimated velocity dispersion of 1000 km s^{-1} (horizontal axis) and a vertical axis of 4 Mpc ($2 R_A$) at the mean HRS redshift ($20,000 \text{ km s}^{-1}$).

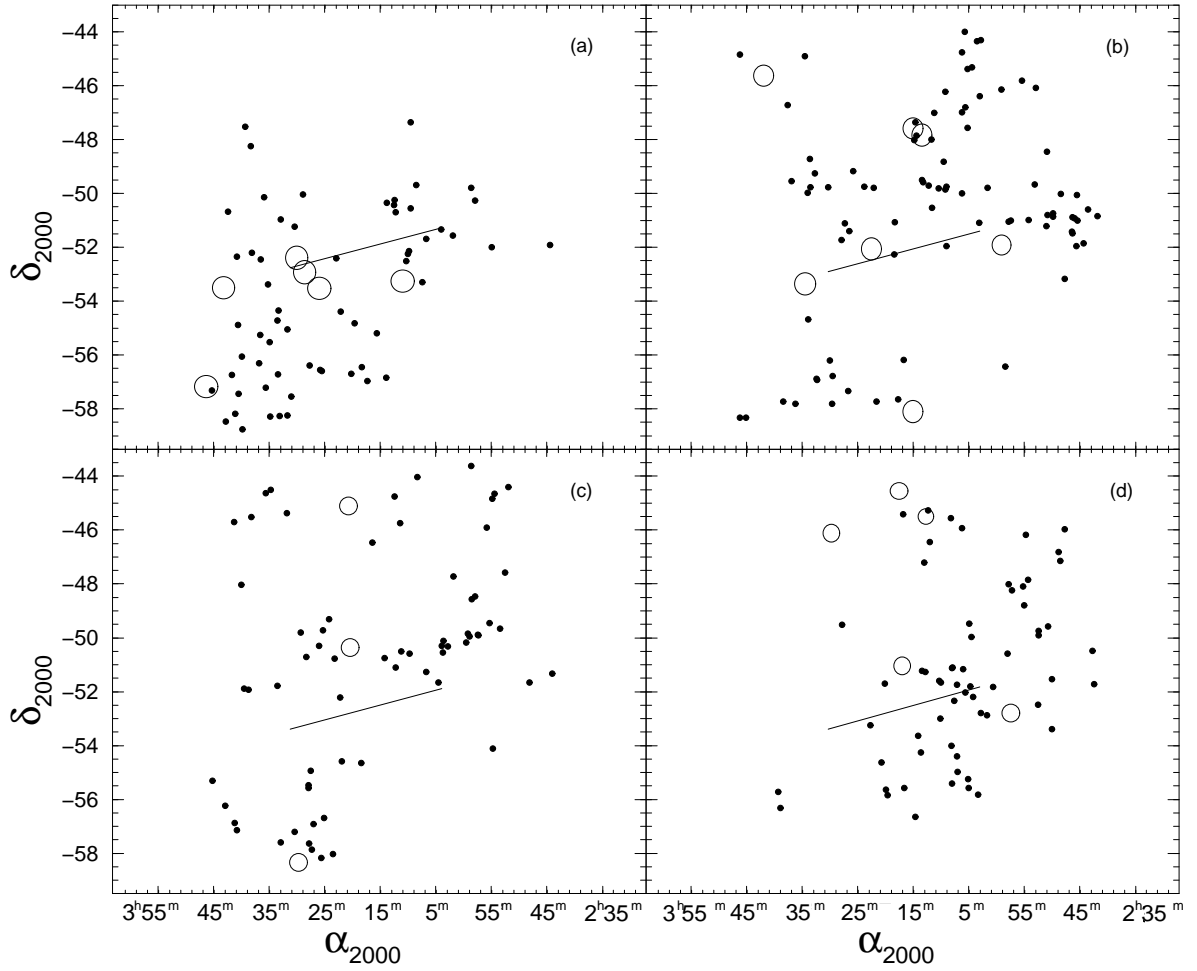


Figure 3.3 Redshift slices are plotted for the 6dF data in the range of the HRS. Each panel covers a 1500 km s⁻¹ redshift slice. Individual galaxies are plotted as small filled circles. Clusters from Figure 2 are also included in their respective redshift ranges. The short solid lines in each panel show the best-fit axis from the spatial-cz correlation analysis (PA = -80°). Only a short line is drawn because of the curvature produced by the non-equal area of the conventional $\alpha - \delta$ coordinate projection. Panel (a) 17,000 – 18,500 km s⁻¹, Panel (b) 18,500 – 20,000 km s⁻¹, Panel (c) 20,000 – 21,500 km s⁻¹, Panel (d) 21,500 – 23,000 km s⁻¹.

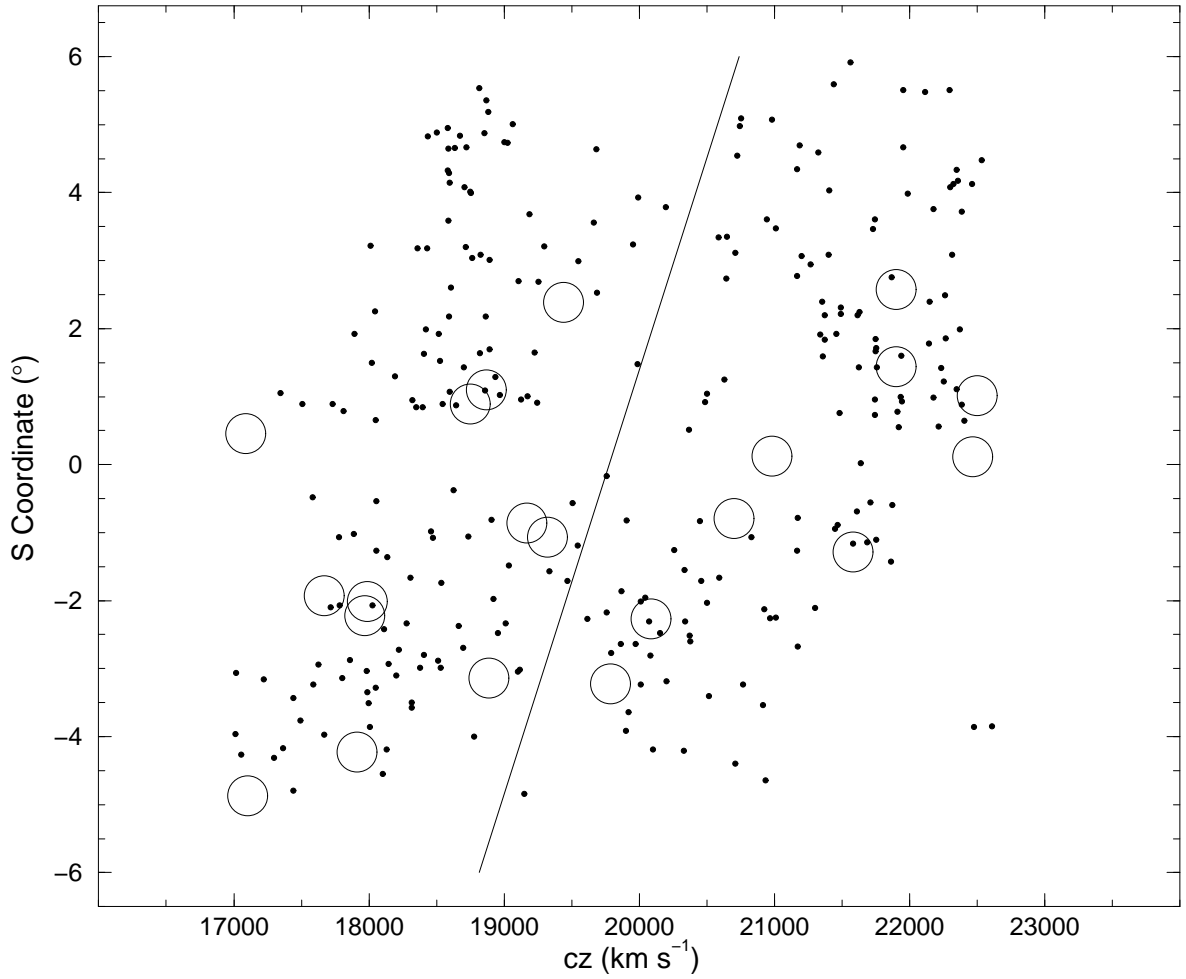


Figure 3.4 Projected angular S -coordinate (see text) is plotted versus redshift for 6dF galaxies between 17,000 and 22,500 km s^{-1} . The position angle (PA) of the principal axis of projection is at -80° (as measured East from North), with positive S values in the NW. Individual galaxies are plotted as small filled circles, while open *circles* represent clusters in the region. The best fit linear regression is plotted as a solid line.

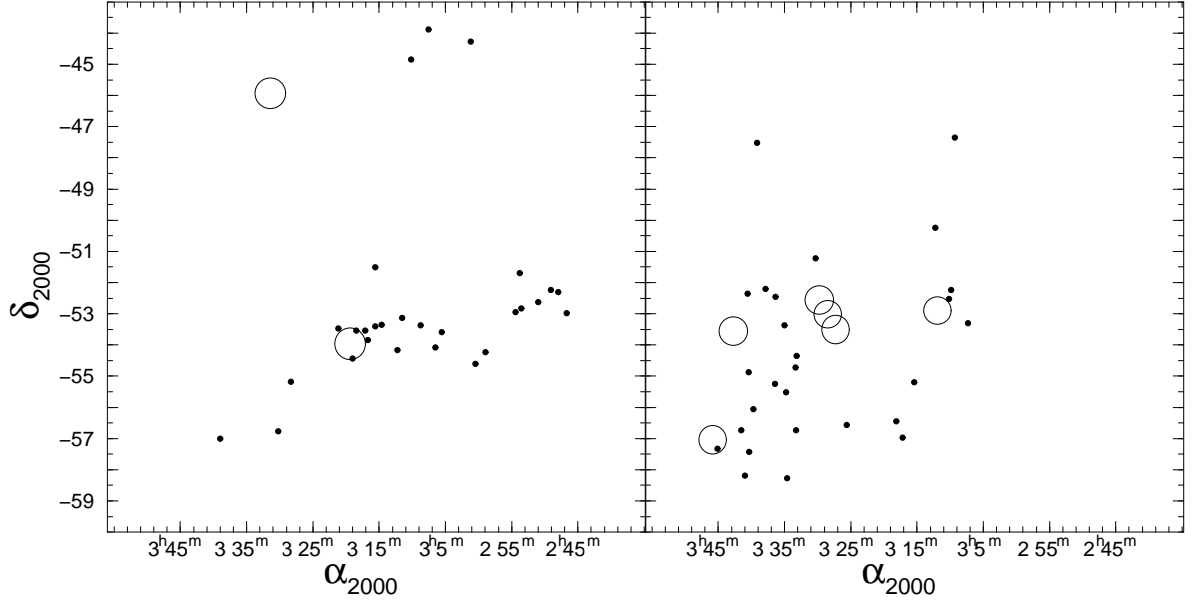


Figure 3.5 Separation of the $16000\text{--}18000\text{ km s}^{-1}$ redshift slice into low- and high-redshift bins. The $16,000\text{--}17,000\text{ km s}^{-1}$ and $17,000\text{--}18,000\text{ km s}^{-1}$ galaxy populations are plotted in the left and right panels, respectively. Symbols as in Figure 2.3.

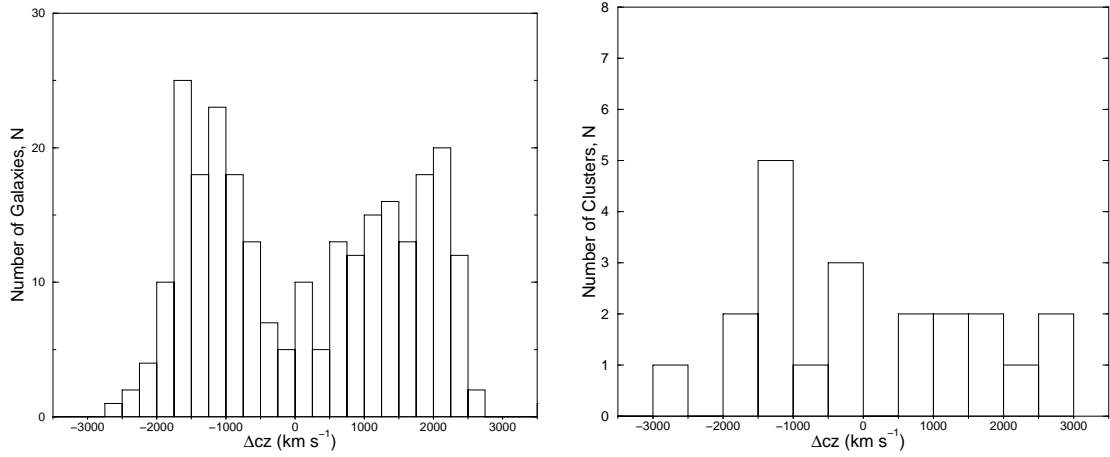


Figure 3.6 Residual redshift histograms for galaxies and clusters within $17,000\text{--}22,500\text{ km s}^{-1}$. The residual redshift is measured relative to the linear regression line that represents the best fit between projected S coordinate and redshift for an assumed principal axis oriented at $\text{PA} = -80^\circ$, i.e., the best fit line in Figure 3.5. Left panel: 6dF galaxies, 250 km s^{-1} bin size ; Right panel: Clusters of known redshift, 500 km s^{-1} bin size.

Table 3.1. Clusters of Known Redshift in the Observed Region

Cluster	α_{2000}	δ_{2000}	List	Redshift	cz (km s $^{-1}$)	Source
A3047	02 45.2	−46 27.0		0.0950	28500	1
A3074	02 57.9	−52 43.0	B	0.0730	21900	1
A3078	03 00.5	−51 50.0	B	0.0648	19440	2
A3093	03 10.9	−47 23.0	B	0.0830	24900	2
M031027	03 11.9	−52 54.0		0.0570	17088	1
A3100	03 13.8	−47 47.0	B	0.0629	18870	2
A3104	03 14.3	−45 24.0	B	0.0730	21900	1
A3106	03 14.5	−58 05.0	B	0.0639	19170	2
A3108	03 15.2	−47 37.0	B	0.0625	18750	3
A3109	03 16.7	−43 51.0	B	0.0920	27580	3
A3110	03 16.5	−50 54.0	B	0.0749	22470	2
A3111	03 17.8	−45 44.0	E	0.0775	23250	4
A3112	03 17.9	−44 14.0	B	0.0750	22500	4
S0339	03 19.0	−53 57.4		0.0546	16369	1
S0345	03 21.8	−45 32.3		0.0700	20985	1
A3120	03 21.9	−51 19.0	B	0.0690	20700	2
M391	03 22.3	−53 11.3		0.0780	23384	1
A3123	03 23.0	−52 01.0	B	0.0644	19320	2
M03233	03 24.8	−58 35.1		0.0670	20086	1
A3125	03 27.4	−53 30.0	B	0.0589	17670	5
M399	03 28.4	−53 01.3		0.0600	17988	1
A3126	03 28.7	−55 42.0		0.0856	25680	4
S0356	03 29.6	−45 58.8		0.0720	21585	1
A3128	03 30.2	−52 33.0	B	0.0599	17970	4
A3133	03 32.7	−45 56.0	B	0.0543	16290	2
M421	03 35.5	−53 40.9		0.0630	18887	1
A3144	03 37.1	−55 01 0		0.0443	13290	2
M433	03 41.1	−45 41.5		0.0660	19786	1
A3158	03 43.0	−53 38.0	B	0.0597	17910	4
A3164	03 45.8	−57 02.0	B	0.0570	17100	2

Note. — Numbers in parentheses apply to column numbers. (1) A-ACO, S-poor clusters from ACO, M- APM Galaxy Survey; (2) Right Ascension in hours and minutes (J2000); (3) Declination in degrees and minutes (J2000); (4) B-HRS membership listed in both Zucca et al. (1993) and Einasto et al. (2001), E-HRS membership listed only in Einasto et al. (2001); (7) ¹Dalton et al. (1994), ²Struble & Rood (1999), ³den Hartog (1995), ⁴Katgert et al. (1998), ⁵Caldwell & Rose (1997).

Chapter 4

Redshifts and Velocity Dispersions of Galaxy Clusters in the Horologium-Reticulum Supercluster

4.1 Determination of Mean Cluster Redshifts and Dispersions

Given that galaxy clusters are thought to form via accretion along intersecting filaments (e.g., West & Blakeslee 2000), and that such processes are particularly pronounced in a dense environment like the HRS, we expect the assumption of a gaussian velocity distribution for the galaxies within the HRS clusters to be problematic. Specifically, the probability of both projected and truly overlapping groups and/or clusters will be enhanced within the supercluster environment. Furthermore, the calculation of the cluster mean redshift and velocity dispersion under an assumption of gaussian statistics is neither robust nor efficient (Pearson 1931; Box 1953). Beers et al. (1990, hereafter BFG90) define a number of reliable estimators for the mean cluster redshift (location) and dispersion (scale) that are more robust to the presence of outliers and less wed to the gaussian assumption. For a small number of galaxy redshifts per cluster ($N_{\text{gx}} < 20$), we utilize the biweight estimator for calculating both the location (C_{BI})

and the scale (S_{BI}) of each cluster according to the following:

$$C_{\text{BI}} = M + \frac{\sum_{|u_i| < 1} (x_i - M)(1 - u_i^2)^2}{\sum_{|u_i| < 1} (1 - u_i^2)^2}, \quad (4.1)$$

where M is the sample median and u_i are the individual weights as defined by:

$$u_i = \frac{(x_i - M)}{c(\text{MAD})}. \quad (4.2)$$

The tuning constant, c , establishes the low and high velocity cutoff for each cluster. The median absolute deviation, MAD, is defined by: $\text{MAD} = \text{median}(|x_i - M|)$. Improvements are made in the final location (and scale) of the cluster by iteratively substituting the most recently calculated C_{BI} for the value of M , and then re-calculating a new C_{BI} until convergence is achieved (BFG90). Although we experimented with different values of c to evaluate the sensitivity of the results on that parameter, the c parameter was held at the suggested value of 6.0, which excludes all data that are more than 4 standard deviations from the central location. While c was varied from 4.0 – 10.0 for the C_{BI} parameter, the maximum change observed for each cluster remained within the estimated uncertainty of C_{BI} in Table 4.1 (column 8).

In a similar way, the biweight estimator for scale, S_{BI} , is given by:

$$S_{\text{BI}} = n^{1/2} \frac{[\sum_{|u_i| < 1} (x_i - M)^2 (1 - u_i^2)^4]^{1/2}}{|\sum_{|u_i| < 1} (1 - u_i^2)(1 - 5u_i^2)|}, \quad (4.3)$$

with the same definitions as above only here, as suggested, c was set to 9.0. Again, the routine was iterated until convergence. Moreover, varying c from 5.0 – 11.0 resulted in a typical total scale change of only $\Delta S_{\text{BI}} \leq 50 \text{ km s}^{-1}$. Although BFG90 adopt the terminology of “location” and “scale” because of the difference in definition between these parameters and the canonical mean and dispersion, we retain the common usage of the cluster mean redshift and velocity dispersion for the rest of the paper.

Data on the cluster mean redshifts (location) and velocity dispersions (scale) are summarized in Table 4.1. The previously published value for the mean redshift is given in column (5), with the source for that redshift in column (6). In column (7) we list the number of galaxies (i.e., those from Table 2.5, columns (5) and (6), excluding foreground and background galaxies) on which our new mean redshift is based. The new

cluster redshift and associated uncertainty are given in column (8). Finally, the newly determined velocity dispersion is given in column (9). For the three cases in which the cluster appears to consist of multiple components, and thus has a less-reliable mean redshift and σ , we have followed the values in column (8) and (9) with a colon (:). These three special cases are discussed further in § 5.

For the remaining ten clusters in the study, the new observations provide a sufficient increase in the number of known redshifts to allow us to determine a reasonably secure velocity dispersion. Furthermore, all of the clusters are Abell richness class, $R = 0$ (or APMCC equivalent), hence we can assess the mean and scatter in velocity dispersion for $R = 0$ clusters in the HRS. Given the modest size of our sample of cluster velocity dispersions, we utilize the same routine for the biweight location estimator, C_{BI} , to determine an effective mean velocity dispersion for our cluster sample. After excluding three values as outliers, the remaining ten clusters give a mean velocity dispersion of $420 \pm 50 \text{ km s}^{-1}$ for Richness 0 clusters. This result is intermediate between published values for galaxy groups (both loose at 165 km s^{-1} in Tucker et al. (2000) and compact at $\sim 250 \text{ km s}^{-1}$ in Hickson (1997)) and rich galaxy clusters (i.e., larger structures) at $\sim 700 \text{ km s}^{-1}$ (Mazure et al. 1996).

4.2 Results for Individual Clusters

The new observational data in three clusters result in velocity dispersions that are quite large in comparison with the $\sim 400 \text{ km s}^{-1}$ mean value for Richness 0 clusters found above. Although Mazure et al. (1996) find a large intrinsic scatter in velocity dispersion for rich clusters, the derived dispersions for these three clusters rival (and exceed) the *upper* limits observed by the same authors for $R \geq 1$ clusters. Therefore, the presence of multiple components and/or spatial projection of multiple clusters/groups is suggested. We examine these three systems in greater detail, since their true composition remains unclear.

4.2.1 Abell 3047/ APMCC 290 (02^h 45^m.25 –46° 26′.0)

The structure of this $R = 0$, $D = 6$ cluster is quite regular in shape and centers around the brightest cluster galaxy (BCG), 2MASX J02451334–4627194 ($b_J = 16.68$), whose previously published redshift is $27,581 \text{ km s}^{-1}$ (Grazian et al. 2002). We observe a redshift of $28,279 \pm 65 \text{ km s}^{-1}$ for the same galaxy, where the difference is most likely due to the higher resolution of the DBS spectra (4.5 \AA compared to $15\text{--}20 \text{ \AA}$). This result is consistent with the mean cluster redshift given in SR99 of 0.0950 ($28,500 \text{ km s}^{-1}$), which is based on fewer than 4 galaxy redshifts (“ $N_{\text{gx}} < 4$ ”). X-ray emission is also detected at a level of $L_x = 3.86 \times 10^{43} \text{ ergs s}^{-1}$ (Cruddace et al. 2002) and is centered on the BCG, thereby strengthening the idea that at least one significant cluster is present.

The iterative biweight estimator routine does not exclude any of the 8 proposed members, and the following results are obtained: $\overline{cz} = 27,382 \text{ km s}^{-1}$ and $\sigma = 1225 \text{ km s}^{-1}$. While the mean redshift of the cluster is somewhat similar to the previous result for the BCG, the derived velocity dispersion is too inflated for a cluster of Richness 0. In seeking an alternative explanation, we notice that three of the four brightest galaxies have a noticeably different recessional velocity ($\leq 2000 \text{ km s}^{-1}$) than the majority. Therefore, we may be viewing the projection of two separate systems, or a physical overlap/merger, giving the appearance of a single $R = 0$ cluster. By subdividing out the galaxies in the following way, a more logical result is obtained:

C1: $N=3$, $\overline{cz} = 26,285 \text{ km s}^{-1}$, $\sigma = 620 \text{ km s}^{-1}$; C2: $N=5$, $\overline{cz} = 28,275 \text{ km s}^{-1}$, $\sigma = 725 \text{ km s}^{-1}$.

We note that the dispersions for the two components are still excessive for a Richness 0 cluster. On the other hand, the presence of X-ray emission at the observed level is consistent with a $R = 1$ or 2 cluster (Ledlow et al. 2003, Figure 9), which lends support to the high velocity dispersions found for the two components. Furthermore, such a large value of L_x is also consistent with a cluster merger along the line of sight. In any case, the redshifts of both components are well outside the kinematic core of the HRS.

4.2.2 Abell 3109 (03^h 16^m5 –43° 51'0)

Although we add no new observations in this cluster, a compilation of 14 previously published galaxy redshifts provides more established kinematic properties. The ESO Nearby Abell Cluster Survey (ENACS, Katgert et al. 1998) focused on rich clusters with $R \geq 1$. The periphery of Abell 3112 (03^h 17^m9 –44° 14'0, $R = 2$, $cz = 22,500$ in Mazure et al. 1996) overlaps with A3109, providing us with 9 redshifts from the ENACS data. The assumed BCG in A3109, 2MASX J03163934–4351169, $b_J = 15.60$, has a published redshift of $18,594 \text{ km s}^{-1}$ (Muriel et al. 1995), which is inconsistent with the published value for the cluster ($27,581 \text{ km s}^{-1}$ in SR99, see their note).

By incorporating all galaxy redshifts within the prescribed radius, the biweight estimator selects 11 cluster members with the following kinematic properties: $\overline{cz} = 18,950 \text{ km s}^{-1}$ and $\sigma = 850 \text{ km s}^{-1}$. Reducing the radial extent to $13'$ and thereby excluding 2 proposed members, we obtain a slightly decreased dispersion: $\overline{cz} = 18,850 \text{ km s}^{-1}$ and $\sigma = 700 \text{ km s}^{-1}$. Even though the dispersion remains greater than the $\sim 400 \text{ km s}^{-1}$ mean for $R = 0$ clusters that we obtained earlier, the archived redshift information establishes a reliable cluster location (i.e., mean redshift) and places A3109 within the HRS.

4.2.3 Abell 3120 (03^h 22^m0 –51° 19'0)

The $R=0$, $D=5$ cluster, A3120, for which we have obtained 5 galaxy redshifts, is the nearest cluster to the published spatial center of the HRS (Zucca et al. 1993). Its published redshift of $20,700 \text{ km s}^{-1}$ (SR99) is also close to the $\sim 19,900 \text{ km s}^{-1}$ mean redshift of the HRS (Paper I). While A3120 does not meet the specific cluster criteria for the APMCC, it does contain the bright galaxy, 2MASX J03215645–5119357 ($b_J = 15.91$), with a previously published redshift of $21,040 \text{ km s}^{-1}$ (Lucey et al. 1983). The biweight estimator routine accepts all observed galaxies, and we derive the following cluster properties: $\overline{cz} = 20,525 \text{ km s}^{-1}$, $\sigma = 1400 \text{ km s}^{-1}$. While the mean derived velocity is in accord with the published value, the large dispersion is clearly inconsistent with an $R=0$ cluster. Furthermore, the five galaxies with redshift information show

no discernible spatial or kinematic segregation, as one might expect with a cluster. Hence there is reason to suspect that A3120 is not a cluster but the projection of many intercluster galaxies near the center of the HRS.

On the other hand, Romer et al. (2000) find X-ray emission at a level of $L_x = 2.22 \times 10^{43} \text{ ergs s}^{-1}$, centered on 2MASX J03215645–5119357, and propose that the X-rays are emitted by a “fossil group” (see their Figure 20). These groups form as a result of multiple mergers within the group or a cluster that lead to a single dominant giant elliptical surrounded by an X-ray halo (Ponman et al. 1994; Jones et al. 2003). However, the X-ray position also coincides with a radio source from the Sydney University Molonglo Sky Survey (SUMSS), SUMSS J032156–511935, with a flux density of 49.0 mJy (Mauch et al. 2003). Considering the wide range of X-ray luminosities in active galactic nuclei (AGN), it is conceivable that some (or all) of the X-ray emission is a result of the AGN, rather than the fossil halo. Because the galaxy’s redshift is taken from the literature and no optical spectrum is available, we conclude that the situation in A3120 is not soluble with the current observational data. In Table 4.1 we give the formal mean redshift (location), uncertainty, and dispersion (scale) as deduced from the biweight estimator analysis. However, since we believe that the most likely value of the actual cluster redshift is that of the (presumed) BCG 2MASX J03215645–5119357 ($cz = 21,040 \text{ km s}^{-1}$), we adopt this value for the mean redshift of A3120 in Table 4.2 (noted by the “1” in column 7). Fortunately, the difference in redshift between $20,700 \text{ km s}^{-1}$ in Table 4.1 and $21,040 \text{ km s}^{-1}$ in Table 4.2 is within the biweight uncertainty.

4.3 Redshift Distribution of the HRS Clusters

4.3.1 Consistency with the intercluster Galaxies

In Paper I, the intercluster galaxies within the range $17,000 - 22,500 \text{ km s}^{-1}$ (i.e., the HRS kinematic core) were found to exhibit a systematic $\sim 1500 \text{ km s}^{-1}$ increase in redshift with position along a southeast-northwest axis. To quantify this spatial-redshift correlation, we projected the intercluster galaxies in the HRS onto an (assumed) prin-

principal axis through the spatial center of the HRS. The projected distance along the principal axis was referred to as the S -coordinate. We then performed a linear correlation analysis between the redshift and the S -coordinate. After varying the position angle (PA) of the principal axis over the full range of PA and repeating the correlation analysis at each PA, we found that the intercluster galaxies show the highest correlation coefficient ($R = 0.3$) and lowest probability for no correlation ($P < 10^{-6}$) at a PA $\approx -80^\circ$ (as measured east from north). Further details are provided in Paper I. In Figure 4.1, we plot the projected S position versus redshift for all intercluster galaxies and clusters with redshift between 17,000 and 22,500 km s^{-1} at a PA of -80° . As is discussed in Paper I, the distribution of redshifts in Figure 4.1 is clearly divided into two main components; one centered at $\sim 18,000 \text{ km s}^{-1}$ and the other at $\sim 21,000 \text{ km s}^{-1}$. Furthermore, there is a correlation between the S -coordinate and redshift for both of the components in the sense that the redshift increases systematically from the southeast (negative S -coordinate) to the northwest (positive S -coordinate). Once the kinematic trend is accounted for and removed, the bi-modal nature of the redshift distribution of the intercluster galaxies becomes even more apparent. We have plotted the histogram of residual redshifts (after removal of the overall kinematic trend) for the intercluster galaxies in the left panel of Figure 4.2. Using the KMM statistical test (Ashman et al. 1994), we find that a two-gaussian fit to the redshift histogram is preferred to a single gaussian at a confidence level of $>99.9\%$.

Although the published cluster redshifts in Paper I followed the spatial-redshift trend of the intercluster galaxies, we found that the histogram of residual redshifts showed no evidence for bi-modality. This fact appeared somewhat puzzling given the expectation that intercluster galaxies and clusters in the same area of the sky should have similar redshift distributions. However, the new cluster redshift data compiled in Table 4.2 shows a different signature. Plotted as large open circles in Figure 4.1, the HRS clusters with reliable redshifts now also appear to divide into two main components. Furthermore, this impression is supported by the histogram of cluster residual redshifts, plotted in the right hand panel of Figure 4.2. Again, the KMM statistical test is applied to the histogram, and we find that a two-gaussian fit is favored over a single gaussian

at the 99.8% confidence level. Moreover, the separation of $\sim 3000 \text{ km s}^{-1}$ between the two peaks of the cluster redshift distribution is consistent with the similar figure found between the two peaks in the intercluster galaxy redshifts. Upon implementing the spatial-redshift correlation analysis described above (i.e., projection of the cluster positional data onto a principal axis), we find a correlation coefficient of $R = 0.5$ and a probability of no correlation of 10^{-2} at a PA of -80° for the principal axis. In summary, with the improved mean redshift data for many of the clusters in the HRS, we conclude that the overall redshift distributions of the clusters and the intercluster galaxies are now consistent with each other. A closer examination of the inter-relationship between clusters and intercluster galaxies in the HRS (e.g., an evaluation as to whether the clusters are indeed located at the intersection of galaxy filaments) awaits a more comprehensive dataset that is in progress.

4.3.2 Re-determination of the Kinematic Core

As mentioned in §2 and above, we determined rough kinematic boundaries in Paper I for the the HRS complex, referred to as the kinematic core, by fitting a gaussian to the redshift distribution of the Abell clusters listed as HRS members by both Zucca et al. (1993) and Einasto et al. (1994). We used the mean redshift and the FWHM of the distribution to define the kinematic core. Given that we now have reliable mean redshifts for 16 of these 17 Abell clusters (we exclude A3120 for reasons discussed in §5.3), it is worth investigating whether the kinematic core changes significantly as a result of the improved redshift data. Using column (6) in Table 4.2 for the 15 Abell clusters (“A” designation) plus the redshift for A3093 ($\overline{cz} = 24,900 \text{ km s}^{-1}$, Katgert et al. 1998), the following values for the mean (location) and the dispersion (scale) are obtained by utilizing the biweight estimator: $\overline{cz} = 20,150 \pm 525 \text{ km s}^{-1}$ and $\sigma = 2125 \text{ km s}^{-1}$. These values imply that the kinematic core of the HRS lies between 17,700 and 22,700 km s^{-1} . Hence the kinematic center of the HRS is slightly higher than the previous value, and the core is slightly narrower.

In light of the above discussion, none of our previous results are significantly altered

if we use these revised values to define which clusters should be included in the redshift bi-modality analysis. Furthermore, the intercluster galaxies from Paper I continue to show a preferred spatial-redshift axis at $PA = -80^\circ$ with similar correlation values over the somewhat-modified range of $17,700 - 22,700 \text{ km s}^{-1}$. Moreover, our definition of the kinematic core is only suggestive of what should be included in a detailed analysis of the complex structure of the HRS. Clearly, the actual boundaries of the HRS can be expected to extend to some clusters and intercluster galaxies outside the immediate kinematic core.

4.4 Comparisons with the Shapley Supercluster

Finally, we compare the improved cluster redshift distribution for the HRS with that of the Shapley supercluster (hereafter SSC, Quintana et al. 1995, 2000). While the 23 Abell clusters in the SSC for which reliable redshift information is published definitely show a bi-modal distribution, there is a 3:1 number imbalance between the two cluster redshift peaks in the SSC. That is, there are many more clusters in the higher redshift peak, which contains the most massive cluster in the complex, Abell 3558 ($\overline{cz} = 14,500 \text{ km s}^{-1}$), than there are in the lower redshift peak at $\sim 11,000 \text{ km s}^{-1}$. In contrast, the HRS clusters are equally split between the two redshift peaks as determined from Figure 4.2. The difference in mean redshift for the two peaks is slightly higher for the SSC ($\sim 3500 \text{ km s}^{-1}$) as opposed to the $\sim 3000 \text{ km s}^{-1}$ difference in the HRS. Furthermore, as discussed in Paper I, the redshift distribution for the intercluster galaxies in both the HRS and SSC are bi-modal, with a roughly equal split between the two redshift peaks for both clusters (Drinkwater et al. 2004). In short, while there are striking similarities between the two largest mass concentrations in the local universe, the 3:1 imbalance in the number of clusters in the redshift peaks of the SSC represents an interesting contrast with the more evenly distributed HRS.

4.5 Conclusions

We have obtained 76 new optical redshifts within 12 galaxy clusters of the Horologium-Reticulum supercluster (HRS). These observations, augmented by 42 previously unpublished redshifts, have led to the determination of more accurate cluster properties. Using the methods for calculating robust mean redshifts (location) and velocity dispersions (scale) described in BFG90, we have calculated mean redshifts and dispersions for 13 clusters, including A3109 for which no new observations are reported. The mean redshifts for several clusters have changed by at least 750 km s^{-1} (in 6/13 observed) from their previously reported values. In addition, three clusters are observed to consist of multiple components (A3047, A3109, and A3120). The new cluster redshift data have been compared to previously compiled redshift data for the intercluster galaxies in the HRS from Fleenor et al. (2005). Primarily, we now find consistency between the large-scale kinematic features of the clusters and the intercluster galaxies. Specifically, there is a principal kinematic axis in the HRS at a PA of -80° east from north, along which a systematic increase in redshift with position is observed for both clusters and intercluster galaxies. After this overall spatial-kinematic trend is removed, the distribution in redshift for both clusters and intercluster galaxies is distinctly bi-modal, with the two redshift peaks separated by $\sim 3000 \text{ km s}^{-1}$.

We thank the Australian National University and Mount Stromlo/Siding Spring Observatories for facilitating and supporting these observations. We also thank Clair Murrowood for her assistance with the observations, Ilana Klammer for supplying her unpublished 2dF data of A3104, and Bruce Peterson for the use of Mathams' thesis data. M. C. F. acknowledges the support of a NASA Space Grant Graduate Fellowship at the University of North Carolina-Chapel Hill. R. W. H. acknowledges grant support from the Australian Research Council. M. J. H. acknowledges support through IRGS Grant J0014369 administered by the University of Tasmania. A portion of this work was supported by NSF grants AST-9900720 and AST-0406443 to the University of North Carolina-Chapel Hill. This research has made use of the NASA/IPAC Extragalactic Database (NED) which is operated by the Jet Propulsion Laboratory,

Table 4.1. Revised Mean Redshifts and Velocity Dispersions for HRS Clusters

Cluster	α_{2000}	δ_{2000}	$N_{\text{gx,prev}}$	cz_{prev} (km s $^{-1}$)	Source	$N_{\text{gx,new}}$	$\overline{\text{cz}}_{\text{obs}} \pm u_{\text{cz}}$ (km s $^{-1}$)	σ (km s $^{-1}$)
(1)	(2)	(3)	(4)	(5)	(6)	(7)	(8)	(9)
A3047	02 45.2	−46 27.0	< 4	28500	1	8	27550: \pm 425	1225:
A3074	02 57.9	−52 43.0	< 4	21900	1	7	21575 \pm 125	325
A3078	03 00.5	−51 50.0	> 0	19440	1	8	22100 \pm 200	575
A3100	03 13.8	−47 47.0	> 0	18870	1	9	19050 \pm 75	250
A3104	03 14.3	−45 24.0	< 4	21885	1	28	21725 \pm 125	700
A3106	03 14.5	−58 05.0	> 0	19170	1	7	19600 \pm 115	300
A3109	03 16.6	−43 51.0	1	27240	2	11	18950: \pm 250	850:
A3120	03 21.9	−51 19.0	> 0	20700	1	5	20525: \pm 675	1400:
A3123	03 23.0	−52 01.0	> 0	19320	1	11	18475 \pm 100	375
A3133	03 32.7	−45 56.0	> 0	16290	1	7	21325 \pm 175	475
APMCC 421	03 35.5	−53 40.9	2	18887	2	11	18550 \pm 100	300
APMCC 433	03 41.1	−45 41.5	2	19786	2	11	20725 \pm 125	425
A3164	03 45.8	−57 02.0	3	17100	1	7	17875 \pm 225	575

Note. — Numbers in parentheses apply to column numbers. (1) Cluster name; (2) Right Ascension in hours and minutes (J2000); (3) Declination in degrees and minutes (J2000); (4) Number of galaxies used to establish previously published mean redshift, where “ $N_{\text{gx}} > 0$ ” and “ $N_{\text{gx}} < 4$ ” are designations given by SR99 to reflect the ambiguity regarding the number of individual velocities from the original source; (5) previously published mean redshift; (6) Source for published mean redshift: 1 – SR99 and 2 – Dalton et al. (1994, 1997); (7) Number of galaxies on which the new cluster properties were based; (8) new mean cluster redshift and associated uncertainty; (9) new cluster velocity dispersion.

California Institute of Technology, under contract with the National Aeronautics and Space Administration.

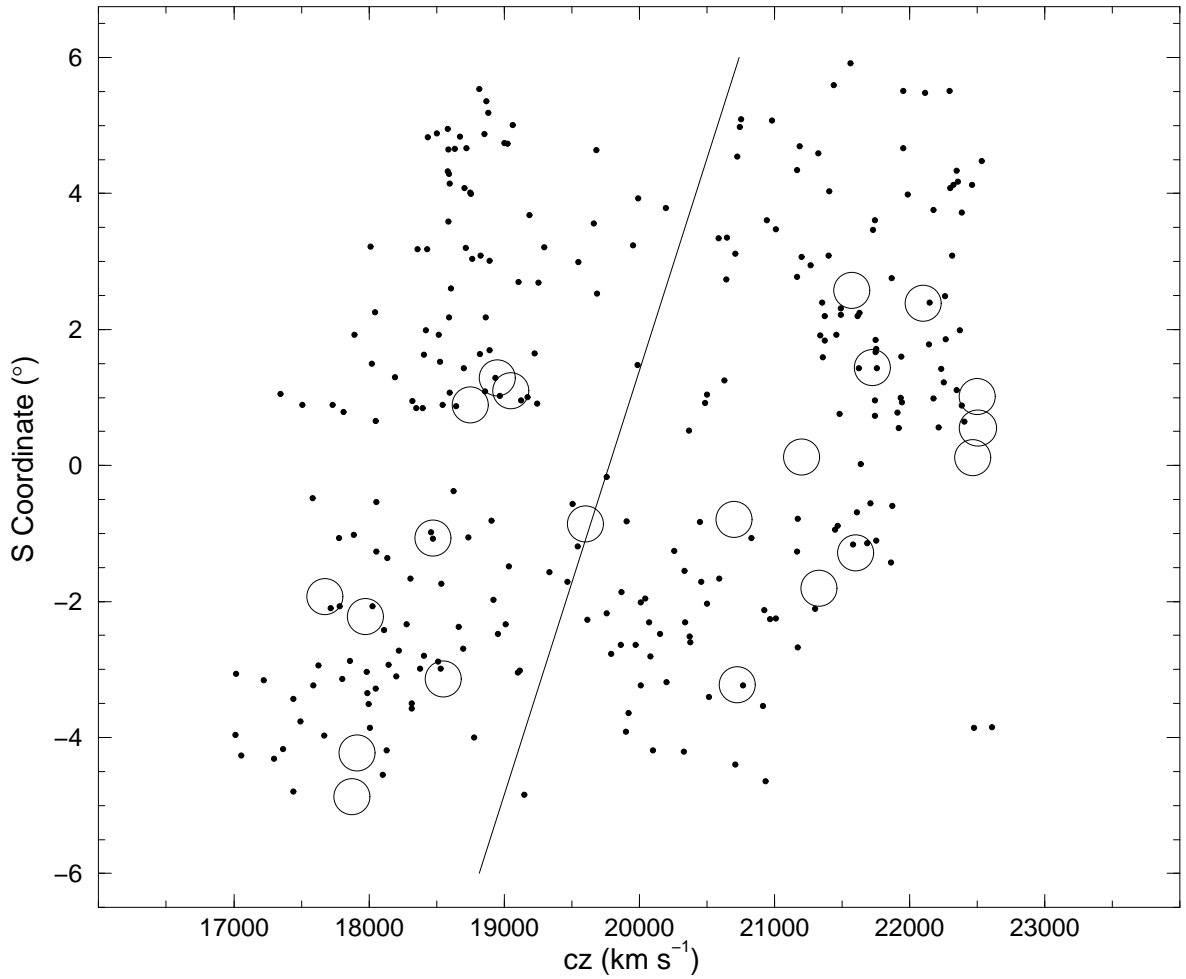


Figure 4.1 Projected angular S -coordinate is plotted versus redshift for 6dF intercluster galaxies from Paper I (small filled circles) between 17,000 and 22,500 km s^{-1} at a PA $= -80^\circ$. Open circles represent the location and approximate extent of the clusters in the region with mean redshifts listed in Table 4.2. The solid line is the best fit to the intercluster data at this PA.

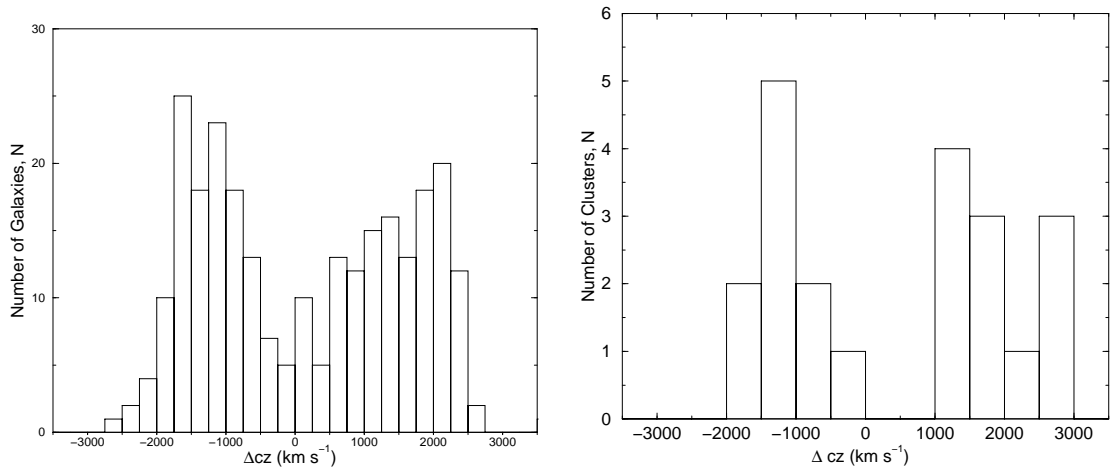


Figure 4.2 Histograms of residual redshifts along the best-fit line at a $PA = -80^\circ$, shown as the solid line in Figure 4.1. **Left:** Previous results for the HRS intercluster galaxies; **Right:** New results for the HRS clusters as listed in Table 4.2.

Table 4.2. Reliable Cluster Redshifts in the HRS Kinematic Core

Cluster	α_{2000}	δ_{2000}	Richness	Redshift, \bar{z}	\overline{cz} (km s $^{-1}$)	N_{gx}	Source	E:?
(1)	(2)	(3)	(4)	(5)	(6)	(7)	(8)	(9)
A3074	02 57.9	−52 43.0	0	0.071917	21575	7	1	Y
A3078	03 00.5	−51 50.0	0	0.073767	22100	8	1	Y
A3100	03 13.8	−47 47.0	0	0.063500	19050	9	1	Y
A3104	03 14.3	−45 24.0	0	0.072417	21725	28	1	
A3106	03 14.5	−58 05.0	0	0.065333	19600	7	1	Y
A3108	03 15.2	−47 37.0	1	0.062500	18750	7	2	Y
A3109	03 16.7	−43 51.0	0	0.063167	18950	11	1	Y
A3110	03 16.5	−50 54.0	0	0.074900	22470	10	3	Y
APMCC 369	03 17.5	−44 38.5	0	0.075000	22500	29	3	
A3112	03 17.9	−44 14.0	2	0.075000	22500	77	2	Y
S0345	03 21.8	−45 32.3	0	0.070667	21200	18	4	
A3120	03 21.9	−51 19.0	0	0.070133	21040	1	5	Y
A3123	03 23.0	−52 01.0	0	0.061583	18475	11	1	Y
A3125	03 27.4	−53 30.0	0	0.058900	17670	40	6	Y
S0356	03 29.6	−45 58.8	0	0.072000	21600	8	3	
A3128	03 30.2	−52 33.0	3	0.059900	17970	158	2	Y
A3133	03 32.7	−45 56.0	0	0.071083	21325	7	1	Y
APMCC 421	03 35.5	−53 40.9	0	0.061833	18550	11	1	
APMCC 433	03 41.1	−45 41.5	0-1	0.069083	20725	11	1	
A3158	03 43.0	−53 38.0	2	0.059700	17910	105	2	Y
A3164	03 45.8	−57 02.0	0	0.059583	17875	7	1	Y

Note. — Numbers in parentheses apply to column numbers. (1) Cluster name, where “S” denotes poor clusters from ACO; (2) Right Ascension in hours and minutes (J2000); (3) Declination in degrees and minutes (J2000); (4) ACO Richness or APMCC equivalent; (5) Average redshift taken from Source; (6) Recessional velocity; (7) Number of galaxies used to calculate kinematic properties, for A3120 see §5.3; (8) 1— This study, 2— Katgert et al. (ENACS, 1998), 3— Alonso et al. (1999), 4— I. Klammer (private communication), 5— Lucey et al. (1983), 6—Caldwell & Rose (1997); (9) Was the cluster excised for the 6dF observations.

Chapter 5

The Panorama of the HRS

“A great window stands before us. We raise our eyes & see the glass; we note its quality, & observe its defects; we speculate on its composition. Or we look straight through it on the great prospect of land & sea & sky beyond.”

—Benjamin B. Warfield

5.1 Galaxy Viewer Visualization Software, GyVe

The remainder of the survey project and the following chapters have relied heavily on the visual appearance of the intercluster galaxy distribution in shaping our impressions of the HRS environment. In fact, both the theoretical and observational sides of large-scale structure research have emphasized the qualitative visual aspects of matter distribution with phrases like the “cosmic web.” To accomplish this in the HRS, we have employed the interactive visualization software tool, GyVe (Miller et al. 2006). Where some visualization techniques do not allow for user interface, GyVe was designed to receive input from the user related to the potential structures observed. Not only is the galaxy distribution fully rendering in 3-D, but it also provides a means of user-defined groupings for export. Simultaneous datasets, e.g., clusters and intercluster galaxies, are compatible within the GyVe environment, so that intuition is gained regarding how different constituents are arranged. Besides the manner in which GyVe is utilized for the quantitative analysis of voids in §6, we have spent many hours appreciating the magnificent structure of the HRS region. A full discussion of the GyVe software is presented in Appendix A.

5.2 Largest-scale Visual Impressions

An overview of the 6dF intercluster fields ($b_J \leq 17.5$) reveals the existence of large-scale inhomogeneities within the previously-defined supercluster region (16,000 – 23,000 km s^{-1} in Paper I). Figure 5.1 shows the 6dF sample from 12,000–27,000 km s^{-1} at a preferred 3-D viewing angle optimized to highlight the contrast between the network of connected overdensities and regions of sparse numbers of galaxies (the orientation is almost equivalent to a $\delta - cz$ plot). Coinciding with the list in Table 5.1, the galaxy clusters with known mean redshift in the observed volume are labeled as orange cylinders. By plotting a single symbol for each cluster, rather than the individual galaxies, we avoid the “finger-of-god” redshift distortion (Kaiser 1987) that otherwise complicates our view of the intercluster distribution. Because there is a variety of structures within the HRS survey volume, one of our primary goals is examination of the region with an eye toward answering the question, “What specific substructures comprise this supercluster of galaxies?” While original cataloging of superclusters sought to define a minimum number of rich clusters located at an optimum linking scale (e.g., Bahcall & Soneira 1984; Zucca et al. 1993; Einasto et al. 1994, 1997), more recent surveys of individual superclusters highlight their different characteristics and the structures contained within them (e.g., Small et al. 1998; Barmby & Huchra 1998; Quintana et al. 2000; Porter & Raychaudhury 2005).

We begin by highlighting 6 regions within our survey volume as large underdense regions in terms of galaxy counts (numbered in Fig. 5.1). So-called voids reportedly comprise a large portion (up to 40% of the total volume, see Hoyle & Vogeley 2004) of the universe in contrast to the overdense cosmic web of clusters and filaments. As mentioned previously in Paper 1 (see Fig. 5), there are two regions of low galaxy density that stand out *within* the actual volume of the supercluster region (labeled “1” and “2” in Fig. 1). Their approximate diameters in the $cz - \delta$ projected dimensions are ~ 30 Mpc each. Regions 3 and 6 might be partially biased to be underdense due to the sparse sampling at the survey boundaries. These possible voids are therefore included within “ ” to denote their contingency. Regions 4 and 5 contribute to the formation of

the apparent cz limits of the HRS (upper and lower, respectively), although the precise boundaries of the HRS are difficult to specify exactly.

Besides the actual presence of the underdense regions, we highlight at least four other relevant observations to Figure 5.1. First, we note that the low density environments seem to extend throughout most of the (or even, the entire) volume of observation. That is, it is not clear that any of the six regions are fully enclosed by our current survey volume. The preferred viewing angle in Figure 5.1 exacerbates this issue, since the α dimension is the smallest in our observed volume (~ 65 Mpc as compared with 85 Mpc in δ and >300 Mpc in cz). Therefore, it may be more accurate to describe these features as “tunnels,” rather than spherical voids.

Second, we note that none of the known rich clusters reside within the void regions, as will be demonstrated in §6.6. The galaxy clusters presented in Figure 5.1 (and Table 5.1) represent a complete ACO sample within the survey volume for richness class ≥ 0 and distance class ≤ 5 (Fleenor et al. 2006). There are also several APMCC clusters (without ACO corollaries) included in the sample. Since we exclude the cluster regions from the 6dF survey (i.e., $1R_{\text{Abell}} = 1.5 h^{-1}$ Mpc), one must consider whether the voids are actually just the additive effect of several excluded clusters. Alternatively, if clusters are artificially creating voids by excision, (1) void-like features will extend through the full range of cz , and (2) there will be clusters within the voids.

Third, with the significant increase of intercluster redshift data, the simplified “two redshift component” model discussed in Paper I needs re-evaluation in light of the complexity of substructures now observed. It is straightforward, however, to see that such an interpretation was concluded since the narrow overdense ridge between voids 1 and 2 is located at $\sim 18,000 \text{ km s}^{-1}$ (i.e., the low-redshift component from Paper I with the smaller FWHM) with the more broad overdensity running roughly between voids 2–3–5 from $21\text{--}22,500 \text{ km s}^{-1}$ (the high-redshift component, in Fig. 9, Paper I). With the undersampling ($\sim 23\%$ for intercluster galaxies) and uneven coverage (particularly in the northeast) associated with Paper I now improved, the interconnective network between these two structures is revealed, and a more detailed interpretation is justifiable.

Lastly it is important to note that although the HRS presents itself as a connected

overdensity network in Figure 5.1, it is difficult to determine from this snapshot whether or not the overdense structures are “filamentary” (as opposed to sheet-like). The extension of megaparsec-scale overdensities in one or multiple dimensions is a current topic in observational studies (Doroshkevich et al. 1996; Colberg et al. 2000a). Though the qualitative term “filamentarity” is often used to describe large-scale structure, some studies show that the intercluster environment is not as (exclusively) filamentary as we might have previously thought (e.g., $\sim 40\%$ from 2dFGRS in Pimbblet et al. 2004a; Colberg et al. 2005a, uses CDM to give $\sim 20\%$ filaments, according to their own definitions).

5.3 The Complete Cluster Picture

With the conclusion of the 2005 2.3m/DBS observations, a complete sample of rich ACO clusters in the HRS was obtained. Figure 5.2 shows the Hammer-Aitoff projection of the current cluster picture in the HRS. Solid open circles denote galaxy clusters with mean velocity in the HRS bounds ($17,000\text{--}22,500\text{ km s}^{-1}$). Gray filled circles denote clusters whose mean velocities are fore/background to the HRS. Two clusters, A3111 and S0339, have mean velocities very near these bounds, $23,200\text{ km s}^{-1}$ and $16,500\text{ km s}^{-1}$, respectively. It is still undetermined whether or not these two clusters are actually members of the HRS. Red outlined circles are those clusters that were observed in 2004 with the DBS/2.3m, where the 2005 clusters are given by the green circles. All cluster radii have been scaled to $1R_{\text{Abell}}$ ($\approx 2\text{ Mpc}$) at their respective mean velocity. The pertinent spatial and dynamical information for all clusters in this Figure is given in Table 5.1, which is discussed fully in the next section.

Examination of the spatial arrangement of the HRS clusters, in conjunction with the mean redshift data in Table 5.1 (col. 6), leads to the conclusion that a majority of northern clusters have a higher velocity $\approx 21,000\text{ km s}^{-1}$, while the southern HRS is more populated by clusters whose mean velocity is more closely associated with $19,000\text{ km s}^{-1}$. Furthermore, it appears from Figure 5.1 that the underdense regions 1 and 2 contribute to this arrangement. Specifically, a majority of lower velocity clusters are present “in front of” (i.e., at lower velocity) underdense region 2, while a majority of

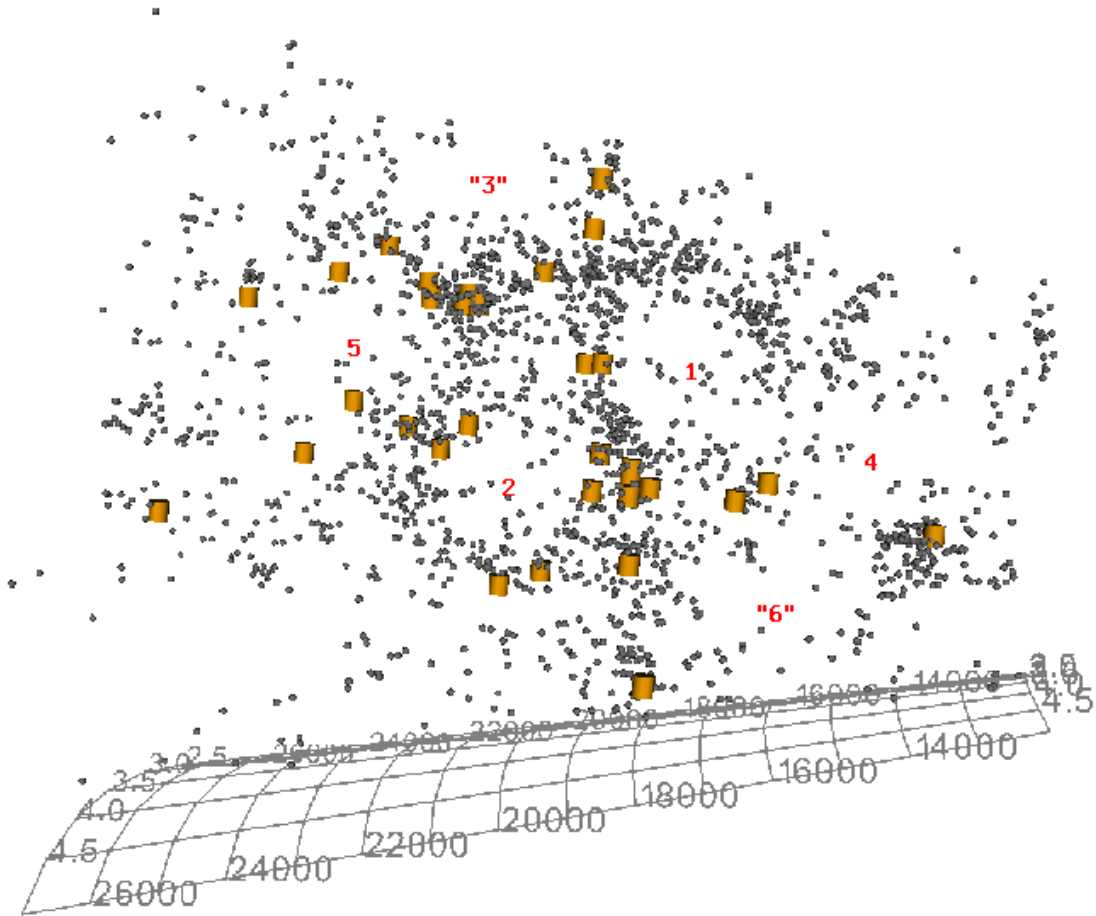


Figure 5.1 Preferred viewing angle snapshot of the 6dF sample from 12,000–27,000 km s^{-1} , as taken from the GyVe software. The vantage point is almost equivalent to a $\delta - cz$ plot. Numbers show the centers of the potential voids in the area (discussed in §6), where the “ ” refer to less certain structures due to the decreased coverage at the boundary (for 3 and 6). The orange cylinders are the galaxy clusters listed in Tab. 5.1. The cz axis is shown at the bottom of the GyVe snapshot.

northern clusters are situated “behind” (i.e., at higher velocity) underdense region 1 along the line of sight. In apparent contrast, the intercluster galaxies in Figure 5.1 tend to cover the underdense peripheries more uniformly. This seeming interconnection between under- and overdensity, from which the HRS emerges, is the subject of focus in the following chapters.

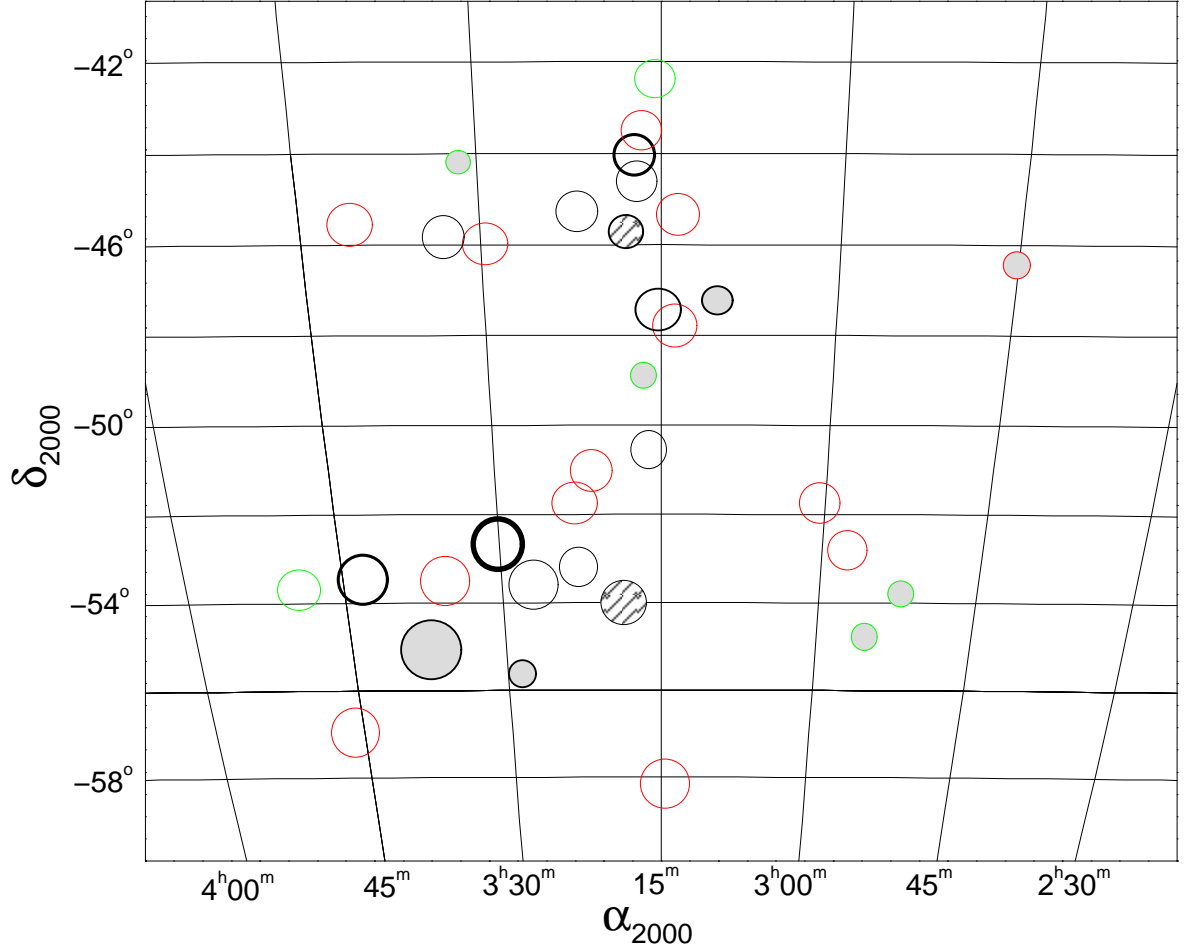


Figure 5.2 Hammer-Aitoff, equal-area projection map of the complete cluster sample for the HRS region. The radius of each cluster is scaled with the mean redshift to 0.5 Abell radii (~ 1 Mpc). The thickness of each outline represents the Abell Richness, where thicker lines are clusters of greater richness class. Open circles represent clusters within the HRS kinematic limits ($17,000\text{--}22,500 \text{ km s}^{-1}$), and filled circles are fore-/background to the HRS. The two hatched clusters, A3111 and S0339, have mean redshift very near the HRS limits, and their membership is uncertain. Red outlines represent clusters observed in the 2004 DBS/2.3m allocation (§2.4.1), and green outlines correspond to the 2005 allocation (§2.4.3). The spatial, kinematic, and dynamical information for all clusters is given in Tab. 5.1.

5.4 Determination of Mean Cluster Masses

As a final overall look at the HRS, a mass estimate is determined from the individual calculation of cluster masses. Every discussion of the mass of various large-scale astrophysical structures begins with the virial theorem (e.g., Longair 1998), a measured los velocity dispersion, σ_{los} , and an estimate of the projected virial radius. Although there are assumptions made in how the system mass is estimated from the two observables, it does provide a reasonable order-of-magnitude estimate of the mass content of the HRS. As discussed in §4.1, we have employed the bi-weight estimator of BFG90 rather than a simple Gaussian fit to the velocity distribution, in determining the mean velocity and σ_{los} of each cluster. The velocity dispersions for all known clusters in the HRS with more than 8 identified members are given in Table 5.1, column (7). Columns (1)–(3) give the cluster name and coordinates, and column (4) lists the cluster richness according the Abell et al. (1989) designation. Column (5) gives the number of individual galaxies on which the BFG90 location (mean, in col. 6) and scale (dispersion, col. 7) are based. A value for σ_{los} was not calculated in 5 clusters that contain only a small number of observations ($3 \leq N_{\text{GX}} \leq 6$), which were collected during the weather-affected, 2005 ANU/2.3m allocation. Two of these clusters are located within the HRS velocity bounds from Paper I and will slightly affect our mass estimate.

For gravitationally bound astrophysical structures in equilibrium, the virial theorem states that the (assumed isotropic) kinetic energy of a system, $T = \frac{3}{2}M\sigma_{\text{los}}^2$, is equal to one-half its gravitational potential energy, $|U| = GM^2/R$. From this, we derive the following equation for the mass of the system:

$$M_c = \left(\frac{3\pi}{2}\right) \left(\frac{\sigma_{\text{los}}^2 r_{\text{vir,p}}}{G}\right) (1 - \Delta), \quad (5.1)$$

where $r_{\text{vir,p}}$ is the projected virial radius (The & White 1986; Andernach et al. 2005). Δ is an estimator related to the anisotropy of galaxy orbits within the system, and we take the median value of 0.19 found in Girardi et al. (1998) for 170 ACO clusters. Furthermore from Girardi et al. (1998, equation 10), we find an estimate for

$$r_{\text{vir,p}} = 1.193r_{\text{vir}} \left(\frac{1 + 0.032(r_{\text{vir}}/R_c)}{1 + 0.107(r_{\text{vir}}/R_c)}\right), \quad (5.2)$$

where the core radius, $R_c = 0.05r_{\text{vir}}$ from the observations of Girardi et al. (1995). After substituting into Girardi et al. (1998, equation 9),

$$r_{\text{vir,p}}^3 = \frac{\sigma_{\text{los}}^2}{6\pi} \frac{r_{\text{vir,p}}}{H_0^2}, \quad (5.3)$$

we arrive at an estimate for the mass based on our only observable,

$$M_c = 1.2 \times 10^6 \sigma_{\text{los}}^3 h^{-1} M_{\odot}, \quad (5.4)$$

where σ_{los} is measured in km s^{-1} . The masses for all HRS clusters with ample redshift information are given in Table 5.1, column 8. The sum of these masses gives a total of $9 \times 10^{15} M_{\odot}$ for the HRS, which includes an estimate for the two remaining clusters without a calculated σ_{los} . This serves as a lower limit for the mass of the HRS, where the intercluster distributions are not accounted for directly.

Table 5.1. Galaxy Clusters Throughout the HRS Region

Cluster	α_{2000}	δ_{2000}	Richness	N_{gx}	\overline{cz} (km s^{-1})	σ_{los} (km s^{-1})	Mass ($\times 10^{14} M_{\odot}$)
(1)	(2)	(3)	(4)	(5)	(6)	(7)	(8)
A3047	02 45.3	−46 25.9	0	7	27500	1225	...
A3067	02 54.6	−54 06.9	1	5	36975
A3074	02 57.9	−52 43.0	0	9	21575	325	0.6
A3078	03 00.5	−51 50.0	0	8	22100	575	3.3
A3093	03 10.9	−47 23.0	2	22	24900	425	...
A3100	03 13.8	−47 47.0	0	9	19050	250	0.3
A3104	03 14.3	−45 24.0	0	28	21725	700	5.9
A3106	03 14.5	−58 05.0	0	7	19600	300	0.5
A3108	03 15.2	−47 37.0	1	7	18750	450	1.6
A3107	03 15.4	−42 45.0	0	6	19600
A3109	03 16.7	−43 51.0	0	11	18950	850	5.9
A3110	03 16.5	−50 54.0	0	10	22470	750	7.3
APMCC369	03 17.5	−44 38.5	29	29	22500	700	5.9
A3111	03 17.8	−45 44.0	1	35	23250	775	...
A3113	03 17.8	−48 49.0	1	3	48975
A3112	03 17.9	−44 14.0	2	77	22500	950	14.8
S0339	03 19.0	−53 57.4	0	27	16369	375	...
S0345	03 21.8	−45 32.3	0	18	21200	550	2.9
A3120	03 21.9	−51 19.0	0	8	21475	550	2.9
APMCC391a	03 22.3	−53 11.3	0	32	23575	1300	...
APMCC391b	03 22.3	−53 11.3	0	22	17925	425	1.3
A3123	03 23.0	−52 01.0	0	13	18475	375	0.9
A3125	03 27.4	−53 30.0	0	40	17675	400	0.5
A3126	03 28.7	−55 42.0	2	38	25680	1050	...
S0356	03 29.6	−45 58.8	0	8	21600	525	2.5
A3128	03 30.2	−52 33.0	3	158	17975	875	8.9
A3132	03 32.2	−44 11.9	1	3	48350
A3133	03 32.7	−45 56.0	0	11	21325	475	1.9
APMCC421	03 35.5	−53 40.9	0	11	18550	300	0.5
A3144	03 37.1	−55 01.0	1	10	13290	500	...
APMCC433	03 41.1	−45 41.5	0-1	12	20725	425	1.3
A3158	03 43.0	−53 38.0	2	105	17910	875	8.9
A3164	03 45.8	−57 02.0	0	8	17875	650	3.7
A3170	03 47.9	−53 49.0	1	6	21550

Note. — See §5.4 for a description of the column contents.

Chapter 6

Voids in the HRS

“What is unnamed is often unnoticed.” –Eugene Peterson

6.1 Void Definition and Examination

Since the most readily observable features in Figure 5.1 are the underdense regions, we begin with their definition and properties. Though originally thought not as important as overdense galaxy clusters, some early studies do suggest that voids play a formative role in the cosmological landscape, generally (Icke 1984; Regos & Geller 1991), and megaparsec-scale overdensities, specifically (Dubinski et al. 1993; van de Weygaert & van Kampen 1993). In recent years, “voids” have received more attention as playing a primary role in the formation of the landscape of large-scale structures (El-Ad & Piran 1997; Peebles 2001; Hoyle & Vogeley 2002; Croton et al. 2004; Sheth & van de Weygaert 2004).

By examining voids as they appear observationally, we make the implicit assumption that the peculiar velocities of individual intercluster galaxies are not a significant contributor to the overall redshift of any particular galaxy. This is not an unwarranted assumption, since all 6dF survey galaxies are chosen well outside of the non-linear regime of galaxy clusters ($> 1 R_{Abell} \sim 2$ Mpc at the HRS redshift) and thought to be within global overdensities of $\delta < \sim 10$. Identifying voids within redshift-space is not thought to cause significant distortions, since the galaxy’s peculiar velocity is small compared to the void diameter (from recent CDM simulations see Fig. 2 in Padilla et al. 2005,

but also earlier in Regos & Geller 1991; Bothun et al. 1992). However, we acknowledge the existence of peculiar outflow velocities of galaxies within voids, either perpendicular to the void boundaries (Padilla et al. 2005) and/or tangentially along the boundaries themselves on the order of $< 10^3 \text{ km s}^{-1}$ (Regos & Geller 1991; Dubinski et al. 1993). Such velocities, regardless of direction, could produce distortions of $\approx 3 \text{ Mpc}$ in the apparent positions of galaxies near the location of voids. Consequently, any interpretation of voids with radii less than $\sim 5 \text{ Mpc}$ is certainly vulnerable, since peculiar velocity effects could give similar distortions.

The centers of the 6 large voids in our survey volume were defined by a two-step process. First, from the interactive GyVe software (Fig. 5.1; Miller et al. 2006), at least 70 galaxies (i.e., ≥ 35 diametrically opposed pairs) were chosen by eye from the peripheral rim of each underdense region in such a way that all (pairs of) galaxies enclose the circumference (or attempt to). In calculating a midpoint (in α , δ , and cz) from every (diametrically opposed) galaxy pair, two coordinate transformations occurred around the sky center of the HRS ($\alpha_c = 3^{\text{h}}4$, $\delta_c = -50^{\circ}0$). All calculated midpoints were then averaged without the high and low values for all coordinates in each void. Therefore, an average of 30 midpoints per void were retained for the calculation. This initial process gives an estimate for each void center defined by the coordinate triplet (α_c , δ_c , and cz_c). Since the galaxy pairs are selected in an approximate $\delta - cz$ projection, our center estimate for the α -coordinate has the greatest variance.

Second, we examined the radial galaxy counts around the newly calculated void center, while incrementally varying the value of each coordinate of the void centers in a two iteration routine. In order to calculate the radial distance of each intercluster galaxy, an equal area transformation occurred for the coordinates of each individual galaxy with respect to the center of every void successively. By taking all galaxies within a radial distance of 25 Mpc from each void center, we maximized the void radius to the distance where 2 or more galaxies are found, i.e., the radius is not determined by the presence of only one galaxy. For example, on the first iteration we varied the center α_{eff} estimate by $\pm 5\%$ while holding the δ_{eff} and cz_{eff} center estimates constant. Therefore, we examine the galaxy number counts as a function of void radius for each

Table 6.1. Voids Throughout the Surveyed Region

Number	Center			R_{void}	V_{sphere}
	α_{2000}	δ_{2000}	cz (km s $^{-1}$)	(Mpc)	(Mpc 3)
(1)	(2)	(3)	(4)	(5)	(6)
1	03 ^h 21 ^m	−46°33′	17300	14.5	12200
2	03 ^h 22 ^m	−53°42′	19925	11.7	6700
3	03 ^h 27 ^m	−41°33′	21150	16.5	18800
4	03 ^h 29 ^m	−49°06′	14750	22.0	44600
5	03 ^h 37 ^m	−48°02′	22800	16.5	18800
6	03 ^h 40 ^m	−58°54′	15875	11.8	6700

Note. — (1) Void Number; Void center from §6.1: (2) Right Ascension (J2000), (3) Declination (J2000), and (4) cz ; (5) Void radius; (6) Total contained volume.

coordinate until more than one galaxy is found and an optimum (first-pass) triplet is obtained.

To demonstrate the process, we continue with the example above and present the histograms in Figure 6.1 that show the intercluster galaxy counts as a function of radius for incremental values of α_{eff} in Void 1. Here, a first-pass value of $\alpha = 3^{\text{h}}43$ was chosen because it specifies the largest radius where no galaxy is found. A second iteration is then completed for each coordinate (α_{eff} , δ_{eff} , and cz_{eff}) with an increment of $\pm 1\%$ to locate the final void center. The final calculated centers for each void are presented in Table 6.1 with other geometrical properties. The numbers of each void in Figure 5.1 are placed approximately at the calculated center. After determining the 6 void centers by this two-step process of radial galaxy number counts, we now calculate the galaxy underdensities with these voids in order to determine an accurate radius and to place them on equal footing with those defined in the literature.

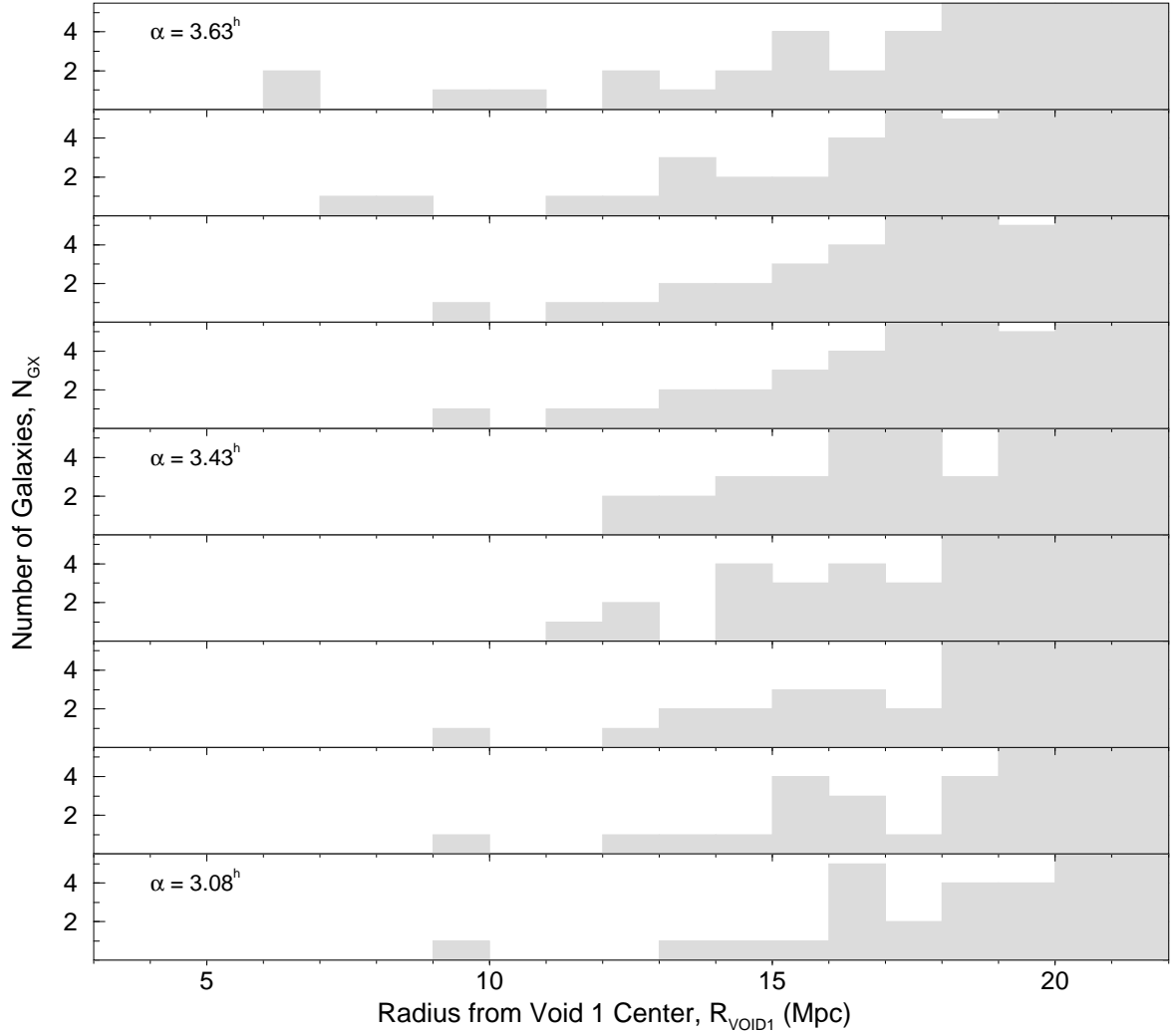


Figure 6.1 Radial profile distribution of galaxy number counts as a function of incremental changes in the α -coordinate of the void center. For each histogram strip, the α is altered by 0.05^h , while the δ and cz -coordinates remain constant. These are the results of the galaxy minimization procedure that serves as the second step for defining the void center. Here, the optimal void center with $\alpha = 3.43^h$ was chosen as it is the largest radius for which no galaxies are found. The procedure is then repeated for incremental changes in both δ and cz .

6.2 Void Sizes and Galaxy Underdensity

With the center of each void properly established, we now calculate the underdensity within each void, as well as a definitive radius, under the assumption that voids are spherical. Although the void radius was estimated in the previous section by examining radial galaxy number counts, all studies in the literature use an underdensity criterion to specify the void radius and to validate the structure as a void. Therefore, it is imperative to calculate such values for comparative purposes. The expected uniform distribution of galaxy counts was constructed by accounting for the radial selection function and survey incompleteness (see §2.2.2). Since the selection function does not vary appreciably ($< 5\%$) across the void diameter as a function of redshift, we averaged the weighting values within the assumed sphere. Furthermore, we utilize the mean completeness values that are found within each estimated void extent in Figure 6.2. When calculating the underdensity within Voids 3 and 6, a partial volume of 70% is employed because they are both located on the Declination boundary of the survey.

Having established the expected galaxy counts associated with each void, we proceed with the canonical underdensity calculation according to the following:

$$\delta = \frac{n_{\text{gx}}(z)_{\text{observed}} - n_{\text{gx}}(z)_{\text{B}}}{n_{\text{gx}}(z)_{\text{B}}}, \quad (6.1)$$

where $n_{\text{gx}}(z)_{\text{B}}$ is the number counts of galaxies for the uniform background distribution calculated from the selection function and completeness mask. Literature-defined voids are based on an underdensity criterion, between $-0.5 \leq \delta \leq -0.9$, that is calculated either by incremental volumetric shells or a cumulative spherical volume. Furthermore, studies sometimes set a minimum radius threshold, e.g., $R_{\text{VOID}} \geq 10 h^{-1} \text{ Mpc}$, below which empty volumes are just referred to as “holes,” rather than actual voids (Hoyle & Vogeley 2004, hereafter HV04). The void radius is defined by the distance to which the underdensity constraint is maintained. Void properties are established either theoretically via CDM simulations (Mathis & White 2002; Colberg et al. 2005b) or observationally (El-Ad & Piran 1997; Müller et al. 2000; Hoyle & Vogeley 2002; Croton et al. 2004).

We present in Figure 6.3 the cumulative galaxy number counts normalized by volume as a function of scaled radius for the 6 large voids in our survey region. Since the void centers are not at the same mean redshift, and therefore sample the LF differently, the 6dF counts are normalized to ensure voids sample the galaxy LF equally. The normalization factor uses the selection function for expected galaxy counts (in §2.2.2) and displaces all voids to the HRS mean redshift of $z = 0.06$. Furthermore, the galaxy counts are normalized by the radial volume factor, $(R_i/R_{\text{VOID}} \times 15)^3$, where 15 Mpc is the average void radius determined from §6.1. This is carried out to separate the actual increase in galaxy density due to the presence of overdense structures from the expected increase in counts with volume. Values of constant underdensity for the mean HRS redshift at $\delta = -0.5$ and $\delta = -0.9$ are shown as dot-dashed lines. Each void profile is truncated at the radius where its volume crosses the survey boundary. This is seen most easily in Voids 3 and 6, where symbols are used to mark their profiles for $R/R_{\text{VOID}} \leq 1$ (see inset, Fig. 6.3). Although all voids are scaled to $1R/R_{\text{VOID}}$ in the Figure, the actual radial values are listed in Table 6.1, column 5.

Strikingly, we see that the profile of the one void fully located within the HRS boundaries from Paper I and the survey volume is fundamentally different than the other profiles. Specifically, Void 2 increases in galaxy counts until reaching the survey boundary at $2.25R/R_{\text{VOID}}$. We also note that Void 2 has the smallest radius in our sample, which is fully discussed in §6.6. In contrast, Void 4 also displays a different profile by maintaining a nearly constant underdensity of $\delta \approx -0.9$ throughout the survey volume. This fact is discussed more fully in §6.5.2. Though volume normalized, all voids maintain a complete absence of 6dF intercluster galaxies for a normalized radius of $R/R_{\text{VOID}} < 0.8$ (see inset, Fig. 6.3), with the exception of one galaxy in Void 4 located at $R/R_{\text{VOID}} < 0.5$ (§6.5.2). Voids 1 and 5 are located near the HRS kinematic boundaries, $\approx 17,000$ and $\approx 22,500 \text{ km s}^{-1}$, respectively, and seem to maintain a similar profile out to $1.75R/R_{\text{VOID}}$. Although Void 1 has mean velocity *within* the kinematic bounds of Paper I at $17,300 \text{ km s}^{-1}$, its radial profile fits more with the boundary subset. This fact is apparently due to a lack of neighboring clusters, since most of the northern HRS clusters are located closer to $21,000 \text{ km s}^{-1}$ (see §5.3). Therefore, it appears that

the voids in our sample can be segregated into one “embedded” (Void 2) and two other “boundary” voids (1 and 5). Void 3 (at 21,000 km s⁻¹) and Void 6 (at 16,000 km s⁻¹) seem to follow this trend also, but their radial profiles are interrupted by the survey boundary at $R/R_{\text{VOID}} < 1$. A further examination of the profile of Void 3 is given in §6.6, with the addition of non-6dF redshift information. Although the faint limit of our 6dF observations extends to one magnitude below $M_{b_j}^*$ ($= -19.75 - 5 \log_{10} h$ from the 2dFGRS in Norberg et al. 2002) at $-18.5 < M_{b_j} < -21.5$, we conclude that the HRS voids fit within the normal underdensity ($\delta < -0.9$) and radial ($R_{\text{VOID}} \geq 10 h^{-1}$ Mpc) constraints used in the literature.

6.3 Are Voids Spherical?

Since an actual radius for each void was calculated under the assumption of its spherical nature, we now check the claim of void sphericity. As mentioned earlier, the galaxy density enclosing the underdense regions does not appear uniform in all directions (i.e., the galaxy counts are not equal on all sides of the void). If the voids extend throughout the range of α within the survey volume, a more accurate description of the shape of the underdensities would be ellipsoidal, rather than spherical. Though newly-formed voids may originate as ellipsoidal or more elongated, theoretical predictions expect evolved voids in the present epoch to have reached a more spherical state (Bertschinger 1985; Blaes et al. 1990). The condition of void sphericity is initially checked in the following way.

First, from the intercluster galaxy sample for each void with scaled radius, $R_i/R_{\text{VOID}} \leq 1.75$, we segregate the intercluster galaxies into two distinct categories (rim and cone). Since not all voids have the same radius, equivalent relative populations are examined for each void by using a scaled radius sample (e.g., $R_i/R_{\text{VOID}} = 1.75$, rather than $R_i < 25$ Mpc). When this sample is projected into the $\delta - cz$ plane, approximately from the view in Figure 5.1, we select all galaxies located in the double-cone volume formed by an opening angle, $\theta = \pm 45^\circ$, along the α direction (i.e., the cone galaxies). The remaining galaxies within the $R_i/R_{\text{VOID}} \leq 1.75$ sample are declared members of

the rim category. Next using the previously established void centers from Table 6.1, we carry out the same procedure for the galaxy number counts as a function of radius for only the *cone* galaxies. This process determines a void radius exclusively along the α -coordinate, which is approximately ‘into the page’ in Figure 5.1. Though the total number counts for cone galaxies is significantly smaller (usually a factor of ~ 5 less), we find that this void radius is within $\pm 10\%$ ($\approx 1 - 2$ Mpc) when compared to the same procedure in §6.1 for all galaxies with $R_i/R_{\text{VOID}} \leq 1.75$. Therefore, in these two nearly perpendicular directions, the radial distance to more than one galaxy is quite similar and seemingly consistent. Moreover, these findings do not conflict with the assumption of sphericity within HRS voids.

Seeking further clarification of the galaxy distribution with respect to the void center, we now examine the population of adjacent galaxies near each void by projecting these galaxies onto a Hammer-Aitoff, equal-area projection. Initially for each void, the $R_i/R_{\text{VOID}} = 1.75$ sample is observed with an interest in how are the intercluster galaxies distributed on the surface of the void. We also extend the sample population to $R_i/R_{\text{VOID}} = 2.5$ to obtain a better estimation of how adequately the galaxies “cover” the void periphery. Figures 6.4 – 6.9 show the intercluster galaxy populations for the two different values of scaled radii; the top plots show the $R_i/R_{\text{VOID}} = 1.75$ sample, while the bottom shows the galaxies for $R_i/R_{\text{VOID}} = 2.5$. Galaxies are represented as small filled circles, while the galaxy clusters are represented as orange cylinders. Each map is projected from the viewpoint of an observer at the center of the void, with α increasing from the bottom to top of the map. The shaded ellipses are drawn individually for each void along the axis where it is possible to “see through” the void in the GyVe software.

At this point, a few comments are warranted regarding the general coverage of the voids by the intercluster galaxies. First, it is clear from all the plots that the coverage for *both* scaled radii is highly structured and leaves large areas of the void surface vacant. Even for the voids found near the Paper I-defined HRS bounds and fully enclosed by the survey volume (Voids 1, 2, and 5), the coverage is not uniform. Moreover, the addition of more galaxies at larger scaled radii does not necessarily imply more uniform coverage.

That is, new galaxies that enter our view from within the HRS voids tend to populate the same regions already inhabited by the $R_i/R_{\text{VOID}} = 1.75$ sample. For the average HRS void radius of $\bar{R}_{\text{VOID}} = 15$ Mpc, we will begin to pick up galaxies associated more closely with neighboring voids rather than the void in question, when the radius for galaxy projection is increased far beyond a scaled radius of $R_i/R_{\text{VOID}} > 3$. In other words, increasing the sample beyond $R_i/R_{\text{VOID}} = 2.5$ is more likely to confuse, rather than further clarify, the void boundaries. In summary, the arrangement of galaxies around most voids appears to be highly structured as is expected from the highly structured “cosmic web.”

6.4 Void Volume within the HRS

While being mostly devoid of light (and dark?) matter, it is well-established that voids occupy a significant volume of the universe (de Lapparent et al. 1986; Geller & Huchra 1989; Shectman et al. 1996; El-Ad & Piran 1997). More recently for example, HV04 report a volumetric void-filling fraction of up to 40% in the 2dFGRS for large voids, $R_{\text{VOID}} \geq 10 h^{-1}$ Mpc, which is also consistent with their earlier findings in Hoyle & Vogeley (2002). CDM numerical simulations report similar percentages for the volume of voids based on various values of a minimum R_{VOID} , either somewhat greater ($\sim 60\%$ in Colberg et al. 2005b) or smaller ($\sim 30\%$ in Padilla et al. 2005). The total volume of voids within the HRS is found by summing the entire volume of Void 2 with significant fractions of Voids 1 (0.70), 3 (0.70), and 5 (0.33) from Table 6.1, column 5. Because Voids 4 and 6 do not intersect the kinematic boundaries of the HRS established in §3.1 (17,000–22,500 km s^{-1}), they are not included in the calculation. Furthermore, we use a spatial area of $12^\circ \times 16^\circ$ with the kinematic extent above to define the volume of the HRS. Therefore, a void filling fraction of 10% is found when compared with the estimated total HRS volume. This percentage for larger voids with $R_{\text{VOID}} \geq 10 h^{-1}$ Mpc is somewhat similar to the CDM simulations of Colberg et al. (2005b, Fig. 4), where $\sim 90\%$ of the total void volume is filled by $R_{\text{VOID}} \leq 2.5 h^{-1}$ Mpc voids, and thus $\sim 5\%$ of the volume is covered by voids with radii $\geq 10 h^{-1}$ Mpc. Contrastingly,

observational studies (El-Ad & Piran 1997; Hoyle & Vogeley 2002, and HV04) tend to find a value closer 40% for the filling fraction of voids with $R_{\text{VOID}} \geq 10 h^{-1} \text{ Mpc}$.

While admittedly we are studying one of the most dense superclusters in the local Universe, what is not clear is the disparity between the HRS and the observational studies of HV04, where they find 40% of the volume in the 2dFGRS is filled by larger voids. One important difference is that the location of the voids in this study are in the overdense (by a factor of ~ 2) HRS, while the 2dFGRS covers a more representative sample of the universe. Specifically, only two structures as large as the HRS are found in the 2dFGRS (Erdoğdu et al. 2004). Following from this, the only void totally enclosed by the HRS and survey bounds is the smallest in radius, Void 2. HV04 find that the underdensity for ~ 300 voids in the 2dFGRS at $2R_{\text{VOID}}$ is $\delta \leq -0.5$ (see their Fig. 4). We note that only Void 4 resembles the mean underdensity profiles for the 2dFGRS voids at $\sim 2R_{\text{VOID}}$, i.e., $\delta < -0.5$ (and possibly Void 6), while Void 1 shows such behavior at $1.5R_{\text{VOID}}$. The question then arises as to whether the relatively small volume filled by large voids in the HRS when compared to that found by HV04 for the 2dFGRS could be due to the generally overdense nature of the HRS. We turn now briefly to CDM simulations, where the internal structure of individual voids can be studied in more detail.

6.5 Internal Structure of HRS Voids

6.5.1 Comparisons with CDM simulations

We begin by noting that CDM simulations appears to reproduce many of the large-scale features within the cosmological landscape (e.g., van de Weygaert 1991; Loken et al. 2002), though not without some difficulties (e.g., Peebles 2001; Floor et al. 2004). Sheth & van de Weygaert (2004, hereafter SvdW04) provide a detailed analysis of the void hierarchy for SCDM model (i.e., $\Omega_{\text{m}} = 1$) and list basic features exhibited by evolving voids; three of which are comparable with observational studies: i) evacuation, ii) sphericity, and iii) ridge boundaries. We examine the HRS voids in light of these

characteristics found within similar simulated structures. With the exception of one galaxy in Void 4 (see discussion below), there are no 6dF intercluster galaxies in our survey found within the inner 10 Mpc of any void. While some results show that low mass CDM halos populate the inner regions of voids in a regular network (Gottlöber et al. 2003, with more recent observational confirmation in Patiri et al. 2006), the HRS voids are seemingly devoid of the fairly bright galaxy sample in our flux-limited survey out to $R_{\text{VOID}} = 0.8$ (Fig. 6.3).

Secondly, we have also shown that 6dF intercluster galaxies appear in several directions at similar distances and cover the surface of the void to some degree (e.g., Fig. 6.4). Furthermore, for each void, we have separated the associated galaxies along perpendicular directions. We find the void radius is quite similar along these directions in §6.3, to within $\pm 10\%$ along all lines-of-sight. Although there are low number counts perpendicular to the line of sight (i.e., along the α coordinate), we conclude the voids observed in our survey maintain a roughly spherical shape.

Lastly, a sharp transition (i.e., a spike or ridge) from underdensity to overdensity is also mentioned by SvdW04 as a feature of evolving simulated voids (see their Fig. 3). This is followed by shell crossing, the underdense equivalent of non-linear growth, where the void's inner shells pass across the outer. With a thickness of 3–5 Mpc, the two voids mostly closely with the kinematic bounds of the HRS (Voids 1 and 2) and fully contained within the survey volume show a similar increase in galaxy counts. Figure 6.10 shows the incremental radial profile for intercluster galaxies as a function of radius from the void center. On the initial ascent of galaxy counts near the void boundary (at $R_i \sim 12$ Mpc, a similar peak is observed, which is followed by an intermediate decrease in galaxy counts. The noticeable rims of most voids in Figure 5.1 also corroborates with the idea of a sharp increase at the void boundary. It is difficult to determine the extent of non-linearity within these voids, and any outflow velocities will enhance this effect (Praton et al. 1997; Thomas et al. 2004). Since such information is suppressed, no claims about the extent of non-linearity can be made for the HRS voids, although these voids have maintained sustainability within the overall overdense HRS environment. In summary, the voids contained within the survey volume and the HRS bounds show

similar indications of evolved internal structure, even though the HRS voids are much larger than the simulated voids in comparison. It is not clear, therefore, how well an accurate comparison can be made between these observed voids and those in CDM simulations.

6.5.2 Unique structure of Void 4

In closing this section on void structure, we return to the interesting characteristics of HRS void 4. While having the largest radius in our survey (~ 20 Mpc), Void 4 deviates from the adopted definition by the presence of one galaxy at a small void radius ($R_{\text{VOID}} = 6$ Mpc). It also does not show a sharp ridge like the other voids in the survey, while maintaining a fairly significant underdensity, $\delta < -0.5$, at $3R_{\text{VOID}}$. We further note that the Void 4/6 combination spans a significant portion of the survey volume, which forms the low redshift boundary of the supercluster (though Void 6 falls into the embedded category). While first noted by Shanks (1990), many subsequent authors mention the possible existence of a large local “hole” in the Southern sky (near the Galactic cap), observed as both a minimum in galaxy cluster density (Cross et al. 2001; De Propris et al. 2002) and as a measurement of galaxy underdensity (Norberg et al. 2002; Erdoğdu et al. 2004). Frith et al. (2003) uses a combination of 2dFGRS and 2MASS data to describe this “superhole” as having a linear size of $\sim 200 h^{-1}$ Mpc and bound by overdensities at $z \sim 0.03$ and ~ 0.06 , which rivals the current scales of cosmological isotropy and homogeneity. The patchy structure of Void 4 and its more extended underdense surroundings substantiate this claim, as does our own redshift histogram in Figure 2.10, though many bright galaxies were excluded from our sample ($b_J < 10.0$, in Fig. 2.2). Furthermore, Void 4 pushes through the survey volume at an underdensity of ~ -0.9 , as shown in Figure 6.3. Although the coincident position of the southern HRS (at $z \sim 0.06$) also corroborates for the existence of this structure, the presence of A3144 (richness = 2, at $z = 0.044$) does not. In summary, the voids in the HRS, not unlike their overdense counterparts, also show unique structure seemingly based on their location within the “web” of cosmic structures.

6.6 Reality of the HRS Voids

6.6.1 Overview

Because we have not intentionally observed galaxies within 1° radius of several of the clusters in the HRS, one must consider whether this cluster excision radius, by creating holes in the HRS intercluster sample, has somehow artificially generated voids in our survey. There are two reasons why the 6 voids in the HRS sample are unlikely to be the result of such a selection effect. First, as seen in Figure 6.2, the centers of voids are not at all correlated with the positions of the excised clusters. Rather, the excised (and other) clusters are concentrated along the void peripheries, a result that is reinforced in 3-D using GyVe. Second, if the voids are due to the excised regions, they should all pass entirely through the volume in redshift, which they do not, as seen also in GyVe. However, we test the reality of the voids by attempting to add excised *intercluster* members of the HRS back into our sample, as well as fainter galaxies across the entire HRS field. To do so, we augment the 6dF intercluster survey with available redshifts from the literature throughout the HRS (see Tab. 2.4, §2.3). This test is particularly important for the possibly embedded voids (2 and 3), because we have been building the case for their uniqueness compared to voids found in lower density environments. We begin by recalling the overview of the HRS from the GyVe snapshot in Figure 5.1; while not a single cluster was found within any of the potential voids, there are a number of clusters found near the rims of voids (especially Voids 1, 2, and 3). The two primary regions with several overlapping HRS clusters are in the north (Voids 1 and 3) and south (Void 2) of the survey volume. Figure 6.2 shows black rectangles where the majority of galaxies were added back, while Table 2.4, columns 1 and 2, lists the specific clusters near each sample and its associated region of the HRS. In both the north and south, the extra contributing surveys provide redshifts for significantly fainter objects ($18.0 \leq b_J \leq 20.0$). Though incomplete at these magnitudes, the observations aid our understanding of how populated are the 6 voids defined by our brighter sample of galaxies.

We begin by determining the cluster members from the augmented samples within each previously excised ACO cluster, as substantial peculiar velocities will significantly distort the positions of these galaxies (Kaiser 1987). Though cluster membership may have been defined differently in previous work within HRS clusters, we apply the bi-weight estimator from BFG90, used in §4.1, to all augmented samples. When deciding on cluster membership in §2.4.1, a more generous areal radius of $0.5R_{\text{Abell}}$ (≈ 1 Mpc) was used; whereas a different approach is taken here since we want to retain a maximum number of non-cluster galaxies. Therefore, a tighter radial (areal) constraint of $0.25R_{\text{Abell}}$ (≈ 0.5 Mpc) is employed. After the cluster members are determined and excluded, all other galaxies are declared intercluster galaxies and are added back to the 6dF intercluster sample regardless of their apparent brightness. The “intercluster” catalog now contains redshifts for over 6,000 galaxies ranging in brightness $11.0 \leq b_J \leq 20.5$. Though this augmentation severely distorts the relatively uniform selection effects of the original 6dF sample, our primary interest is discovering *any* galaxies within the HRS voids, regardless of position and/or brightness.

6.6.2 Augmented sample for the northern HRS

The primary survey in the northern HRS regions ($\delta > -50^\circ$) is the Las Campanas Redshift Survey (LCRS, Shectman et al. 1996), which adds ~ 3000 galaxies to the sample. The 3 southern slices of the LCRS at -39° , -41° , and -43° are $\sim 2^\circ$ wide and pass through the center of Void 3 and the upper portion of Void 1. In fact, the LCRS is a better sample for determining the true extent and nature (embedded or not) of Void 3, since it is located at the 6dF survey boundary. Though somewhat brighter ($m_R < 17.1$) and less complete ($f \sim 0.5$) than the southern HRS augmentation, the red-magnitude limit of the LCRS still constitutes a fainter blue magnitude for most galaxies (e.g., $b_J - m_R \approx 1.1$ for S0/Sab, Fukugita et al. 1995) than the $b_J = 17.5$ of our 6dF sample, and there is no cluster excision bias. Therefore, this sample, along with the ENACS (Katgert et al. 1998), provides a useful test for whether or not fainter galaxies, and those excised by our anti-cluster bias, populate the central portions of these voids.

Figure 6.11 shows the normalized galaxy counts as a function of scaled radii for the HRS voids including the augmented catalog. To maintain the same underdensity curves as presented in the previous profiles (Fig. 6.3) in the presence of samples with widely varying number counts and limiting brightness, we have implemented the following straightforward weighting. When a particular survey covers a void in question by at least 50%, the relative number density of that survey when compared to the 6dF survey is divided into the total galaxy number counts for the void. For example, the LCRS has $3\times$ the number of galaxies when compared with the 6dF survey in that region. Therefore, around Voids 1 and 3, we divide the total number counts by 3 at $R/R_{\text{VOID}} \leq 1.0$. Furthermore outside of $1.25R/R_{\text{VOID}}$, the total number counts around *all* voids are reduced by a factor of 1.5, since there are many contributing surveys at those distances from the void centers.

The radial profiles for northern voids (1, 4, and 5), with a reliably established profile from the 6dF sample in Figure 6.3, maintain a similar shape under the inclusion of the augmented samples and the proper weighting reduction in number counts. Specifically, all three voids intersect the $\delta = -0.9$ criterion at $0.9 \leq R/R_{\text{VOID}} \leq 1.0$ in the inset portion of Figure 6.11. Moreover, it also appears that Voids 1 and 5 continue to show a consistent “boundary” profile by rising less steeply than Void 2 (discussed below), although Void 1 does rise sharply when the reduction criterion is relaxed at $1.5R/R_{\text{VOID}}$. More interestingly, it appears that Void 3 has a profile more consistent with the HRS boundary when the LCRS galaxies are included, since it straddles the $\delta = -0.5$ criterion out to $1.5R/R_{\text{VOID}}$. We note, however, that it is unclear whether or not the strips of LCRS ($> 1^\circ$ between the each of the three slices) and/or the artificial reduction in number counts has compromised the profile of Void 3 at larger radii. In summary, we see that the voids in the northern HRS defined by the brighter 6dF sample maintain their underdensity and the previously established radii, even after the addition of several thousand galaxies with a fainter limiting magnitude.

6.6.3 Augmented sample for the south HRS

The situation around A3128 and its neighbors, A3158 and A3125, is much more difficult to interpret, since this region is observed to undergo multiple merging activity on various scales (§7.3 and Rose et al. 2002, hereafter RGC02). RGC02 reported the existence of “gaps” in the A3128/A3125 velocity distribution, which were interpreted as significant gravitationally-induced, infall velocities, resulting from the HRS potential. They also statistically defined several spatial/kinematic substructures associated with infall into/out from the cluster complex.

After adding back the catalogs in Table 2.4 and applying the above correction for more heavily sampled surveys, Figure 6.11 shows the effect of ~ 10 galaxies with $b_J > 17.0$ that raise the underdensity of Void 2 to $\delta > -0.5$ at $R/R_{\text{VOID}} \leq 1.0$. This correlates to 23 actual galaxies since a factor of 2.5 was divided into the number counts for Void 2, due to the A3128/ A3158 catalog containing over 1500 galaxies in a $4^\circ \times 4^\circ$ area on the sky. Over half of the filling galaxies (13 of 23) are previously identified with infalling groups/filaments near A3128/A3125 (specifically F1, F2, G4, and G5 in RGC02). The 9 remaining galaxies were not included in the RGC02 study, but could also be members of the recently merging substructure, since most (7 of 9) are similar to one another in position and relative velocity. For example, a small group of four faint galaxies ($b_J \geq 18.0$) are located at a distance of $0.4R_{\text{VOID}}$, while confined within $r_{\text{PROJECTED}} \leq 5''$ (0.5 Mpc) on the sky and a relative velocity width of $\sim 200 \text{ km s}^{-1}$. Therefore, it is not unreasonable to imagine that the positions of galaxy systems on the high velocity side of A3128/3125 are distorted in redshift-space due to peculiar infall, causing them to appear within the inner half of Void 2.

We attempt to correct the Void 2 profile in Figure 6.3 by subtracting away definite members of RGC02-defined groups. The darker (blue) *long-dashed* line in the Figure represents a subtraction of only RGC02 members that were confined spatially and kinematically. Since the slope of the “uncorrected” Void 2 profile is quite constant for $R/R_{\text{VOID}} \leq 1.0$, the subtraction of RGC02 groups has a noticeable effect. Therefore, a similar Void 2 profile is recovered by extracting infalling groups. Fur-

thermore, we have also identified 5 potential “void galaxies” by adding the augmented samples. These galaxies were not observed by RGC02, have $b_J > 19.0$, and are located at $R/R_{\text{VOID}} \leq 0.6$. Since the factor of 2.5 was applied for the augmentation of the A3128/A3125 catalog, the underdensity criterion of $\delta < -0.9$ holds for Void 2 at $R/R_{\text{VOID}} \leq 0.8$. One last observation bodes well for the actual existence of Void 2, even though it has the smallest void radius in our sample (11.8 Mpc). Both RGC02 and the extended redshift catalog examined in §7.2 observe a significant overdensity of galaxies at 22–23,000 km s^{-1} . The implied distance between the A3128–A3158 overdensity (at $\sim 18,000 \text{ km s}^{-1}$) and 22,500 km s^{-1} is ~ 55 Mpc, which provides ample volume for a void of similar size to that determined for Void 2. Therefore, we conclude that most of the current observational information points to the existence of a real Void 2, situated in a similar position to that defined in §6.1.

In summary, even when fainter and more complete galaxy samples are added back to the 6dF survey sample to account for cluster excision, only Void 2 shows some signs of void filling by fainter ($b_J > 18.0$) galaxies. Some of these galaxies are (and others could be) associated with the merging substructure surrounding the A3128/A3125 double-cluster system. Other galaxies have characteristics that more closely associate them with the voids themselves, i.e., faint, closer to the void center, and late in type. Such galaxies are expected, in fact, and the brightness limit of the 6dF survey does not allow a proper search for these “void galaxies.” High-resolution CDM simulations in Gottlöber et al. (2003), now with some observational confirmation in Patiri et al. (2006), suggest that low mass halos/galaxies populate voids in a similar arrangement as the large-scale structure of the Universe (i.e., with filamentarity). Such filamentary “mini-universes” of dwarf galaxies, if confirmed, would continue to widen the panorama of uniqueness of structures on a variety of scales.

6.7 Summary: Voids

From the interactive GyVe software, we identified 6 underdense regions by first defining a rim of galaxies in the $\delta - cz$ projection, and then iteratively calculating a

center for each structure. These regions are found to exhibit the generally prescribed characteristics for larger void regions, which are ubiquitous within the large scale structure. Namely, the 6 HRS voids have a mean radius of $R_{\text{VOID}} = 14 \pm 2$ Mpc and maintain $\bar{\delta} < -0.9$ throughout their extent. In fact, HRS voids harbor no 6dF galaxies for $R/R_{\text{VOID}} \leq 0.8$, except for the presence of 1 galaxy in an extremely isolated void (Void 4, §6.5.2). Furthermore, in an attempt to fill the voids with fainter galaxies from augmented samples (Fig. 6.11), we find that only Void 2 is susceptible to becoming filled. We explain the majority of galaxies in Void 2 by identifying them with merging substructure in the region via RGC02.

When we display the normalized galaxy counts as a function of scaled radius for both samples (Figs. 6.3 and 6.11), different subsets of radial profiles are observed and associated primarily with their immediate surrounding environment. The radial profiles for voids more closely associated with the HRS redshift boundaries (i.e., “border” voids 1, 5, and 6) show a less steep increase in galaxy counts compared to Void 2 (Fig. 6.3), which is embedded within the HRS kinematic bounds and the survey volume. With $\delta < -0.5$ at $1.75R/R_{\text{VOID}}$, only Void 4 shows similarities with the *mean* void profiles of the 2dFGRS in HV04. Though located on the survey boundary, an attempt was made with LCRS data to recover the radial profile of Void 3, whose mean velocity is consistent with the HRS ($21,000 \text{ km s}^{-1}$). While the radial constraint of $\delta \leq -0.9$ was maintained, a somewhat expected embedded radial profile was not observed.

To gain a better understanding of the manner in which galaxies are arranged around the surface of the voids, we create projection maps from the vantage point of the void center. We observe that galaxies do not cover the void surface in an isotropic manner, even at $2.5R/R_{\text{VOID}}$, but rather the distribution is highly structured and preferred orientations seem to govern the arrangement of intercluster galaxies. While attempting to fill the voids with fainter galaxies, we identify 5 potential void galaxies, which are faint ($b_J > 19.0$) and located near the void center $R_{\text{VOID}} < 0.5$. Lastly, there appear to be similarities in shape (sphericity) and structure (evacuation and outer rim) between the embedded HRS voids and evolved, isolated voids in CDM simulations. Smaller simulated voids are destined to constriction by the surrounding overdense structures, yet

the larger HRS voids seemingly embedded have maintained resiliency to this constriction, or have overcome this tendency due to their size. Since the radial profiles of HRS voids appear dependent on their location within the survey and HRS clusters appear preferentially arranged near $1R_{\text{VOID}}$, the voids in the HRS seem to play an integral part in the formation of overdense structures and the supercluster landscape in general. We now turn to an examination of the overdensities themselves to weigh this claim against our observations of the HRS environment.

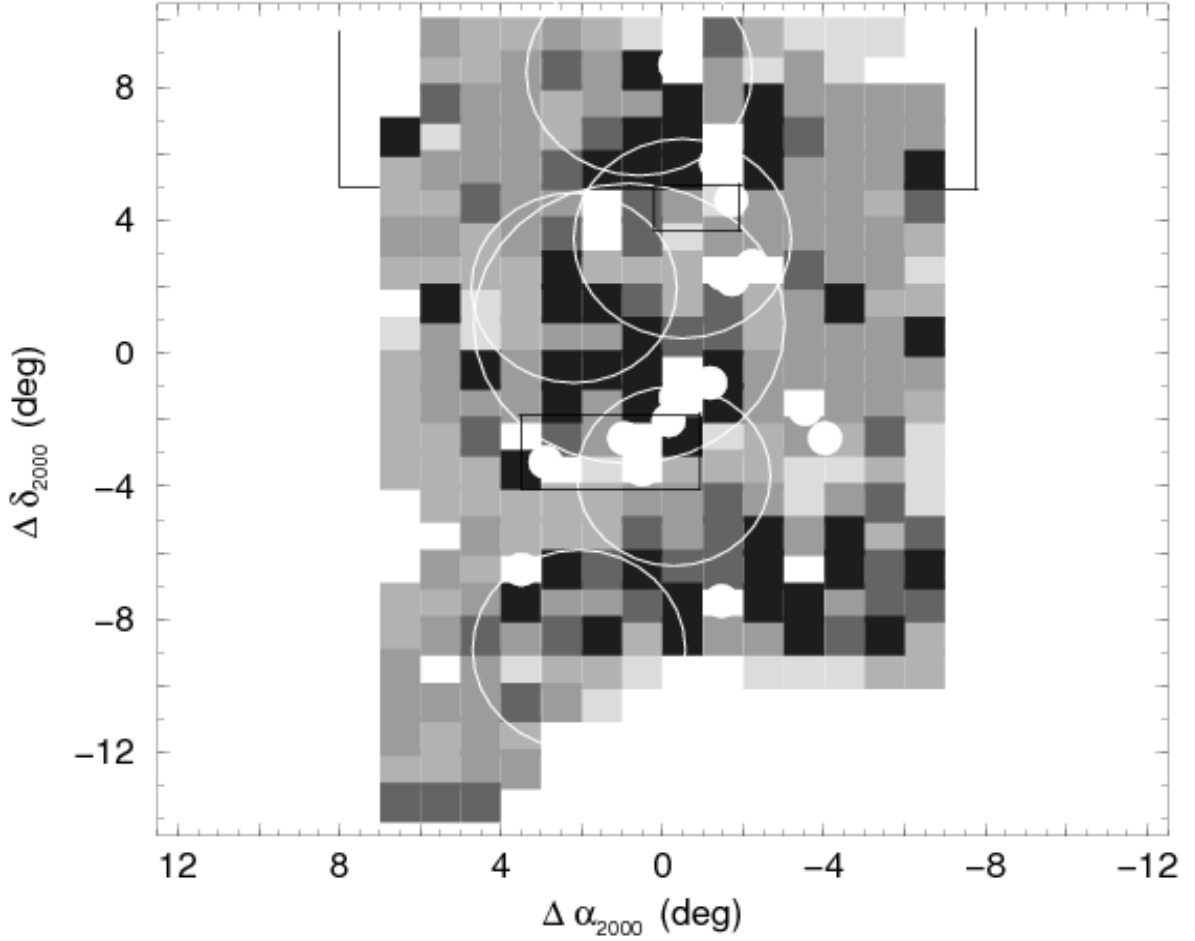


Figure 6.2 Equal area survey mask displaying observational completeness as a function of grayscale. The 300+ deg² of the HRS are divided into 1 deg² blocks with five levels of grayscale measuring the completeness of SuperCOSMOS galaxies with $b_J \leq 17.5$: 0.00 (white), 0.00–0.20, 0.20–0.40, 0.40–0.60, 0.60–0.80, 0.80–1.00 (black). Open white circles show the extent of the 6 HRS voids defined in §6.1. Note that Voids 3 and 6 intersect the survey boundary in Declination. The excised clusters are shown as filled white circles, where the actual excision radius is twice what is shown. The black lines denote the major surveys that augmented the 6dF observations in §6.6. See Fig. 2.8 and §2.2.2 for more discussion. All coordinates are offset from the chosen HRS center at 3^h20^m, –51° 00′.

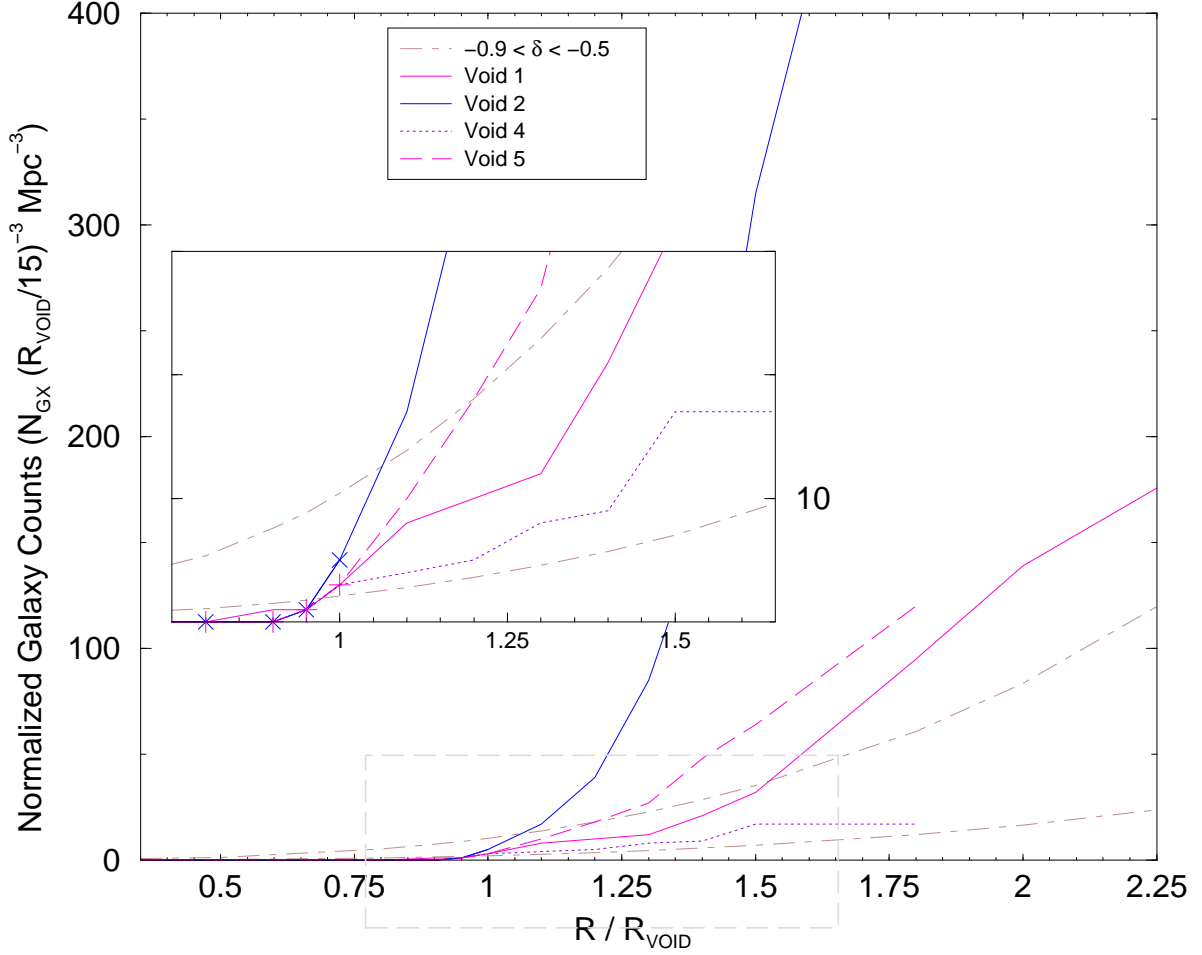


Figure 6.3 Volume-normalized, galaxy number counts as a function of scaled radius for the 6 large voids in our survey. Constant underdensities for the mean redshift of the HRS at $\delta = -0.9$ (lower) and $\delta = -0.5$ (upper) are shown with dot-dashed lines. All void profiles have counts consistent with a sampling of the LF at the HRS mean redshift ($z = 0.06$) and are truncated where they intersect the survey boundary. The location of Void 2 is consistent with the HRS mean velocity, whose profile is noted with a solid, blue line. Voids 1 and 5 are located at the Paper I-defined boundaries of the HRS, and their profiles are labeled with magenta lines. Void 4 is noted with a dotted line, where the profile maintains number counts consistent with $\delta = -0.9$. The inset portion shows the boxed area in more detail to determine the exact void radius as defined by the $\delta = -0.9$ criterion. Voids 3 (“×”) and 6 (“+”) cross the survey boundary at $(R/R_{\text{VOID}} \leq 1$ and their truncated profiles are marked with symbols. Note that the two samples (solid and long-dashed) have fundamentally different profiles.

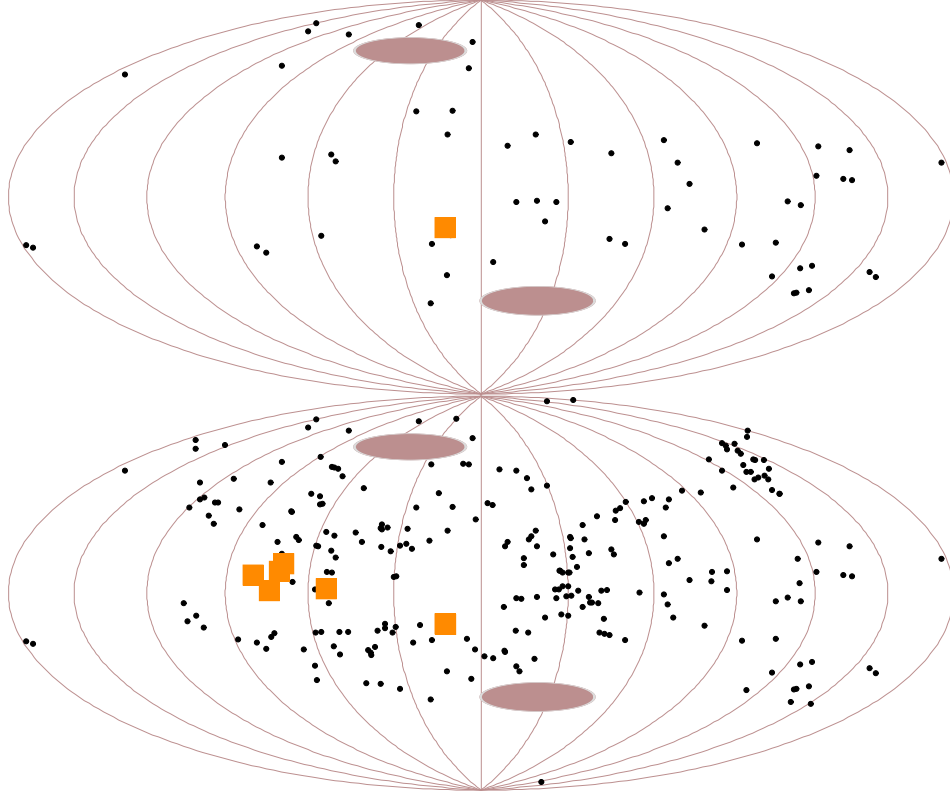


Figure 6.4 Hammer-Aitoff, equal-area projection maps of Void 1. The projection is made from the vantage point of the void center. Small filled circles represent the intercluster galaxies, while the orange cylinders are clusters. The orientation of the projection is synonymous with the snapshot in Fig. 5.1, such that the horizontal axis is the $\delta - cz$ plane, and α decreases from the top to bottom. The shaded ellipses show a preferred axis where it is possible to “see through” the void. Top: Population of galaxies and clusters for $R_i/R_{\text{VOID}} = 1.75$. Bottom: Population of galaxies and clusters for $R_i/R_{\text{VOID}} = 2.5$.

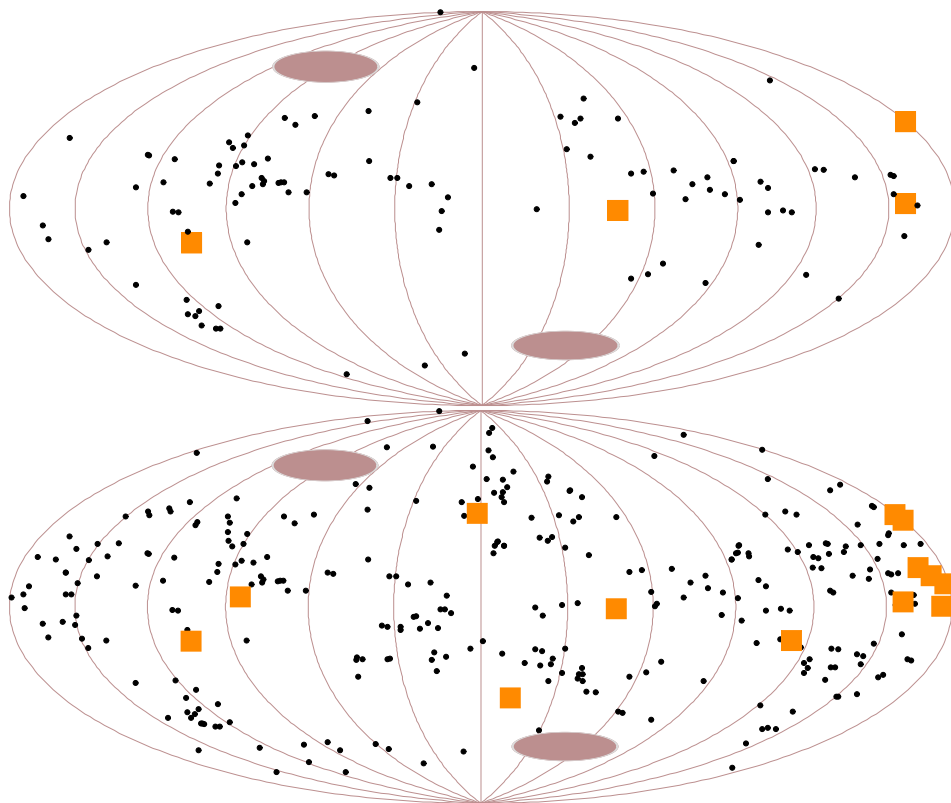


Figure 6.5 Hammer-Aitoff, equal-area projection maps of Void 2. Same symbols and references as Fig. 6.4

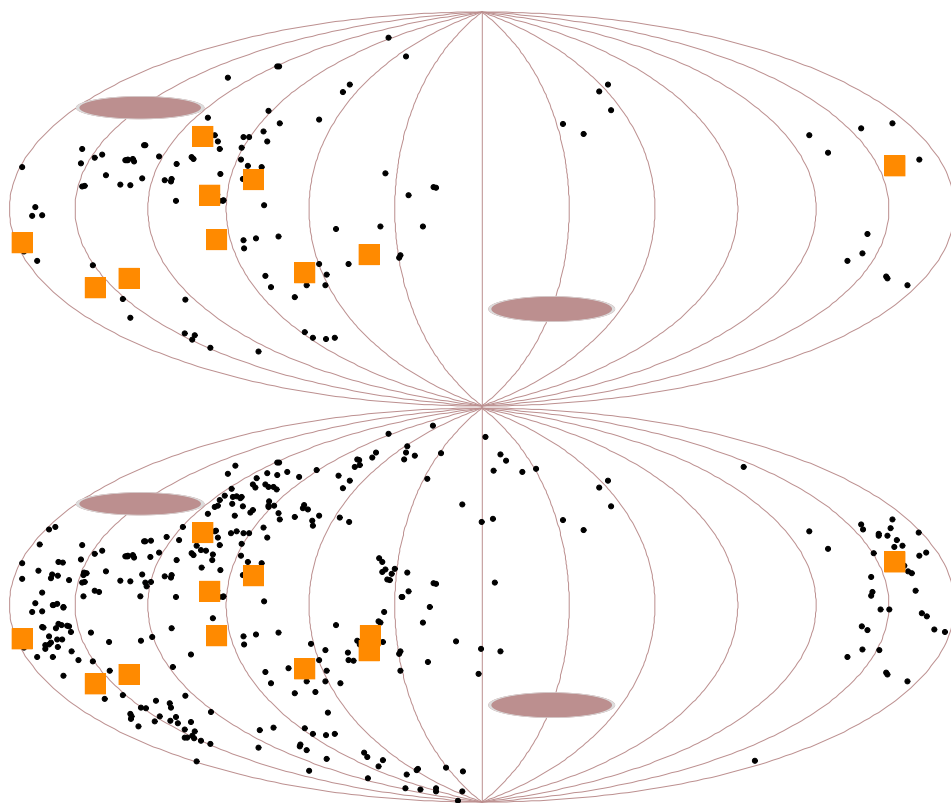


Figure 6.6 Hammer-Aitoff, equal-area projection maps of Void 3. Same symbols and references as Fig. 6.4

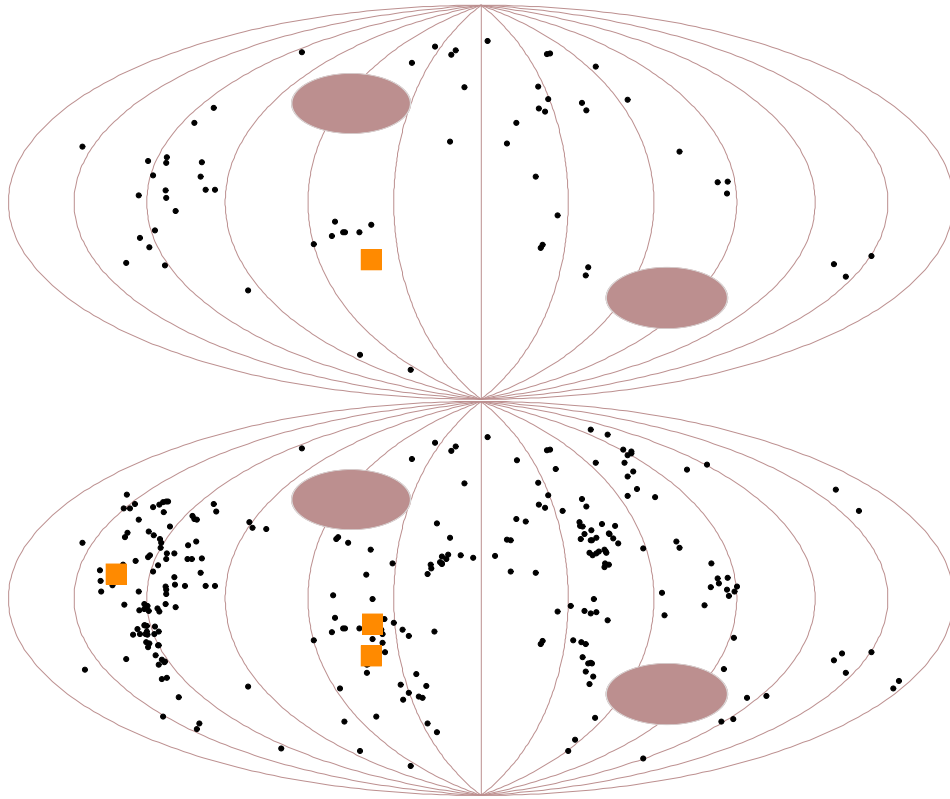


Figure 6.7 Hammer-Aitoff, equal-area projection maps of Void 4. Same symbols and references as Fig. 6.4

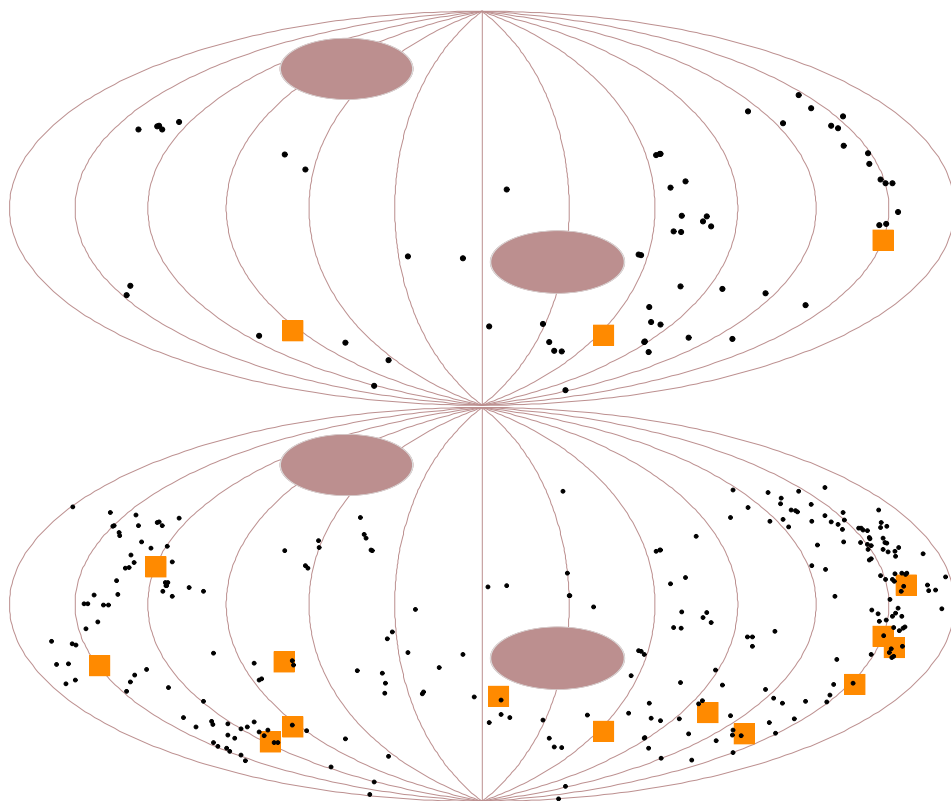


Figure 6.8 Hammer-Aitoff, equal-area projection maps of Void 5. Same symbols and references as Fig. 6.4

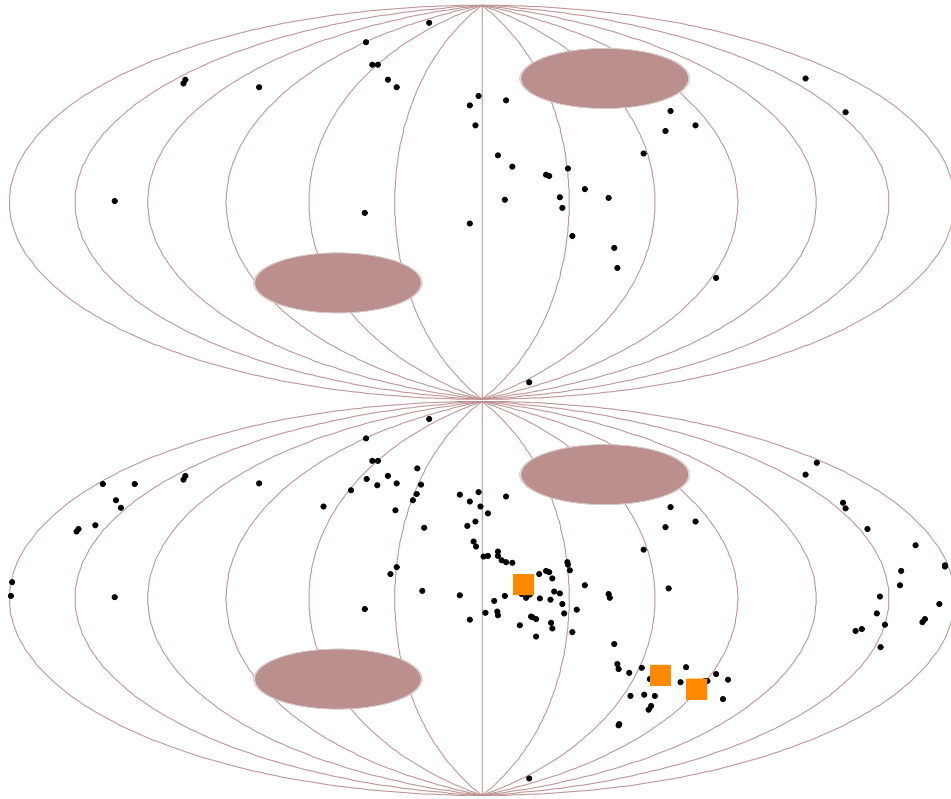


Figure 6.9 Hammer-Aitoff, equal-area projection maps of Void 6. Same symbols and references as Fig. 6.4

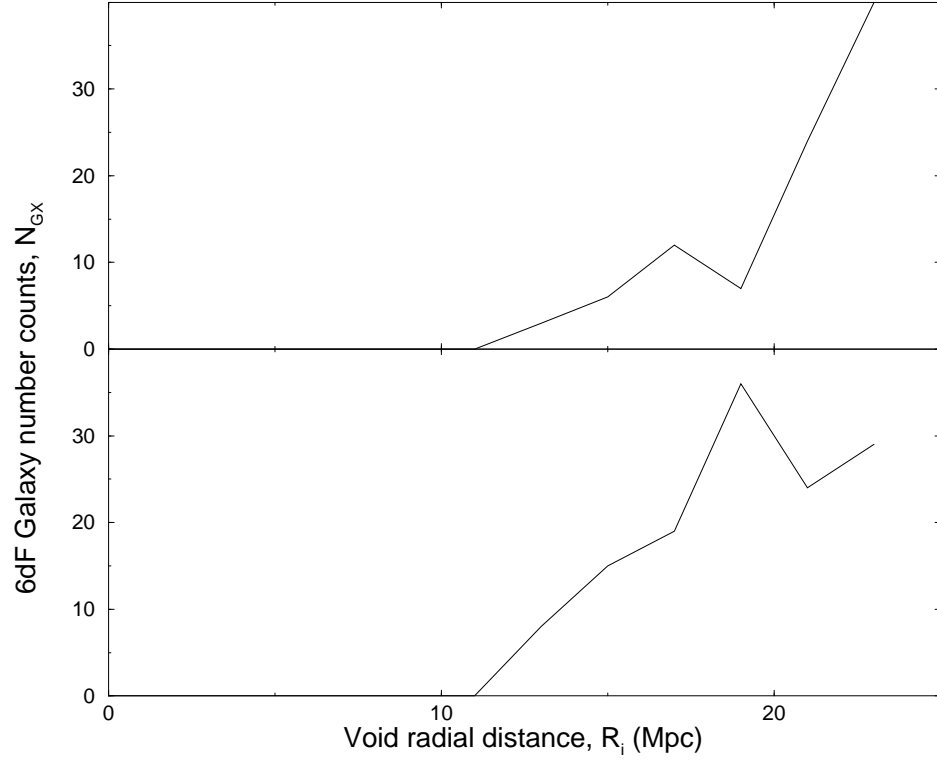


Figure 6.10 Incremental radial profile of intercluster galaxy counts for Voids 1 (top) and 2 (bottom). In each profile, a small spike 10–15 galaxies is located on the larger peak of increasing galaxies. This peak is followed in both voids by a decrease in counts before encountering significant intercluster counts.

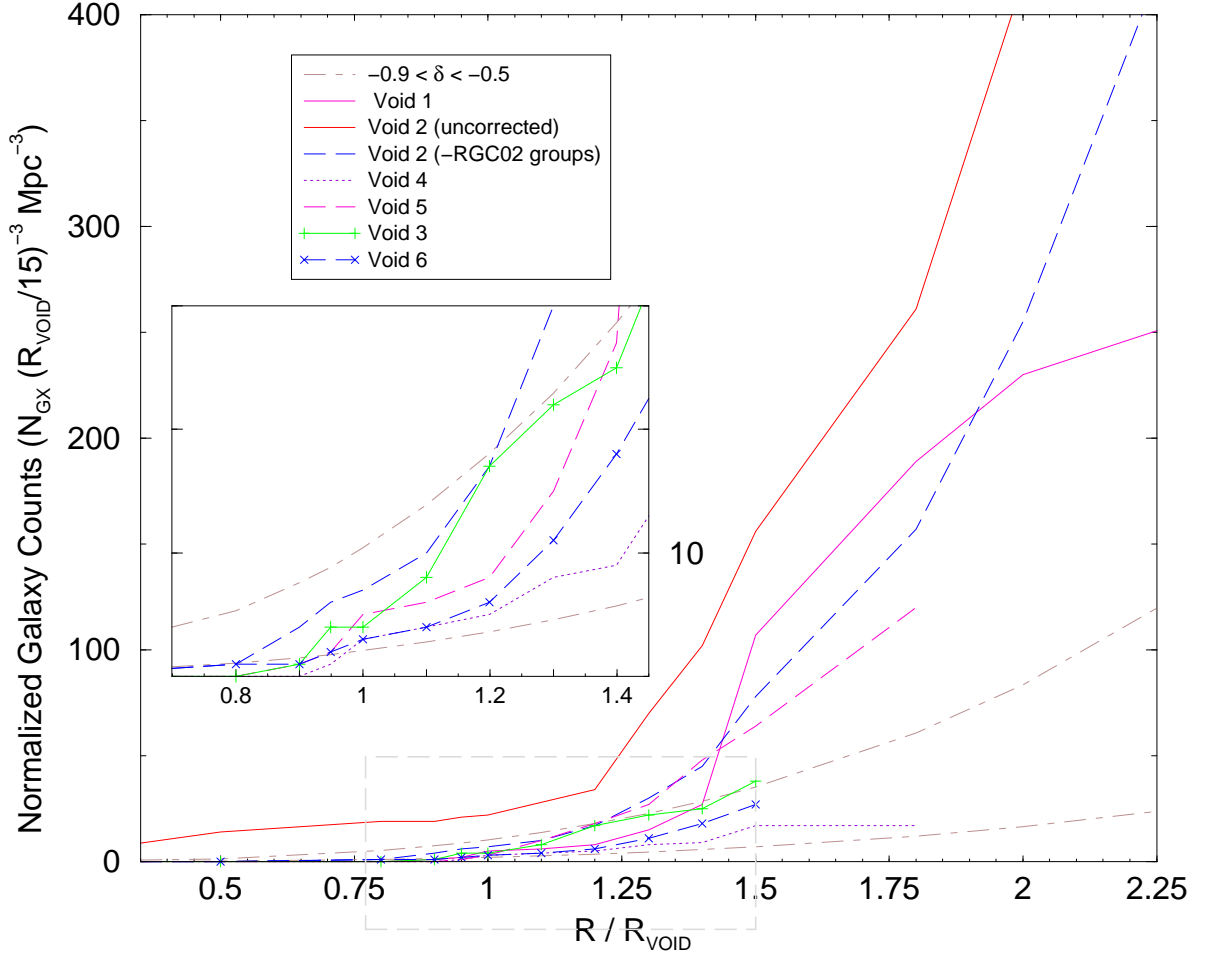


Figure 6.11 Volume-normalized, galaxy number counts with the augmented samples included as a function of scaled radius for the 6 HRS voids. Symbols are the same as those in Fig. 6.3, with the following exceptions: the darker (blue) long-dashed line represents the attempt to reconstruct the actual intercluster population for Void 2 without the presence of merging substructure. The red line represents the profile of Void 2 *before* the attempt to extract group members. The green line represents the profile of Void 3, whose radius has been confirmed due to LCRS addition. The profile for Void 6 was estimated out to $1.5R/R_{\text{VOID}}$, though the survey boundary problem persists.

Chapter 7

Intercluster Overdensities of the HRS

“There is some secret stirring in the world, a thought that seeks impatiently its word.” –Thomas L. Beddoes

DISCLAIMER: The word filament has become a general buzzword for the qualitative nature of large-scale structure. While we don’t deny that structures do often, at first glance, appear filamentary, we try to reserve that particular word in the following for objects that are extended in only one spatial dimension and are kinematically coherent.

7.1 Overview

The various regions of galaxy overdensities outside of the rich clusters in the HRS lend themselves to individual examination. We will begin with HRS regions already discussed in the literature, typically on the cluster scales and their infall regions ($< 10 h^{-1}$ Mpc). This approach affords us the opportunity to examine the published hypotheses for structure arrangement as well as to examine the relationship between structures on varying scales. There are two primary references to individual structural phenomena within the HRS that are discussed: (i) the existence of a $\sim 10 h^{-1}$ Mpc intercluster ‘bridge’ in the region of rich clusters A3128 and A3158 as initially proposed in L83, and (ii) the A3125/A3128 intercluster axis along which multiple merging events are believed to have occurred (RGC02). In (i) and (ii), where a 100% increase in redshift

information (due primarily to the Mathams data) warrants a more detailed examination, we seek to relate finer scale structure (~ 1 Mpc) to the intercluster environment (5–10 Mpc scales).

7.2 A3158/A3125 “Bridge:” Hints of Superclustering

In the original study of HRS structure, L83 focused on a $6^\circ \times 6^\circ$ region in the southern HRS, centered around two of the richest clusters in the HRS, A3128 (Richness = 3, $\sigma_{\text{los}} \approx 950 \text{ km s}^{-1}$) and A3158 (Richness = 2, $\sigma_{\text{los}} \approx 1100 \text{ km s}^{-1}$, Mazure et al. 1996). Among the interesting findings in L83, a galaxy “bridge” was found to extend between A3158 and the less-rich and more-diffuse A3125 (Richness = 0, $\sigma_{\text{los}} = 300 \text{ km s}^{-1}$, Caldwell & Rose 1997). Since all three clusters have approximately the same velocity ($cz \approx 18,000 \text{ km s}^{-1}$), the projected, co-moving distance between A3158 and A3125 of ~ 11 Mpc is thought to be fairly accurate. The bridge connection is somewhat surprising, since simulated CDM filaments are found to preferentially lie between the most massive constituents in a particular region (Colberg et al. 1999). Most-massive constituent connection is also confirmed observationally between the galaxy clusters A1367 and Coma (Gregory & Thompson 1978; de Lapparent et al. 1986), A1367 and Virgo (Jones & Forman 1999), and even all three clusters (Zeldovich et al. 1982; West & Blakeslee 2000). The intercluster bridge in L83 consisted of 7 galaxies with mean velocity of $18,150 \text{ km s}^{-1}$ and a rather large velocity dispersion of 900 km s^{-1} . L83 notes, however, that reducing the bridge by one member reduces the σ_{los} significantly to 355 km s^{-1} . Furthermore, the semi-major axis of all bridge member galaxies had a narrow distribution of position angle (PA) at $131^\circ \pm 19^\circ$ (east of north). With several hundred more galaxy redshifts located near these three clusters, we examine the existence of the bridge as a primary example of an intercluster overdensity.

7.2.1 Spatial and Redshift Distribution

Since the spectroscopic redshift is the best indicator of the volumetric distribution of galaxies at these cosmological distances, Figure 7.1 shows the $2^{\circ}5 \times 2^{\circ}5$ region under study, centered at $03^{\text{h}}33^{\text{m}}$ and $-53^{\circ}00'$, where all galaxies with observed redshifts are displayed as small open circles. The completeness in this area is $\sim 75\%$ for galaxies with $b_J \leq 17.75$, and is sporadic as a function of area at fainter magnitudes. Specifically, one can see that almost halfway between the A3128/25 complex and A3158 there is a sudden decrease in the number of observed galaxies, which is due to the eastern boundary of the Mathams dataset (shown as short-dashed lines in Fig. 7.1). The three major ACO clusters in the region (3125, 3128, and 3158) are shown with larger open circles, drawn at $0.5R_{\text{Abell}}$ (~ 1 Mpc). The less-rich APMCC421 ($\bar{cz} = 18,550 \text{ km s}^{-1}$ and $\sigma_{\text{los}} = 300 \text{ km s}^{-1}$, Paper II) is approximately halfway between the ACO cluster concentrations and drawn with a short-dashed circle. Also shown as solid lines is the potential position of the bridge, though L83 restricted the bridge only to the region from A3158–A3125. In conjunction with the spatial distribution of galaxies, the line-of-sight velocity (cz_{los}) histogram is also presented as the inset portion of Figure 7.1 for all galaxies bounded by the solid lines, i.e., the *potential* bridge members but not including the ACO cluster members (3158, 3128, and 3125). Readily noticeable from the histogram is the presence of a large peak of galaxies (with maximum around $18,250 \text{ km s}^{-1}$), which was recognized by L83, and is due in part to APMCC421. Since intercluster filaments of galaxies are thought to contain no more (light and/or dark) matter than is present in clusters (Cen & Ostriker 1999), and a smaller velocity dispersion ($\sim 350 \text{ km s}^{-1}$) was hinted at by L83, we now seek to better constrain the location, direction, and dynamical state of the proposed bridge.

With the location of APMCC421 approximately halfway between A3158 and A3128/25, we utilize the conclusions from CDM halo simulations that clusters separated by short distances (i.e., ≤ 7 Mpc) are always connected by a filament (Colberg et al. 2005a), in conjunction with the observational finding that straighter filaments are observed for closer cluster-cluster separations (Pimbblet et al. 2004b). This leads to segment-

ing the problem, i.e., the bridge, into two halves: east, between A3158–APMCC421, and west, between APMCC421–A3128/25. Furthermore, since the peak of the velocity histogram at $\sim 18,250 \text{ km s}^{-1}$ coincides with the mean velocity of the two adjoining clusters (e.g., APMCC421 and A3158 or A3128), we consider this value as an initial estimate for the mean velocity of the bridge with a dispersion, σ_{los} , of 350 km s^{-1} . This value for the dispersion is intentionally chosen to be comparable with the less-rich clusters in the HRS found in Paper II. In Figure 7.1, all galaxies in the same region with $17,550 < cz_{\text{los}} < 18,950 \text{ km s}^{-1}$ ($\pm 2\sigma$ of $\overline{cz}_{\text{los}}$) are shown as filled circles. In the eastern half of the proposed bridge region, i.e., between A3158 and APMCC421, there is confirmation for the existence of a connecting structure for the galaxies observed (7 of 18), though small number statistics are a problem. For the western side, the exact path of the connection is more difficult to determine, in terms of whether the connection is with A3125, A3128, or somewhere in between. We note that the region to the north of APMCC421 is almost devoid of galaxies within the proposed velocity range, while south of APMCC421 suffers from a lack of observations (to the east of dashed lines in Fig. 7.1).

By examining in more detail various cuts in velocity, we note that there are no intercluster galaxies in the bridge area with velocities $18,575\text{--}18,950 \text{ km s}^{-1}$ (excluding the APMCC421 core). Therefore, we restrict the velocity range on the high side to this value. Moreover, by increasing the velocity range of the overdensity by $\sim 1\sigma$ on the low velocity side (to $17,250 \text{ km s}^{-1}$), we incorporate several more galaxies within the already populated regions. Within the range of $16,000\text{--}17,250 \text{ km s}^{-1}$, there are only two galaxies found within the originally bounded, bridge region. For these reasons, we report a bridge velocity range of $17,250\text{--}18,575 \text{ km s}^{-1}$ for both the east and west portions, which contains 52 galaxies besides the 14 confirmed members of APMCC421 (Paper II). These 52 members have the following properties and are designated with open diamonds in Figure 7.1: $\overline{cz}_{\text{los}} = 18,000 \pm 50 \text{ km s}^{-1}$, $\sigma_{\text{los}} = 350 \text{ km s}^{-1}$. As to the original conclusion of L83, the proposed bridge does *not* seem to be directed toward the center of A3128. However, we also mention that the projected spatial width of the A3128/25 (west) side is twice that of the A3158 (east) half ($\sim 2.0 : 4.0 \text{ Mpc}$). It is

possible that this is due to the splitting of the bridge to the west of APMCC421, i.e., a connection running to both A3128 and A3125. In the 2dFGRS, Pimbblet et al. (2004b) find a greater number of filaments for increasingly richer clusters. Alternatively, Colberg et al. (2005a) find a flattening of CDM filaments when approaching cluster-size halos. Having established the existence of a coherent collection of galaxies in velocity space, we now calculate an overdensity and compare the value to the surrounding intercluster volumes.

7.2.2 Galaxy Overdensity

In order to determine the approximate overdensity, an accurate determination of the expected galaxy counts in the region is required. The discussion of the radial selection function is found in §2.2.2, and here, only different limiting magnitudes are chosen. Therefore, we calculate the number galaxy overdensity according to Equation 6.1. We have carried out the overdensity calculation for two different limiting magnitudes ($b_J < 17.75$ and < 18.60), in order to examine the effects of mass (presumably) within the collection of galaxies. Next, a comparison area(s) adjacent to the overdense region is required. Though intercluster filaments may/not be embedded within an encompassing sheet-like region (Colberg et al. 2000a), we still expect the overdensity should rise (considerably) within the actual coherent volume when compared to its immediate surroundings.

We begin by calculating the overdensity of the collection for the brighter galaxies, i.e., the 24 (of 52 galaxies) with $b_J < 17.75$. Figure 7.2 shows these galaxies as darker filled circles, while the entire SuperCOSMOS sample of $b_J < 17.75$ galaxies is shown as small open circles. Lighter filled circles are those galaxies with an observed redshift that fall outside of the specified velocity range. The long-dashed lines mark our estimate of the boundaries of the connecting region, and the hatched areas are the adjacent control volumes used for the comparative regional overdensity. Because the adjacent volumes still reside within the HRS, it is possible to find an overdensity of galaxies there also, though presumably not as great as in the region of interest. The three

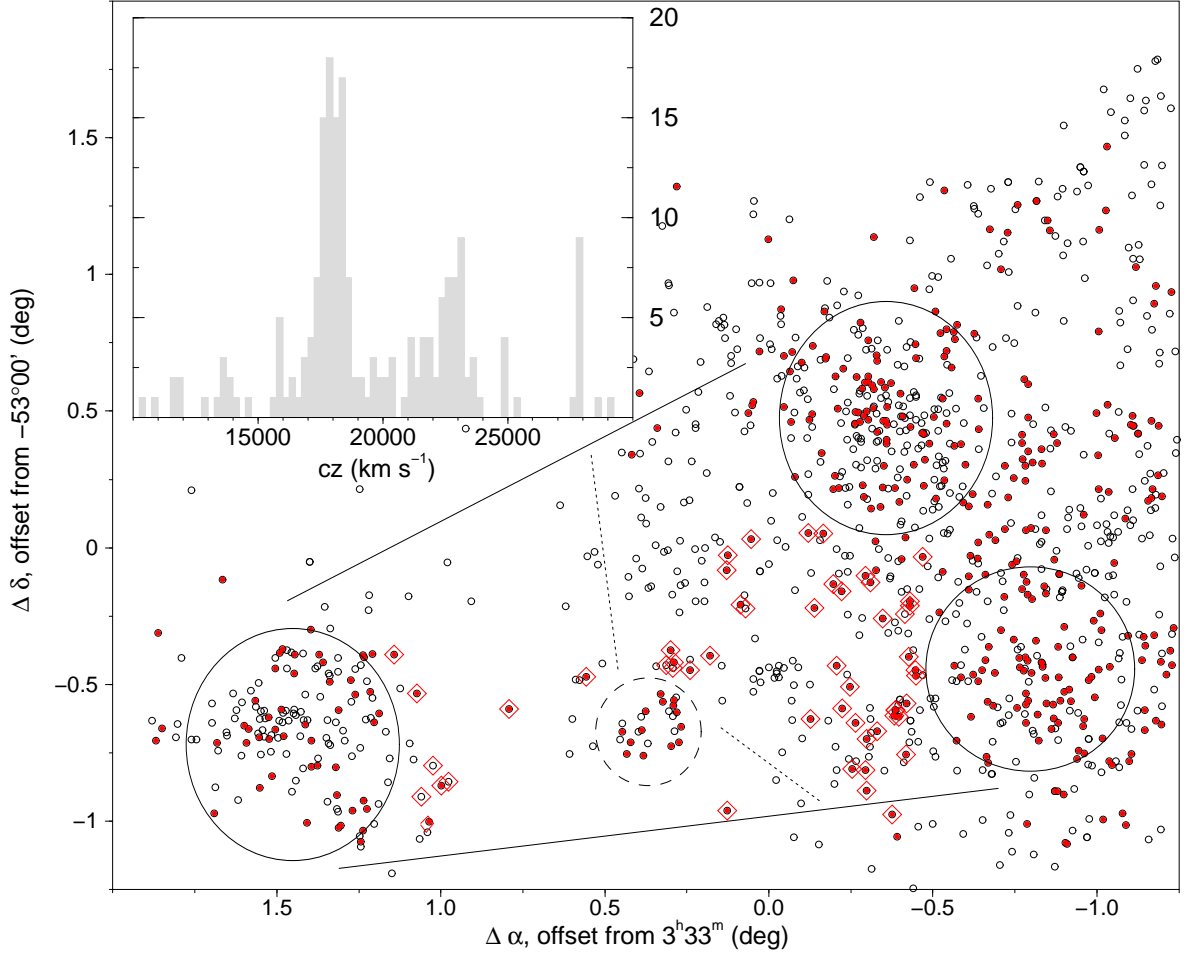


Figure 7.1 Equal-area, sky map of the A3128/3158 region showing all galaxies with an observed redshift in our catalog as small open circles (incomplete, $11.0 \leq b_J \leq 20.5$). The proposed filament area is bound by the solid lines to the north and south, and by the ACO clusters (solid circles) to the east (A3158) and west (A3128/25). APMCC421 is halfway between the ACO clusters and shown with the long-dashed circle. Shown as filled circles are all galaxies in the velocity range, $17,550 \leq cz \leq 18,950 \text{ km s}^{-1}$. Open diamonds show the 52 proposed filament members with $17,250 \leq cz \leq 18,575 \text{ km s}^{-1}$. The figure is offset from $03^{\text{h}}30^{\text{m}}, -53^{\circ}00'$. Dotted lines in the vicinity of AMPCC421 mark the western boundary of the Mathams dataset. The inset velocity histogram contains the observed number counts as a function of redshift for all galaxies in the bridge area (i.e., bound by the solid lines).

areas are comparable in size at $\sim 1.0 \text{ deg}^2$, and the average galaxy density for $17,250 \leq cz \leq 18,575 \text{ km s}^{-1}$ is 1.6 gxs deg^{-2} using the type-specific “ $k + e$ ” corrected curve for the expected galaxy counts (Croton et al. 2005). Though the determination of the areal boundaries is somewhat arbitrary, there is a trade-off between the size and the incompleteness of the area used for the calculation. That is, while a larger area without a galaxy effectively reduces the overdensity, the inclusion of a galaxy for which no redshift exists increases the incompleteness, which effectively increases the overdensity. We have excised APMCC421 (solid circle) from the calculation, and we segment the overdensity calculation due to different values of the observational completeness in the east (0.4 deg^2) and west of APMCC421 (0.6 deg^2).

When defining the galaxy overdensity according to Equation 6.1, we calculate the following average values for the $b_J < 17.75$ end of the connecting region: $\bar{\delta}_{\text{control}} \approx 4$ and $\bar{\delta}_{\text{filament}} \approx 27$. We remark that the control volume overdensities vary significantly between one another (1.3 and 6), where the higher value (south of the extension) is particularly uncertain due to incompleteness ($f \sim 0.15$). Compared to the mean *inter-cluster* overdensity found in Paper I, $\bar{\delta}_{\text{HRS}} = 1.4$, our chosen control average is actually more dense by a factor 3. This is not unexpected since even the control fields lie within regions that were excluded from the overdensity calculation in Paper I, due to their proximity ($\sim 1^\circ$) to a cluster. Alternatively, we find that the overdensity of the connection is almost $20\times$ that of the supercluster and $\sim 7\times$ that of the control volume. If we increase the sample limiting magnitude to $b_J < 18.60$, the overdensity calculations in all volumes are comparable to the brighter limit, with similar completeness in each area. We find that the $\bar{\delta}_{\text{control}} \approx 3$ and the $\bar{\delta}_{\text{filament}} \approx 22$. As before, the control overdensity is twice that of the mean HRS, and the coherent extended collection of galaxies remains $\sim 7\times$ more overdense than our chosen control volumes. CDM halo simulations of intercluster filaments find an average value of $\delta_{\text{CDM}} \sim 7$ for filaments whose intercluster separation is $> 5 h^{-1} \text{ Mpc}$ (Colberg et al. 2005a). When considering the eastern and western halves as separate, the distances are less than this value ($\sim 3.5 h^{-1} \text{ Mpc}$ to both sides of APMCC421), so the CDM overdensity may be better compared against HRS regions further away from rich clusters. We now attempt to utilize individual galaxy

alignments to help determine the direction of the extension, particularly to the western side of APMCC421.

7.2.3 Galaxy Alignments in Intercluster Overdensities

Though the idea that individual galaxy alignments are related to their surrounding environment has been observationally demonstrated in various scenarios (e.g., Binggeli 1982; Fuller et al. 1999), it was not until very recently that the concept was applied to intercluster filaments in Pimbblet (2005). In the cosmic web of hierarchical scenarios, matter (presumably gas, galaxies, and dark) funnels along filaments, and rich galaxy clusters are thought to originate at their intersections (Bond et al. 1996; Colberg et al. 2000a; Kitzbichler & Saurer 2003; Pimbblet 2005). Since theories of galaxy cluster elongation (and their central galaxies as well, see Rhee & Katgert 1987) appeal to a similar mechanism (West & Blakeslee 2000), it is straightforward to apply a similar preferred alignment direction to the proposed members of intercluster filaments. Namely, the bulk motion of the funnel causes the semi-major axis of a galaxy to elongate in that preferred direction (Kitzbichler & Saurer 2003).

Before beginning the orientation calculation, however, it is important to establish whether or not there exists PA biases in the chosen galaxy sample. To demonstrate this, we have taken the Fourier components of the galaxy PAs as given in Struble & Peebles (1985):

$$C_n = \left(\frac{2}{N}\right)^{1/2} \sum_1^N \cos 2n\theta_i \quad (7.1)$$

$$S_n = \left(\frac{2}{N}\right)^{1/2} \sum_1^N \sin 2n\theta_i. \quad (7.2)$$

For an isotropic distribution, i.e., a randomly distributed sample, the samples should have mean = 0 and standard deviation = 1 for integer values of n . We now consider the PAs of the galaxy sample with $b_J < 18.60$ in the A3128/3158 region, which is shown as open circles in Figure 7.3. This sample is chosen because the galaxy numbers are greater (than the $b_J < 17.75$ sample), and the overdensity of the collection was fairly

independent of magnitude. The SuperCOSMOS catalog calculates the PA from the digital measurements of the semi-major and semi-minor axes (Hambly et al. 2001b), and MCF has conducted follow-up calculations for a limited subsample ($\approx 5\%$) to ensure that the PA is given in the traditional east from north fashion.

The first 10 values of n give the following values for C_n and S_n when considering the SuperCOSMOS PAs: $\bar{C}_n = -0.25$, $\sigma_{C_n} = 1.02$; $\bar{S}_n = 0.61$, $\sigma_{S_n} = 1.17$. Furthermore, we find that no value of any single C_n or S_n (nor its σ) is greater than ± 2.1 . When compared with the values in related studies measuring galaxy orientations and alignments (see Struble & Peebles 1985; Plionis et al. 2003; Pimbblet 2005), these values are considered to be consistent with isotropy (e.g., C_n or $S_n \geq 3$ implies systematic directional bias at the 3σ level). As a further test of PA homogeneity, Figure 7.4 (top) shows the fraction of galaxy number counts as a function of PA in histogram form. The 1σ error bars are shown, where all bins should be equal for a completely isotropic distribution ($f_{N_{\text{gx}}} = 0.055$). Since some bins fall outside of the 1σ range and there is an overall tendency for lower numbers at $90^\circ \leq \text{PA} \leq 180^\circ$, we have checked a larger $10^\circ \times 10^\circ$ HRS area of the SuperCOSMOS catalog with $b_J < 17.5$, and it shows no sign of deviation from isotropy of the PAs. The histogram for our larger region covering the inner $10^\circ \times 10^\circ$ of the survey region is shown in Figure 7.4, bottom.

We now introduce a statistical measure of alignment that reliably quantifies the orientation of the position angle (PA) of a galaxy’s semi-major axis with respect to some predefined axis. For the most part, we follow a close adherence to the tests laid out in Plionis et al. (2003) and Pimbblet (2005), which were originated to display the degree of isotropy for BCGs by Struble & Peebles (1985). Consider a sample of N galaxies each with a canonically defined PA, θ_i , where $0^\circ \leq \theta_i \leq 180^\circ$, and some reference axis oriented at a PA of θ_{REF} . In calculating the difference, $\phi_i = |\theta_i - \theta_{\text{REF}}|$, we expect that the average, $\langle \phi_i \rangle$, has the following implications for the sample: $\sim 0^\circ$, the galaxies show perfect alignment to the reference axis; $\sim 45^\circ$, the galaxies display isotropy toward the reference axis; $\sim 90^\circ$, the galaxies are perpendicularly aligned with the reference axis. Since an orientation actually “points” in two directions, then for $\phi_i > 90^\circ$, we subtract ϕ_i from 180° to get the alignment angle for any individual galaxy.

The degree of isotropy for the collection is characterized by the parameter, ϵ , where

$$\epsilon = \sum_i \frac{\phi_i}{N} - 45. \quad (7.3)$$

Therefore, ϵ has the following implications: $\epsilon \approx 0$ indicates the sample is distributed nearly isotropically around the reference axis, $\epsilon < 0$ indicates an alignment of the sample with the reference axis, and $\epsilon > 0$ indicates a misalignment between the sample and the reference axis. The standard deviation of ϵ for the sample is given by

$$\sigma_\epsilon = \frac{90}{(12N)^{1/2}}. \quad (7.4)$$

Now we systematically apply the orientation test above to the previously defined filament volumes. Specifically, the test is applied through the full range of assumed reference axes and a total ϵ is calculated at each assumed PA. The alignment test is carried out for the galaxies with $17,250 \leq cz \leq 18,575 \text{ km s}^{-1}$, including the 52 proposed filament galaxies and 14 confirmed members of APMCC421. Figure 7.5 shows the individual volumes for which the alignment is calculated, where intercluster regions are enclosed by long-dashed lines and clusters with solid circles. The numbers and arrows within the areas are associated with the alignment results in Figure 7.6. Specifically, the length of the arrows in Figure 7.5 correspond to the relative strength of the alignment signal in Figure 7.6, where regions 3 and 6 show $\sim 1\sigma$ results. By pre-defining these areas, we deviate slightly from the prescription of Pimbblet (2005), because we are using the *a priori* redshift information to define the filament. Since the orientation of galaxy PAs is proposed as a stand-alone test for intercluster filament detection, it should serve as a confirmation test for the structures previously identified using the spectroscopic information.

Figure 7.6 shows the alignment parameter, ϵ , for the galaxies associated with the filament (i.e., intercluster galaxies with $17,250 \leq cz \leq 18,575 \text{ km s}^{-1}$) as a function of the assumed PA of the reference axis. The numbers in the upper right-hand corner of each individual plot correspond to the numbered regions in Figure 7.5, where the red symbols are associated with galaxy clusters. 1σ error bars are shown for each alignment

calculation according to Equation 7.4. The numbers in the bottom right-hand corner of each plot give the number of galaxies for which the alignment was calculated. Any sample of galaxies displays a preferred alignment with the reference axis when its $\epsilon < 0$.

In examination of the results shown in Figure 7.6, 4 of the 8 specified regions show a preferred orientation $> 1\sigma$. Two other regions (“2” and “5”) have $\epsilon < 0$, but at less than 1σ level. With the exception of APMCC421 (PA $\approx 140^\circ$), the remaining 4 volumes (4, 5, 7, and 8) have similar preferred alignments between 65 – 85° . More specifically, the east region and APMCC421 show alignments greater than 90° , while all regions west of APMCC421 (except A3128) have alignments of $< 90^\circ$. To highlight this fact, we combine the samples to the west of APMCC421 (4, 5, 7, and 8) and apply the correlation test to the conglomerate. Figure 7.7 shows the results, where a $> 3\sigma$ alignment at PA $\approx 70^\circ$ is obtained when A3125 is included (bottom). Even though the correlation is not significant for either ACO rich cluster (3128 or 3158), the spatially confined sample of galaxies having a significant overdensity also shows a significant ($> 3\sigma$) alignment signal at $\sim 70^\circ$ for the region to the west of APMCC421. In summary, while there may be a splitting/flattening of the filament region to the west of APMCC421, we note these galaxies do *not* show a preferential alignment toward the core of the richer cluster A3128 (e.g., PA ≈ 135 deg).

7.2.4 Summary

From the original assertions of L83, a sample of ~ 65 galaxies is found between the two richest cluster complexes in the southern HRS (A3158 and A3128/25), which is ~ 11 Mpc in projection. This includes the non-rich galaxy cluster APMCC421, which is situated approximately halfway between the richer ACO clusters. The sample of 52 intercluster galaxies has the following dynamical properties as determined by the biweight estimator (see §4.1): $\overline{cz}_{\text{los}} = 18,000 \pm 50 \text{ km s}^{-1}$, $\sigma_{\text{los}} = 350 \text{ km s}^{-1}$. The spatial confinement of the collection is ~ 2 Mpc to the east of APMCC421 and ~ 4 Mpc to the west. The mean overdensity of the sample, $\bar{\delta} \approx 25$, is $7\times$ greater than the adjacent control volumes and $15\times$ greater than the mean HRS overdensity from Paper

I. Moreover, we find that subset of these galaxies to the west of APMCC421 displays a significant preferred alignment ($> 3\sigma$) of their semi-major axes at $\approx 70^\circ$, as shown in Figure 7.5. We note this orientation is not directed toward the center of A3128, but rather these galaxies have an orientation more closely associated with A3125. While the richest clusters seem to give an orientation most closely associated with an isotropic arrangement, the general alignment of the galaxies within the intercluster portions follows the defined direction from the redshift information alone.

7.3 A3128/3125: A Preferred Axis for Merging Clusters

7.3.1 Overview

In light of the findings in the previous section that galaxies in the bridge between A3158 and A3125/28 show an alignment of their PAs along the bridge, it is logical to briefly examine the double cluster system, A3128/3125. A highly dynamic state was concluded for this system by RGC02, with A3125 in a partially disrupted condition after suffering a tidal passage through A3128 along a northeast-southwest axis. This was primarily established through the analytical synthesis of X-ray imaging and 2dF optical spectroscopy. Specifically, the twin-peaked morphology of the smoothed Chandra X-ray image of A3128 (20ks, ACIS-1) is elongated in the same direction as the spatial axis connecting the two clusters ($\text{PA} \approx 50^\circ$). However, distinctly different timescales were derived for these two features implying that multiple merging events occurred along a preferred axis. This type of repeated dynamical activity along a similar axis is supported by other observational studies citing that the flow of matter follows the filamentary nature of large-scale structure (e.g., West & Blakeslee 2000; Cortese et al. 2004). Another pertinent result of the RGC02 study is the statistical identification of several distinct substructures in the region, proposed as infalling groups and filaments that have passed through the dynamic cluster environment. Specifically, the inference was made that the large gravitational potential of the HRS accelerated the infall velocities of groups in the

region.

Because several new spectroscopic observations also encompass A3128/25, the *intra*-cluster region in this area is examined in three specific ways. Here, we are interested primarily in examining more finely scaled structure (< 7 Mpc) as it relates to the A3128/25 northeast-southwest axis. Figure 7.8 shows galaxies with known velocity between $16,500\text{--}20,500 \text{ km s}^{-1}$ (i.e., confirmed members of the A3128/25 complex by RGC02) and $b_J < 18.60$ for the 6 deg^2 covering the A3128/25 double cluster system. The map is approximately 90% complete to this magnitude. The orange diamonds mark the two X-ray peaks in A3128 imaged with Chandra. The numbered areas mark specific locations of interest in this section: (1) the smoothed galaxy distribution as it relates to the less-rich cluster APMCC399 ($z = 0.060$, where the number “1” marks the center, Dalton et al. 1994, 1997, hereafter DEMS94); (2) re-examination of groups and filaments found in A3125 by RGC02, in light of the orientation tests defined above, new redshift information, and extended radio emission from two host galaxies; and (3) the confirmation of a compact group of galaxies in A3128.

7.3.2 APMCC399 + A3128/25: An Axis?

Given the dispersed appearance of A3125, its similar mean velocity to A3128, as well as the association of A3125’s post-passage condition with N-body simulations (Caldwell & Rose 1997), we examine more closely the distribution of galaxies between these two clusters. Specifically, with a nearly complete sample of 382 relatively faint galaxies (90% down to $b_J < 18.60$), further structure in the connecting region between A3128/3125 is seen. Though the cluster-finding algorithm in DEMS94 locates a cluster, APMCC399, approximately halfway between A3128/25 with the same redshift as A3128/25, the mean cluster redshift is based on only two galaxies. First, we collect all galaxies within a radius of $0.5 R_{\text{ABELL}}$ ($15'$) of the published center in DEMS94, and then apply the biweight estimator. We have taken a relatively small cluster radius for two reasons; we did not want to overlap with the adjacent clusters, and this is the same radius is used in DEMS94. The 13 galaxies (of 19 observed) found to be members of APMCC399 have

the following properties: $cz_{\text{los}} = 18,050 \pm 50 \text{ km s}^{-1}$, $\sigma_{\text{los}} = 175 \text{ km s}^{-1}$. As previously found by DEMS94, the mean velocity is quite consistent with the more massive A3128 ($17,950 \text{ km s}^{-1}$, 850 km s^{-1}) and A3125 ($17,675 \text{ km s}^{-1}$, 400 km s^{-1}), but the dispersion seems quite narrow for even a non-rich cluster (see §4.1).

Having confirmed that a low-richness cluster is situated between A3128 and A3125, we smooth the HRS galaxy distribution using the following method. The $2^{\circ}0 \times 3^{\circ}0$ area in Figure 7.8 is gridded into square bins, and the galaxies are summed for each cell. A Gaussian kernel with constant smoothing radius of $0^{\circ}25$ ($\sim 1 \text{ Mpc}$) is applied to each bin successively, and then the relative contributions are summed. Other smoothing radii were attempted, and a relative balance between substructure was sought out. Therefore, a continuous galaxy density map is produced, which is then contoured at 10% intervals. Figure 7.9 presents the smoothed map of the A3128/25 region, where darker contours indicate denser regions. Although the map appears to be rich with substructure, we make three points regarding the overall galaxy distribution. First, the less-rich APMCC399 cluster does connect the A3128/25 complex on a similar axis to that of the X-ray peaks and the arrangement of the ACO clusters. Second, it does not appear that the connection would fall into the class of “straight filament” as determined by previous authors (Pimbblet et al. 2004b; Colberg et al. 2005a), since the main chain with A3128–APMCC399 seems to bend to include A3125. Third, A3125 seems to sit at the intersection of the A3128/25 connection and the coherent connection between A3158 and A3125 discovered in the previous section, as does APMCC399 to a lesser degree. Furthermore, apparently the same connection between A3158–A3125 extends $\sim 4 \text{ Mpc}$ (1°) to the west of A3125.

7.3.3 A3125: A Crossroad?

It is the dispersed nature of A3125, recognized in previous studies (Dressler 1980; Lucey et al. 1983; Caldwell & Rose 1997), that provides an interesting opportunity to examine the possible alignment orientation of galaxies from apparently different populations. Armed with the knowledge that A3125 is found above to be associated

with two different connections to other clusters (A3158 to the west and A3128 to the north), we show in Figure 7.10 the spatial and kinematic distribution of faint galaxies within the inner ~ 2 Mpc ($0.5R_{\text{ABELL}}$) of A3125. All galaxies with $b_J < 19.0$ are shown as open circles, with the 177 observed galaxies ($\sim 75\%$) completeness shown as dark open circles. We also highlight two primary groupings of galaxies that populate this region; a lower redshift grouping (filled blue) that is consistent with the bridge from A3158 discussed in §7.2.1 ($17,250\text{--}18,575 \text{ km s}^{-1}$), and a higher redshift conglomeration (red) associated with the G2/F2 (i.e., group designation in RGC02, $18,600\text{--}20,000 \text{ km s}^{-1}$). The Figure is offset from the published spatial center of $03^{\text{h}}27^{\text{m}}4, -53^{\circ}30'$ (Caldwell & Rose 1997). The velocity histogram is shown as the inset portion of the Figure, where the color coding corresponds to the spatial map. However by reducing the cluster radius that defines the sample, the velocity distribution shifts toward a more even population of galaxies for the two groups (i.e., the high redshift galaxy grouping is concentrated toward the center of the cluster). For example, at a radius of $10'$ (inner circle in Fig. 7.10), the number of members is equal in the two groupings. Since the slight spatial elongation of the high-redshift grouping coincides with the approximate orientation of the connection with A3128/APMCC399 ($\text{PA} \approx 0^\circ$), there is added justification to the idea that the G2/F2 conglomeration is infalling along the A3128–APMCC399–A3125 axis.

We now draw attention to the two open diamonds (magenta) in Figure 7.10, located very near the spatial center of A3125 ($r_{\text{PROJECTED}} < 2'$). These diamonds represent two powerful ($> 200 \text{ mJy}$), extended (tailed) radio sources each associated with an optical galaxy counterpart (see details in Johnston-Hollitt et al. 2004). The ATCA 20cm radio-continuum map of the area surrounding these sources is presented in Figure 7.11 and shows in detail the nature of jet bending within both tails. Such tailed emission is thought to result from the bulk motions of the intra-cluster medium (ICM), on the order of 1000 km s^{-1} (Gomez et al. 1997; Sakelliou & Merrifield 2000), and possibly combined in part with individual motion of the host galaxy (Klamer et al. 2004). As can be seen from Figure 7.10, the galaxies hosting these sources greatly differ in redshift space ($\sim 1500 \text{ km s}^{-1}$) though only separated by 0.25 Mpc as projected on the sky. Furthermore,

the projected PAs of the tailed emission approximately align with their respective optical associations. That is, the west radio tail with a PA near 5° is associated with the high velocity group slightly elongated along the north-south axis. Moreover, the eastern radio tail has a velocity consistent with the A3158–A3125 conglomeration and a PA closer to 90° , which is more similar to the alignment of those galaxies found in Figure 7.7. Therefore, this situation presents an ideal opportunity to test the alignment of the PAs of the member galaxies with their presumed larger scale structure (in this case, filaments), which would further substantiate the findings from the redshift information and radio emission.

We again employ the alignment techniques discussed in §7.2.3 to examine the orientation of the galaxies in the high velocity group with their presumed parent filament. By looking at the smoothed galaxy distribution between A3128 and A3125 in Figure 7.9, it appears that the preferred PA for the A3125 grouping should be near $0/180^\circ$ if alignments are indicative of their originating infall axis. Figure 7.12 shows the results of alignment testing for the high velocity (red) and primary filament (blue) groupings. We find that both the high velocity (red) and primary filament (blue) groups show a preferred galaxy alignment at the $\sim 2\sigma$ level (2.1σ for the high velocity group and 2.4σ for the primary filament). However, the PA of the preferred axis, rather than being orthogonal, are at similar orientations, PA $\sim 30^\circ$ for high-velocity group and $\sim 40\text{--}70^\circ$ for the low-velocity group. Therefore, the idea that the galaxies align with the direction of the filaments is not supported by our analysis.

To verify our visual examination of the A3125 region with quantitative consistency, we apply the same overdensity tests as in §7.2.2 to the volume to the *west* of the cluster. The 4 Mpc protrusion extends to the northwest in Figure 7.9 from the A3125 core up to APMCC391. APMCC391 is another less-rich cluster, which is actually found to be two overlapping conglomerations in projection at $\sim 18,000$ and $\sim 23,000 \text{ km s}^{-1}$ (see Tab. 5.1). It is located to the northwest of A3125 and approximately due west from APMCC399 (“4” in Fig. 7.9). Since the velocity range plotted in the smoothed map is much larger than the $17,250\text{--}18,575 \text{ km s}^{-1}$ filament range, we ensure that the galaxies contained therein have the same velocity range as the collection to the *east* from §7.2.2.

After taking two parallel 0.25 deg^2 rectangular strips (with the control volume to the north), we calculate an overdensity of $\bar{\delta}_{\text{filament}} \approx 60$ for the extension between A3125-APMCC391, which is compared to $\delta_{\text{control}} \approx 3$ (1 galaxy observed in the control field compared to 22 in the extension with similar completeness and area). Furthermore, the overdensity along the extension axis is fairly constant up to and including APMCC391. Knowing further that the region overlaps with a concentration of galaxies at $22,800 \text{ km s}^{-1}$, it is not certain that APMCC391 could be considered an actual cluster. We also note that there is a small redshift gradient as a function of projected spatial position, in that, the average velocity increases by 700 km s^{-1} along the 4 Mpc extension from A3125 ($17,750 \text{ km s}^{-1}$) to APMCC391 ($18,300 \text{ km s}^{-1}$). Including the “members” of APMCC391 and when compared to the eastern portion of the filament, the 30 galaxies within this extension have a slightly lower $\overline{cz}_{\text{los}}$ ($= 17,825 \text{ km s}^{-1}$) and σ_{los} ($= 325 \text{ km s}^{-1}$). No significant galaxy orientation alignment is seen in the western extension. In short, the available data indicate that the A3158–A3125 axis extends a total projected distance of $\sim 16 \text{ Mpc}$, beginning at A3158 and extending $\sim 4 \text{ Mpc}$ to the west of A3125. Hence, we conclude that A3125 is situated at the near perpendicular intersection of elongated overdensities, which are confined into filaments. We re-iterate that according to CDM conclusions of hierarchical formation models, it is the *richer* clusters that show more preference for location at filament intersections (e.g., Colberg et al. 1999), while A3125 is less-rich than A3128.

7.3.4 A3128: Mixed Signals?

We now turn northward to the more massive A3128, by a factor of 4 in numbers, when compared to A3125. Specifically, we examine suspected infalling groups and filaments defined by RGC02. According to some current theories of structure formation, the infalling population of galaxies should have an imprint of the parent filament from which they came (e.g., Novikov et al. 1999; Plionis & Basilakos 2002; Kitzbichler & Saurer 2003, see laminar flow model). We were not successful in detecting this imprint in A3125, if in fact, the high-velocity group is a remnant of the perpendicular parent

filament, so we now turn to the two major groups in A3128 defined by RGC02. We also show that within the assumed dynamic turbulence of this cluster, there is room for a compact galaxy group, normally associated with more quiescent environments. Finally, the question is raised whether these populations could have originated outside the A3128 complex.

Galaxy Orientations

The galaxy orientation alignment tests are now applied to the pre-defined groups and filaments by RGC02, specifically G1 and F1 in A3128. From Figure 7.9, the smoothed galaxy map definitely shows the outer periphery of A3128 to be non-uniform. Particularly to the north, there are approximately perpendicular protrusions of galaxy density at PAs of $\sim 50^\circ$ and $\sim 135^\circ$. We further note the PA of the X-ray peaks in A3128 (orange diamonds in Fig. 7.9) is near 45° and parallel to the northeast nodule. Figure 7.13 shows the 53 galaxies in A3128 associated with G1 (green open circles) and F1 (red filled squares) as defined in RGC02. These galaxies cover the velocity range from 18,600–20,500 km s^{-1} , with A3128-G1 occupying the lower velocity end at 18,600–19,400 km s^{-1} . We note the X-ray peaks in A3128 shown as orange diamonds in both Figures, which serve as a reference point to the larger-scale landscape in Figure 7.9. Since the spatial arrangement of these groups seems to correspond to the structure in the smoothed galaxy distribution on larger scales, these kinematic associations provide an opportunity to test the strength of the galaxy-substructure alignment. Specifically, do the RGC02-defined G1 and F1 show alignment with the noticeable protrusions in the A3128 periphery?

After subjecting the kinematically-defined groups to the orientation tests used in the previous sections, we do not find a clear correlation between the axial directions of larger-scale features (e.g., the protrusions in the A3128 galaxy distributions) and the individual galaxies that populate them. Specifically, A3128-G1 gives a 2σ result for a PA $\approx 25^\circ$, and A3128-F1 gives no clear result. Even when considering the mildly significant alignment of A3128-G1, it appears to be uncorrelated with the projected spatial arrangement of the galaxies. That is, A3128-G1 is arguably more elongated

toward the northwest-southeast direction, while a $PA = 25^\circ$ is nearly perpendicular to that direction. Therefore, it is unclear how the arrangement of subsamples of cluster galaxies correspond to their surrounding large-scale environment.

Southwest Compact Galaxy Group

In further examination of the smaller-scale structure in A3128, we focus our attention on a spatially compact group (CG) of galaxies very near the southwest X-ray core. RGC02 also notices this group and speculates on its relative connection to the hot X-ray gas, suggesting that the southwest CG (SWCG) is a portion of an infalling substructure on its initial passage into the cluster core. Spectroscopic observations of all potential group members are reviewed in §2.7, and we test against the outlined criteria for Hickson CGs (HCG, Hickson et al. 1992; Hickson 1997). According to the following formal definition, any HCG satisfies these criteria (all magnitudes in b_J): i) membership— $N_{\text{gx}} \geq 4$, whose optical magnitudes differ by less than 3; ii) isolation—no galaxy less than 3 magnitudes fainter than the brightest member can be present within 3 radii of the center of a circle enclosing the geometrical centers of all CG members; and iii) compactness— $\mu < 26$ mags arcs $^{-2}$ within the smallest circle enclosing the geometrical centers of all CG members. We examine Figure 7.14 in light of the above criteria for HCG inclusion. Regarding group membership, Galaxies P (15.50) and W (18.50) provide the largest possible difference, but the optical magnitude of W is not well-known because SuperCOSMOS does not resolve galaxies V and W. Therefore, the greatest difference between the remaining six members is 2.33 magnitudes (P and T). When considering the larger circle in Figure 7.14 that marks 3 times the radius of the smaller, all three galaxies appearing within this circle—G (19.21), H (19.15), and I (19.70)—are > 3 mags from brightest member P (15.50). To measure μ from the smaller circle in the Figure, a grid was marked out in $10'' \times 10''$ squares (about the extent of one galaxy with $b_J = 16.0$), and each grid square was assigned an average optical magnitude, b_J . The background sky was measured, and the optical magnitudes of the galaxies were known. From this calculation, the average μ was ~ 21.7 mags arcs $^{-2}$, which fits well below the required 26. Therefore, according to the requirements (outlined below), the

SWCG does meet the primarily spatial criteria and can confidently be labeled a HCG. This fact is quite remarkable considering that A3128 is a cluster of Richness = 3, and therefore richer than 95% of all other clusters.

Even though the redshifts of the newly-established HCG and the diffuse X-ray peak are in good agreement, there are some difficulties with the dynamical interpretation by associating them with one another. Specifically, the X-ray temperature of the diffuse emission centered upon Galaxy P at 3.3 keV coincides more with cluster values than those reported temperatures for HCGs (cf., Fig. 5, Hickson 1997). In contrast, the β value for the surface brightness profile of the diffuse emission (~ 0.3) is consistent with the majority of HCGs. When considering the group’s kinematic properties, a velocity dispersion of 495 km s^{-1} for the A3128 SWCG pushes the extreme range for elliptically-dominated HCGs ($< 5\%$ in Fig. 3, Hickson 1997). However, the velocity dispersion from the SWCG fits nicely with the virialized velocity dispersion of the SW X-ray peak derived from the Chandra observations of RGC02 ($\sim 425 \text{ km s}^{-1}$). The similar velocity dispersions, combined with the common understanding that HCGs are associated with loose groups (Vennik et al. 1993; Ramella et al. 1994), favor the view that the SW X-peak is associated with an in-falling group, in which the HCG resides (see also §6.4.4, in RGC02).

7.4 Summary: Overdensities

From a combination of previous studies of the HRS (in L83 and RGC02) with an expanded dataset of redshifts, we examine the intercluster environment as it relates to finer scale substructure, in and around the galaxy cluster complexes of A3158–A3128–A3125. We define an 11 Mpc intercluster filament that maintains a projected spatial width of ~ 3 Mpc from the rich cluster A3158 to the A3128/A3125 complex. The galaxies within this filament have the following kinematic properties: $\overline{cz}_{\text{los}} = 18,000 \pm 50 \text{ km s}^{-1}$, $\sigma_{\text{los}} = 350 \text{ km s}^{-1}$. With an average overdensity, $\bar{\delta}$, of ≈ 25 , we find that this confined filament is $7\times$ more dense than adjacent control volumes. Furthermore, we show that there is preferred alignment of this filament at the 3σ level with an $\bar{\epsilon} \approx 75^\circ$ *only* when

the less-rich A3125 is incorporated. This finding corroborates with the smoothed galaxy distribution, which shows the filament to extend 4 Mpc to the west of A3125, to give a total filament length of ~ 16 Mpc. The western end of the filament increases in overdensity to $\bar{\delta} \approx 60$. We find that A3125 sits at the “crossroads” of two intercluster filaments, since the smoothed galaxy distribution shows a clearly cluster chain from A3128, through APMCC399, to A3125. We note that it is the less-rich A3125 that seems to sit at the intersection of intercluster filaments and not the more rich A3128.

We use the presence of intersecting filaments in A3125 to explain the odd arrangement of substructure near its core. The velocity histogram of the galaxies closest to the cluster core is equally split among members whose velocity is synonymous with the A3158–A3125 filament and the high velocity component (red in Fig. 7.13) of 1600 km s^{-1} . Because the slight projected spatial elongation of the component coincides with the approximate entry PA of the A3128–A3125 filament *and* the projected PA of extended radio emission in one of its members, an alignment along the apparent infall orientation axis within this group seemed likely. We found, however, that the galaxy orientation test for alignment with a preferred axis, which helped confirm the general direction of the filament between A3158–A3125/28, did *not* provide consistent confirmation when applied to galaxy groups. This was observed for groups in both A3128 and A3125, where spatially projected substructure and kinematic information was indicative that such an alignment could exist.

Lastly, two observations were made regarding the nature of galaxy clusters as it relates to their richness and the assumption of dynamic equilibrium (virialization). First, the $\bar{\delta}$ value in the APMCC391 “cluster” core is very similar to that throughout the extension connecting it to A3125 ($\bar{\delta} \sim 60$). When connected with the information that APMCC391 consists of an overlapping projection of two coherent structures at $18,500$ and $23,250 \text{ km s}^{-1}$, it calls into question the existence of an actual “cluster.” Second, we find evidence for a compact galaxy group residing in A3128’s core that meets the criteria of Hickson (1997). While we do concur with the speculation of RGC02 that the SWCG is associated with infall, the richest cluster in the HRS displays an extremely interesting oddity that further complicates the virialized state of even the

richest clusters.

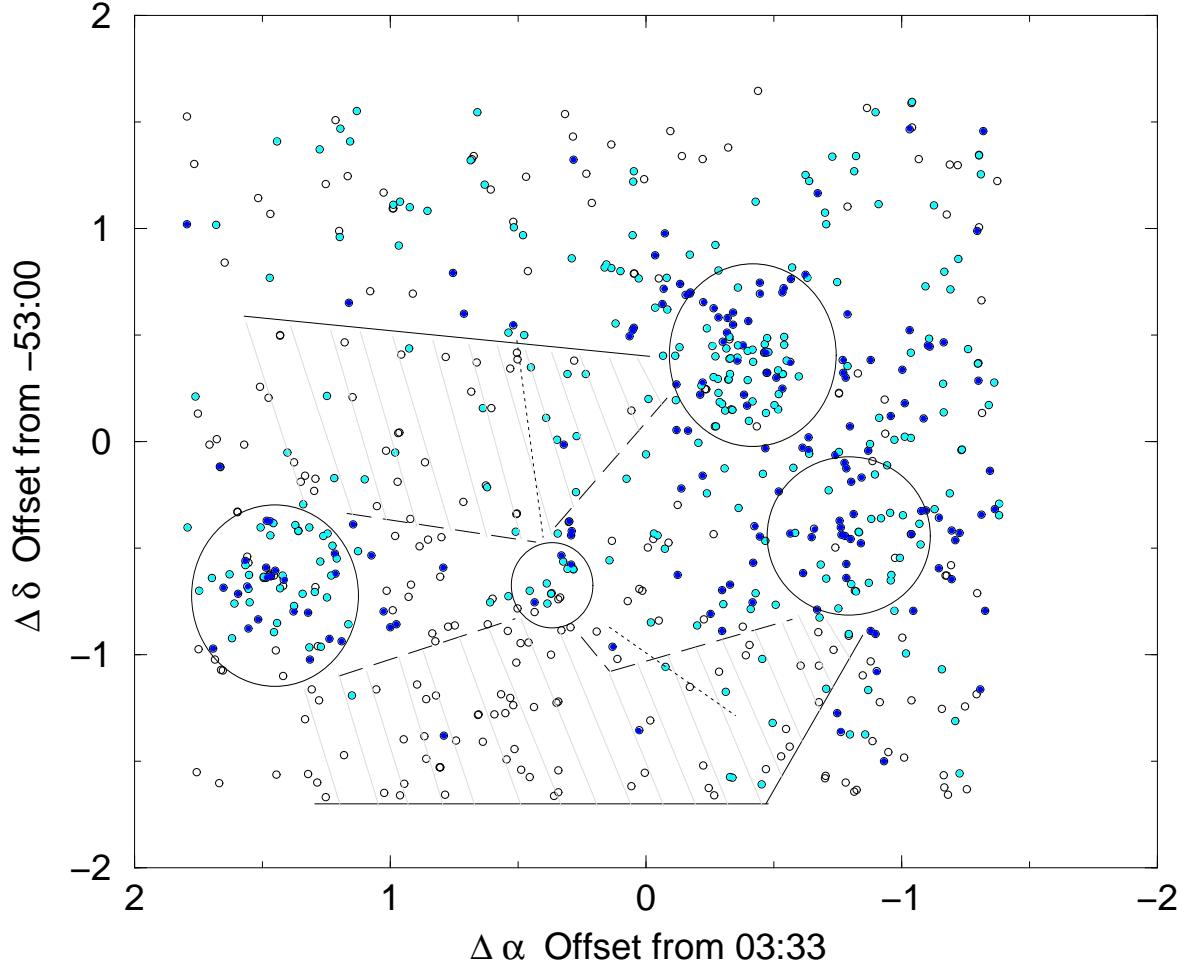


Figure 7.2 A3128/3158 spatial map showing all SuperCOSMOS galaxies with $b_J \leq 17.75$ as small open circles. Lighter filled circles mark galaxies for which a redshift has been determined, and darker filled galaxies mark those with $17,250 \leq cz \leq 18,575 \text{ km s}^{-1}$. The long-dashed lines mark the connected extension area, while the hatched areas mark the two comparison control volumes. Larger open circles and dotted lines are the same as indicated in Fig. 7.1.

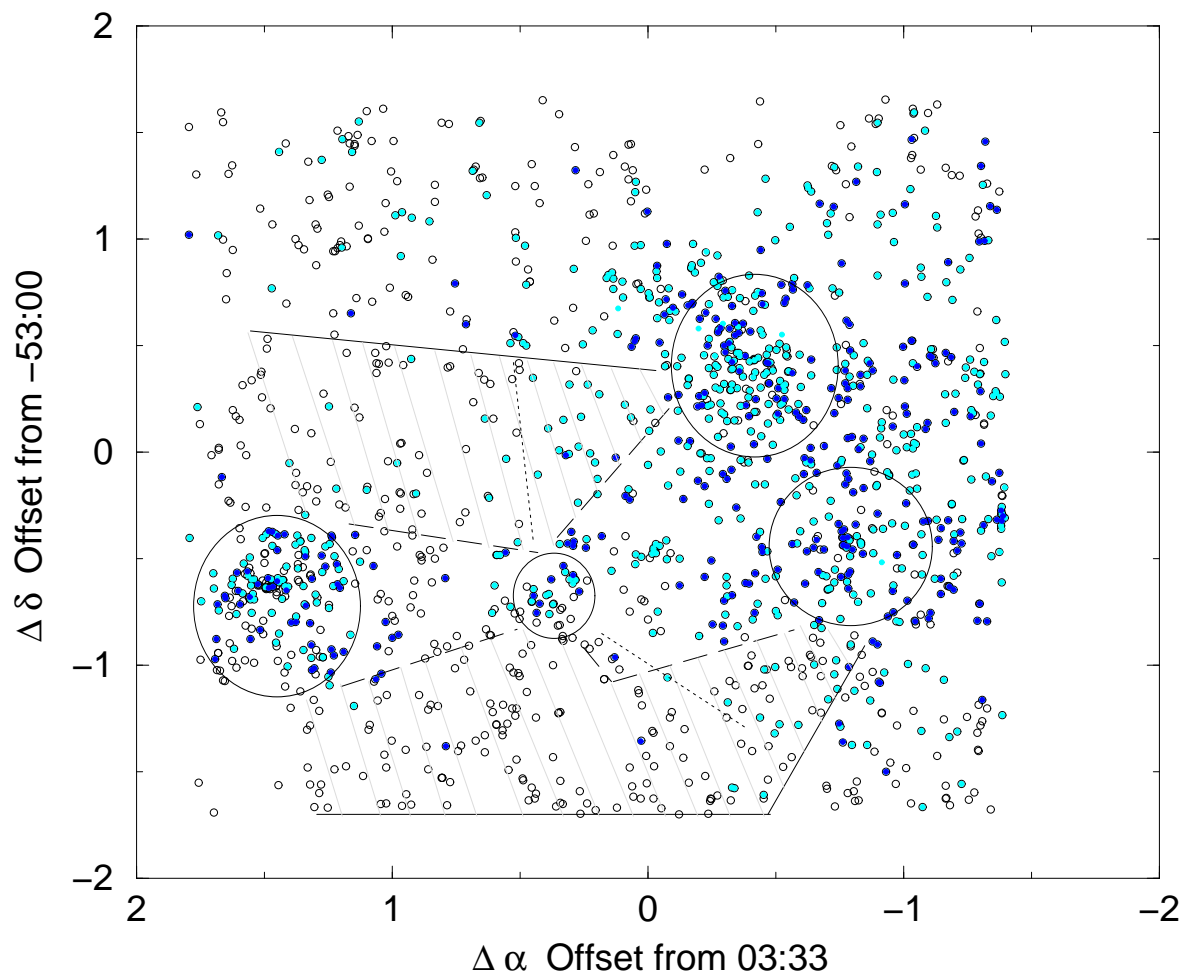


Figure 7.3 A3128/3158 spatial map showing all SuperCOSMOS galaxies with $b_J \leq 18.60$ as small open circles. All symbols are the same as those in Fig. 7.2.

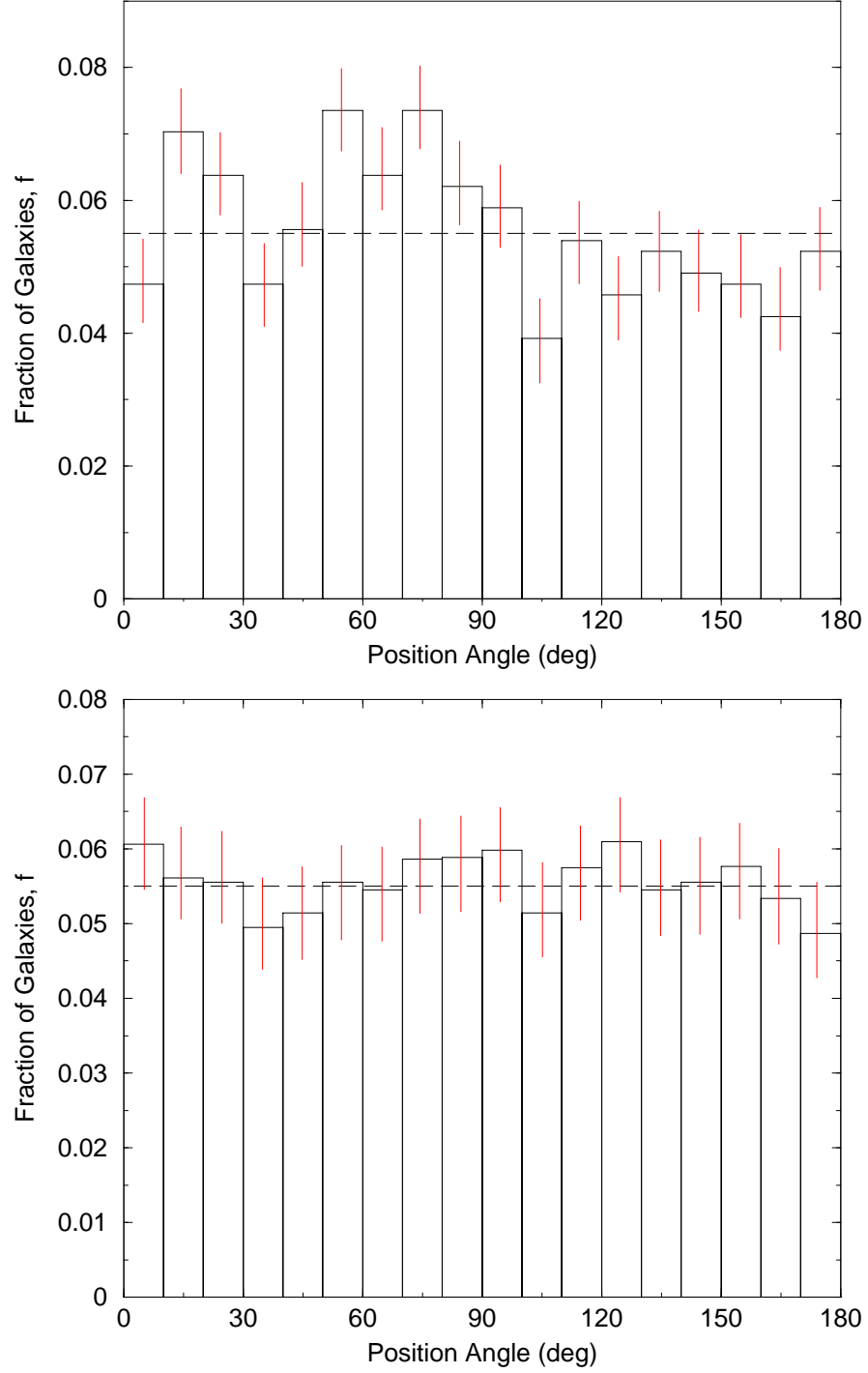


Figure 7.4 Fractional number of galaxies with $b_J < 18.60$ as a function of PA. **Top:** the 3.0×3.0 area in Fig. 7.3. 1σ error bars are shown and do *not* encompass the mean value of $f = 0.055$ for all bins. **Bottom:** 10.0×10.0 area within the HRS to confirm the isotropy of the entire sample. Notice that all 1σ error bars are within the mean value of f consistent with isotropy.

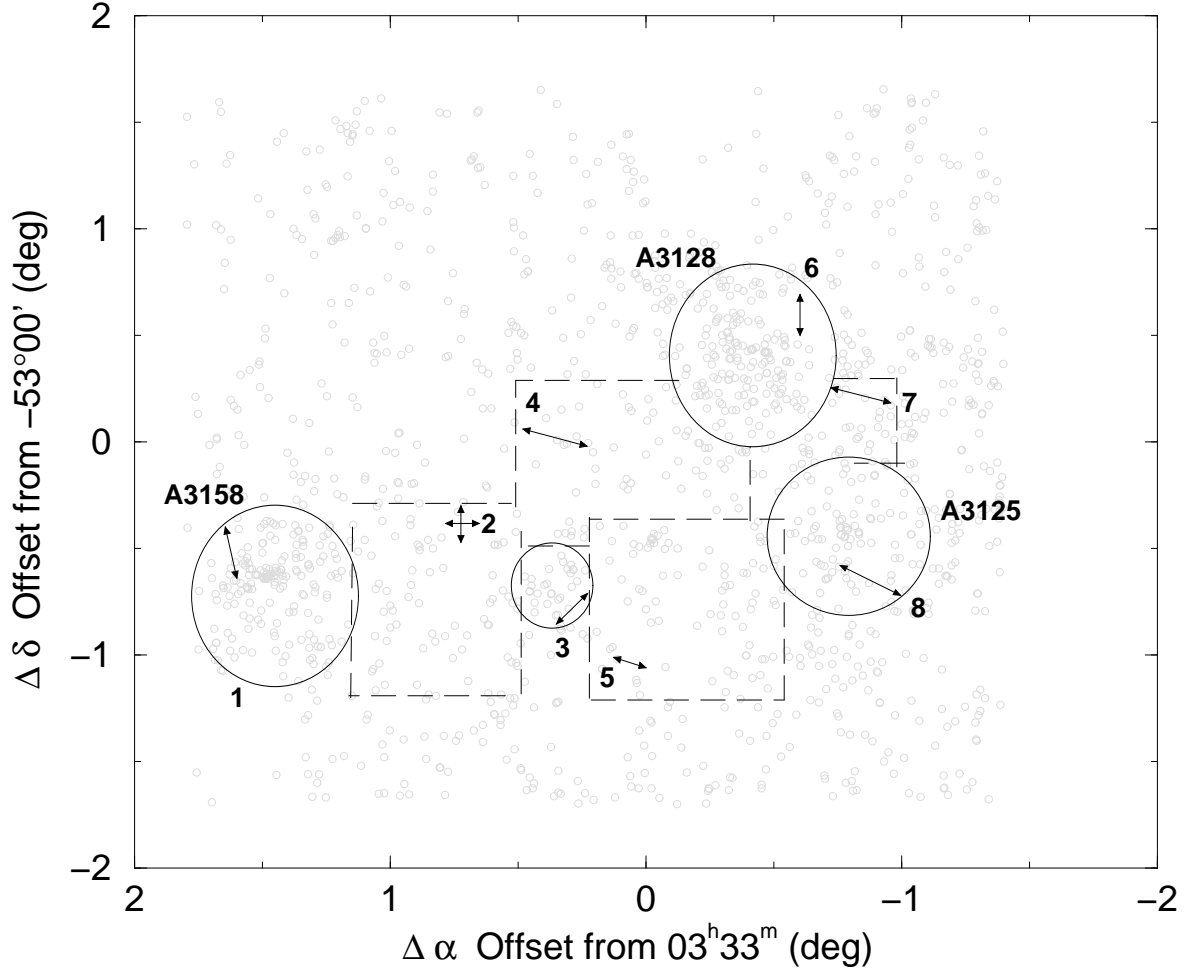


Figure 7.5 A3128/58 spatial map displaying the different areas for which the orientation test was completed. The galaxy clusters are shown as large open circles, while the intercluster areas are enclosed by long-dashed lines. Each area is numbered and corresponds to an $\epsilon - \text{PA}$ plot in Fig. 7.6. The arrows within the numbered regions indicate the directional alignments given by $\min(\epsilon)$ also in the same Fig., and their lengths correspond to the relative strength of the ϵ . SuperCOSMOS galaxies with $b_J < 18.60$ are shown in the background as small open circles. The richest clusters in the region (A3158 and A3128) do *not* show a preferred orientation for this velocity range, 17,250 – 18,575 km s⁻¹.

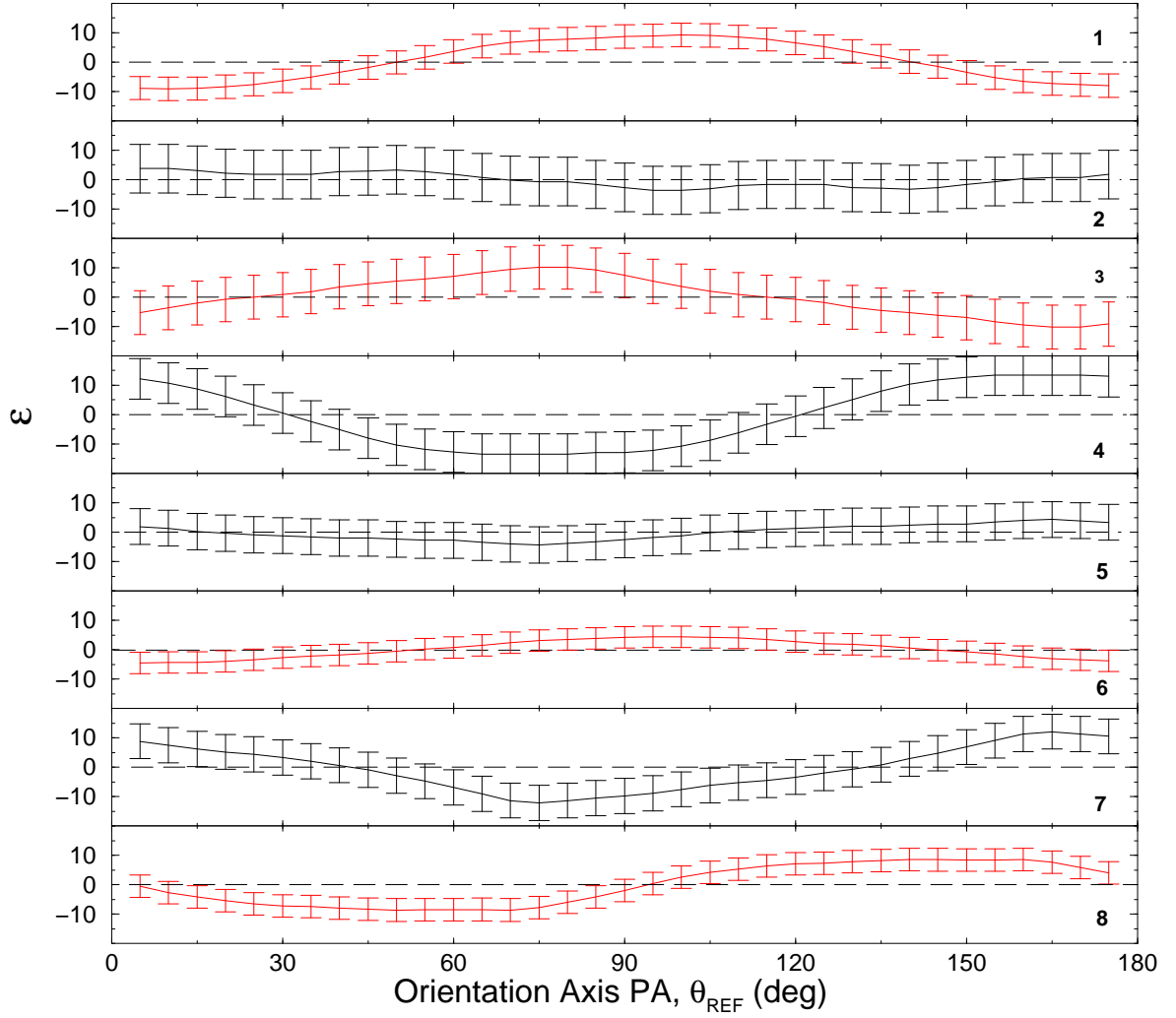


Figure 7.6 Orientation parameter, ϵ , as a function of PA for the galaxies within the range, $17,250 \leq cz \leq 18,575 \text{ km s}^{-1}$ that populate the sub-volumes in the A3128/58 region. The 1σ error bars are included, and the numbers in the lower right-hand corner correspond to the numbers in Fig. 7.5. The cluster alignment diagrams are shown as gray (red), and horizontal long-dashed lines mark an $\epsilon = 0$, which is the value for isotropy.

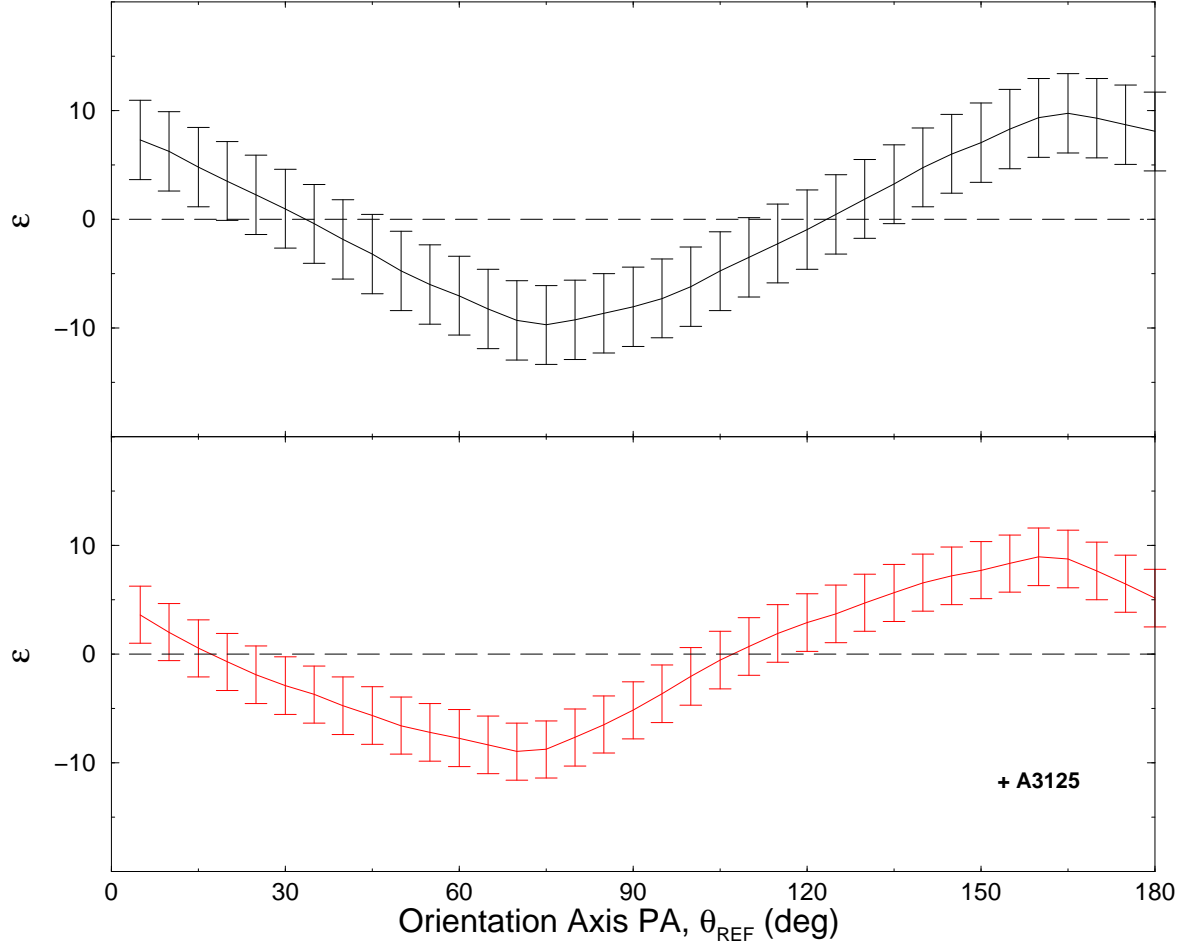


Figure 7.7 Orientation parameter, ϵ , as a function of PA for galaxies within the range, $17,250 \leq cz \leq 18,575 \text{ km s}^{-1}$ for the A3128/58 region. Here, the individual volumes in Fig. 7.6 are stacked for better number statistics. The 1σ error bars are included. The bottom plot includes the cluster A3125 and gives a 3σ orientation at 70° . Horizontal long-dashed lines mark an $\epsilon = 0$.

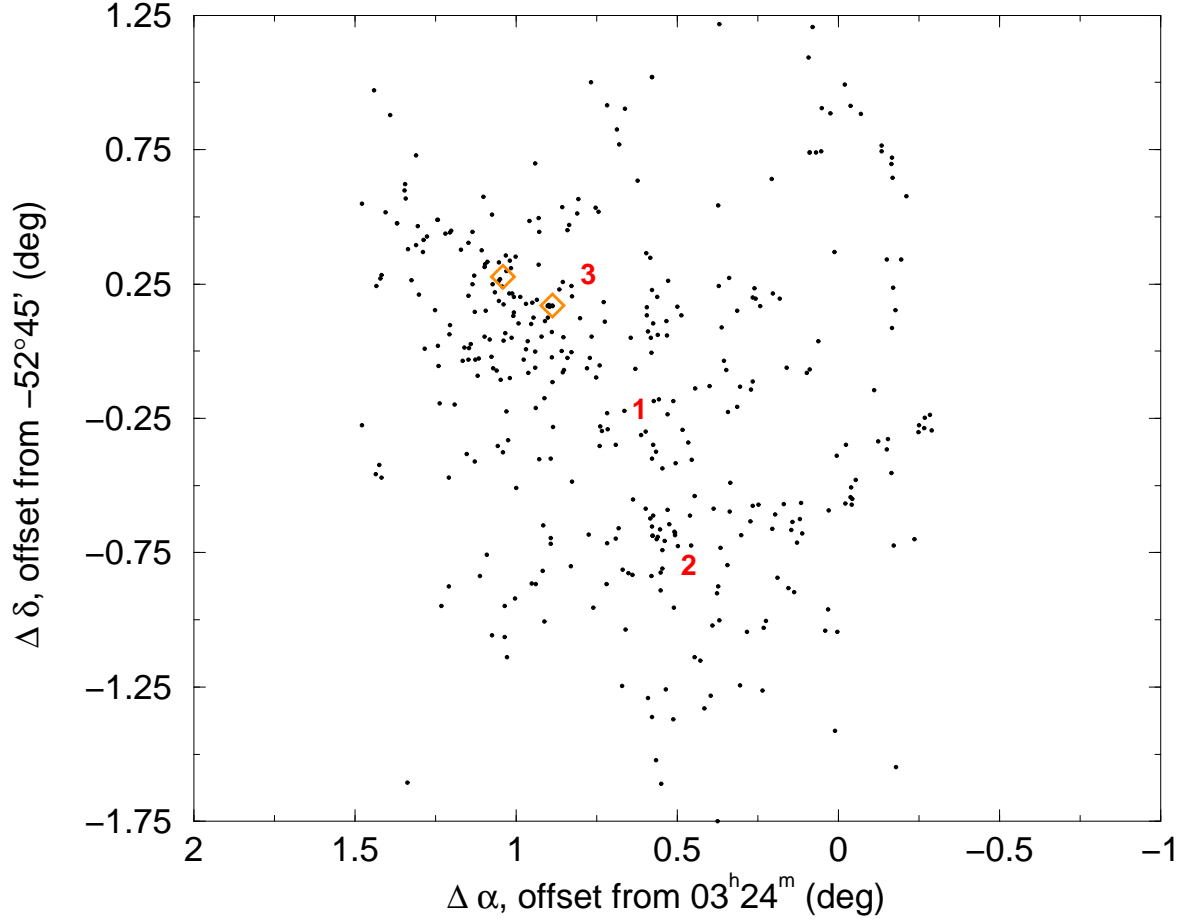


Figure 7.8 Spatial map of the A3128/25 region with $b_J < 18.50$ galaxies shown as small filled circles. Only galaxies with $16,500 \leq cz \leq 20,500 \text{ km s}^{-1}$ are shown in the equal area map, which is offset from $03^{\text{h}}24^{\text{m}}, -52^{\circ}45'$. Open orange diamonds represent the positions of the two X-ray emission peaks at a similar PA to the A3128–A3125 spatial axis. The numbered regions mark the areas of specific interest for this section: 1) APMCC399 is a low-richness cluster that connects A3128 and A3125; 2) The dispersed, rich cluster A3125 as it relates to extended radio emission; 3) Smaller-scale substructure within the richest HRS cluster, A3128.

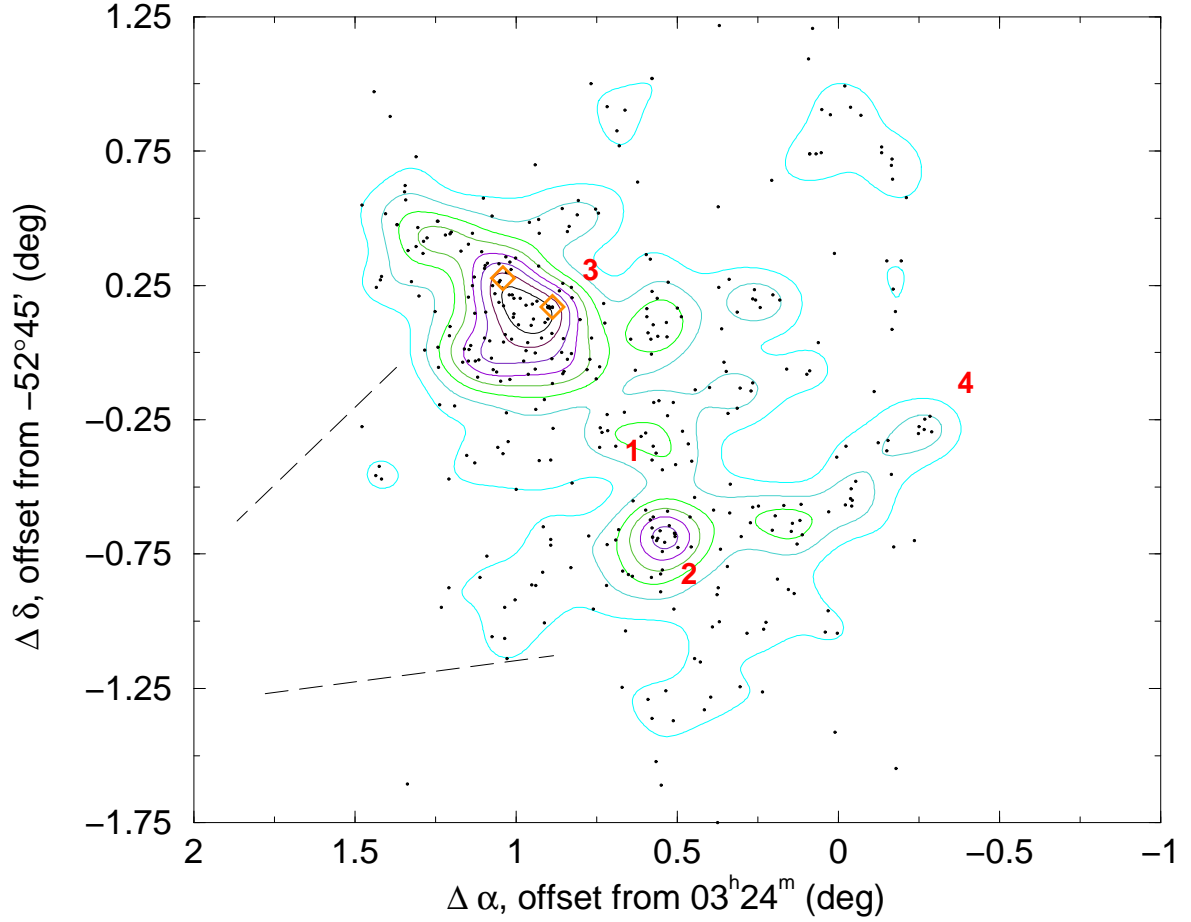


Figure 7.9 Smoothed distribution of $b_J < 18.50$ galaxies in the A3128/25 region with $16,500 \leq cz \leq 20,500 \text{ km s}^{-1}$. The smoothing radius of the Gaussian kernel was fixed at 0.25° ($\sim 1.5 \text{ Mpc}$), after varying both the grid mesh and the radius. The galaxies used to create the smoothed map are shown as small filled circles. The orange diamonds representing peaks of X-ray emission nearly align with the bulge in galaxy distribution to the northeast. The extension of A3125 in a near perpendicular direction to the A3128–A3125 axis is noticeable. The equal area map is offset from $03^{\text{h}}24^{\text{m}}, -52^\circ45'$. The numbers refer to the same clusters in Fig. 7.8, where “4” corresponds to APMCC391. The arrow denotes the approximate direction of the filament from A3158 in §7.2.

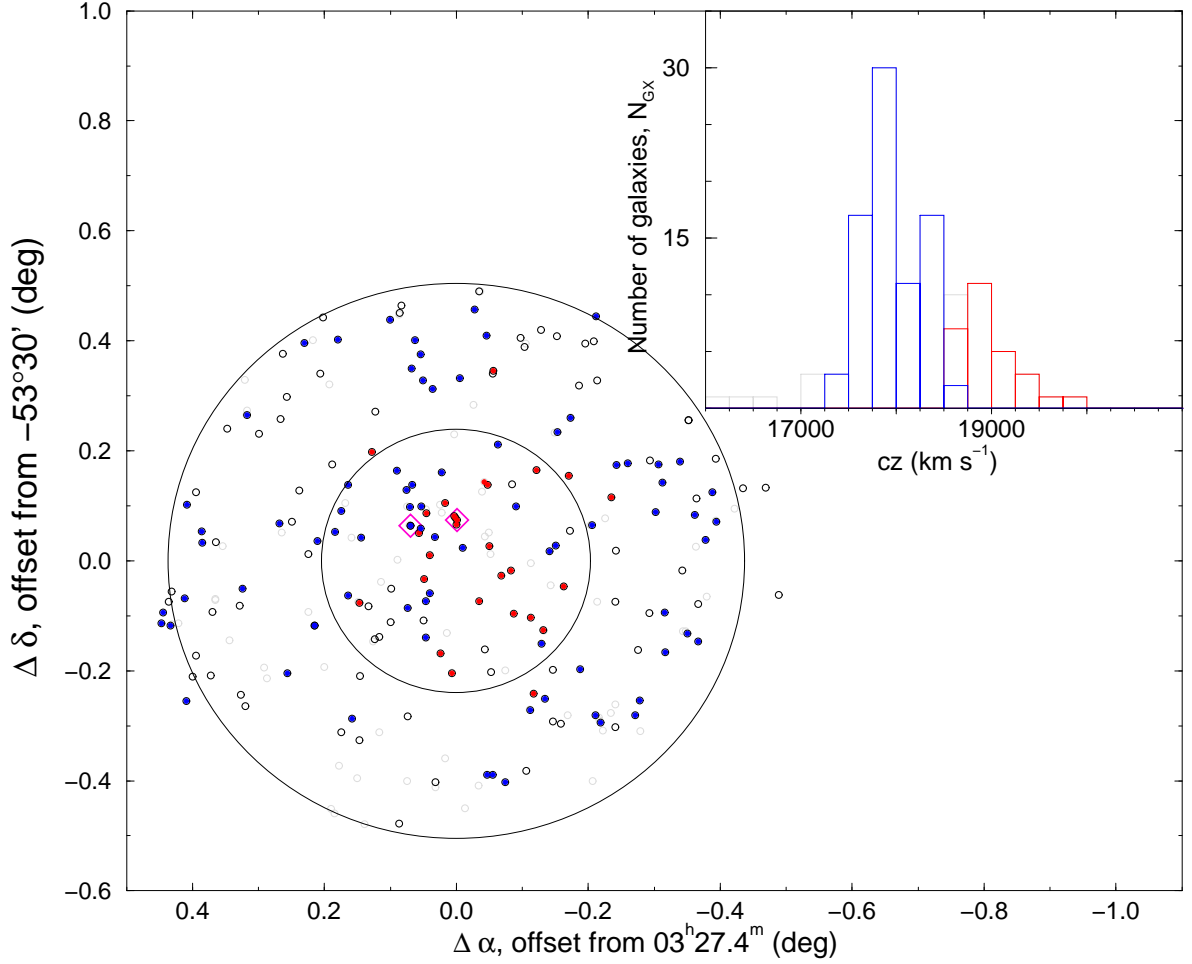


Figure 7.10 Equal-area map of $b_J < 19.0$ galaxies within the inner 0.5° of A3125. The completeness is $\sim 75\%$, where all galaxies are shown as light open circles. Back/foreground galaxies are shown as darker open circles. The cluster population ($17,000\text{--}19,500 \text{ km s}^{-1}$) is comprised of two distinct populations (red and blue filled circles), which is more noticeable as the cluster radius decreases. The inset histogram shows the two populations as a function of cz . Two open diamonds in the spatial map indicate two extended radio sources near the center of the cluster, but belonging to different cluster populations.

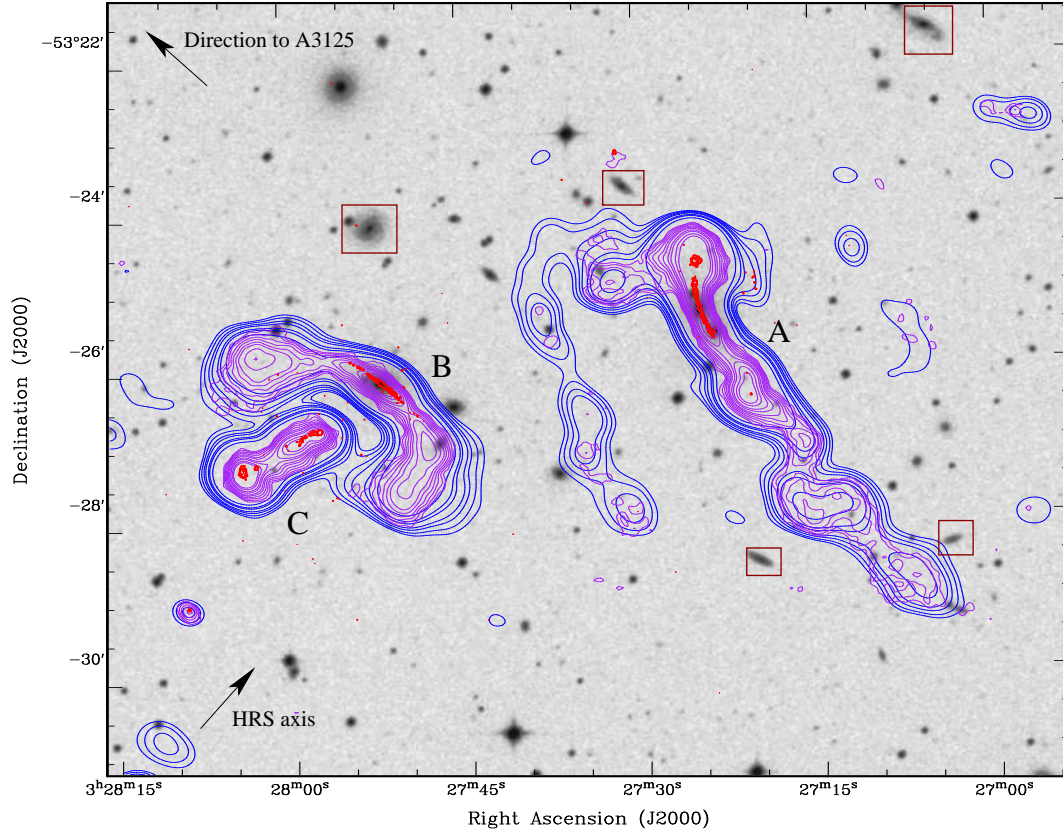


Figure 7.11 20cm image, obtained with the ATCA, of tailed radio sources in A3125. 20cm continuum emission contours of increasing intensity are shown. A galaxy association with the radio source to the east (left) is a member of the blue population in Fig. 7.10, with a velocity of $17,700 \text{ km s}^{-1}$, while a galaxy associated with the radio source to the west (right) has a higher velocity at $19,300 \text{ km s}^{-1}$ and is a member of the red group. The radio emission to the far east (in between the tails) is believed to be a background source with no visible optical counterpart.

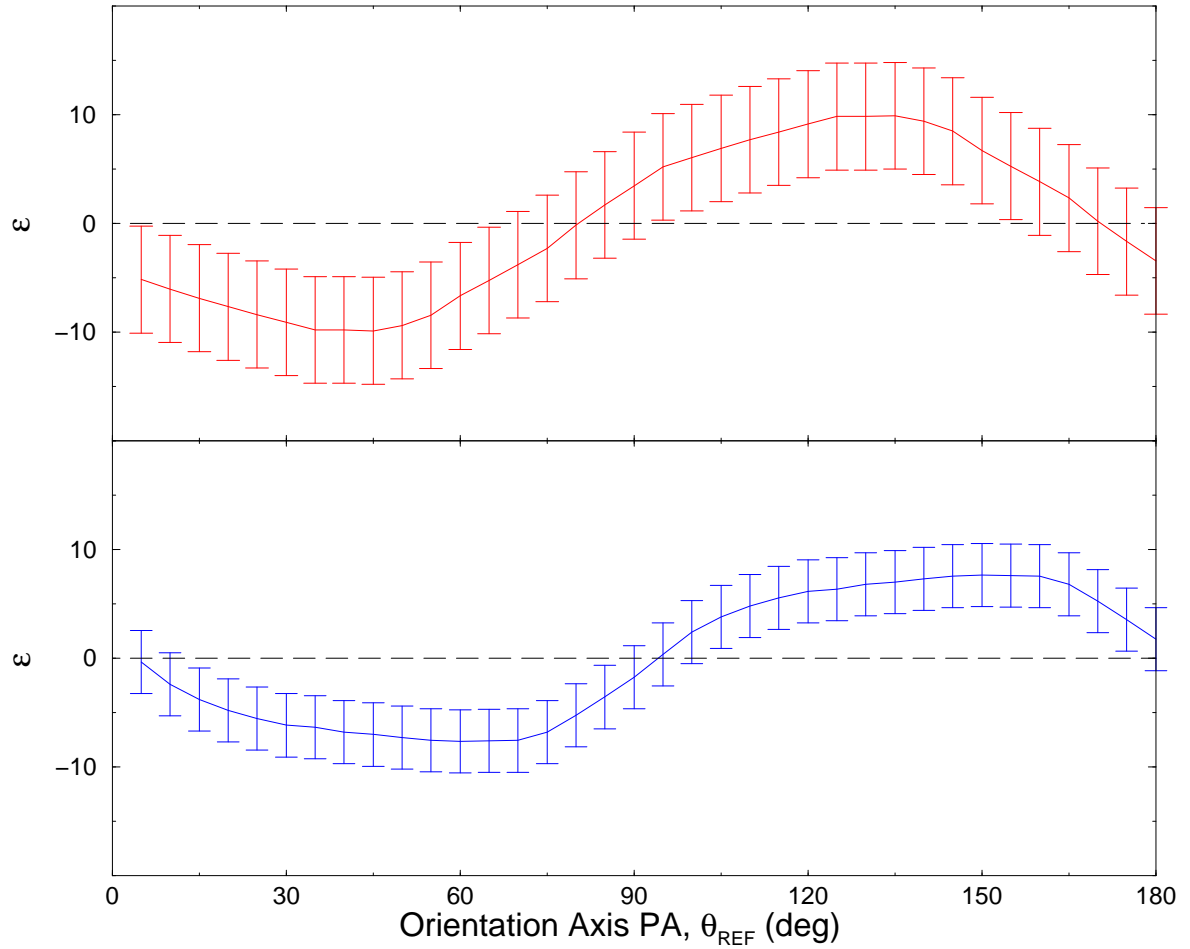


Figure 7.12 Orientation parameter, ϵ , as a function of PA for the two individual populations in A3125. Colors of the curves match the populations in Fig. 7.10. A significantly different orientation is not noted between the groups, though neither group shows a significant orientation away from isotropy, i.e., both tests give an $\approx 2\sigma$ result.

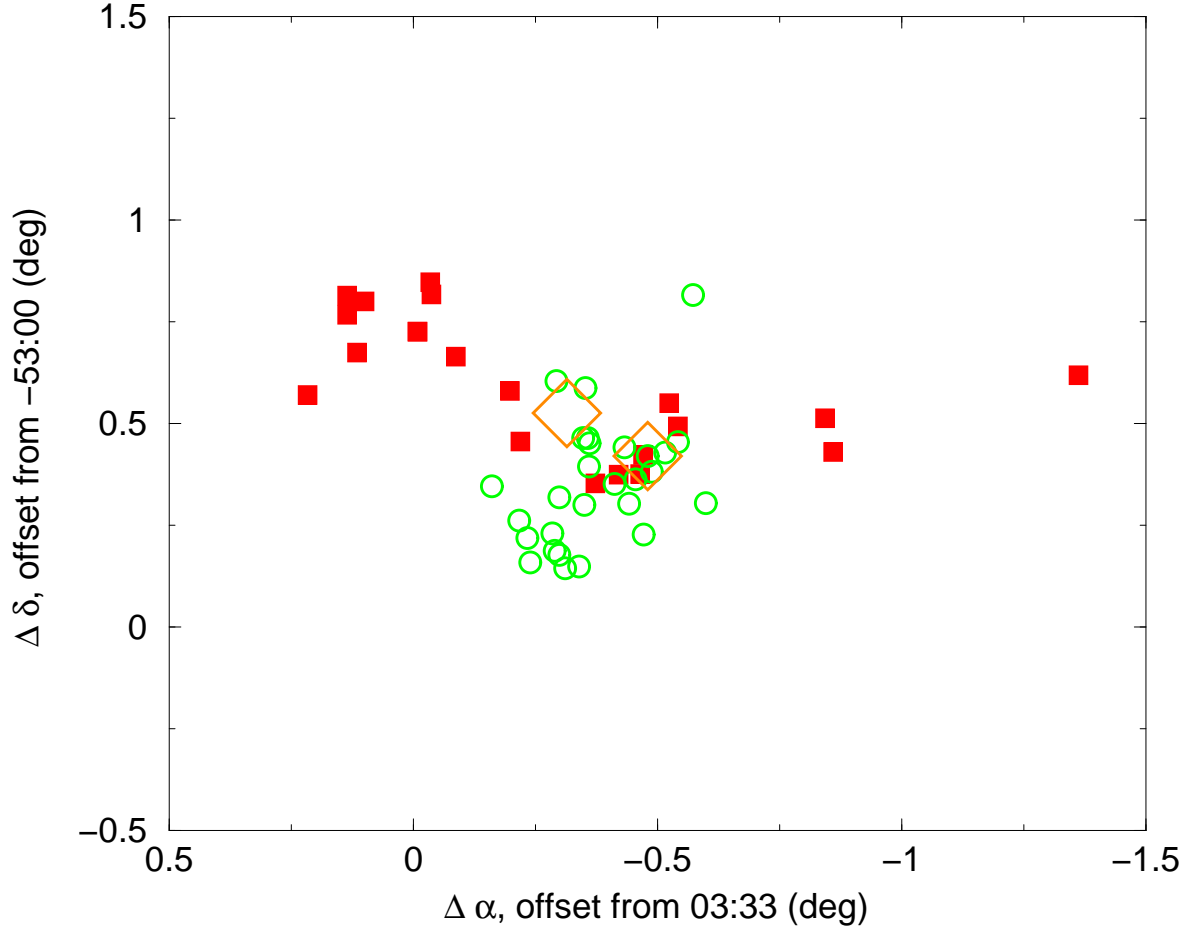


Figure 7.13 Equal-area sky map of A3128 galaxies within the pre-defined A3128-G1 (open circles) and A3128-F1 (open squares) designations by RGC02. Filled circles, light and dark, were segregated on the basis of PA to examine the possibility of directional infall. As shown in the bottom right-hand corner, the orientation of the galaxies is perpendicular to the presumed infall direction. The open orange diamonds indicate the X-ray peaks, which align with the A3128-F1 designation as discussed in RGC02.

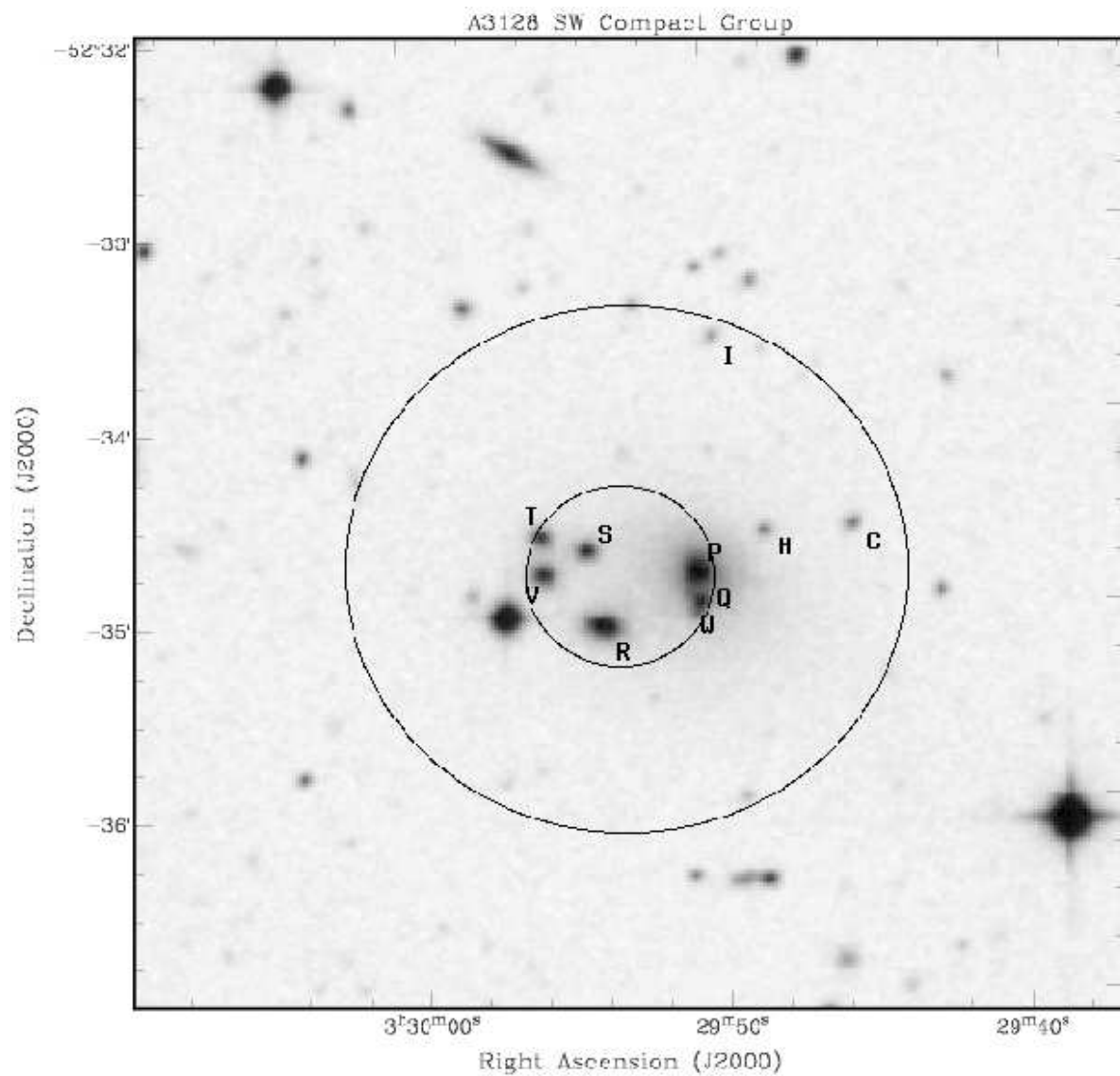


Figure 7.14 Digitized sky survey image of the southwest compact group in A3128. Letters of group members (inner circle) refer to Table 2.6, column 1, and other galaxies are referenced in §7.3.4. The inner circle refers to the smallest area that contains the geometrical centers of all potential members, while the outer circle is three times the inner diameter.

Chapter 8

CONCLUSION

“It is a sheer illusion to think that in relation to truth there is an abridgement, a short cut that dispenses with the necessity of struggling for it.”—Søren Kierkegaard

8.1 Our Initial Look at the HRS

The aim of this thesis is to provide a comprehensive view of one of the most overdense structures in the low-redshift universe. We have approached the problem from **four** different angles. First, we have shown that the HRS is not one large conglomeration of intercluster galaxies, spherically collapsing under its own mass. On the contrary and quite clearly, the HRS displays two primary redshift components extending over the full area of our survey. We demonstrated that the mean overdensity in the HRS rivals that of the Shapley supercluster within the intercluster regions (1.4:2.3). The redshift bounds were fairly well marked by significant ($\sim 1500 \text{ km s}^{-1}$) breaks in the galaxy distribution. The galaxy clusters, however, which are normally thought to accurately trace the large-scale, intercluster structure, did not show the same arrangement as the less-dense intercluster galaxies, initially.

We were then given the opportunity to observe all the known galaxy clusters in the HRS, which had previously not revealed the two-component nature of their intercluster counterparts. Many of these clusters had published redshifts that were based on only one or two (or even “ $N_{\text{gx}} > 0$ ”) individual redshifts. Reliable mean cluster velocities

and adequate dispersions, like those which were calculated, need at least 10 individual galaxy redshifts. When a reliable velocity was established for each cluster, the two distributions within the HRS, both intercluster galaxies and galaxy clusters, displayed a similar arrangement.

But what was that arrangement exactly? Was it just two big clumps instead of one? And what about the formation of these two “clumps”? How were we to put in perspective the “small-scale” arrangement of wispy radio tails pointing in different directions? Was there some connection?

8.2 A Fifth Wheel?

I told you that there was ‘four distinct angles,’ and there are, I think. But without GyVe, (GalaxyViewer) I’d be feeling infinitely worse than I already do, for having such a great dataset and so little results. GyVe is a fully interactive software tool that allows us to obtain that comprehensive viewpoint, with the opportunity to see intercluster galaxies and galaxy clusters cohabiting the same space.

With the help of GyVe, we have learned:

(I) **Voids dominate the landscape.** From the first time we viewed the extended 6dF data in GyVe, it was the empty spaces that left the greatest impression. I don’t think I ever would have gotten that point, otherwise. Hopefully, this work highlights that viewpoint. We see that 6 modest size voids ($R_{\text{VOID}} \approx 10 h^{-1}$ Mpc), which take up only about 10% of the HRS volume, really aid in determining one of the most *overdense* regions. The Aitoff projections show that clusters and galaxies reside together. Even at large radii, e.g., the $2.5R_i/R_{\text{VOID}}$ plots really do show that as more galaxies fall onto the surface of the void, they do so in predominantly the same places. Or, if they don’t pileup in the same places, they extend away from the pileups in some organized fashion. What is ironic, and somewhat scary, are the Aitoff plots presented in Colberg et al. (Fig. 1, 1999) from *inside the clusters*. They bear striking resemblance to the Aitoff plots in

this work from *inside the voids*. How are we to understand this reality, except to say, the large-scale network really is sponge-like and the overdensities and underdensities are interconnected.

Furthermore, it is observed in the radial profiles that there is something different about the voids near the HRS, what we refer to as the embedded void sample. We know now that Voids 1 and 2 were giving the two component structure seen so clearly in Paper I. What Voids 3 and 6 reveal, I believe, is that the “effective” HRS does extend to northern clusters, like A3122, and southern clusters, like A3266. Our dataset barely extends to those values of δ , i.e., to the extreme south or north of the HRS, but it seems that the nature of the voids reveals this fact. But if the overdensity is less in the new larger area, do we then say that the supercluster does *not* extend beyond the 2002 ($12^\circ \times 12^\circ$) area? It seems that we must proceed cautiously and choose the “direction” of the HRS carefully, e.g., along the void boundaries.

(II) **There’s no such thing as a “slam dunk.”** The A3158–A3128–A3125 region is truly unique, because these structures are sitting so neatly at the same redshift, perpendicular to the plane of the sky. The contiguous overdensity from A3158 to what I argue is more A3125 is fairly certain, I think. The perpendicular continuity from A3128–APMCC399–A3125 is also fairly certain. So here we have it, the prototypical filament intersection occurring at a non-rich cluster, A3125. Furthermore, why does seeming “slam dunk”, triple alignment in A3125 of the kinematic substructure, the radio extended emission, and the perpendicular filament axis, come up empty (i.e., “Buckley’s”) when the orientation test is applied?

8.3 Continuing Work!

There’s so much.

Regarding the filaments, we have only scratched the surface of calculating, at least, the overdensities, if not velocity dispersions, for a host of potential elongated structures.

What is the true shapes (in redshift space) of the HRS voids? Are they as spherical as we claim? Or, is there a way to map the surface to reveal a more ellipsoidal shape? Do they, in fact, extend through the volume as tunnels? We aim to create isodensity surfaces of the voids, which will aid greatly in visualizing the underdense regions.

What is the relationship between the intercluster (or inter-void) galaxies and the clusters, especially as they relate to the thicknesses between the voids? Although we have known for some time that overdensities lie on the surface of voids, but how is that effected by the presence of multiple voids located in near proximity? Are the voids in the HRS region more tightly packed, which aids the overdensity of the supercluster?

Of course, we defined some “void galaxies,” and it would be nice to get some high resolution spectra and imaging of these faint guys. In some ways, the discovery of confirmed “void galaxies” would help to further confirm the actual presence of Void 2.

Lastly, with apparent intercluster filaments defined for the HRS, and the hopeful promise of more in the future, I would like to explore the possibility of using the ultraviolet wavelengths to probe the gas content of these filaments. By observing background AGNs, it is possible to observe the $\text{Ly}\alpha$ dropout of the gas in nearby filaments.

REFERENCES

- Aarseth, S. J., Turner, E. L., & Gott, III, J. R. 1979, *ApJ*, 228, 664
- Abell, G. O. 1958, *ApJS*, 3, 211
- Abell, G. O., Corwin, H. G., & Olowin, R. P. 1989, *ApJS*, 70, 1
- Alonso, M. V., Valotto, C., Lambas, D. G., & Muriel, H. 1999, *MNRAS*, 308, 618
- Andernach, H., Plionis, M., López-Cruz, O., Tago, E., & Basilakos, S. 2005, in *ASP Conf. Ser. 329: Nearby Large-Scale Structures and the Zone of Avoidance*, ed. A. P. Fairall & P. A. Woudt, 289–293
- Ashman, K. A., Bird, C. M., & Zepf, S. E. 1994, *AJ*, 108, 2348
- Aubert, D., Pichon, C., & Colombi, S. 2004, *MNRAS*, 352, 376
- Bahcall, N. A. 1988, in *IAU Symp. 130: Large Scale Structures of the Universe*, ed. J. Audouze, M.-C. Pelletan, & S. Szalay, 229–+
- Bahcall, N. A. & Soneira, R. M. 1982, *ApJ*, 258, L17
- . 1983, *ApJ*, 270, 20
- . 1984, *ApJ*, 277, 27
- Bardelli, S., Zucca, E., Zamorani, G., Moscardini, L., & Scaramella, R. 2000, *MNRAS*, 312, 540
- Bardelli, S., Zucca, E., Zamorani, G., Vettolani, G., & Scaramella, R. 1998, *MNRAS*, 296, 599
- Barmby, P. & Huchra, J. P. 1998, *AJ*, 115, 6
- Baugh, C. M., Croton, D. J., Gaztañaga, E., Norberg, P., Colless, M., Baldry, I. K., Bland-Hawthorn, J., Bridges, T., Cannon, R., Cole, S., & the 2dFGRS team. 2004, *MNRAS*, 351, L44
- Beers, T. C., Flynn, K., & Gebhardt, K. 1990, *AJ*, 100, 32
- Benson, A. J., Pearce, F. R., Frenk, C. S., Baugh, C. M., & Jenkins, A. 2001, *MNRAS*, 320, 261
- Bertschinger, E. 1985, *ApJS*, 58, 1
- Binggeli, B. 1982, *A&A*, 107, 338
- Blaes, O. M., Goldreich, P. M., & Villumsen, J. V. 1990, *ApJ*, 361, 331

- Blair, M. & Gilmore, G. 1982, PASP, 94, 742
- Bond, J. R., Kofman, L., & Pogosyan, D. 1996, Nature, 380, 603
- Bothun, G. D., Geller, M. J., Kurtz, M. J., Huchra, J. P., & Schild, R. E. 1992, ApJ, 395, 347
- Box, G. E. P. 1953, Biometrika, 40, 318
- Bregman, J. N., Dupke, R. A., & Miller, E. D. 2004, ApJ, 614, 31
- Bruzual A., G. 1983, ApJ, 273, 105
- Caldwell, N. & Rose, J. A. 1997, AJ, 113, 492
- Cannon, R. D. 1984, in ASSL Vol. 110: IAU Colloq. 78: Astronomy with Schmidt-Type Telescopes, ed. M. Capaccioli, 25–+
- Cen, R. & Ostriker, J. P. 1999, ApJ, 514, 1
- Cen, R., Tripp, T. M., Ostriker, J. P., & Jenkins, E. B. 2001, ApJ, 559, L5
- Chamaraux, P., Cayatte, V., Balkowski, C., & Fontanelli, P. 1990, A&A, 229, 340
- Chincarini, G., Tarengi, M., Sol, H., Crane, P., Manousoyannaki, I., & Materne, J. 1984, A&AS, 57, 1
- Chincarini, G. L., Giovanelli, R., & Haynes, M. P. 1983, A&A, 121, 5
- Colberg, J. M., Krughoff, K. S., & Connolly, A. J. 2005a, MNRAS, 359, 272
- Colberg, J. M., Sheth, R. K., Diaferio, A., Gao, L., & Yoshida, N. 2005b, MNRAS, 360, 216
- Colberg, J. M., White, S. D. M., Jenkins, A., & Pearce, F. R. 1999, MNRAS, 308, 593
- Colberg, J. M., White, S. D. M., MacFarland, T. J., Jenkins, A., Pearce, F. R., Frenk, C. S., Thomas, P. A., & Couchman, H. M. P. 2000a, MNRAS, 313, 229
- Colberg, J. M., White, S. D. M., Yoshida, N., MacFarland, T. J., Jenkins, A., Frenk, C. S., Pearce, F. R., Evrard, A. E., Couchman, H. M. P., Efstathiou, G., & The Virgo Consortium. 2000b, MNRAS, 319, 209
- Colless, M., Dalton, G., Maddox, S., Sutherland, W., Norberg, P., Cole, S., Bland-Hawthorn, J., Bridges, T., Cannon, R., Collins, C., & the 2dFGRS team. 2001, MNRAS, 328, 1039
- Cortese, L., Gavazzi, G., Boselli, A., Iglesias-Paramo, J., & Carrasco, L. 2004, A&A, 425, 429

- Cross, N., Driver, S. P., Couch, W., Baugh, C. M., Bland-Hawthorn, J., Bridges, T., Cannon, R., Cole, S., Colless, M., Collins, C., & the 2dFGRS team. 2001, MNRAS, 324, 825
- Croton, D. J., Colless, M., Gaztañaga, E., Baugh, C. M., Norberg, P., Baldry, I. K., Bland-Hawthorn, J., Bridges, T., Cannon, R., Cole, S., & the 2dFGRS team. 2004, MNRAS, 352, 828
- Croton, D. J., Farrar, G. R., Norberg, P., Colless, M., Peacock, J. A., Baldry, I. K., Baugh, C. M., Bland-Hawthorn, J., Bridges, T., Cannon, R., & the 2dFGRS team. 2005, MNRAS, 356, 1155
- Cruddace, R., Voges, W., Böhringer, H., Collins, C. A., Romer, A. K., MacGillivray, H., Yentis, D., Schuecker, P., Ebeling, H., & De Grandi, S. 2002, ApJS, 140, 239
- Dalton, G. B., Efstathiou, G., Maddox, S. J., & Sutherland, W. J. 1994, MNRAS, 269, 151
- Dalton, G. B., Maddox, S. J., Sutherland, W. J., & Efstathiou, G. 1997, MNRAS, 289, 263
- Davé, R. & Tripp, T. M. 2001, ApJ, 553, 528
- de Lapparent, V., Geller, M. J., & Huchra, J. P. 1986, ApJ, 302, L1
- De Propris, R., Couch, W. J., Colless, M., Dalton, G. B., Collins, C., Baugh, C. M., Bland-Hawthorn, J., Bridges, T., Cannon, R., Cole, S., & the 2dFGRS team. 2002, MNRAS, 329, 87
- de Vaucouleurs, G. 1956, *Vistas in Astronomy*, 2, 1584
- . 1961, AJ, 66, 629
- Dekel, A., West, M. J., & Aarseth, S. J. 1984, ApJ, 279, 1
- den Hartog, R. 1995, Ph.D. Thesis
- . 1997, MNRAS, 284, 286
- Dietrich, J. P., Schneider, P., Clowe, D., Romano-Díaz, E., & Kerp, J. 2005, A&A, 440, 453
- Doroshkevich, A. G., Sunyaev, R. A., & Zeldovich, I. B. 1974, in IAU Symp. 63: Confrontation of Cosmological Theories with Observational Data, ed. M. S. Longair, 213–225
- Doroshkevich, A. G., Tucker, D. L., Oemler, A. J., Kirshner, R. P., Lin, H., Shethman, S. A., Landy, S. D., & Fong, R. 1996, MNRAS, 283, 1281

- Doroshkevich, A. G., Zel'Dovich, Y. B., & Novikov, I. D. 1967, *Soviet Astronomy*, 11, 233
- Dressler, A. 1980, *ApJS*, 42, 565
- Drinkwater, M. J., Parker, Q. A., Proust, D., Slezak, E., & Quintana, H. 2004, *Publications of the Astronomical Society of Australia*, 21, 89
- Drinkwater, M. J., Proust, D., Parker, Q. A., Quintana, H., & Slezak, E. 1999, *Publications of the Astronomical Society of Australia*, 16, 113
- Dubinski, J., da Costa, L. N., Goldwirth, D. S., Lecar, M., & Piran, T. 1993, *ApJ*, 410, 458
- Ebeling, H., Barrett, E., & Donovan, D. 2004, *ApJ*, 609, L49
- Efstathiou, G., Ellis, R. S., & Peterson, B. A. 1988, *MNRAS*, 232, 431
- Einasto, J., Einasto, M., Gramann, M., & Saar, E. 1991, *MNRAS*, 248, 593
- Einasto, M., Einasto, J., Tago, E., Andernach, H., Dalton, G. B., & Müller, V. 2002, *AJ*, 123, 51
- Einasto, M., Einasto, J., Tago, E., Dalton, G. B., & Andernach, H. 1994, *MNRAS*, 269, 301
- Einasto, M., Einasto, J., Tago, E., Müller, V., & Andernach, H. 2001, *AJ*, 122, 2222
- Einasto, M., Jaaniste, J., Einasto, J., Heinämäki, P., Müller, V., & Tucker, D. L. 2003, *A&A*, 405, 821
- Einasto, M., Tago, E., Jaaniste, J., Einasto, J., & Andernach, H. 1997, *A&AS*, 123, 119
- El-Ad, H. & Piran, T. 1997, *ApJ*, 491, 421
- Erdoğan, P., Lahav, O., Zaroubi, S., Efstathiou, G., Moody, S., Peacock, J. A., Colless, M., Baldry, I. K., Baugh, C. M., Bland-Hawthorn, J., & the 2dFGRS team. 2004, *MNRAS*, 352, 939
- Evrard, A. E., MacFarland, T. J., Couchman, H. M. P., Colberg, J. M., Yoshida, N., White, S. D. M., Jenkins, A., Frenk, C. S., Pearce, F. R., Peacock, J. A., & Thomas, P. A. 2002, *ApJ*, 573, 7
- Faber, S. M. & Gallagher, J. S. 1979, *ARA&A*, 17, 135
- Fleenor, M. C., Rose, J. A., Christiansen, W. A., Hunstead, R. W., Johnston-Hollitt, M., Drinkwater, M. J., & Saunders, W. 2005, *AJ*, 130, 957
- . 2006, *AJ*, 131, 545
- Floor, S. N., Melott, A. L., & Motl, P. M. 2004, *ApJ*, 611, 153

- Frith, W. J., Buswell, G. S., Fong, R., Metcalfe, N., & Shanks, T. 2003, MNRAS, 345, 1049
- Fukugita, M., Hogan, C. J., & Peebles, P. J. E. 1998, ApJ, 503, 518
- Fukugita, M., Shimasaku, K., & Ichikawa, T. 1995, PASP, 107, 945
- Fuller, T. M., West, M. J., & Bridges, T. J. 1999, ApJ, 519, 22
- Geller, M. J. & Huchra, J. P. 1989, Science, 246, 897
- Giovanelli, R. & Haynes, M. P. 1985, AJ, 90, 2445
- Giovanelli, R., Haynes, M. P., & Chincarini, G. L. 1986, ApJ, 300, 77
- Girardi, M., Biviano, A., Giuricin, G., Mardirossian, F., & Mezzetti, M. 1995, ApJ, 438, 527
- Girardi, M., Giuricin, G., Mardirossian, F., Mezzetti, M., & Boschini, W. 1998, ApJ, 505, 74
- Goldberg, D. M., Jones, T. D., Hoyle, F., Rojas, R. R., Vogeley, M. S., & Blanton, M. R. 2005, ApJ, 621, 643
- Gomez, P. L., Ledlow, M. J., Burns, J. O., Pinkey, J., & Hill, J. M. 1997, AJ, 114, 1711
- Gott, III, J. R., Dickinson, M., & Melott, A. L. 1986, ApJ, 306, 341
- Gottlöber, S., Lokas, E. L., Klypin, A., & Hoffman, Y. 2003, MNRAS, 344, 715
- Gray, M. E., Taylor, A. N., Meisenheimer, K., Dye, S., Wolf, C., & Thommes, E. 2002, ApJ, 568, 141
- Gray, P. M. 1983, Proc. Soc. Photo-opt. Instr. Eng, 374, 160
- Grazian, A., Omizzolo, A., Corbally, C., Cristiani, S., Haehnelt, M. G., & Vanzella, E. 2002, AJ, 124, 2955
- Gregory, S. A. & Thompson, L. A. 1978, ApJ, 222, 784
- Gregory, S. A., Thompson, L. A., & Tifft, W. G. 1981, ApJ, 243, 411
- Hambly, N. C., Irwin, M. J., & MacGillivray, H. T. 2001a, MNRAS, 326, 1295
- Hambly, N. C., MacGillivray, H. T., Read, M. A., Tritton, S. B., Thomson, E. B., Kelly, B. D., Morgan, D. H., Smith, R. E., Driver, S. P., Williamson, J., & the SuperCOSMOS team. 2001b, MNRAS, 326, 1279
- Hauser, M. G. & Peebles, P. J. E. 1973, ApJ, 185, 757
- Hickson, P. 1997, ARA&A, 35, 357

- Hickson, P., Mendes de Oliveira, C., Huchra, J. P., & Palumbo, G. G. 1992, *ApJ*, 399, 353
- Hoessel, J. G., Gunn, J. E., & Thuan, T. X. 1980, *ApJ*, 241, 486
- Hoyle, F., Rojas, R. R., Vogeley, M. S., & Brinkmann, J. 2005, *ApJ*, 620, 618
- Hoyle, F. & Vogeley, M. S. 2002, *ApJ*, 566, 641
- . 2004, *ApJ*, 607, 751
- Hubble, E. 1929, *Proceedings of the National Academy of Science*, 15, 168
- Huchra, J. P., Geller, M. J., de Lapparent, V., & Burg, R. 1988, in *IAU Symp. 130: Large Scale Structures of the Universe*, ed. J. Audouze, M.-C. Pelletan, & S. Szalay, 105–+
- Hudson, M. J., Smith, R. J., Lucey, J. R., Schlegel, D. J., & Davies, R. L. 1999, *ApJ*, 512, L79
- Humason, M. L., Mayall, N. U., & Sandage, A. R. 1956, *AJ*, 61, 97
- Icke, V. 1984, *MNRAS*, 206, 1P
- Irwin, M. & McMahon, R. 1992, in *IAU Commission on Instruments*, 31–+
- Jacoby, G. H., Hunter, D. A., & Christian, C. A. 1984, *ApJS*, 56, 257
- Joeveer, M. & Einasto, J. 1978, in *IAU Symp. 79: Large Scale Structures in the Universe*, ed. M. S. Longair & J. Einasto, 241–250
- Johnston-Hollitt, M., Fleenor, M., Rose, J., Christiansen, W., & Hunstead, R. W. 2004, in *IAU Colloq. 195: Outskirts of Galaxy Clusters: Intense Life in the Suburbs*, 423–425
- Jones, C. & Forman, W. 1999, *ApJ*, 511, 65
- Jones, D. H., Saunders, W., Colless, M., Read, M. A., Parker, Q. A., Watson, F. G., Campbell, L. A., Burkey, D., Mauch, T., Moore, L., & the 6dFGS team. 2004, *MNRAS*, 355, 747
- Jones, D. H., Saunders, W., Read, M., & Colless, M. 2005, *Publications of the Astronomical Society of Australia*, 22, 277
- Jones, L. A. 1998, *Ph.D. Thesis*
- Jones, L. R., Ponman, T. J., Horton, A., Babul, A., Ebeling, H., & Burke, D. J. 2003, *MNRAS*, 343, 627
- Kaiser, N. 1987, *MNRAS*, 227, 1

- Kalinkov, M., Valtchanov, I., & Kuneva, I. 1998, *ApJ*, 506, 509
- Katgert, P., Mazure, A., den Hartog, R., Adami, C., Biviano, A., & Perea, J. 1998, *A&AS*, 129, 399
- Kauffmann, G., Colberg, J. M., Diaferio, A., & White, S. D. M. 1999, *MNRAS*, 303, 188
- Kennicutt, R. C. 1992, *ApJS*, 79, 255
- Kirshner, R. P., Oemler, Jr., A., Schechter, P. L., & Sheckman, S. A. 1981, *ApJ*, 248, L57
- Kirshner, R. P., Oemler, A. J., Schechter, P. L., & Sheckman, S. A. 1987, *ApJ*, 314, 493
- Kitzbichler, M. G. & Saurer, W. 2003, *ApJ*, 590, L9
- Klamer, I., Subrahmanyam, R., & Hunstead, R. W. 2004, *MNRAS*, 351, 101
- Klypin, A. A. & Kopylov, A. I. 1983, *Soviet Astronomy Letters*, 9, 41
- Knebe, A., Gill, S. P. D., Gibson, B. K., Lewis, G. F., Ibata, R. A., & Dopita, M. A. 2004, *ApJ*, 603, 7
- Kodama, T., Smail, I., Nakata, F., Okamura, S., & Bower, R. G. 2001, *ApJ*, 562, L9
- Kull, A. & Böhringer, H. 1999, *A&A*, 341, 23
- Lachière-Rey, M. & Maurogordato, S. 1987, in *IAU Symp. 124: Observational Cosmology*, ed. A. Hewitt, G. Burbidge, & L. Z. Fang, 359–+
- Ledlow, M. J., Voges, W., Owen, F. N., & Burns, J. O. 2003, *AJ*, 126, 2740
- Lewis, I. J., Cannon, R. D., Taylor, K., Glazebrook, K., Bailey, J. A., Baldry, I. K., Barton, J. R., Bridges, T. J., Dalton, G. B., Farrell, T. J., & the 2dFGRS team. 2002, *MNRAS*, 333, 279
- Loken, C., Norman, M. L., Nelson, E., Burns, J., Bryan, G. L., & Motl, P. 2002, *ApJ*, 579, 571
- Longair, M. S., ed. 1998, *Galaxy formation*, ed. M. S. Longair
- Loveday, J., Peterson, B. A., Maddox, S. J., & Efstathiou, G. 1996, *ApJS*, 107, 201
- Lucey, J. R., Dickens, R. J., Mitchell, R. J., & Dawe, J. A. 1983, *MNRAS*, 203, 545
- Mathis, H. & White, S. D. M. 2002, *MNRAS*, 337, 1193
- Mauch, T., Murphy, T., Buttery, H. J., Curran, J., Hunstead, R. W., Piestrzynski, B., Robertson, J. G., & Sadler, E. M. 2003, *MNRAS*, 342, 1117

- Mazure, A., Katgert, P., den Hartog, R., Biviano, A., Dubath, P., Escalera, E., Focardi, P., Gerbal, D., Giuricin, G., Jones, B., & the ENACS team. 1996, *A&A*, 310, 31
- Mecke, K. R., Buchert, T., & Wagner, H. 1994, *A&A*, 288, 697
- Metcalf, N., Shanks, T., Campos, A., McCracken, H. J., & Fong, R. 2001, *MNRAS*, 323, 795
- Metcalf, N., Shanks, T., Fong, R., & Jones, L. R. 1991, *MNRAS*, 249, 498
- Miller, J., Quammen, C., & Fleenor, M. C. 2006, *IEEE Transactions on Visualization and Computer Graphics Journal*, 13, accepted
- Müller, V., Arbabi-Bidgoli, S., Einasto, J., & Tucker, D. 2000, *MNRAS*, 318, 280
- Muriel, H., Nicotra, M. A., & Lambas, D. G. 1995, *AJ*, 110, 1032
- Neyman, J., Scott, E. L., & Shane, C. D. 1954, *ApJS*, 1, 269
- Norberg, P., Cole, S., Baugh, C. M., Frenk, C. S., Baldry, I., Bland-Hawthorn, J., Bridges, T., Cannon, R., Colless, M., Collins, C., & the 2dFGRS team. 2002, *MNRAS*, 336, 907
- Novikov, D. I., Melott, A. L., Wilhite, B. C., Kaufman, M., Burns, J. O., Miller, C. J., & Batuski, D. J. 1999, *MNRAS*, 304, L5
- Oke, J. B. & Sandage, A. 1968, *ApJ*, 154, 21
- Padilla, N. D., Ceccarelli, L., & Lambas, D. G. 2005, *MNRAS*, 363, 977
- Parker, Q. A., Watson, F. G., & Miziarski, S. 1998, in *ASP Conf. Ser. 152: Fiber Optics in Astronomy III*, 80–+
- Patiri, S. G., Betancort-Rijo, J. E., Prada, F., Klypin, A., & Gottlöber, S. 2006, *MNRAS*, 369, 335
- Pearson, E. S. 1931, *Biometrika*, 21, 114
- Peebles, P. J. E. 1974, *ApJ*, 189, L51+
- . 2001, *ApJ*, 557, 495
- Peebles, P. J. E. & Dicke, R. H. 1968, *ApJ*, 154, 891
- Pimbblet, K. A. 2005, *MNRAS*, 358, 256
- Pimbblet, K. A., Drinkwater, M. J., & Hawkrigg, M. C. 2004a, *MNRAS*, 354, L61
- . 2004b, *MNRAS*, 354, L61
- Plionis, M. & Basilakos, S. 2002, *MNRAS*, 329, L47

- Plionis, M., Benoist, C., Maurogordato, S., Ferrari, C., & Basilakos, S. 2003, *ApJ*, 594, 144
- Poggianti, B. M. 1997, *A&AS*, 122, 399
- Ponman, T. J., Allan, D. J., Jones, L. R., Merrifield, M., McHardy, I. M., Lehto, H. J., & Luppino, G. A. 1994, *Nature*, 369, 462
- Porter, S. C. & Raychaudhury, S. 2005, *MNRAS*, 364, 1387
- Postman, M., Geller, M. J., & Huchra, J. P. 1988, *AJ*, 95, 267
- Praton, E. A., Melott, A. L., & McKee, M. Q. 1997, *ApJ*, 479, L15+
- Press, W. H. & Schechter, P. 1974, *ApJ*, 187, 425
- Quintana, H., Carrasco, E. R., & Reisenegger, A. 2000, *AJ*, 120, 511
- Quintana, H., Ramirez, A., Melnick, J., Raychaudhury, S., & Slezak, E. 1995, *AJ*, 110, 463
- Ramella, M., Diaferio, A., Geller, M. J., & Huchra, J. P. 1994, *AJ*, 107, 1623
- Regos, E. & Geller, M. J. 1991, *ApJ*, 377, 14
- Reisenegger, A., Quintana, H., Carrasco, E. R., & Maze, J. 2000, *AJ*, 120, 523
- Rhee, G. F. R. N. & Katgert, P. 1987, *A&A*, 183, 217
- Rojas, R. R., Vogeley, M. S., Hoyle, F., & Brinkmann, J. 2004, *ApJ*, 617, 50
- . 2005, *ApJ*, 624, 571
- Romer, A. K., Nichol, R. C., Holden, B. P., Ulmer, M. P., Pildis, R. A., Merrelli, A. J., Adami, C., Burke, D. J., Collins, C. A., Metevier, A. J., & the SHARC team. 2000, *ApJS*, 126, 209
- Rose, J. A., Gaba, A. E., Christiansen, W. A., Davis, D. S., Caldwell, N., Hunstead, R. W., & Johnston-Hollitt, M. 2002, *AJ*, 123, 1216
- Sakelliou, I. & Merrifield, M. R. 2000, *MNRAS*, 311, 649
- Sandage, A., Tammann, G. A., & Yahil, A. 1979, *ApJ*, 232, 352
- Sathyaprakash, B. S., Sahni, V., & Shandarin, S. 1998, *ApJ*, 508, 551
- Scharf, C., Donahue, M., Voit, G. M., Rosati, P., & Postman, M. 2000, *ApJ*, 528, L73
- Schechter, P. 1976, *ApJ*, 203, 297
- Shane, C. D. & Wirtanen, C. A. 1954, *AJ*, 59, 285

- Shanks, T. 1990, in IAU Symp. 139: The Galactic and Extragalactic Background Radiation, ed. S. Bowyer & C. Leinert, 269–281
- Shapley, H. 1938, Proceedings of the National Academy of Science, 24, 282
- Shectman, S. A., Landy, S. D., Oemler, A., Tucker, D. L., Lin, H., Kirshner, R. P., & Schechter, P. L. 1996, ApJ, 470, 172
- Sheth, J. V. & Sahni, V. 2005, Current Science, 88, 1101
- Sheth, R. K. & van de Weygaert, R. 2004, MNRAS, 350, 517
- Small, T. A., Ma, C.-P., Sargent, W. L. W., & Hamilton, D. 1998, ApJ, 492, 45
- Smith, S. 1936, ApJ, 83, 23
- Soneira, R. M. & Peebles, P. J. E. 1978, AJ, 83, 845
- Struble, M. F. & Peebles, P. J. E. 1985, AJ, 90, 582
- Struble, M. F. & Rood, H. J. 1999, ApJS, 125, 35
- Sunyaev, R. A. & Zeldovich, Y. B. 1972, A&A, 20, 189
- The, L. S. & White, S. D. M. 1986, AJ, 92, 1248
- Thomas, B. C., Melott, A. L., Feldman, H. A., & Shandarin, S. F. 2004, ApJ, 601, 28
- Tinsley, B. M. 1970, Ap&SS, 6, 344
- Tonry, J. & Davis, M. 1979, AJ, 84, 1511
- Trimble, V. 1987, ARA&A, 25, 425
- Tripp, T. M., Savage, B. D., & Jenkins, E. B. 2001, in ASP Conf. Ser. 240: Gas and Galaxy Evolution, ed. J. E. Hibbard, M. Rupen, & J. H. van Gorkom, 557–+
- Tucker, D. L., Oemler, A. J., Hashimoto, Y., Shectman, S. A., Kirshner, R. P., Lin, H., Landy, S. D., Schechter, P. L., & Allam, S. S. 2000, ApJS, 130, 237
- Tully, R. B., Scaramella, R., Vettolani, G., & Zamorani, G. 1992, ApJ, 388, 9
- Valdes, F., Gupta, R., Rose, J. A., Singh, H. P., & Bell, D. J. 2004, ApJS, 152, 251
- van de Weygaert, R. 1991, MNRAS, 249, 159
- van de Weygaert, R. & van Kampen, E. 1993, MNRAS, 263, 481
- van Haarlem, M. & van de Weygaert, R. 1993, ApJ, 418, 544
- Vennik, J., Richter, G. M., & Longo, G. 1993, Astronomische Nachrichten, 314, 393

- Wakamatsu, K., Colless, M., Jarrett, T., Parker, Q., Saunders, W., & Watson, F. 2003, in ASP Conf. Ser. 289: The Proceedings of the IAU 8th Asian-Pacific Regional Meeting, Volume I, ed. S. Ikeuchi, J. Hearnshaw, & T. Hanawa, 97–104
- West, M. J. 1994, MNRAS, 268, 79
- West, M. J. & Blakeslee, J. P. 2000, ApJ, 543, L27
- West, M. J., Jones, C., & Forman, W. 1995, ApJ, 451, L5+
- Yahil, A., Strauss, M. A., Davis, M., & Huchra, J. P. 1991, ApJ, 372, 380
- York, D. G., Adelman, J., Anderson, Jr., J. E., Anderson, S. F., Annis, J., Bahcall, N. A., Bakken, J. A., Barkhouser, R., Bastian, S., Berman, E., & the SDSS Collaboration. 2000, AJ, 120, 1579
- Zeldovich, I. B., Einasto, J., & Shandarin, S. F. 1982, Nature, 300, 407
- Zel'Dovich, Y. B. 1970, A&A, 5, 84
- Zucca, E., Zamorani, G., Scaramella, R., & Vettolani, G. 1993, ApJ, 407, 470
- Zwicky, F. 1933, Helvetica Physica Acta, 6, 110